



HAL
open science

Adaptation of Proof of Concepts Into Quantitative NMR Methods: Clinical Application for the Characterization of Alterations Observed in the Skeletal Muscle Tissue in Neuromuscular Disorders

Ericky Caldas de Almeida Caldas de Almeida Araujo Araujo

► **To cite this version:**

Ericky Caldas de Almeida Caldas de Almeida Araujo Araujo. Adaptation of Proof of Concepts Into Quantitative NMR Methods: Clinical Application for the Characterization of Alterations Observed in the Skeletal Muscle Tissue in Neuromuscular Disorders. Other [cond-mat.other]. Université Paris Sud - Paris XI, 2014. English. NNT: 2014PA112075 . tel-01067940

HAL Id: tel-01067940

<https://theses.hal.science/tel-01067940v1>

Submitted on 24 Sep 2014

HAL is a multi-disciplinary open access archive for the deposit and dissemination of scientific research documents, whether they are published or not. The documents may come from teaching and research institutions in France or abroad, or from public or private research centers.

L'archive ouverte pluridisciplinaire **HAL**, est destinée au dépôt et à la diffusion de documents scientifiques de niveau recherche, publiés ou non, émanant des établissements d'enseignement et de recherche français ou étrangers, des laboratoires publics ou privés.



Comprendre le monde,
construire l'avenir®



UNIVERSITE PARIS-SUD
ÉCOLE DOCTORALE : *Sciences et Technologies de L'Information des
Télécommunications et des Systèmes*

Laboratoire de *Résonance Magnétique Nucléaire de l'Institut de Myologie
(AIM/CEA)*

DISCIPLINE PHYSIQUE

THÈSE DE DOCTORAT

Soutenue le 06/05/2014

par

Ericky Caldas de Almeida Araujo

**Adaptation of Proof of Concepts Into
Quantitative NMR Methods: Clinical Application for the
Characterization of Alterations Observed in the Skeletal
Muscle Tissue in Neuromuscular Disorders**

Composition du jury :

Directeur de thèse :	Pierre CARLIER	Directeur de Recherches (CEA)
Rapporteurs :	Kieren HOLLINGSWORTH Robert MULLER	Professeur (Newcastle University) Professeur (Université de Mons)
Examineurs :	Luc DARASSE Thomas VOIT	Directeur de Recherches CNRS (Université Paris SUD) Professeur (Faculté de Médecine, UPMC INSERM)
Co-encadrant :	Paulo L. de SOUSA	Ingénieur de recherche CNRS (Université de Strasbourg)

Table of Contents

Table of Contents.....	i
List of Figures	iv
List of Tables.....	xvi
1. General Introduction.....	1-1
1.1. Skeletal muscle structure and histology	1-1
1.1.1. Striated muscle architecture	1-1
1.1.2. Muscle cell (Myofiber)	1-2
1.1.3. Intramuscular connective tissue: epimysium, perimysium and endomysium.	1-5
1.1.4. Structural and histological alterations induced by pathology in the skeletal muscle tissue	1-6
1.2. The role of NMR in myology clinical research	1-9
1.2.1. NMR outcome measures currently available for skeletal muscle studies	1-9
1.3. Thesis overview and contributions.....	1-13
2. Basic Concepts of Nuclear Magnetic Resonance	2-1
2.1. The spin magnetic moment and the precession equation	2-2
2.2. Magnetic polarization (Magnetization)	2-3
2.3. Magnetization excitation and the resonance phenomenon.....	2-4
2.4. Relaxation and the Bloch equations.....	2-6
2.5. Nuclear magnetic resonance spectroscopy	2-8
2.6. Nuclear magnetic resonance imaging	2-9
2.7. Characterization of tissue NMR parameters and NMRI contrasts	2-14
2.7.1. The spin echo	2-14
2.7.2. The gradient echo.....	2-15
2.7.3. Magnetization from repeated RF-pulses and the steady state	2-16
2.7.4. Diffusion effects and T2 measurement	2-19
2.8. The issue of B1 in-homogeneity in practical NMRI applications at high field	2-22
3. A Spin-echo-based Method for T2-Mapping in Fat-infiltrated Muscles.....	3-1

3.1.	Quantitative characterization of muscle inflammation	3–1
3.2.	Separation of ¹H-NMR signals from lipids and water	3–5
3.2.1.	Spectral fat-water separation methods	3–5
3.2.2.	Relaxation-based methods for fat-water separation	3–8
3.3.	Validation of an MSE-based method for quantification of muscle water	
	T2 in fat-infiltrated skeletal muscle	3–9
3.3.1.	Methodology	3–11
3.3.1.1.	<i>Data acquisition</i>	3–11
3.3.1.2.	<i>Data treatment</i>	3–12
3.3.2.	Results	3–16
3.3.3.	Discussion and Conclusions	3–21
4.	A Steady-state-based Method for T2-Mapping in Fat-infiltrated Muscles.....	4–1
4.1.	Introduction	4–1
4.1.1.	Context	4–1
4.1.2.	Theory	4–3
4.1.2.1.	<i>The original T2-pSSFP method</i>	4–3
4.1.2.2.	<i>The extended T2-pSSFP method</i>	4–4
4.2.	Methodology	4–6
4.3.	Results.....	4–12
4.4.	Discussion	4–21
4.5.	Conclusion	4–22
5.	Significance of T2 Relaxation of ¹H-NMR Signals in Human Skeletal Muscle	5–1
5.1.	Relaxation in biological tissues.....	5–1
5.2.	Multiexponential muscle water T2-relaxation and compartmentation	
	hypotheses.....	5–2
5.3.	New insights on human skeletal muscle tissue compartments revealed by	
	in vivo T2-relaxometry	5–4
5.3.1.	Methodology	5–4
5.3.1.1.	<i>Data acquisition</i>	5–4
5.3.1.2.	<i>Data treatment</i>	5–8
5.3.2.	Results	5–13
5.3.3.	Discussion	5–16
5.3.4.	Conclusions	5–19
5.4.	Insights on the T2-relaxometry of diseased skeletal muscle tissue	5–20
5.4.1.	Methodology	5–20
5.4.1.1.	<i>Simulations</i>	5–20
5.4.1.2.	<i>In-vivo data acquisition</i>	5–21

5.4.2.	Results.....	5-23
5.4.3.	Discussion and conclusions.....	5-28
6. Application of Ultra-short Time to Echo Methods to Study Short-T2-components in Skeletal Muscle Tissue6-1		
6.1.	The NMR signal from connective tissues	6-2
6.2.	The UTE method	6-4
6.3.	Application of a 3D-UTE sequence for the detection and characterization of a short-T2-component in skeletal muscle tissue	6-7
6.3.1.	Methodology	6-7
6.3.2.	Results.....	6-8
6.3.3.	Discussion	6-10
6.4.	UTE applications for imaging of short-T2-components in SKM tissue ...	6-11
6.5.	In-vivo NMRI of short-T2-components in SKM tissue.....	6-18
6.5.1.	Methodology	6-18
6.5.2.	Results.....	6-19
6.5.3.	Discussion and conclusions.....	6-20
7. Conclusions and Perspectives7-1		

List of Figures

- Figure 1-1 - *Structural organization of the skeletal muscle as a bundle within a bundle arrangement. From the muscle fibers to the fascicles grouped to form the entire muscle.* 1–2
- Figure 1-2 – *Illustration of a skeletal muscle cell (myofiber). Note the tubular system of sarcolemma invaginations (T-tubules) that are linked to the tubules of the sarcoplasmic reticulum that surround each myofibril. The T-tubules are interconnected and opened to the interstitial space, giving the cell a cylindrical spongy-like structure. The small relative volume left in the sarcoplasm is packed with mitochondria (subsarcolemmal and intermyofibrillar), vesicles, lysosomes, lipid droplets among other cellular structures.* 1–3
- Figure 1-3 - *Sarcomere consisting on a bundle of thin and thick myofilaments made up of protein molecules called actin and myosin, respectively. These proteins are arranged parallel to each other in a cylindrical structure, with usually six actin filaments surrounding one myosin filament. Actin molecules are attached the z-discs, which are constituents of the cytoskeleton and define the boundaries of a sarcomere unit.* 1–4
- Figure 1-4 - *Transmission electron microscope image of a longitudinal section cut through an area of human skeletal muscle tissue; borders of two cells separated by the endomysium. Image shows several myofibrils, each with the distinct banding pattern of individual sarcomeres: the darker bands are called A bands(the A band includes a lighter central zone, called the H band), and the lighter bands are called I bands. Each I band is bisected by a dark transverse line called the Z-line). Paired mitochondria are on either side of the electron opaque Z-line. The Z-Line marks the longitudinal extent of a sarcomere unit.* 1–4
- Figure 1-5 - *Scanning electron micrograph of the cut surface of bovine sternomandibularis muscle after digestion with NaOH to remove muscle cell contents and proteoglycans in the IMCT. In (a) we have a low magnification view showing thicker perimysial sheets covering the fascicles along with the thinner endomysial layers; and in (b) a high magnification oblique view showing the fine network of collagen fibres making up the reticular layer of the endomysial sheets that separate adjacent muscles fibres. From (7).....* 1–6

Figure 1-6 – <i>Light microscopy image of a thin transverse section of SKM tissue revealing: (a) Interstitial inflammation (H&E x170); and (b) Phagocytosis of degenerating fibers (H&E x170). From (8).</i>	1–7
Figure 1-7 - <i>End-stage of disease. Note the massive fat (white cells) and moderate connective tissue replacement surrounding a cluster of disordered myofibers (dark cells) (H&E x68). From (8).</i>	1–8
Figure 1-8 – <i>Light microscopy image of a thin transverse slice of normal SKM tissue....</i>	1–8
Figure 1-9 – <i>Example of a cross sectional NMR image of the thigh of a healthy subject. Muscle tissue, fatty components, fascia and cortical bone may be easily identifiable.</i>	1–10
Figure 1-10 – <i>Example of a cross sectional T1-weighted image of the leg of a patient with necrotizing myopathy showing the resulting fatty infiltration following muscle degeneration, remarkably on the soleus and gastrocnemius medialis.</i>	1–11
Figure 1-11 – <i>T2-weighted image of the thighs with application fat-saturation (STIR). Inflammation sites are indicated by arrows. Note the hypo-signal from subcutaneous fat and bone marrow because of the application of fat saturation.</i>	1–12
Figure 2-1 – (a) <i>The magnetic dipole moment μ produced by a dimensionless particle with an electric charge q, inertial angular momentum L. (b) Illustration of the precession of the spin magnetic moment μ around the external magnetic field B as a consequence of the torque resulting from their mutual interaction. mass m, running within circular trajectory with radius r with a linear moment p and (Taken from Haacke, Brown, Thompson, & Venkatesan., 1999).</i>	2–2
Figure 2-2 - <i>Illustration of the process of magnetization excitation by the application of an oscillatory magnetic field B_1 perpendicular to B_0, at the Larmor frequency. Note that from a referential rotating at the Larmor frequency the excitation process is seen as a precession of M around B_1.</i>	2–5
Figure 2-3 - (a) <i>Illustration of the magnetization tipping by the application of a θ-pulse on the y-direction, and (b) the independent effects of the 180° and the 90° components on the magnetization.</i>	2–6
Figure 2-4 – <i>Illustration of the exponential behaviour of the (a) longitudinal and (b) transverse relaxation processes. Note in (b) the exponential modulation of the spin-spin relaxation by field inhomogeneities leading to the faster T_2^* relaxation.</i>	2–8
Figure 2-5 – (a) <i>1H-NMR signal acquired from within a volume containing muscle tissue and subcutaneous fat. (b) The corresponding extracted spectrum resulting from the Fourier transform of the acquired signal. Contributions from lipids were painted in grey.</i>	2–9

- Figure 2-6 – *Illustration of the physical interpretation of the Fourier transform of the signal acquired in the presence of a gradient field. The acquired signal is the inverse Fourier transform of the projection of the spin magnetization on the direction of the gradient.*.....2–11
- Figure 2-7 – *Illustration of the radial k-space sampling method. (a) Projection of the magnetization distribution, ρ_r , on the direction perpendicular to the gradient, G . (b) The acquired signal corresponds to a k-space line crossing the origin with inclination determined by G . The Fourier transform of the different projections of the spin magnetization distribution correspond to different lines of its k-space representation. These lines cross the origin and have the same direction than the applied gradient.* 2–12
- Figure 2-8 – *Schematic illustration of the linear k-space sampling. Parallel lines of the k-space are acquired at each readout interval. In order to move from the centre of the k-space to the initial point of each line, the phase of $M(r)$ is prepared before readout by application of two orthogonal gradients, say G_x and G_y . Once at the initial point k_{x0}, k_{yj} , all the points k_{xi}, k_{yj} are registered, with $i = 1, 2, \dots, res$, where “res” defines the number of points registered per line, which will be directly related to the spatial resolution of the image.*2–13
- Figure 2-9 - *Illustration of re-establishment of phase coherence following the application of a 180° pulse. $\tau +$ represent the instant just after application of the 180° pulse at the time τ , supposing the effect of the pulse is instantaneous. Note that the individual spin magnetic moments conserve their local precession frequency during all the experiment. Complete refocusing occurs at $t = 2\tau \equiv TE$.*.....2–14
- Figure 2-10 - *Illustration of the spin echo signal. Note the T_2' recovery following phase reversal of the FID signal originated from the 90° pulse after application of the 180° pulse. Note also the irreversibility of the T_2 -decay. (The wiggling inside the T_2^* envelope is due to off-resonance effects).*.....2–15
- Figure 2-11 – *Simplified scheme of the gradient and RF-pulse time sequence for the acquisition of a gradient echo.*2–16
- Figure 2-12 – *Appreciable transverse magnetization generated by a small flip angle,, which leaves the longitudinal magnetization mostly intact.*2–16
- Figure 2-13 – (a) *Method for observing signal decay from a series of 90° - 180° -pulse experiments with different echo times. (b) Multi spin-echo method for observation of signal decay free of diffusion effects.*2–19
- Figure 2-14 – *The signal evolution in the Carr-Purcell method for different echo-times. The shorter the echo-time the shorter the diffusion interval and the closer is the*

<i>observable T2diff* to the intrinsic T2.</i>	2-20
Figure 2-15 – <i>Schematic illustration of the magnetization vector response to two consecutive imperfect refocusing pulses in the (a) Carr-Purcell method, and (b) Meiboom-Gill improved method. Observe the accumulation of the flip angle error in the Carr-Purcell method (a). Notice in (b) that the flip angle error, ϕ, is corrected after the second refocusing pulse. In (b), the 90° component of the first refocusing pulse will tip previously excited transverse magnetization to the longitudinal direction (red vectors). This longitudinally stored magnetization will be re-tipped to the transverse plane completing its 180° flip by the action of the 90° component of the second refocusing pulse. This magnetization will be refocused leading to the so called stimulated echo at a time $t = nTE$ with the same phase of the primary echo refocused by the action of the 180° component (blue vectors).</i>	2-21
Figure 2-16 – <i>Time sequence diagram of the CPMG technique. A series of equally spaced 180°-pulses is launched after an interval $TE/2$ from the 90°-pulse. The phase of the 180°-pulses is shifted of 90° from the 90°-pulses so that imperfect refocusing are corrected for the even echoes.</i>	2-22
Figure 2-17 – <i>Plots of a standing wave at different times. Note that its amplitude at each point in space is modulated by a constant value.</i>	2-23
Figure 3-1 – <i>(a) presents the theoretical T2-decay of muscle and fatty components. In (b) T2-weighted images of the thigh acquired at different echo-times, $TE=10ms$ and $160ms$ (adjusted to the same contrast window level). The contrast between muscle and fatty components depends on the ration of their relative signal intensities which varies in time due to their different T2-values.....</i>	3-2
Figure 3-2 – <i>Signal amplitude vs. echo-time for a voxel within the muscle. Images of the lower legs acquired at different echo times with a multi-spin-echo sequence. Note the exponential T2-relaxation behaviour.</i>	3-3
Figure 3-3 – <i>Pulse sequence diagram of a (a) CPMG-like MSE sequence and (b) a MSE sequence with variable crusher gradients for nulling stimulated echo contributions. The RF-pulse time sequence is the same for both methods, except for the phase of the pulses that are only explicit for the CPMG-like MSE sequence (a). Note in (a) that the gradient moments are identic between refocusing pulses by application of the so called phase rewind gradients.</i>	3-4
Figure 3-4 – <i>Example of a 1H-NMR spectrum acquired at 3T from a volume containing muscle and subcutaneous fat. Peaks containing contributions exclusively from lipids were painted grey.</i>	3-5
Figure 3-5 – <i>Illustration of a selective fat saturation scheme. Fat magnetization is</i>	

selectively excited with a 90°-pulse and spoiler gradients are applied immediately after, in order to null the transverse fat magnetization components. At the end only water longitudinal magnetization components will last, and a imaging sequence may be executed to produce water only images.3-6

Figure 3-6 – (a) Illustration of the idea behind the 2PD method; the phase of fat spin isochromat is inverted at t_{opp} and might be trivially isolated from the water spin isochromat by simply summing or subtraction both images. (b) Illustration of the idea behind the 3PD method; the local B0-shift may be estimated from the phase difference between both in-phase images. Note that when in the presence of a B0-shift, although fat and water signal will be in-phase at t_{in1} and t_{in2} , and in opposed-phase at t_{opp} , they won't be parallel and antiparallel between images due to the shifted local precession frequency.3-7

Figure 3-7 – Illustration of fat and tissue water longitudinal magnetization component recovery during T1-relaxation. In the STIR method, the imaging sequence is executed at the inversion time, TI, where only tissue water has non-zero longitudinal magnetization. M_{0w} and M_{0F} are the equilibrium fat and tissue water magnetizations.3-9

Figure 3-8 – Schematic illustration of a triglyceride molecule along with a proton (1H) NMR spectrum of isolated triglyceride molecules extracted at 14 teslas. Triglycerides consist of one glycerol (to the left) and three fatty acids (to the right). In this example, the fatty acids are: palmitic acid (top), oleic acid (middle), and linolenic acid (bottom). Assignment of the different protons to the resonances A–J is indicated. A virtual water peak is superposed to the spectrum.3-10

Figure 3-9 – Example of ROIs drawn manually to delineate the thigh muscles.3-13

Figure 3-10 - (a) B1+ map (ratio between actual flip angle and the applied one) the area inside the red contours correspond to B1+ ranging between 85% and 130%. (b) The corresponding muscle water T2-map of a healthy volunteer's thigh.3-15

Figure 3-11 - Relationship between B1+ map (expressed as a percentage of the actual flip angle) and water T2-values determined on a group of 20 healthy volunteers.3-17

Figure 3-12 - Box plot of T2-values in voxels with different fat signal fractions calculated using (a) the tri-exponential model (b) the mono-exponential model. With the mono-exponential model, T2-values were systematically more elevated when fat content was higher. Significant differences in T2-values between normal and abnormal subjects were observed using both models ($p < 1e-4$).3-19

Figure 3-13 – Plots of the water T2-values, as determined with the proposed tri-exponential method, and the global T2-values obtained by simple monoexponential

fitting against Dixon-based fat fraction. A strong correlation exists between global T2-value and fat content. In contrast, water T2-values derived from the tri-exponential model were independent from the Dixon fat fraction. Abnormal muscles are also identifiable by elevated global T2-values.3–20

Figure 3-14 - Relationship between fat fractions (F0) extracted from Dixon-based fat fraction and MSME based fat fraction. Fat fraction (F0) values obtained with both techniques were highly correlated: $R^2=0.89$ with a slope close to unity (0.94).3–21

Figure 4-1 - (a) SSFP signal as a function of α and ϕ calculated with Bloch simulation (thin line) or using an approximate analytical model (Eq. 4.2) (thick line). Experimental data (closed circles) acquired in a 0.1 mM MnCl₂ phantom were superimposed on simulated curves. The constant value (dotted line) represents the ideal RF spoiled signal: $S_{\text{spoil}} = S_{\text{eq}} \left(1 - e^{-\frac{TR}{T_1}}\right) \sin\alpha / \left(1 - \cos\alpha e^{-\frac{TR}{T_1}}\right)$. Arrows indicate the largest ϕ ($\alpha\phi\mu\alpha\xi = 1/\xi$) for which Eq. 4.2 is still applicable. In (b) the calculated S ϕ deviation (i.e., the relative difference between S ϕ derived from Eq. 4.2 and from Bloch simulation) is plotted against $\xi\phi$ for the same α and ϕ values, as in (a). Relevant experimental parameters were TR = 5 ms, TE = 3 ms, $\alpha = (20^\circ, 40^\circ$ and $90^\circ)$, $\phi = (1^\circ, 5^\circ, 10^\circ, 15^\circ, 20^\circ$ and $30^\circ)$. Common parameters for both computations in Fig. 1 (Bloch simulation and Eq. 4.2) were TR = 5 ms, $\alpha = (20^\circ, 40^\circ$ and $90^\circ)$, $\phi = 1^\circ$ to 50° , in 0.25° steps, $T_1/T_2 = 886/86 \approx 10$4–13

Figure 4-2 – (a) T_2^{estim}/T_2 ratio as a function of $T_1/T_2/\eta$ calculated using either numerical simulation of Eq. 4.4 (open squares) or the analytical function derived from Eq. 4.8 (solid line). To gain insight on the flip angle dependence of T_2 estimation, T_2^{estim}/T_2 ratio was also plotted as function of α in (b). Experimental data (closed circles) acquired in a 0.1 mM MnCl₂ phantom were superimposed on the simulated curves. The constant value (dotted line) represents $T_2^{\text{estim}}/T_2 = 0.95$. Relevant experimental parameters were TR = 5 ms, $\alpha = (20^\circ, 40^\circ, 60^\circ, 80^\circ$ and $90^\circ)$, $\phi_1 = 1^\circ$, $\phi_2 = 10^\circ$. Computational parameters were $T_1 = 886$ ms, $T_2 = 86$ ms, TR = 5 ms, $\alpha = 5^\circ$ to 90° , in 5° steps, $\phi_1 = 1^\circ$ and $\phi_2 = 10^\circ$4–14

Figure 4-3 - Impact of inaccuracy of T_1 on T_2 computation using Eq. 4.9: Numerical simulations (symbols) and analytical solution (lines) show that the sensitivity of T_2 to T_1 errors becomes more important with decreasing FA or T_1/T_2 ratio. Relevant computational parameters were: TR = 5 ms, $\alpha = 60^\circ$ or 80° , $\phi_1 = 1^\circ$, $\phi_2 = 15^\circ$. 4–15

Figure 4-4 - Flip angle sensitivity in T2-pSSFP mapping: Percent change in T_2 derived values as determined by Bloch simulation for two tissue models ($T_1/T_2 = 10$ and T_1/T_2

= 40) as a function of FA deviation. In the presence of inaccurate FA, T_2 measurement presents a significant bias which becomes more important with increasing T_1/T_2 ratio (solid lines). Accurate T_2 quantification is achieved if actual FA is used in Eqs. 4.4 and 4.9 (dotted lines). Relevant computational parameters were: $T_1 = 886$ ms, $T_2 = 86$ ms, $TR = 5$ ms, $\phi_1 = 1^\circ$, $\phi_2 = 10^\circ$4-16

Figure 4-5 - T_2 -mapping of a liquid phantom at 3T (reference $T_2 = 86$ ms): T_2 -maps and respective histograms derived from Eq. 4.4 (a, b), Eqs. 4.4 and 4.9 (direct approach) (c, d) assuming $T_1 = 886$ ms and from Eqs. 4.13 (iterative approach) (e, f) assuming $T_1 = 886$ ms and starting $T_2 = 80$ ms. Accurate and precise T_2 -mapping was only possible after concomitant T_1 and FA corrections for both approaches (d, f). Relevant experimental parameters were: $TR = 5$ ms, $TE = 3$ ms, $\alpha = 60^\circ$, $\phi_1 = 1^\circ$, $\phi_2 = 10^\circ$4-17

Figure 4-6 - In vivo skeletal muscle T_2 -mapping at 3T: T_2 -maps (axial and sagittal views) derived from 3D pSSFP scans. Images were acquired in quadriceps muscles of a volunteer, immediately before and on the 1st, 2nd, 3rd and 10th day following an eccentric exercise session. FA deviation maps are also shown to illustrate the B_1+ inhomogeneity in the knee coil. Axial views correspond to representative medial and distal sections of the quadriceps muscles and its relative positions are indicated in the anatomical T_1 weighted images (black lines). Parametric maps present large areas of T_2 increases at two days post-exercise, corresponding probably to muscle injury. T_2 changes were predominantly located in the distal portion of the vastus medialis (VM) muscle and close to the muscle-tendon junction (arrow). Experimental parameters for T_2 -pSSFP imaging were $\alpha = 60^\circ$, $\phi_1 = 1^\circ$ and 15° , $TR/TE = 6.3/2.8$ ms, $NEX = 2$. All T_2 -maps were corrected for B_1+ inhomogeneity and T_1 . Overall T_2 -pSSFP acquisition time was ~10 min.4-18

Figure 4-7 - Comparison of T_2 in quadriceps muscles of a volunteer as measured by MSME and T_2 -pSSFP methods: (a) Overall T_2 measurements (all days, all slices, all ROIs) as a function of FA deviation (symbols). Error bars were omitted for the sake of clarity. On average, standard deviation for both methods was ~3 ms. Dashed lines are just guidelines. (b) Bland-Altman plots showing the limits of agreement between T_2 as determined by pSSFP (Eq. 4.9) and standard MSME method. The center line represents the mean differences between the two methods, and the other two lines represent ± 1.96 SD from the mean. To limit the impact of B_1+ inhomogeneity in Bland-Altman analysis only five slices localized at the center of the transmitter coil were considered. Relevant experimental parameters for MSME scans were: $TR = 3$ s, 17 echo times (TE) range = 8.1 to 137.7 ms, in-plane resolution = 1.4×1.4 mm², 11

slices, slice thickness = 8 mm, slice gap = 20 mm, acquisition time ~ 5 min.4-19

Figure 4-8 - Axial T2-maps obtained from T2-pSSFP experiments carried out in a myopathic patient (a) and in a healthy volunteer (c). For comparison, a fat-suppressed T2-weighted image from the same patient is displayed in (b). An FA deviation map measured in the volunteer is also shown to illustrate the asymmetric B₁+ inhomogeneity in the thighs (d). Histograms extracted from T2-maps are shown in (e). A homogeneous distribution of T2-values, centered on 37 ms, is observed for the healthy volunteer (thin line), whereas for the patient (thick line), median T₂ is shifted to 44 ms. Note regions of increased T₂ (up to 180 ms) in the patient, reflecting muscle edema. Experimental pSSFP parameters were: in-plane resolution = 1.4 x 1.4 mm², slice thickness = 5 mm, 64 slices, α = 60°, φ₁ = 1° and 15°, TR/TE = 6.3/2.8 ms, NEX = 1. Total T2-pSSFP acquisition time was ~3 min. T2-maps were corrected for B₁+ inhomogeneities and T₁. SNR₁ was higher than 50 for all analysed muscles. Relevant experimental parameters for T₂w imaging were: TR = 3 s, TE = 45 ms, Turbo-factor = 2 ms, in-plane resolution = 1 x 1 mm², 27 slices, slice thickness = 5 mm, slice gap = 5 mm, acquisition time ~ 5 min.4-20

Figure 5-1- RF-pulse and B₀ gradient time sequence diagram representing the implemented ISIS-CPMG method. In the ISIS module adiabatic inversion pulses are selectively turned on following an 8 steps combination as indicated. Fat saturation is accomplished with a 90° hard pulse with 1.5 ms long 90° hard pulse centred at -432 Hz from water proton frequency, and is launched just after each of the ISIS steps. CPMG pulse train is launched 2 ms after the Fat-Sat module.5-5

Figure 5-2 – (a) plot the x and y components of the designed RF-B₁ field wave form and (b) the simulated 20 mm slice profiles for short and long T₂-species. Short T₂-species are characterized by T₂/T₁ = 1/350 ms, and long T₂-species were characterized by T₂/T₁ = 40/1200 ms.5-5

Figure 5-3 – Experimental demonstration of CPMG phase cycling. Plots of echo amplitude vs. echo-time resulting from two CPMG acquisitions with opposed refocusing pulse phases (red and blue). Note that after summation (black), FID signal contributions cancel out and signal amplitude approaches zero asymptotically.5-6

Figure 5-4 – Picture of a subject’s leg, placed on the inferior half of the transceiver coil, after step 1 of the vascular draining procedure. Note the cuff wrapped around the thigh.5-7

Figure 5-5 - Protocol timeline for the T₂-spectra acquisitions at different vascular filling conditions: (i) With the patient in « supine, foot first » orientation, and its calf positioned in the transceiver coil, the vascular draining procedure was first applied;

(ii) Localized CPMG signal was acquired with the VOI located within the soleus during 5 min; (iii) Vascular filling step is performed and another CPMG acquisition of 5 min is launched over the same VOI after a 5 min interval; (iv) Pressure is released from the cuff and another CPMG acquisition of 5 min is performed over the same VOI after a 5 min interval.5–8

Figure 5-6 - Illustration of a virtual non-exchanging system that presents T2-relaxation behaviour identical to that of a real exchanging system. The apparent T2-values and relative fractions characterizing the pseudo compartments of the virtual system are functions of the intrinsic relative fractions, T2-values and exchange rates of the real system. In this case, a tri-compartmental two-exchange system with no direct exchange between compartments 1 and 3.5–11

Figure 5-7 - (a) Plot of T2-decay curves obtained for a subject under different vascular filling conditions. The lines passing through the points correspond to the fitted curves resulting from the regularized inversion solution, and (b) presents the corresponding obtained T2-spectra.5–13

Figure 5-8 - Characteristic relaxation curves of the vascular draining (triangles), normal (squares) and vascular filling (circles) conditions, and the corresponding fitted curves characterized by the extracted intrinsic parameters of the 2SX model for both transcytolemmal (crosses) and transendothelial (lines) exchange regimes.5–15

Figure 5-9 - (a) Characteristic relaxation curves of the vascular draining (triangles), normal (squares) and vascular filling (circles) conditions, and the corresponding fitted curves (lines) characterized by the extracted intrinsic parameters of the 3S2X model; (b) Obtained T2-spectra from regularized inversion of the fitted curves resulting from the 3S2X model.5–16

Figure 5-10 - Projection of the VOIs on the sagittal, coronal and axial T1-weighted FLASH images of the calf of the patients (from left to right). (a) VOI located within the soleus of a patient diagnosed with Charcot-Marie-Tooth disease; (b) and (c) show the VOIs located within the soleus and tibialis anterior of a patient diagnosed with eosinophilic fasciitis, respectively; (d) VOI located within the tibialis anterior of a patient diagnosed with a necrotizing myopathy.5–22

Figure 5-11 – Extracted T2-spectra characterizing each system defined by the intrinsic parameters presented in Table 5-4, representing respectively: (a) Normal tissue; From (b) to (d) there is progressive increase in interstitial oedema; (e) inflammation, characterized by interstitial oedema and higher perfusion; and (f) is supposed to represent necrotizing tissue, characterized by inflammation with high membrane permeability. T2-spectra are plotted with logarithmically scaled abscise for correct

visualization of peak area. The T2-value and relative fraction (Eqs. 5.6, 5.7) characterizing the T2-peaks are indicated in the plots.	5–25
Figure 5-12 – T2-decay curves and the T2-spectra obtained for each in vivo data set: (a) soleus of the patient diagnosed with Charcot-Marie-Tooth disease; (b) soleus and (c) tibialis anterior of the patient diagnosed with Shulman’s syndrome; (d) tibialis anterior of the patient diagnosed with a necrotizing myopathy; and (e) soleus of a healthy subject. T2-spectra are plotted with the abscise in logarithmic scale for correct visualization of peak area.	5–28
Figure 6-1 – Comparative morphologic features of SKM histology between control (a) and Duchenne muscular dystrophy (DMD) cases (b, c). The intracellular matrix occupies a much smaller volume fraction in control (a), resulting in capillary-to-muscle fiber distances which are minimal, in contrast with the dystrophic tissue (b). Collagen I immunostaining highlights the endomysial layers which are abnormally thick in the dystrophic tissue (c). Taken from (141).	6–2
Figure 6-2 – The hypo-signal of compact collagenous tissue structures observed in NMR images. (a) Spin-echo PD image (TE = 9.5 ms) of the thighs. The arrows point to the dark visible fascia with its characteristic hypo-signal. (b) Spin-echo T1-weighted image (TE = 16 ms) of both buttocks. The Arrows point to a dark visible thin fibrotic cord in atrophic right gluteus maximus muscle. Normal left side may be used for comparison. Image in (b) was taken from (144).	6–3
Figure 6-3 – Simplified FR-pulse and gradient time sequence for (a) 2D-GRE and (b) 3D-GRE NMRI techniques. For both methods, the phase encoding gradients imposes a minimum dead time in which no signal is acquired. For the 2D case, a slice selection mode is applied which elongates the dead time due to relaxation effects during excitation process.	6–4
Figure 6-4 – Schematic illustration of k-space sampling for (a) 3D and (b) 2D radial acquisition methods.	6–5
Figure 6-5 – Principle of half RF-pulse selection for acquisition of short relaxing NMR signal. Slice profile is completely selected after summation of acquisitions with inverted polarity of selection gradient.	6–6
Figure 6-6 - Simplified FR-pulse and gradient time sequence for (a) a 2D-GRE sequence with half excitation pulse and (b) a 3D-GRE sequence. Radial acquisition allows acquiring data right after the excitation. The dead time is determined by the time it takes for the RF system to change from transmission to acquisition mode, usually on the order of 10 to 100 μ s.	6–6
Figure 6-7 – (a) The ROIs drawn inside the gastrocnemius (medial head), gastrocnemius	

(lateral head), soleus, peroneus longus and tibialis anterior over the central slice. (b) ROIs A and B delimiting fascia and aponeuroses between the gastrocnemius and the soleus; ROI-B was traced in order to include adjacent muscle structures.6–8

Figure 6-8 – Logarithmic plot of the time evolution of the signal amplitude obtained from the ROIs traced in the gastrocnemius lateral (a), gastrocnemius medial (b), peroneus longus (c), soleus (d) and tibialis anterior (e), along with the corresponding fitted curves.....6–9

Figure 6-9 - Logarithmic plot of the time evolution of the signal amplitude obtained from the ROI-A delimiting the fascia between the soleus and the gastrocnemius and the enlarged ROI-B including adjacent muscle tissue, along with the corresponding fitted curves.....6–10

Figure 6-10 – NMRI of an axial slice of the calf of a healthy volunteer using a 2D-UTE sequence with an echo-time of 0.2 ms, TR = 30 ms and FA = 5°. Note that structures with elevated relative fraction of short-T2-components such as fascia and cortical bone still present smaller signal intensity. However, cortical bone presents higher contrast with other tissue structures due to the high relative fraction of its short-T2-components and to the very short T2-value that characterizes them.6–12

Figure 6-11 – Plot of amplitude modulation of the theoretical fat signal as a function of time for the fat model given in Table 6-3. Two fat signals were simulated; one in which no T2-relaxation was considered (blue) and a second inserting the T2 of each individual hydrogen group of the lipid molecule. Note that the impact of the phase shift accumulation between the different hydrogen groups in the amplitude modulation is much more important than the T2-relaxation effects.6–13

Figure 6-12 - image resulting from the subtraction of an UTE image acquired at 2.5 ms from another UTE image acquired at 0.2 ms (see Figure 6-10).Note the high residual signal from short-T2 structures such as cortical bone and fascia. Notice also the important residual signal on the subcutaneous fat.....6–16

Figure 6-13 – Extracted Short T2-map fraction, using the dual-echo method with correction for T2* of long T2-components and fat signal contributions.6–19

Figure 6-14 – Histogram of the relative fraction, S_f , of signal from short-T2 for pixels with $S_f \geq 0.2\%$6–20

Figure 6-15 - Sensitivity profiles of the short-T2-imaging technique describe in Eq. 6.12 to tissues with different short T2-values (1 μ s to 10ms) for different minimum echo-times (10, 50 and 200 μ s). The horizontal dashed line represents the limit of 20% contribution from a short-T2-component. Note that the T2 of maximum sensitivity decreases with the minimum echo time, along with the minimum T2 whose

contributions to the image will be greater than 20% of its own total signal.6-21

List of Tables

Table 3-1 - <i>Spectral model of the fat resulting from spectroscopy data. For each peak were reported: the relative shifts to the water, the T2-relaxation time and the relative amplitude with respect to the fat component of the voxel.</i>	3–14
Table 3-2 - <i>Mean (Eq. 3.3) and mean squared deviation with respect to a reference value (33.9 ms) of water T2 (Eq. 3.4), with respect to different B1+ range as well as the fraction of muscle voxels that are in the specified B1+ range with the respect to the total number of voxels.</i>	3–18
Table 4-1 - <i>Typical values for $\xi(\alpha)$, which must be determined numerically, for different flip angles, α.</i>	4–4
Table 5-1 - <i>Results obtained from the mono- and biexponential fits and regularized Laplace inversions for the relative fractions and corresponding T2-values, by means of mean(SD), between subjects for each vascular filling condition.</i>	5–14
Table 5-2 - <i>Extracted intrinsic parameters of the 2SX model for the three vascular filling conditions at transcytolemmal and transendothelial exchange regimes; SE is presented within brackets.</i>	5–14
Table 5-3 - <i>Extracted intrinsic parameters of the 3S2X system characterizing the intracellular, interstitial and vascular spaces for the three vascular filling conditions; SE is presented within brackets.</i>	5–15
Table 5-4 – <i>Intrinsic parameters characterizing the simulated systems modelled in order to represent oedematous, inflamed and necrotizing tissue.</i>	5–20
Table 6-1 - <i>Results for the extracted mean relative fraction and T2*-value of the short component, and the T2*-value of the long component for the ROIs traced in the muscles (see Figure 6-7 a) and for the ROIs A and B traced around the fascia (see Figure 6-7 b). Results are presented as mean(SD) for the muscles and as mean(SE) for each ROI around the fascia.</i>	6–10
Table 6-2 – <i>Observed T2* values of some tissue structures at 3 T.</i>	6–11
Table 6-3 – <i>Relative fraction and Larmor precession frequency of the different peaks in the fat spectrum at 3T.</i>	6–14

CHAPTER 1

General Introduction

In recent years Nuclear Magnetic Resonance (NMR) techniques have demonstrated their significant importance in the field of neuromuscular diseases (NMD), getting increasing attention from the scientific community for their potential applications as non-invasive monitoring and investigative tools. The present work consisted on the adaptation of proof of concepts into clinically applicable research tools for characterization of skeletal muscle (SKM) tissue, with the objective of contributing to the consolidation of quantitative NMR tools for studying muscle pathology.

In this chapter, we shall recall the macroscopic and histological architecture of the normal SKM tissue and the most common alterations observed in NMD. The main current NMR clinical tools to characterize these alterations are introduced. We shall discuss their current limitations and the potential applications that shall outcome from their optimization and further development, highlighting the current need for quantitative tools in clinical research.

Finally the limitations of the clinical application of the currently available quantitative NMR tools are discussed, and we describe how the methods that were applied and explored in the present work to expand these limits are organized in this manuscript.

1.1. Skeletal muscle structure and histology

1.1.1. Striated muscle architecture

Muscle tissues are structurally classified as: smooth, mostly found in the walls of digestive organs, uterus and blood vessels; cardiac, found only in the heart; and skeletal, attached to bones by bundles of collagen fibers known as tendons and are responsible for skeletal movement and posture maintenance.

Skeletal muscle is designed as a bundle within a bundle arrangement (Figure 1-1). The entire muscle is surrounded by a connective tissue layer called *epimysium* and is made up of multiple smaller bundles containing hundreds (100-200) of muscle cells (myofibers)

called fascicles. The fascicles are held together by a thinner layer of connective tissue called perimysium which provides pathway to the major blood vessels as well as arterioles, venules and nerves through the muscle. Each muscle cell in a fascicle is surrounded by an even thinner connective tissue sheath known as the *endomysium* which is the pathway for capillaries. The connective tissue covering gives support and protection to the myofibers, allows them to withstand the forces of contraction and plays an important role in the force transmission between muscles and from muscles to tendons and bones.

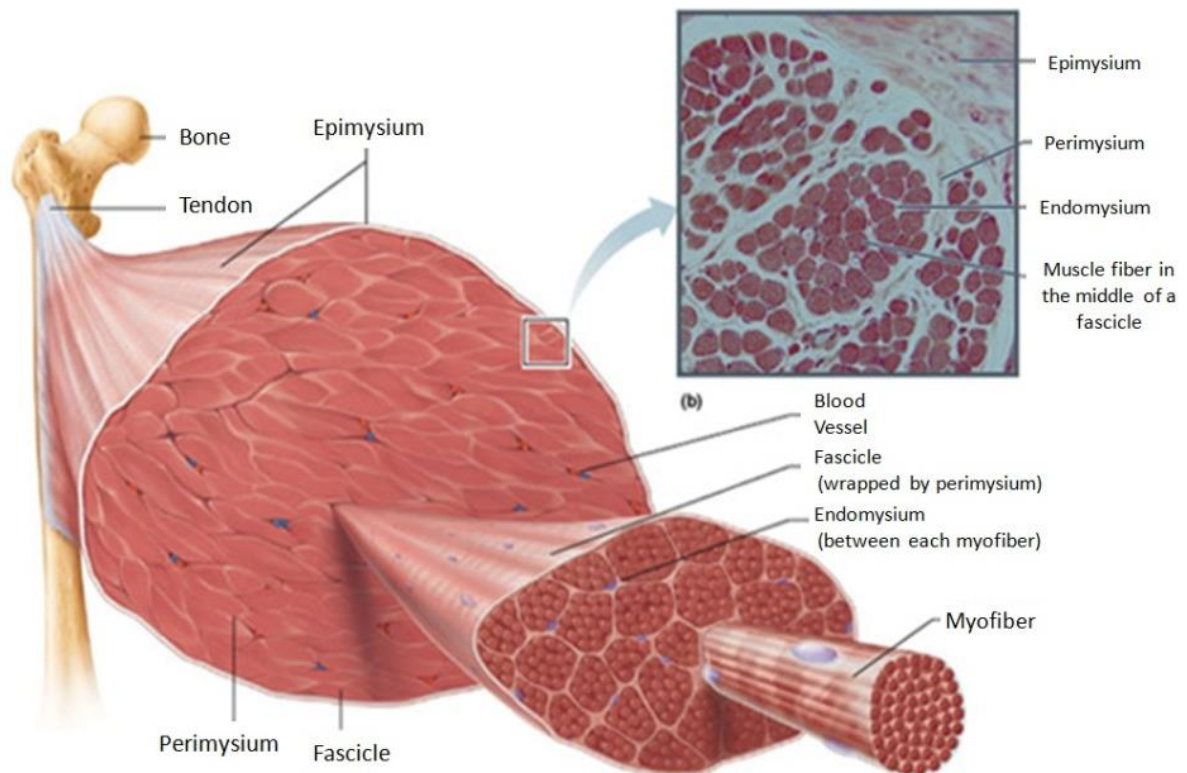


Figure 1-1 - Structural organization of the skeletal muscle as a bundle within a bundle arrangement. From the muscle fibers to the fascicles grouped to form the entire muscle.

[Copyright © 2011 Pearson Education, Inc., publishing as Benjamin Cummings,

<http://classconnection.s3.amazonaws.com/811/flashcards/141811/jpg/fascia1320418174703.jpg>]

Water makes up approximately 76% of muscle tissue weight (1), and is distributed within intracellular, interstitial and vascular spaces, with corresponding average relative fractions of approximately 85, 10 and 5%, respectively (Robertson 1961; Ling & Kromash 1967; Neville & White 1979).

1.1.2. Muscle cell (Myofiber)

Myofibers are long cylindrical multinucleated cells that run along the entire length of the muscles. Figure 1-2 illustrates their intracellular organization. The nuclei are located at the periphery just beneath the sarcolemma (cell membrane) and the cell is densely packed

with hundreds to thousands of myofibrils, which consist of compactly packed cylindrical bundles of contractile myofilaments, disposed parallel to each other and to the axis of the cell.

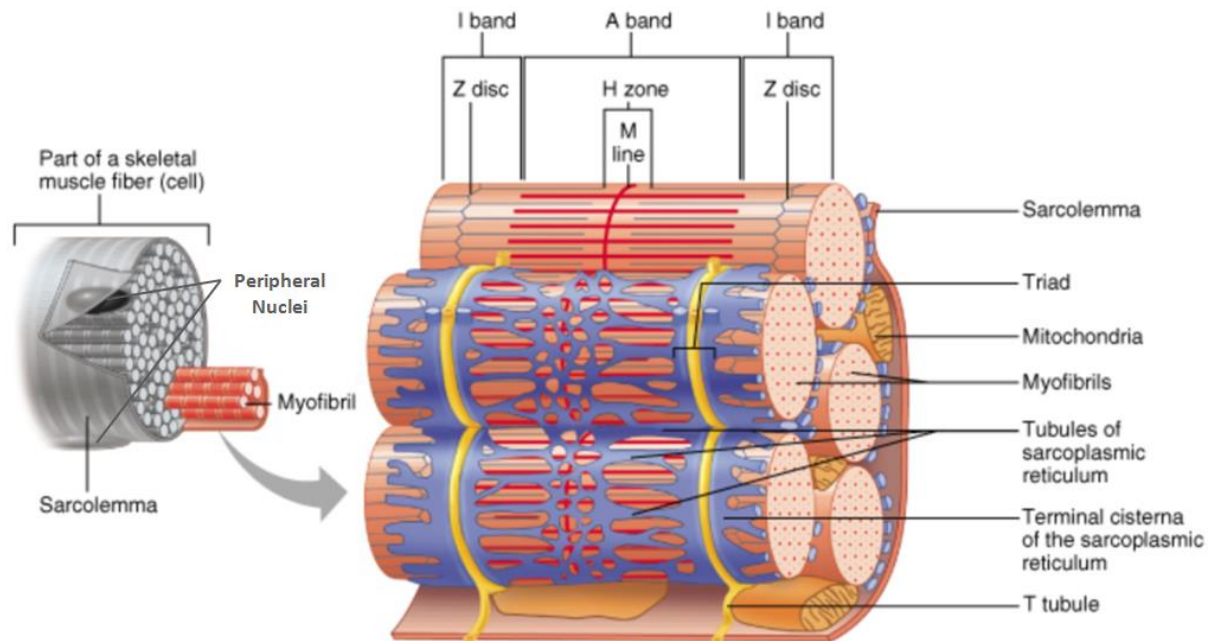
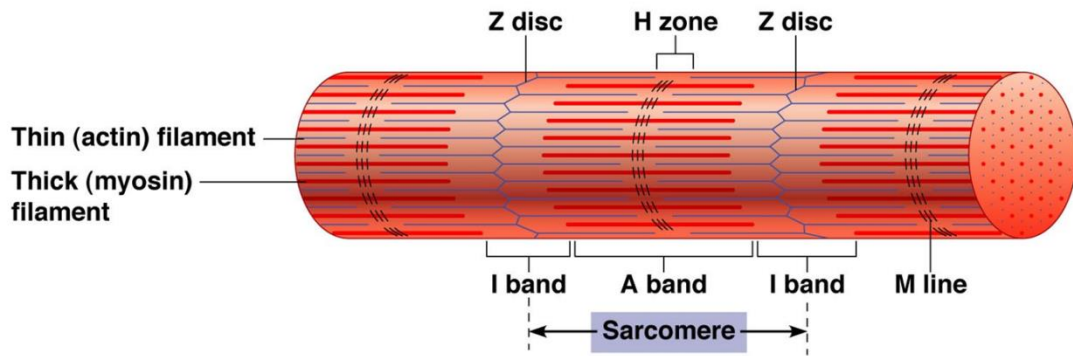


Figure 1-2 – *Illustration of a skeletal muscle cell (myofiber). Note the tubular system of sarcolemma invaginations (T-tubules) that are linked to the tubules of the sarcoplasmic reticulum that surround each myofibril. The T-tubules are interconnected and opened to the interstitial space, giving the cell a cylindrical spongy-like structure. The small relative volume left in the sarcoplasm is packed with mitochondria (subsarcolemmal and intermyofibrillar), vesicles, lysosomes, lipid droplets among other cellular structures.*

[Found at: [http://classes.midlandstech.edu/
http://classes.midlandstech.edu/carterp/Courses/bio210/chap09/lecture1.html](http://classes.midlandstech.edu/http://classes.midlandstech.edu/carterp/Courses/bio210/chap09/lecture1.html)]

The reduced space left in the cytoplasm (sarcoplasm) is packed with mitochondria (subsarcolemmal and intermyofibrillar), vesicles, lysosomes, lipid droplets, glycogen granules among other cellular structures.

Myofibrils are composed of repeating sections of sarcomeres, which are mainly composed of two long fibrous proteins; actin and myosin (see Figure 1-3). These proteins are arranged parallel to each other in a cylindrical structure, with each myosin filament usually surrounded by 6 actin filaments.



Copyright © 2009 Pearson Education, Inc., publishing as Pearson Benjamin Cummings.

Figure 1-3 - Sarcomere consisting on a bundle of thin and thick myofilaments made up of protein molecules called actin and myosin, respectively. These proteins are arranged parallel to each other in a cylindrical structure, with usually six actin filaments surrounding one myosin filament. Actin molecules are attached the z-discs, which are constituents of the cytoskeleton and define the boundaries of a sarcomere unit.

[Copyright © 2009 Pearson Education, Inc., publishing as Benjamin Cummings, <http://classes.midlandstech.edu/carterp/Courses/bio210/chap09/lecture1.html>]

Figure 1-4 presents a transmission electron microscope image of a longitudinal section cut through an area of human skeletal muscle tissue, where it is possible to identify each sarcomere unit, whose schematic illustration is presented in Figure 1-3.

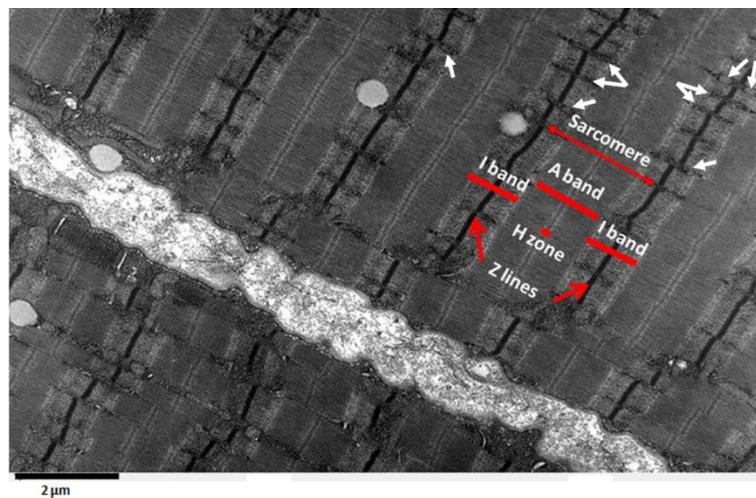


Figure 1-4 - Transmission electron microscope image of a longitudinal section cut through an area of human skeletal muscle tissue; borders of two cells separated by the endomysium. Image shows several myofibrils, each with the distinct banding pattern of individual sarcomeres: the darker bands are called A bands (the A band includes a lighter central zone, called the H band), and the lighter bands are called I bands. Each I band is bisected by a dark transverse line called the Z-line). Paired mitochondria (white arrows pointing to some of them) are on either side of the electron opaque Z-line. The Z-Line marks the longitudinal extent of a sarcomere unit.

[Found at: <http://remf.dartmouth.edu/>, <http://remf.dartmouth.edu/images/humanMuscleTEM/source/2.html>, by Louisa Howard]

The myofibrils occupy approximately 80-90% of the myofiber volume (4). In humans, the cross-sectional diameter of muscle fibers varies with age; sizes remain relatively constant in adulthood and tend to decline with old age. The average diameter of a myofiber in adults is around 50-80 μ m, while the diameter of a myofibril is around 1 μ m.

Myofibers may be differentiated by their metabolic and functional characteristics (i.e., oxidative vs. glycolytic, fast vs. slow twitch (contraction)). These differences reflect histochemical and physiological variations between myofibers, such as: number of mitochondria, content of myoglobin, capillary density, lipid and glycogen storage, etc. These differences lead to the classification of myofibers into: type-1, which present slow twitch, predominant oxidative metabolism and high resistance to fatigue; type-2B, which present fast twitch, predominant glycolytic metabolism and low resistance to fatigue; and type-2A, which presents a fast twitch, high glycolytic and oxidative metabolism and higher resistance to fatigue than type-2B fibers.

In average, fiber types are approximately evenly distributed within muscles. Variations on their relative fractions reflect muscle activity and function, and have been shown to change as a response to specific training (5).

1.1.3. Intramuscular connective tissue: epimysium, perimysium and endomysium.

Intramuscular connective tissue (IMCT) is principally composed of fibers of the proteins collagen and elastin, surrounded by a proteoglycan (PG) matrix. The collagen and elastin contents as percentage of dry tissue weight are 1-10% and less than 0.1-2% respectively, varying with age and muscle (6). Within the anatomical relevant structures of the IMCT, besides the endomysial, perimysial and epimysial layers, is the basal lamina, a thin connective tissue sheet linking the fibrous (reticular) layer of the endomysium to the sarcolemma. Between the sarcolemma and the basal lamina there are small mononuclear cells called satellite cells, which play a fundamental role in myofiber regeneration.

The proteins and macromolecules forming the IMCT are immersed in the so called interstitial fluid, which is composed of water, salts and plasma proteins. Figure 1-5 presents electron micrograph images of the cut surface of bovine sternomandibularis muscle after digestion with NaOH to remove muscle cell contents and proteoglycans, leaving the perimysial and endomysial layers of the IMCT clearly visible.

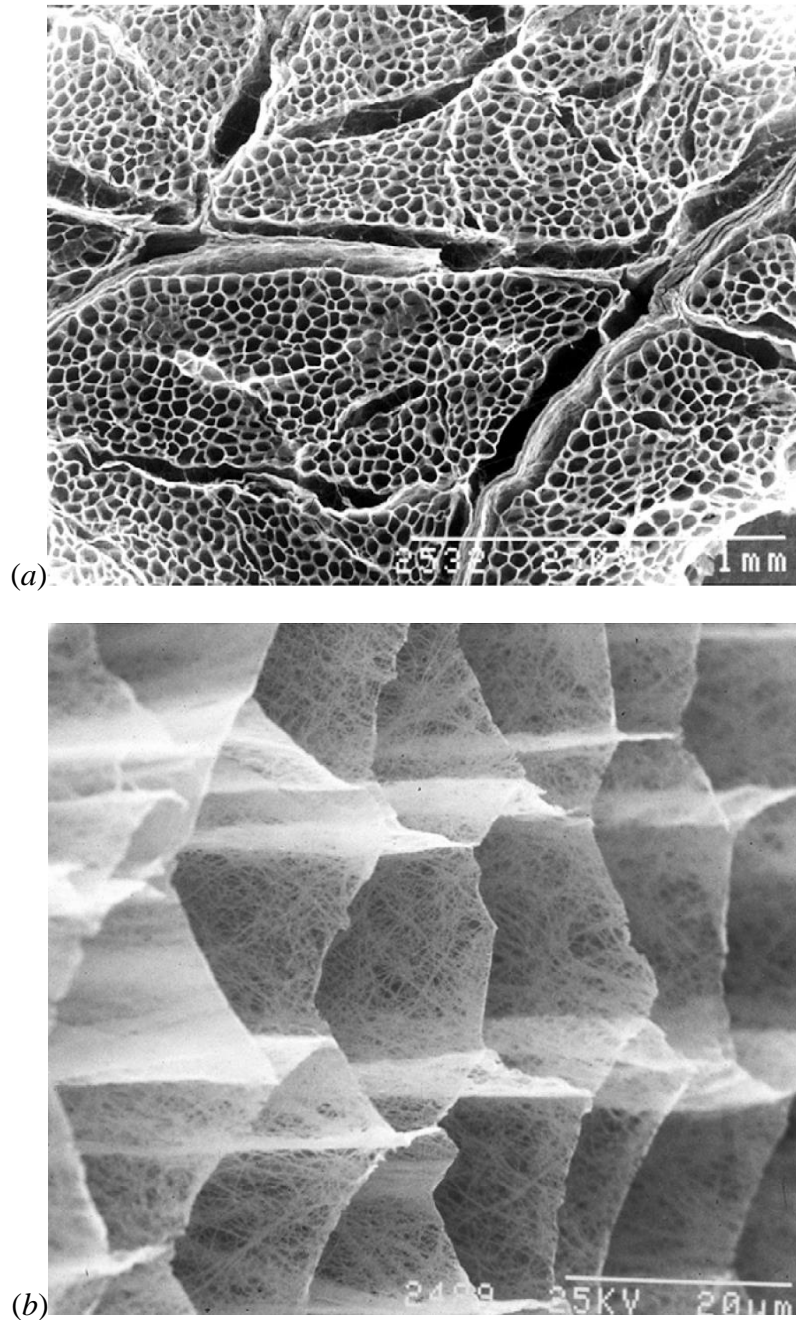


Figure 1-5 - Scanning electron micrograph of the cut surface of bovine sternomandibularis muscle after digestion with NaOH to remove muscle cell contents and proteoglycans in the IMCT. In (a) we have a low magnification view showing thicker perimysial sheets covering the fascicles along with the thinner endomysial layers; and in (b) a high magnification oblique view showing the fine network of collagen fibres making up the reticular layer of the endomysial sheets that separate adjacent muscles fibres. From (7).

1.1.4. Structural and histological alterations induced by pathology in the skeletal muscle tissue

The goal of this section was to describe the main structural and histological tissue

alterations that are commonly observed in NMD, and that are expected to appreciably impact proton (^1H) NMR observations, without getting into the details concerning the disease-specific mechanisms underlying such alterations.

Neuromuscular disorders encompass a large number of diseases that impair the functioning of muscles. An important consequence of the disease activity common to most NMDs is injury at the cellular level. The term cell injury refers to the destruction of the integrity of the sarcolemma, which results in an outflow of cellular organelles into the interstitial space leading to myofiber necrosis. Local inflammation takes place as a response to the degeneration of the cell(s) resulting in interstitial oedema and phagocytosis Figure 1-6.

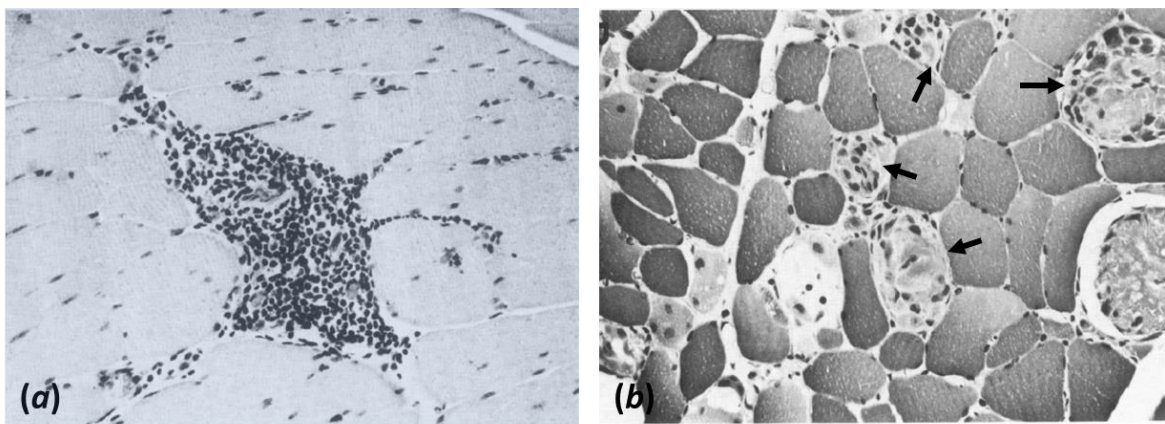


Figure 1-6 – Light microscopy image of a thin transverse section of SKM tissue revealing: (a) Interstitial inflammation (H&E x170); and (b) Phagocytosis of degenerating fibers (arrows) (H&E x170). From (8).

Sarcolemma disruption and inflammation are hypothesised to activate the satellite cells that proliferate and differentiate, mostly into myocytes that will fuse with one another or with the myofiber end-fragments to regenerate the injured cell, but also into myofibroblasts that fuse together to form fibrous connective tissue. However, the continuous degeneration processes that take place in some NMD, e.g. Duchenne muscular dystrophy, result in persistent inflammatory response. Although the etiology and pathophysiology of fibrosis is still investigated and debated, it is becoming widely accepted that this chronic nature of the inflammatory response is a key driver of the fibrotic response (9–11), by inhibiting myofiber regeneration and promoting the formation of fibrotic tissue. As a consequence, the disease activity may lead to progressive enlargement of the endomysium and, eventually, complete myofiber replacement by fibrous connective tissue, usually referred to as fibrosis.

The continuous tissue degeneration is followed by ingrowth of fat and connective tissue, and muscle biopsies at advanced stages of disease often reveal important or

complete myofiber replacement by fat and fibrosis (Figure 1-7).

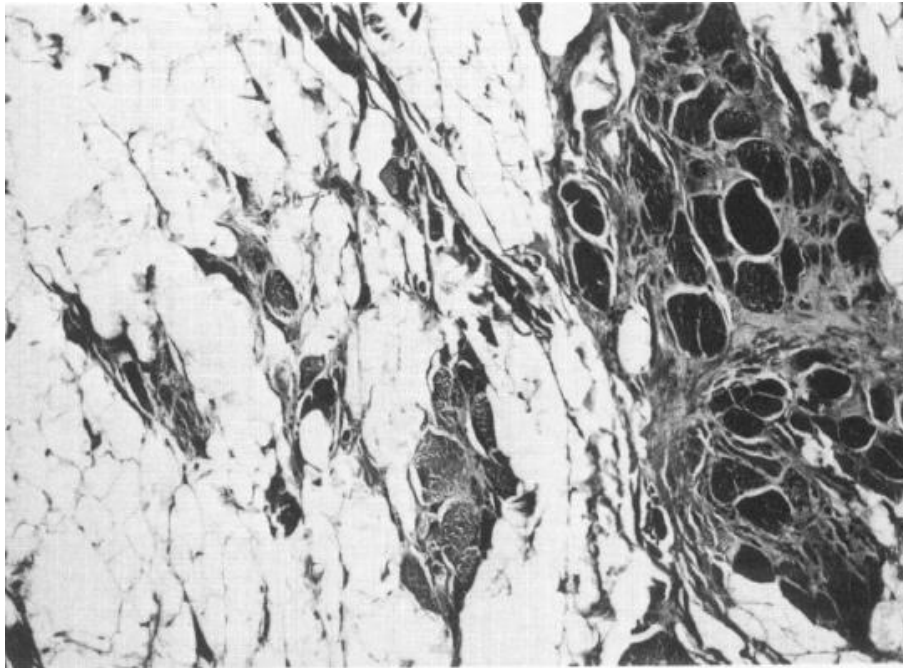


Figure 1-7 - *End-stage of disease. Note the massive fat (white cells) and moderate connective tissue replacement surrounding a cluster of disordered myofibers (dark cells) (H&E x68). From (8).*

As in comparison to normal skeletal tissue (Figure 1-8), the above discussed alterations share the common features of altered water content and distribution within tissue compartments, and increased content of intramuscular fat and fibrosis.

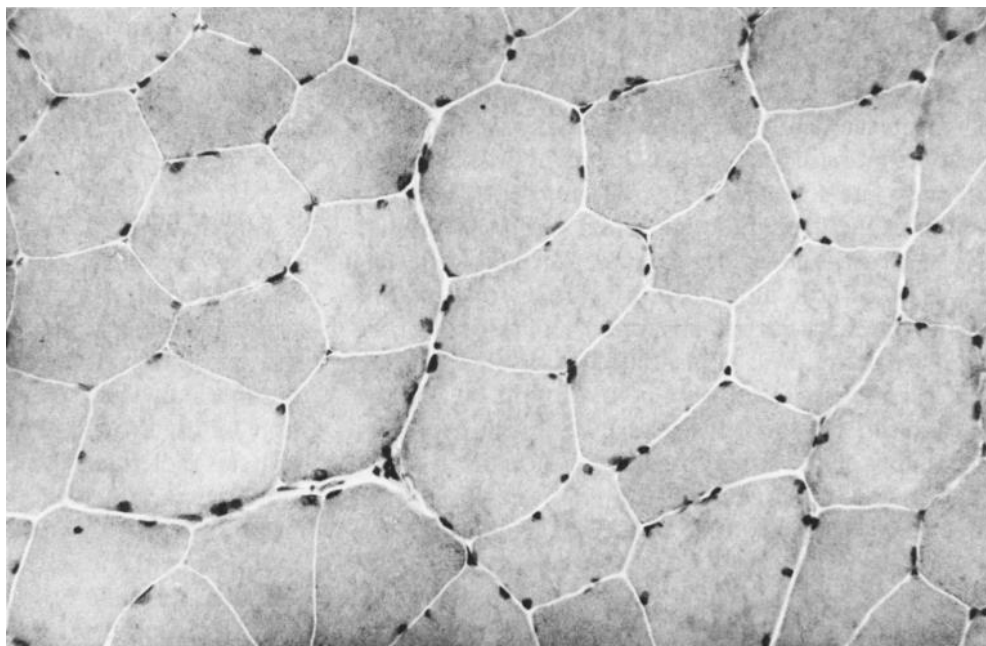


Figure 1-8 – *Light microscopy image of a thin transverse slice of normal SKM tissue.*

1.2. The role of NMR in myology clinical research

The continuous advances of NMR techniques, especially the recent progress on the development and optimization of quantitative examination tools, have driven increased attention to Nuclear Magnetic Resonance Imaging (NMRI) and Nuclear Magnetic Resonance Spectroscopy (NMRS) and extended their applications in the neuromuscular field, from supplementary diagnostic tools to quantitative non-invasive outcome measures in clinical studies.

Muscle NMRI is sensitive to pathology induced changes such as fat degeneration and inflammation, and has been proven capable of revealing disease-specific patterns of selective muscle involvement (12–16), lending itself well for guiding genetic tests and for optimal muscle selection for biopsy (17), improving the diagnostic workup (18). Furthermore, progressive characterization of such patterns shall help to better understand the pathogenesis of neuromuscular disease.

Quantitative NMR methods have provided non-invasive outcome measures for NMD, offering the possibility of realising longitudinal studies for the follow-up of therapeutic trials and disease progression (19–24), which was just not feasible with purely qualitative techniques, incapable of detecting short duration changes in slow progressing diseases. Moreover, detailed description of disease progression may elucidate still unknown aspects of onset and progression of pathology.

Besides NMRI, Nuclear Magnetic Resonance Spectroscopy (NMRS) techniques have also demonstrated their utility in the clinical field of NMD, as it is a consolidated non-invasive tool for quantifying pathology induced metabolic alterations (25, 26). With correct manipulation, NMR techniques can be made sensitive to different tissue-characteristic physical properties and physiological processes, making it an important investigative tool for studying the physiological mechanisms underlying disease activity.

1.2.1. NMR outcome measures currently available for skeletal muscle studies

An adult human body is mainly composed of water (60-70 %), proteins (15-25 %) and lipids (5-15%), and these components are distributed at different relative fractions within each type of tissue in the body. Hydrogen nuclei are present in all molecules forming these components and are the most abundant atoms in the human body, which makes it them nuclei of choice for most NMRI applications. In practice, the signal from hydrogen (proton) in proteins is not observable with usual NMRI techniques due to its extremely short T₂-relaxation time (T₂) (~ 10 μs) (see 2.4), so that most of the signal that is processed in ¹H-NMRI techniques comes only from protons in water and lipids.

The relaxation of water in tissue is very different from the relaxation of pure water, and is usually dominated by the interactions of the water molecules with the macromolecules constituting the tissue. As a consequence, there will be three independent sources of contrast in magnetic resonance images: (i) the volumetric density of detectable protons; (ii) the different intrinsic NMR parameters characterizing water and lipids; and (iii) the different tissue-characteristic NMR parameters of water protons, which are determined by the chemical composition and structure of the tissue.

The different tissues or structures that are identified in standard clinical NMRI of SKM are: muscle, fat, fascia and cortical bone (Figure 1-9); the two last being recognizable by a characteristic lack of signal.

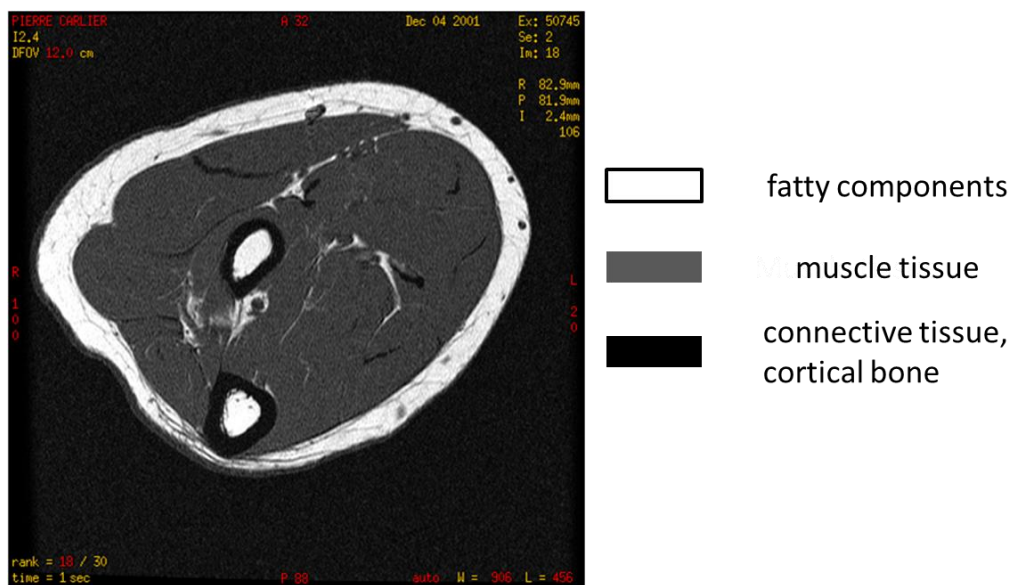


Figure 1-9 – Example of a cross sectional NMR T1-weighted image of the forearm of a healthy subject. Muscle tissue, fatty components, fascia and cortical bone may be easily identified.

The main explored NMR parameters in current SKM studies are: the chemical shift (see 2.5), which quantifies the different precession frequencies of the magnetization from protons in water and lipid molecules (see 2.5), and is explored to produce separate images of these compounds; and the relaxation times T1 and T2, which are defined in 2.4. NMRI techniques may be specifically adjusted in such a way that the acquired signal will selectively depend mostly on either T1 or T2, and the corresponding image will be referred to as T1- or T2-weighted, respectively, with their contrast determined by the specific relaxation time differences between tissues. As tissue relaxation and composition is usually altered by disease activity, NMRI techniques can be made sensitive to pathology induced tissue alterations such as oedema, inflammation, necrosis, fat infiltration and fibrosis. However, qualitative approaches, such as T1- and T2-weighted imaging, for

assessing such tissue alterations lack of specificity and are subjective, depending on visual identification of contrast differences. Furthermore, image intensity will be influenced by tissue-independent factors such as technical imperfections of the imaging system. These issues impose the necessity of developing quantitative methods that might offer objective biomarkers for precise characterization of tissue alterations.

Signal detection from thick connective tissue layers or cords such as fascia and fibrosis is a rather complicated issue; some of the NMR parameters of water molecules within the dense collagen matrix of these structures are altered and are only visible with special techniques which have been explored in the present work and will be discussed in details on chapter 6.

Muscle atrophy may be investigated by muscle volumetry, which may be easily obtained after individual muscle segmentation from NMR images. Fat degeneration may be identified in T1-weighted images (see Figure 1-10) and chemical shift-based quantitative NMRI (qNMRI) approaches for quantification of fat infiltration are in relatively advanced stage of development. Furthermore, fat infiltration has already been shown to serve as an outcome measure for characterizing disease progression in some pathologies (20, 21).



Figure 1-10 – *Example of a cross sectional T1-weighted image of the leg of a patient with necrotizing myopathy showing the resulting fatty infiltration following muscle degeneration, remarkably on the soleus and gastrocnemius medial head.*

Although more easily detected and quantified, fat infiltration reflects advanced states of pathology, and are particularly useful for characterizing further disease progression and for pattern recognition, improving later diagnosis workflow. On the other hand, inflammation is an indicative of disease activity and could probably be used to detect early

stages of diseases. However, quantifying inflammation is a rather complicated issue. Inflammation and fat are highlighted in T2-weighted images and it is impossible to distinguish inflamed from moderately fat infiltrated muscle with such contrast. An alternative to distinguish between fat infiltration and inflammation is the application of the so called spectrally selective excitation or fat suppression techniques (see 3.2), resulting in theoretically water only images (see Figure 1-11). Still the detection of inflammation sites in such images is limited by the contrast between inflamed and non-inflamed muscles, which is by itself very sensitive to signal in-homogeneity caused by system imperfections. Furthermore, it is important to realize that sensitivity to progression of pathology or response to treatment relies on the detection of small changes in the explored NMR parameters, which demands the application precise quantitative methods. The solution to overcome the difficulties associated with the characterization of inflammation sites relies on the actual measurement of the relaxation time T2, which has been shown to be abnormally elevated in presence of inflammation.

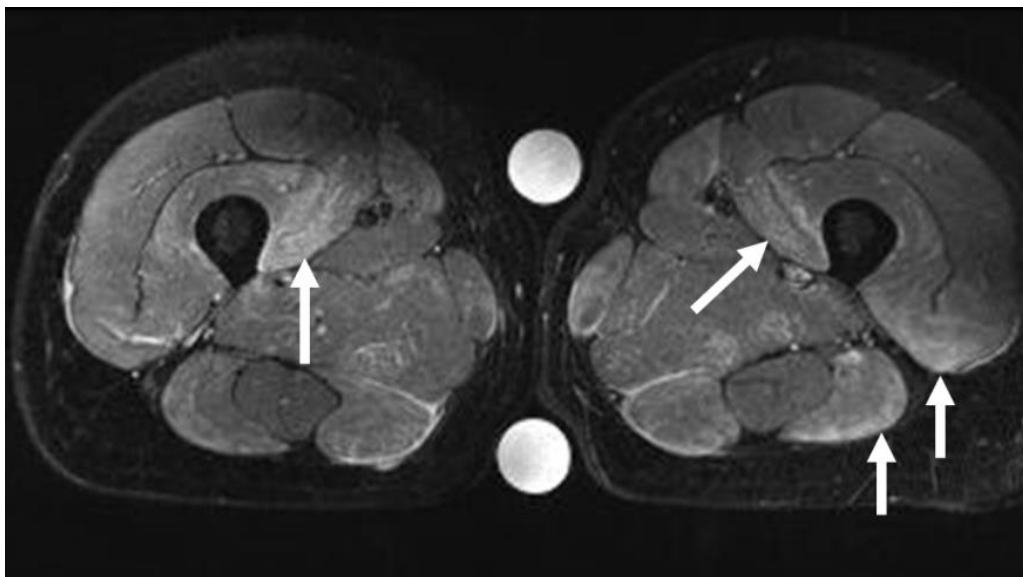


Figure 1-11 – T2-weighted image of the thighs with application fat-saturation (STIR). Inflammation sites are indicated by arrows. Note the hypo-signal from subcutaneous fat and bone marrow because of the application of fat saturation.

Quantitative NMRI methods have been and are still being developed, and some clinical studies have already revealed their potential to offer outcome measures of disease progression (20, 21, 24) and the effects of treatment (22, 27). However, these trials also pointed out the precision limitations of the currently available quantitative approaches for the characterization of inflammation, which may result in similar lack of sensitivity depending on the applied methodology.

Moreover, similar abnormalities of T2-value have been shown to be related to different

physiological alterations, such as necrosis, intracellular or/and interstitial oedema, which may all occur separately or at the same time in some pathological scenarios. These features are responsible for the lack of specificity of T2 on the characterization of pathophysiological processes responsible for the disease progression.

In this work we present, in a first moment, two different methodologies that allow extracting muscle T2-value free of confounding fat signal contributions. Secondly, we present a technique to access information about water distribution within tissue (intracellular, interstitial and vascular), which is presented as a promising solution for addressing the sensitivity and specificity problem related with the observation of muscle T2. Finally, we describe our attempts to detect initial fibrotic tissue accumulation by exploring an especial imaging technique that allows signal acquisition from structures with very short T2-values.

1.3. Thesis overview and contributions

In this section we explain the organisation of the thesis manuscript. In chapter 2 we briefly present the basic physical principles underlying the NMR phenomena, and the resulting properties underlying the contrast mechanisms on NMRI techniques introduced in 1.2.

In chapter 3, we describe a methodology for the quantification of myowater T2-value on NMR images. In contrast to T2-weighted images, this technique allows the extraction of so called T2-maps, which are images of the actual T2-value distribution. This technique characterizes muscle tissue oedema, lesions and damages, by T2 quantification, and simultaneously also the degree of local fat infiltration, which make of it an interesting tool to study inflammation in fat infiltrated muscles. This technique was validated in vivo in healthy volunteers and myopathic patients. The study presented in this chapter was published in the *Journal of Magnetic Resonance Imaging* (Azzabou et al. 2014, *Validation of a generic approach to muscle water T2 determination in fat-infiltrated skeletal muscle*).

In chapter 4, we describe in details the application of another NMRI technique for the extraction of T2-maps. In contrast to the method proposed in Ch. 3, in this technique only water magnetization is selected, allowing simpler post processing. The proposed method also offers simpler approaches for correcting errors caused by system imperfections. This technique was validated in vivo, and the results presented in this chapter were the object of an article published in the journal *Magnetic Resonance in Medicine* (de Sousa et al. 2012. *Factors controlling T2-mapping from partially spoiled SSFP sequence: optimization for skeletal muscle characterization*).

In chapter 5 the issues related with the interpretation of T2-relaxometry in SKM tissue

and the specificity of T2-measurement are approached. The theory of relaxation in tissue is briefly reviewed along with the resulting hypotheses concerning the interpretation of muscle T2-relaxation data. We detail the implementation of a clinical protocol, from the acquisition technique to the post-processing, which allowed us to demonstrate the feasibility of quantifying myowater distribution within intracellular, interstitial and vascular spaces. We also validated a theoretical compartmental exchange model capable of predicting T2-relaxation data in healthy SKM tissue. These results are the object of two international communications (Araujo et al. 2013; Araujo et al. 2014) and an article published in the *Biophysical Journal* (Araujo et al. 2014. *New Insights on skeletal muscle tissue compartments revealed by T2 NMR relaxometry*). Finally, we further developed the validated compartmental exchange model in order to represent expected tissue alterations, such as cellular oedema, inflammation and necrosis, characteristics of many NMDs. Simulated data from such altered models were analysed with the aim of getting some insight about the potential applications of the developed methodology for studying muscle pathology, and were compared with in-vivo data obtained in patients with NMD.

In chapter 6 we describe the application of an NMRI technique which allows the detection of signal from fast relaxing tissue structures such as fascia, cortical bone and as recently verified (33) fibrosis, for imaging IMCT. First, we describe a study in which we demonstrated the feasibility of detecting a short-T2-component ($T_2 < 1$ ms) in SKM, and collected indices suggesting that it shall represent connective tissue. The results of this first study were communicated in two international conferences, including an oral presentation (Araujo et al. 2011, 2012). Then we proposed and validated in-vivo a post-processing method for imaging the short-T2-components observed in SKM.

Chapter 7 resumes the conclusions from all the obtained results and presents the perspectives for future developmental work, from the application of clinical protocols to the implementation of more sophisticated techniques to complement and extend the limits of application of the methodologies developed and applied in this thesis work.

CHAPTER 2

Basic Concepts of Nuclear Magnetic Resonance

In the early 1920's elemental particles (atomic nuclei, electrons, etc.) have been shown to possess a fundamental property, other than mass and electric charge, called spin. The spin may be seen as the intrinsic angular momentum of elemental particles. Analogously to the magnetic moment associated to the orbital kinetic moment of a particle, we associate a spin magnetic moment to every elemental particle. This intrinsic magnetic property was investigated by studying the interactions of spin with magnetic fields. These studies, first piloted by Rabi and coworkers in the early 1930's, have shown that, when immersed in an external magnetic field, some atomic nuclei are capable of absorbing and emitting photons (classically, electromagnetic waves) at specific frequencies that univocally identify each element. Their work established the basis for the understanding of the interactions between spin magnetic moments and magnetic fields. These works were further explored by the research groups led by Felix Bloch and Edward Mills Purcell that were awarded the 1952 Nobel Prize for "their development of new ways and methods for nuclear magnetic precision measurements". Their works described the time evolution of the electromagnetic signal in NMR experiments and constitute the basis for the development of NMRI.

The techniques that apply the NMR phenomenon to study a given physical system consist of at least three basic steps:

- i- Polarization of the spin magnetic momenta of the system by application of an external magnetic field.
- ii- Excitation of the system by absorption of specific frequency selective electromagnetic radiation.
- iii- Detection of the electromagnetic signal during the relaxation of the system from the excited to the minimum potential energy state (thermal equilibrium).

The combination of specific and precisely controlled excitation and detection techniques allows one to extract different physical information about the studied system, and still

make the object of study of researchers and engineers that work on the present development of NMRS and NMRI tools.

In the following sections we will briefly present the main theoretical aspects of NMR with the minimum formalism necessary for the understanding of the methodological developments of the present work. The following sections were inspired by the work of Haacke et al. (36).

2.1. The spin magnetic moment and the precession equation

Classically, a magnetic dipole moment might be conceived as an infinitesimal planar current loop (Figure 2-1 a) encircling an area A and is defined as

$$\vec{\mu} = IA\hat{n} = q \frac{v}{2\pi r} \pi r^2 \hat{n} = \frac{q}{2m} \vec{r} \times \vec{p} = \frac{q}{2m} \vec{L} \equiv \gamma \vec{L} \quad 2.1$$

where q , m , v and \vec{p} are the electric charge, the mass, the speed and the linear momentum of a particle running the loop, respectively, \vec{r} is the vector pointing to its position from the centre of the loop, and I is the electric current resulting from its movement. Eq. 2.1 states that the magnetic moment $\vec{\mu}$ is proportional to the angular momentum \vec{L} , and the proportionality constant γ is called the *gyromagnetic* (or *magnetogyric*) ratio.

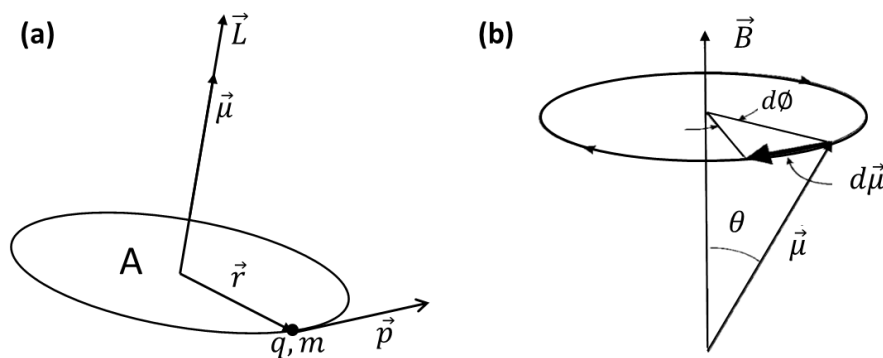


Figure 2-1 – (a) The magnetic dipole moment $\vec{\mu}$ produced by a dimensionless particle with an electric charge q , inertial angular momentum \vec{L} . (b) Illustration of the precession of the spin magnetic moment $\vec{\mu}$ around the external magnetic field \vec{B} as a consequence of the torque resulting from their mutual interaction. mass m , running within circular trajectory with radius r with a linear momentum \vec{p} and (Taken from Haacke, Brown, Thompson, & Venkatesan., 1999).

The electrodynamics theory says that an infinitesimal loop placed in an external magnetic field \vec{B} experiences a torque given by

$$\vec{\tau} = \vec{\mu} \times \vec{B} = \frac{d\vec{L}}{dt} \stackrel{(1)}{\Rightarrow} \frac{d\vec{\mu}}{dt} = \gamma \vec{\mu} \times \vec{B} \quad 2.2$$

Eq. 2.2 describes a precession of $\vec{\mu}$ around the direction determined by \vec{B} with an angular frequency $\frac{d\phi}{dt}$ (see Figure 2-1 b). Opening Eq. 2.2 in spherical coordinates and realising that $|\vec{\mu}|$ is constant, one gets to the relation for the precession frequency

$$\frac{d\vec{\mu}}{dt} = |\vec{\mu}| \sin \theta \frac{d\phi}{dt} \hat{\phi} = \gamma |\vec{\mu}| \sin \theta |\vec{B}| \hat{\phi} \Rightarrow \frac{d\phi}{dt} = \gamma |\vec{B}| \equiv \omega_B \quad 2.3$$

known as the Larmor precession frequency.

The experience shows that there is an intrinsic magnetic dipole moment $\vec{\mu}_s$ connected to the intrinsic spin angular momentum, \vec{S} , given by $\vec{\mu}_s = \gamma_s \vec{S}$. The *spin* is a quantum-physical property to which no classical representation has ever been found, and $\gamma_s \neq \frac{q}{2m}$. We usually define the so called g-factor, g , such that $\gamma_s = g \frac{q}{2m}$. The g-factor reflects intrinsic physical properties of the elemental particle or nucleus. The *gyromagnetic ratio* γ_s of a nucleus is a fundamental quantity in NMR and we will represent it simply by γ on the following for sake of simplicity.

One may now see Eq. 2.2 as the fundamental equation describing the interaction between a spin magnetic moment and an external magnetic field, which is the key for understanding the NMR phenomena.

2.2. Magnetic polarization (Magnetization)

The potential energy associated with the interaction between a magnetic dipole moment, $\vec{\mu}$, and an external magnetic field, \vec{B} , is given by

$$U = -\vec{\mu} \cdot \vec{B} \quad 2.4$$

The Boltzmann's law of statistical mechanics states that for a system of particles in thermal equilibrium, the probability, $P(\epsilon)$, of observing the particles composing the system in a given arrangement varies exponentially with the negative of the potential energy of that arrangement, divided by kT , where k and T are the Boltzmann constant and the absolute temperature of the system, respectively.

$$P(\epsilon) \propto e^{-\epsilon/kT} \quad 2.5$$

Equations 2.4 and 2.5 state that, when immersed in an external magnetic field, the magnetic momenta of the particles constituting the system will have a higher probability to be observed aligned to it, resulting in a measurable magnetic moment aligned to the

external field. We will say that the system is magnetized, defining the magnetization vector, $\vec{M}(\vec{r}, t)$, as the spatial density distribution of the magnetic moment aligned to the external field at a time t . As the average thermal energy, kT , at human body temperatures ($\sim 310K$) is much higher than the magnetic potential energy, $-\vec{\mu} \cdot \vec{B}$, the probability advantage of observing spin magnetic momenta aligned to \vec{B} is very small ($\sim 10^{-5}$ at 3 teslas). That is the reason why such high fields are usually used in NMR systems.

The relation between \vec{M} and $\vec{\mu}$ is linear and Eq. 2.2 may be easily generalized so that

$$\frac{d\vec{M}(\vec{r}, t)}{dt} = \gamma \vec{M} \times \vec{B} \quad 2.6$$

2.3. Magnetization excitation and the resonance phenomenon

Let's define the non-zero net-magnetization aligned to the external magnetic field, \vec{B}_0 , by

$$\vec{M}(t) = \int d^3r \vec{M}(\vec{r}, t) \quad 2.7$$

We will call *magnetization excitation* the process of breaking the thermal equilibrium of a system by tipping the net magnetization vector away from the \vec{B}_0 direction. This might be done by applying a second magnetic field, \vec{B}_1 , orthogonal to \vec{B}_0 . In practice $\frac{|\vec{B}_1|}{|\vec{B}_0|} < 10^{-3}$, and it is easy to notice that a static field \vec{B}_1 will only bring the system to a second thermal equilibrium state with $\vec{M} \parallel (\vec{B}_0 + \vec{B}_1)$. As the field $\vec{B}_{eff} \equiv \vec{B}_0 + \vec{B}_1 \cong \vec{B}_0$, practically nothing will change. If instead, an oscillating transverse \vec{B}_1 is applied at the Larmor precession frequency, γB_0 , i.e., in resonance with the precessing magnetization, for a duration τ , the net magnetization will be tipped away by an angle $\varphi(\tau) = \gamma |\vec{B}_1| \tau$. To see this, let's observe the system from a referential rotating at the Larmor frequency (Figure 2-2). From this point of view the \vec{B}_1 field will be static and no precession of \vec{M} around \vec{B}_0 would ever be observed. It follows that in this referential $\vec{B}_{eff} = \vec{B}_1$ and, from Eq. 2.6 it follows that

$$\frac{d\vec{M}}{dt} = \gamma \vec{M} \times \vec{B}_1 \quad 2.8$$

which describes a simple precession of \vec{M} around the \vec{B}_1 field.

Different frequency and amplitude modulations of \vec{B}_1 may be applied depending on

how one wants to tilt the net magnetization vector. For most of the NMR systems the Larmor frequency is on order of MHz and the magnetic field $\vec{B}_1(t)$ is usually referred to as a *radio frequency (RF) pulse*. An RF-pulse that tips the magnetization by an angle φ away from its original direction will be referred as to a φ -pulse.

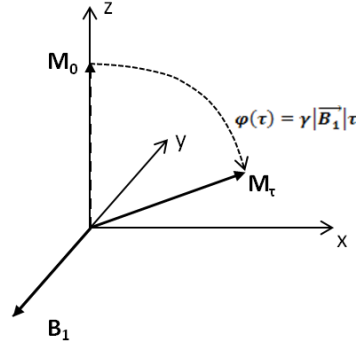


Figure 2-2 - Illustration of the process of magnetization excitation by the application of an oscillatory magnetic field \vec{B}_1 perpendicular to \vec{B}_0 , at the Larmor frequency. Note that from a referential rotating at the Larmor frequency the excitation process is seen as a precession of \vec{M} around \vec{B}_1 .

The magnetization vector resulting from the excitation described in Figure 2-2, is given by

$$\vec{M} = M_0(\cos \varphi \hat{z} + \sin \varphi \hat{x}) \quad 2.9$$

By applying the trigonometric identity $\cos(a + b) = \cos^2 a - \sin^2 b$, eq. 2.9 may be re-written on the form

$$\vec{M} = M_0 \left[\left(\cos^2 \frac{\varphi}{2} - \sin^2 \frac{\varphi}{2} \right) \hat{z} + \sin \varphi \hat{x} \right] \quad 2.10$$

In reality, the net-magnetization represents the observed average behaviour of the system, in which each composing spin magnetic moment is constantly evolving in a mixture states. As a consequence the action of the RF-pulse is not the same for each individual spin magnetic moment and Eq. 2.10 may be interpreted as stating that a fraction $\cos^2 \frac{\theta}{2}$ of the magnetization will not be tipped at all, as if no RF pulse had been applied to it, a fraction $\sin^2 \frac{\theta}{2}$ will be inverted, as if a 180° pulse had been applied to it, and a fraction $\sin \theta$ will be tipped 90° away from \hat{z} , as if a 90° pulse had been applied to it (Figure 2-3). The fraction $\sin \theta$ of the magnetization will be perpendicular to the \vec{B}_0 field and we shall refer to it as the *transverse magnetization*, while the remaining $\cos \theta$ is referred to as the *longitudinal magnetization*.

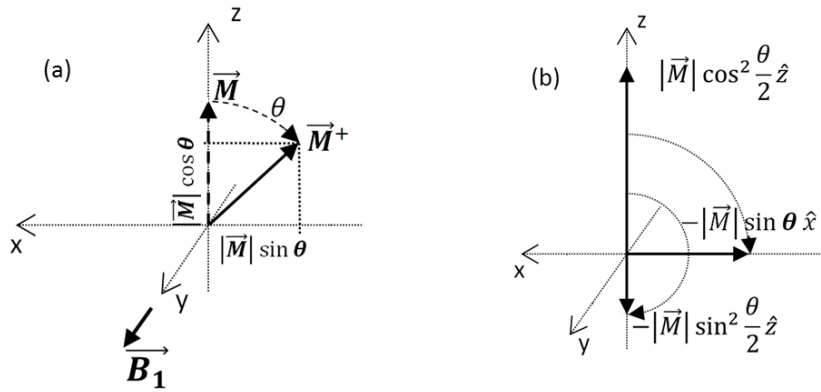


Figure 2-3 - (a) Illustration of the magnetization tipping by the application of a θ -pulse on the y -direction, and (b) the independent effects of the 180° and the 90° components on the magnetization.

2.4. Relaxation and the Bloch equations

After excitation, the system will not be in equilibrium anymore and a process of energy redistribution will take place, leading to re-attainment of Boltzmann equilibrium and realignment of magnetization to the longitudinal magnetic field, \vec{B}_0 . Energy redistribution is accomplished by interactions between the magnetic moments of the excited nuclei and the molecules in the lattice, converting magnetic potential into kinetic energy. For each downward transition of a nuclear spin there will be an acceleration of a rotational, translational, or internal motion of the molecule in which the transition occurred. As for the process of excitation, most efficient interactions of $\vec{\mu}$ with external fields occur at the Larmor frequency. Consequently there must be a component of the molecular motion at that frequency, which makes the process of longitudinal relaxation strictly dependent on the rate of molecular motion. This process of energy redistribution is called longitudinal (or spin-lattice) relaxation.

If at equilibrium the net magnetization is aligned to the longitudinal magnetic field \vec{B}_0 , then there must be no transverse residual magnetization at this point, implying that there is a process of transverse magnetization relaxation related to the restoration of the Boltzmann equilibrium.

$$\lim_{t \rightarrow \infty} \mathbf{M}_\perp(t) = \mathbf{0} \quad 2.11$$

$$\lim_{t \rightarrow \infty} \mathbf{M}_z(t) = \mathbf{M}_0 \quad 2.12$$

However, there is a second independent phenomenon that causes transverse magnetization damping. The molecules in the system are constantly experiencing rotational and translational Brownian motion. The magnetic moment of their protons will

then induce random fluctuations of the magnetic field within the space occupied by each nucleus. The longitudinal components of these fluctuating local fields will induce slightly different local precession frequencies which will result in incoherent dephasing of the spin isochromat, consequently killing the net transverse magnetization. These interactions may occur between protons within the same molecule (intramolecular interactions) or between protons in different molecules (intermolecular interactions). No energy is lost to the lattice in this process, and it is called transverse (or spin-spin) relaxation. In (36) a very simple model in which each individual spin magnetic moment interacts with its local magnetic field, which fluctuates randomly thus leading to a null mean phase dispersion of the whole system, is used to show that these random interactions lead imperatively to an exponential decay of the total magnetization amplitude with the time. Furthermore it is shown that in such a model the rate of decay is proportional to the *correlation time*, τ_c , which may be interpreted as representing the average time taken for the local fields to change significantly. With a more sophisticated mathematical model which takes the dynamics of the molecular motion into account, the correlation time may be derived from the rotational and oscillatory movements of the molecules constituting the system.

The longitudinal and transverse relaxation processes are not included in Eq. 2.6 indicating that it is incomplete. The equations predicting the interactions of the net magnetization with external magnetic fields, taking the relaxation phenomena into account were introduced by the physicist Felix Bloch in 1946 and are known as the Bloch Equations. These are phenomenological equations whose theoretical derivation came out from the quantum mechanics theory, and are out of the scope of this text. The longitudinal and transverse relaxation processes are formally described by

$$\frac{dM_z}{dt} = \frac{1}{T_1}(M_0 - M_z) \quad 2.13$$

$$\frac{d\mathbf{M}_\perp}{dt} = -\frac{\mathbf{M}_\perp}{T_2} \quad 2.14$$

where T_1 and T_2 are defined as the experimental spin-lattice and spin-spin relaxation times respectively. In view of Eqs. 2.13 and 2.14, Eq. 2.6 may be completed resulting on the following equations for the evolution of the magnetization of a system interacting with an external magnetic field

$$\frac{d\vec{M}}{dt} = \gamma\vec{M} \times \vec{B}_{ext} + \frac{M_0 - M_z}{T_1}\hat{z} - \frac{M_x}{T_2}\hat{x} - \frac{M_y}{T_2}\hat{y} \quad 2.15$$

with $\vec{B}_{ext} = \vec{B}_0 + \vec{B}_1$. Equations 2.13 and 2.14 describe the exponential behaviour of the relaxation processes illustrated in Figure 2-4.

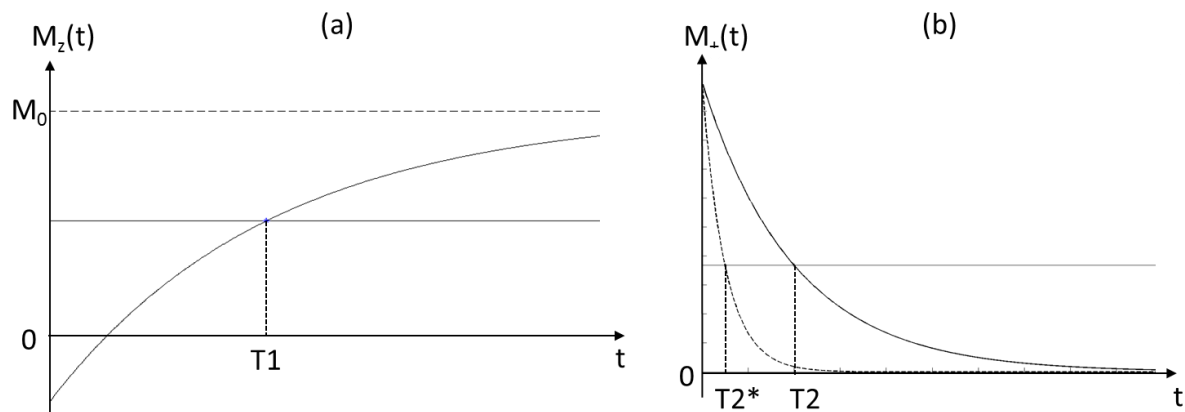


Figure 2-4 – Illustration of the exponential behaviour of the (a) longitudinal and (b) transverse relaxation processes. Note in (b) the exponential modulation of the spin-spin relaxation by field inhomogeneities leading to the faster T_2^* relaxation.

In practice the external magnetic field \vec{B}_0 is not homogeneous and the signal from different points will have slightly different frequencies, thus leading to further dephasing of the transverse magnetization. This results on an exponential modulation of the transverse relaxation (see Figure 2-4-(b)), and T_2 shall be replaced in Eqs. 2.14 and 2.15 by $T_2^* = \frac{T_2 T_2'}{T_2 + T_2'}$, where T_2' is a local quantity, usually both machine and sample dependent.

2.5. Nuclear magnetic resonance spectroscopy

Besides their characteristic intrinsic Larmor precession frequencies which allow different nuclei to be individually studied, the same nucleus experience distinct magnetic environments in different molecules, even if immersed in identical external magnetic fields. These differences will lead to characteristic local magnetic field shifts between different chemical compounds. This means that the characteristic Larmor precession frequency of a nucleus will be chemically shifted to slightly different values depending upon its molecular environment. In practice these chemical shifts are very small so that, in order to be observed, the inhomogeneities of the external magnetic field need to be smaller than the molecular magnetic field shifts within the volume occupied by the studied system. But even for ideal perfectly homogeneous fields, the same random fluctuations of the magnetic field that lead to the spin-spin relaxation process will limit the spectral resolution of each nucleus at any given chemical compound. However, the characteristic chemical frequency shifts are proportional to the external magnetic field, so that resolution of NMR spectra may be increased by increasing the external magnetic field.

In NMRS, the signal collected from the sample has contributions from all its chemical

compounds containing the nucleus of study. By Fourier transforming the acquired signal one may map the time domain back into a frequency domain and thus quantify the individual contributions of each chemical compound resolvable in the extracted spectrum. An example of ^1H -NMR signal acquired from a volume containing subcutaneous fat and muscle tissue at an external field of 3T and the corresponding spectrum extracted by Fourier transforming the signal is presented in Figure 2-5; the chemical shift between the methylene group in the triglycerides and water molecules is around 3.5 ppm, which corresponds to approximately 430 Hz at 3T.

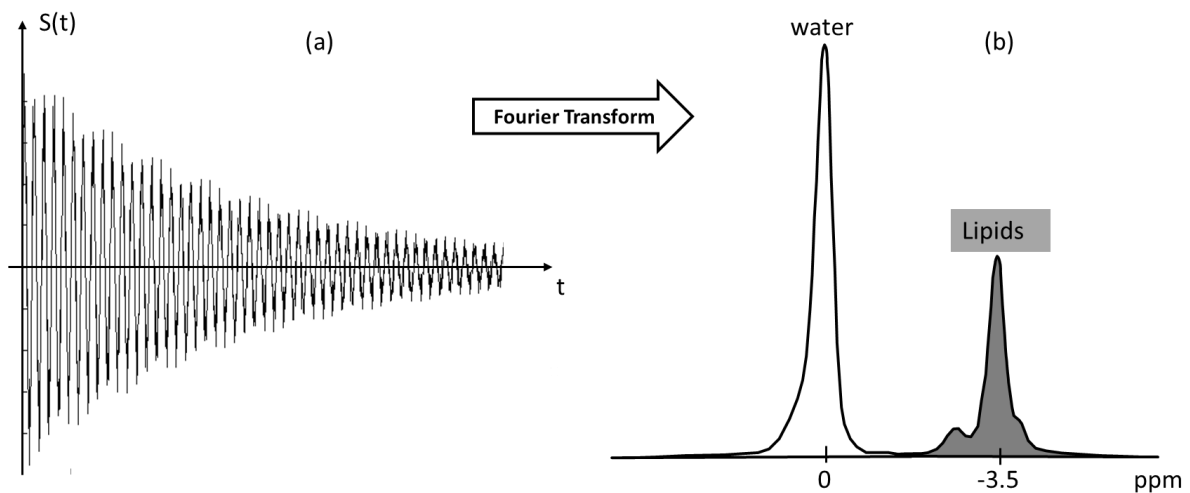


Figure 2-5 – (a) ^1H -NMR signal acquired from within a volume containing muscle tissue and subcutaneous fat. (b) The corresponding extracted spectrum resulting from the Fourier transform of the acquired signal. Contributions from lipids were painted in grey.

The signal from a spin density distribution of chemical compounds, $\rho(\omega)$, may be written as the sum of the signal from all nuclei over the entire frequency domain and will be given by

$$S(t) = \int \rho(\omega) e^{i\omega t} d\omega \quad 2.16$$

But Eq. 2.16 is precisely the definition of the inverse Fourier transform of $\rho(\omega)$, and the linearity of the transformation imposes that

$$\rho(\omega) = \int S(t) e^{-i\omega t} dt \quad 2.17$$

2.6. Nuclear magnetic resonance imaging

In contrast to NMRS techniques in which the goal is to quantify the total signal from different chemical compounds regardless of their spatial location in the uniform external magnetic field, in NMRI the objective is to prepare the signal acquisition in such a way to

allow extraction of information about the spatial distribution of the chemical compound irradiating the observed signal. This may be done by applying a controlled spatial variation on the external magnetic field through the studied body, which leads to a spatially encoded Larmor precession frequency, $\omega(\vec{r})$. The spatial variations of the external field, $\vec{B}_0 = B_0(\vec{r})\hat{z}$, may be determined by the gradient field given by

$$\vec{G}(\vec{r}) = \frac{\partial B_0(\vec{r})}{\partial x} \hat{x} + \frac{\partial B_0(\vec{r})}{\partial y} \hat{y} + \frac{\partial B_0(\vec{r})}{\partial z} \hat{z} \quad 2.18$$

If the gradient $G(\vec{r})$ is applied during the signal acquisition, then the frequency of the signal coming from a chemical compound in the position \vec{r} , will be given by

$$\omega(\vec{r}) = \gamma(\mathbf{B}_0 + \vec{G} \cdot \vec{r}) \quad 2.19$$

so that the position of the irradiating nuclei will be encoded in the frequency. This idea was first proposed by Lauterbur and Mansfield in 1973 (37). If the spatial frequency variations imposed by the application of the gradient are big enough so that the chemical shift variations are negligible, then the Fourier transform of the signal will be the projection of the spin magnetization density on the direction containing the gradient vector (see Figure 2-6).

The gradient may be chosen to be spatially uniform and the signal may be easily demodulated to exclude the constant frequency component $\omega_0 = \gamma\mathbf{B}_0$. Analogously to the NMRS acquisitions, the acquired signal will be described as the sum of the signal from all nuclei over the entire frequency domain and will be given by

$$S(\mathbf{t}) = \int \tilde{\rho}(\omega) e^{i\omega t} d\omega = \int P(\vec{r}) e^{i\gamma\vec{G}\cdot\vec{r}t} d\vec{r} \equiv s(\vec{k}) = \int P(\vec{r}) e^{i2\pi\vec{k}\cdot\vec{r}} d\vec{r} \quad 2.20$$

where $\vec{k} = \frac{\gamma}{2\pi} t\vec{G}$. Analogously, the linearity of the Fourier transform implies that

$$P(\vec{r}) = \int s(\vec{k}) e^{-i2\pi\vec{k}\cdot\vec{r}} d\vec{k} \quad 2.21$$

The function $s(\vec{k})$ is the representation of the projection $P(\vec{r})$ in the so called *k-space*.

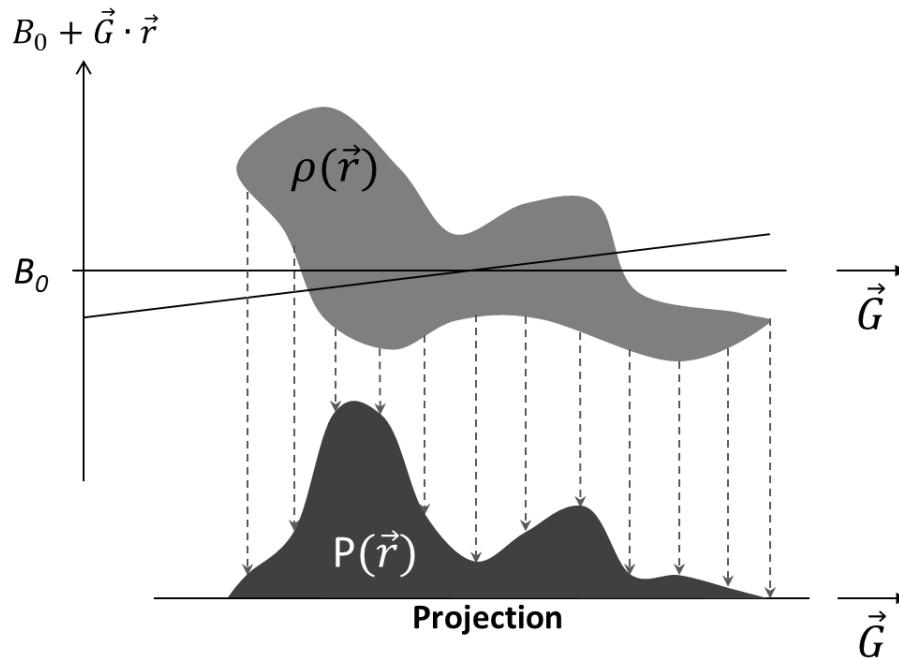


Figure 2-6 – Illustration of the physical interpretation of the Fourier transform of the signal acquired in the presence of a gradient field. The acquired signal is the inverse Fourier transform of the projection of the spin magnetization on the direction of the gradient.

Analogously to our perception of objects in our everyday life, we may intuitively note that a large enough number of projections in different directions offer enough information about the spatial distribution of spin magnetization. Indeed tomographic images of the spin magnetization distribution may be reconstructed for a desired level of precision from a large enough number of projections in all the different directions.

Using the approach of space representations, the projections in different directions may be seen as different lines in different directions in the k-space as illustrated in Figure 2-7.

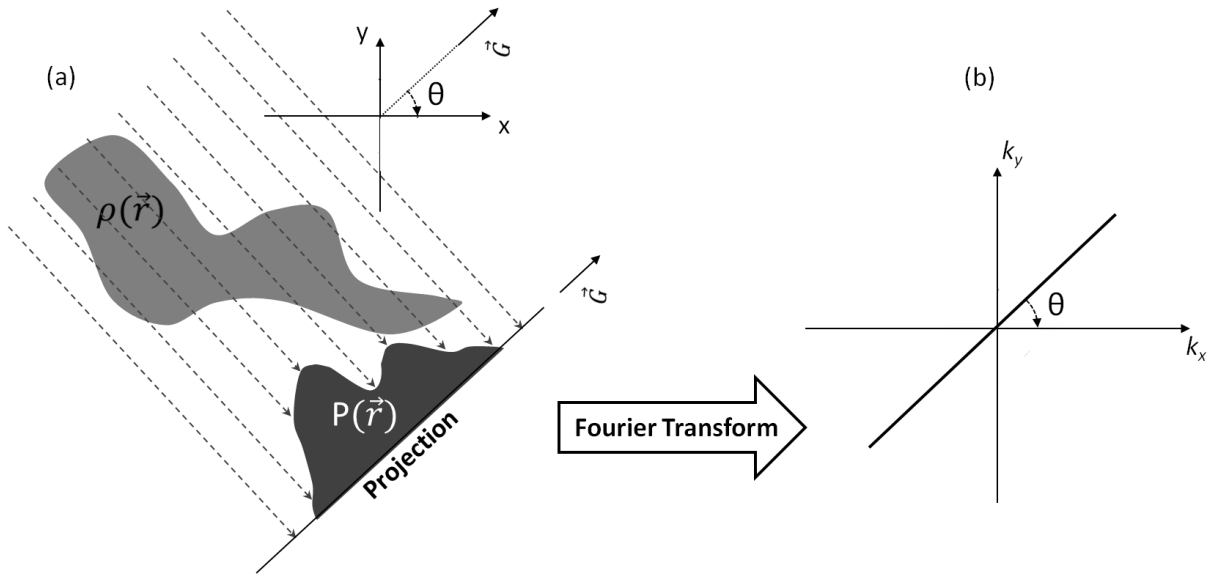


Figure 2-7 – Illustration of the radial k -space sampling method. (a) Projection of the magnetization distribution, $\rho(\vec{r})$, on the direction perpendicular to the gradient, \vec{G} . (b) The acquired signal corresponds to a k -space line crossing the origin with inclination determined by \vec{G} . The Fourier transform of the different projections of the spin magnetization distribution correspond to different lines of its k -space representation. These lines cross the origin and have the same direction than the applied gradient.

A tomographic image of the spin magnetization distribution may be reconstructed by performing a bi-dimensional Fourier transform of the distribution $s(k_x, k_y)$. This imaging method uses rotating gradients and the acquisition technique associated is called radial sampling is crucial for imaging samples with very short T2-values (38).

The concept of the k -space representation may be further explored, and in principle the distribution $s(\vec{k})$ may be sampled in any arbitrary way, leading to a huge variety of k -space sampling and related acquisition methods. A more complete and detailed description of NMRI methods may be found in (36). It is though worthy to briefly describe the linear k -space sampling method. It is the most common method applied in NMRI techniques, some of which are applied in this thesis work. From the definition $\vec{k} = \frac{\gamma}{2\pi} t \vec{G}$, one may interpret a point $(k_x(t), k_y(t))$ in the k -space as describing a phase configuration of the object, $M(\vec{r})$, at an instant t . In the linear sampling different parallel lines of the k -space are acquired at each readout interval. In order to move from the centre of the k -space to the initial point of each line, the phase of $M(\vec{r})$ is prepared before readout by application of two orthogonal gradients, say G_x and G_y (Figure 2-8). Once at the initial point (k_{x0}, k_{y0}) , all the points (k_{xi}, k_{yj}) are registered, with $i = -n, 1, 2, \dots, n - 1$ where $2n$ defines the

number of points registered per k -space line. It is worthy to highlight here that the discretization of the measurement imposes limits on the minimum k -space resolution, Δk . It can be shown that the Fourier transform, $\hat{\rho}$, of a discretized signal, $\hat{s}(p) \equiv \hat{s}(p\Delta k)$, with $p \in [-n, n - 1]$, will be periodic, i.e., $\hat{\rho}(q) \equiv \hat{\rho}(q\Delta x) = \hat{\rho}\left(q\Delta x + \frac{1}{\Delta k}\right) \forall q \in \mathbb{Z}$. As a consequence, the space period, $\frac{1}{\Delta k}$, usually referred to as field of view (FOV), must be larger than the distribution to be reconstructed to avoid spatial aliasing. If we ignore the effect of data truncation (i.e., $n \neq \infty$), the spatial resolution of the reconstructed distribution will be given by $\Delta x = \frac{FOV}{2n} = \frac{1}{2n\Delta k} \equiv \frac{1}{k_{max}}$.

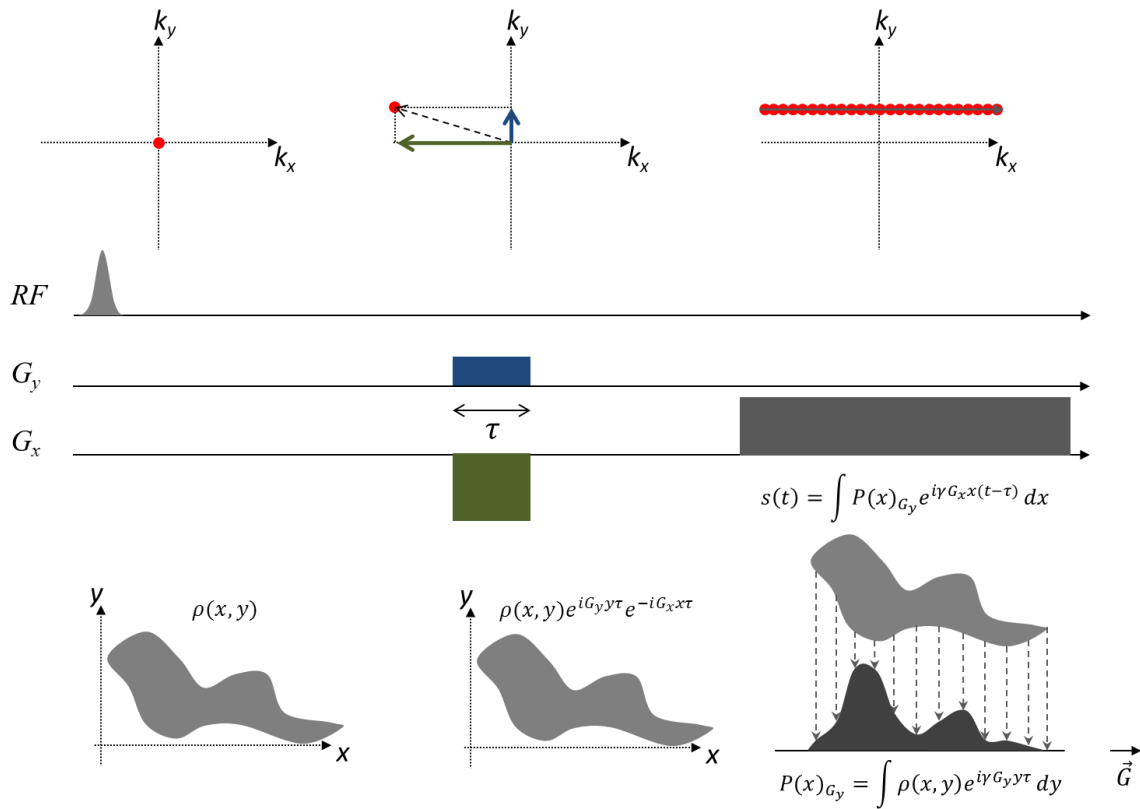


Figure 2-8 – Schematic illustration of the linear k -space sampling. Parallel lines of the k -space are acquired at each readout interval. In order to move from the centre of the k -space to the initial point of each line, the phase of $\mathbf{M}(\vec{\mathbf{r}})$ is prepared before readout by application of two orthogonal gradients, say G_x and G_y . Once at the initial point $(\mathbf{k}_{x0}, \mathbf{k}_{yj})$, all the points $(\mathbf{k}_{xi}, \mathbf{k}_{yj})$ are registered, with $i = 1, 2, \dots, n$, where “ n ” defines the number of points registered per line, which will be related to the spatial resolution of the image.

The concept of k -space may be further generalized to three dimensional (3D) acquisitions. The idea is to excite the entire volume to be imaged, and to sample a 3D k -

space volume by applying combinations of three orthogonal gradients. As for the 2D-acquisition, the most common acquisition strategy for 3D-NMRI is the linear sampling. In this case, two phase encoding gradients are applied in two orthogonal directions before signal acquisition, which will be done under application of the readout gradient in the third orthogonal direction. Analogously to 2D-NMRI, the 3D k -space sampling may be done with arbitrary gradient trajectories, and the 3D magnetization distribution may be obtained from a 3D Fourier transform of the k -space.

2.7. Characterization of tissue NMR parameters and NMRI contrasts

2.7.1. The spin echo

The spin-echo phenomenon was first observed by Erwin Hahn in 1950 (39). He observed that the phase dispersion of the magnetization due to field in-homogeneities, which leads to T2* modulation of the intrinsic T2-decay, may be re-winded by the action of the 180° pulse component which will invert the phase of all spin magnetic moments leading to a time-symmetric re-establishment of phase coherence (or refocusing) (Figure 2-9). The instant of the re-establishment of phase coherence is usually called echo-time (TE).

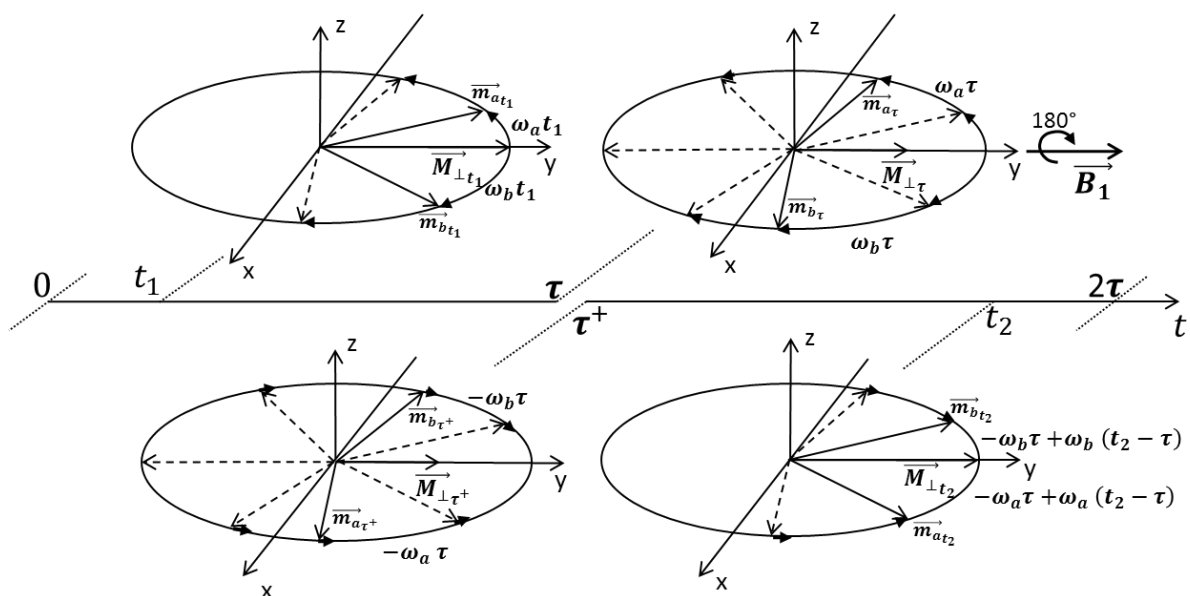


Figure 2-9 - Illustration of re-establishment of phase coherence following the application of a 180° pulse. τ^+ represent the instant just after application of the 180° pulse at the time τ , supposing the effect of the pulse is instantaneous. Note that the individual spin magnetic moments conserve their local precession frequency during all the experiment. Complete refocusing occurs at $t = 2\tau \equiv TE$.

This phenomenon allows one to correct for the B_0 in-homogeneity related T_2' effects and observe the intrinsic transversal relaxation rate $1/T_2$ (Figure 2-10).

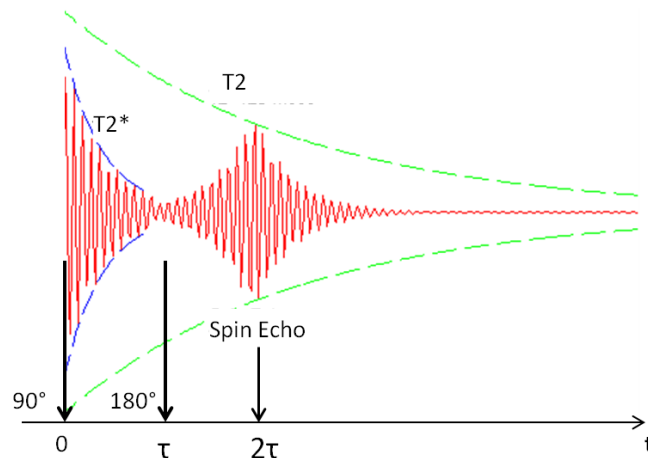


Figure 2-10 - Illustration of the spin echo signal. Note the T_2' recovery following phase reversal of the FID signal originated from the 90° pulse after application of the 180° pulse. Note also the irreversibility of the T_2 -decay. (The wiggling inside the T_2^* envelope is due to off-resonance effects).

The NMR signals acquired at a given echo-time, TE , will be reduced by a factor e^{-TE/T_2} and will be said to be T_2 -weighted. Due to the differences of T_2 between tissues or structures, their individual contribution to the NMR signal will not reflect their real relative magnetization fraction.

2.7.2. The gradient echo

After magnetization excitation the spin phase might be encoded in some given direction, \hat{x} , by the application of a gradient, $\vec{G} = G\hat{x}$, as discussed in 2.6. If the gradient is applied during an interval τ , after its application the phase of the spin isochromats at a position x will be given by

$$\varphi(x) = \gamma G \tau x \quad 2.22$$

If a second gradient, $\vec{G}_2 = G_2\hat{x}$, is applied on the same direction during an interval τ_2 , a Gradient Recalled Echo (GRE) will occur whenever

$$G_2 \tau_2 + G \tau = 0 \quad 2.23$$

Figure 2-11 describes a simplified scheme of the RF pulse and gradient time sequence for the acquisition of a gradient echo.

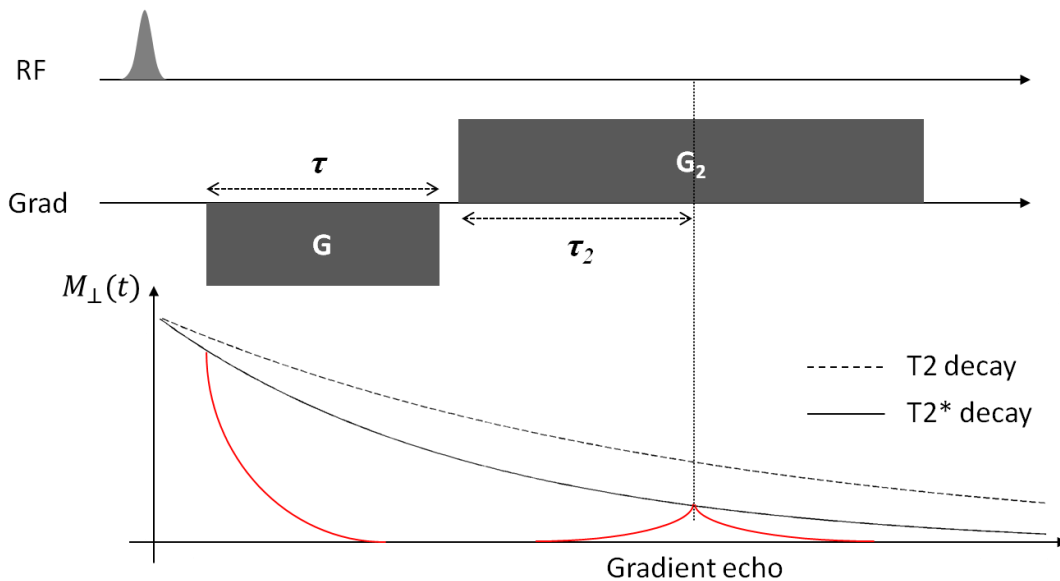


Figure 2-11 – Simplified scheme of the gradient and RF-pulse time sequence for the acquisition of a gradient echo.

No refocusing pulse is applied on gradient echo sequences and the excitation flip angle can be set small enough to leave most of the longitudinal magnetization undisturbed and still generate appreciable transverse magnetization (Figure 2-12). Therefore no lengthy period of time is required for T1-recovery, and the repetition time can be set to very small values, making GRE sequences the best choice for rapid imaging.

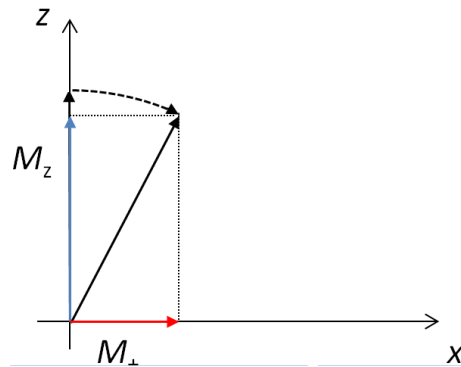


Figure 2-12 – Appreciable transverse magnetization generated by a small flip angle,, which leaves the longitudinal magnetization mostly intact.

Because of the absence of refocusing pulses, the phase of the spin isochromat in the transverse plane accumulates during the entire echo-time and, consequently, the signal will be T2*-weighted (see Figure 2-11).

2.7.3. Magnetization from repeated RF-pulses and the steady state

In practical NMRS applications signal acquisition is repeated a large number of times in order to accumulate signal and increase signal to noise ratio (SNR), while in NMRI

techniques, besides accumulation, signal is repeatedly acquired until obtaining enough k-space sampling for posterior image reconstruction. In both cases magnetization is often re-excited by the same θ -pulse at a constant time interval referred to as repetition time (TR).

The longitudinal magnetization, M_z , will be reduced by a factor $\cos\theta$ after each excitation and will recover with a rate $1/T_1$ while the transverse magnetization, M_{\perp} , will be summed to the freshly excited magnetization $M_z\sin\theta$. Moreover, the 180° components of each RF-pulse will refocus previously excited magnetization leading to the formation of echoes. It can be shown that, after a large enough number of re-excitations, the longitudinal magnetization, M_z , and the transverse magnetization, M_{\perp} , will attain a constant value between consecutive TR intervals. This may be formally defined by

$$\begin{aligned} M_z(t + nTR) &= M_z(t + (n - 1)TR) \\ M_{\perp}(t + nTR) &= M_{\perp}(t + (n - 1)TR) \end{aligned} \quad 2.24$$

with $t \in (0, TR)$

where n is the index of the n^{th} TR-interval. When this condition is established the system is said to be in a *steady state condition*.

The steady state condition is very explored in GRE sequences which are usually classified by the response of the transverse magnetization, M_{\perp} . If the GRE sequence is such that, at the steady state condition, the transverse magnetization, M_{\perp} , just after application of the θ -pulse will only have contributions of the freshly excited steady state longitudinal magnetization, M_z , such that $M_{\perp} = M_z \sin \theta$, then the sequence is said to be *spoiled*. However, if at steady state condition the transverse magnetization, M_{\perp} , just after application of the θ -pulse will have contributions from freshly excited longitudinal steady state magnetization, M_z , and previous transverse magnetization, M_{\perp}^- , such that $M_{\perp} = M_{\perp}^- \cos \theta + M_z \sin \theta$ then the GRE sequence is said to produce a *steady-state free precession (SSFP) condition*. Detailed and formal discussion about GRE sequences and attainment of steady state conditions is presented in (36).

The Spoiled condition may be easily attained by choosing $TR \gg T_2$ so that transverse magnetization will have completely decayed before each excitation. It can be shown (see Bernstein et al., 2004) that for spoiled sequences the longitudinal magnetization equilibrium is attained at

$$M_z = \frac{M_0 \left(1 - e^{-\frac{TR}{T_1}} \right)}{\left(1 - \cos \theta e^{-\frac{TR}{T_1}} \right)} \quad 2.25$$

where n is the number of repetitions. However, GRE sequences are mostly applied for fast

imaging and, in practice, long TR-values are of no interest. When $TR \lesssim T2$, there will be non-null transverse magnetization at the moment of the next RF-pulse. In this case three different magnetization pathways are created by each RF-pulse, following the action of its 0° , 90° and 180° components (see 2.3). As a consequence, the signal will have a complicate dependence on the sequence and tissue parameters.

An alternative method for killing the residual transverse magnetization at the end of each TR-interval is to apply a spoiler (dephasing) gradient. However, if the moment of the spoiler gradient is not varied from one repetition to another, magnetization will be refocused after the next spoiler gradient because of the action of the 180° component on the previously spoiled transverse magnetization, resulting in inefficient spoiling. Moreover, the spoiler gradient moment must be superior to a lower limit in order to produce sufficient magnetization dephasing which limits the gradient variation schemes. It has been observed that even for optimized gradient amplitude variation, the spoiling efficacy is spatially in-homogeneous, which leads to images with intensity in-homogeneity. To solve this issue, a second spoiling method, which consists of phase cycling the RF-pulses, has been proposed to be applied together with the gradient spoiling technique (41–43). The idea behind RF spoiling is to vary the phase of the consecutive excitation pulses in such a way that after a sufficiently large number of excitations, the residual magnetization from previous TR intervals will sum up incoherently and cancel out.

It has been shown that efficient spoiling may be obtained if the total gradient moment is kept constant between TR-intervals, and by applying quadratic variation of the RF-pulse phase as a function of the repetition index, such that

$$\begin{aligned} \phi_n &= \phi_{n-1} + n\Delta\phi + \phi_0 \\ &\text{with } n = 0, 1, 2, \dots \end{aligned} \tag{2.26}$$

where ϕ_0 is the phase of the first RF-pulse and $\Delta\phi$ is referred to as the phase shift increment. However, it has been observed that the degree of spoiling depends quite sensitively on $\Delta\phi$. Particularly, if $\Delta\phi = 0$, spoiling is completely inefficient and SSFP condition is established. Many variants of the SSFP condition exist depending on the RF-pulse sequence, each leading to different steady state magnetization and corresponding signal as a function of the sequence parameters and tissue's T1- and T2-value (44–48). In contrast, for some particularly chosen values, as for example $\Delta\phi = 117^\circ$, spoiling is practically perfect and magnetization is correctly described by Eq. 2.25, which leads to a T_1 -weighted signal.

2.7.4. Diffusion effects and T2 measurement

The spin-echo method is capable of reversing the phase of all spin magnetic moments leading to re-attainment of phase coherence between spin isochromats at different locations within the in-homogeneous external magnetic field. However, the molecules constituting the system continuously experience Brownian motion and the resulting random variation of their positions avoids complete re-attainment of phase coherence. It can be shown that this random movement of the molecules result in a non-null mean squared molecular displacement, d^2 . The property of *diffusivity* is defined by

$$D = \frac{d^2}{2\tau} \quad 2.27$$

where D is referred to as the diffusion coefficient.

Because of the diffusion phenomenon, the phase dispersion of the spin magnetization vectors due to local \vec{B}_0 variations will not be completely re-winded after application of the refocusing pulse as the \vec{B}_0 field experienced by each spin isochromats may not be the same between the dephasing and rephasing intervals. Consequently the T2* modulation will not be nulled at the echo-time. It can be shown that the spin-echo signal from a 90°-180°-pulse experiment (see Figure 2-10) will be given by (p. 626 in ref. 36)

$$S(TE) \propto M_z e^{-\frac{TE}{T_2}} e^{-\gamma^2 G^2 D \frac{TE^3}{12}} \quad 2.28$$

Depending on the diffusivity properties of the studied molecules, the observed signal decay may be dominated by the diffusion effects, so that observed relaxation curves obtained from a series of spin-echo experiments applied with different echo-times (see Figure 2-13 a) will not reveal the intrinsic spin-spin relaxation behaviour of the system. Furthermore, the exponent in the signal decay will not be linear in the observation time, TE.

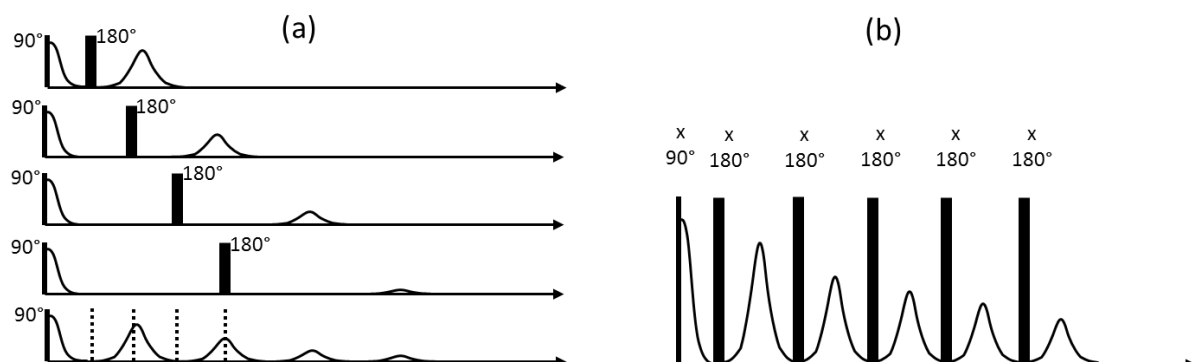


Figure 2-13 – (a) Method for observing signal decay from a series of 90°-180°-pulse experiments with different echo times. (b) Multi spin-echo method for observation of signal decay free of diffusion effects.

Instead of repeating the spin-echo experiment at different echo-times, a series of N 180° -pulses may be inserted after the excitation (49); such a sequence is referred to as *multi-spin-echo* (MSE). The 180° -pulses are equally spaced from each other by twice the interval between excitation and the first refocusing such that spin-echoes will occur at instants $t = nTE$, with $n = 1, 2, \dots, N$ (see Figure 2-13 b). It was shown that the signal from an MSE sequence observed at $t = nTE$ is given by (p. 626 in ref. 36)

$$S(nTE) = M_z e^{-\frac{nTE}{T_2}} e^{-\gamma^2 G^2 TE^2 D \frac{nTE}{12}} \equiv M_z e^{-\frac{nTE}{T_{2_{diff}}^*}} \quad 2.29$$

with

$$\frac{1}{T_{2_{diff}}^*} = \frac{\gamma^2 G^2 TE^2 D}{12} + \frac{1}{T_2} \quad 2.30$$

Note that in contrast to the spin-echo signal (Eq. 2.28), in the MSE sequence, TE represents the constant inter-echo-spacing. As a consequence, the entire exponent in the signal decay is linear in the observation time nTE (Eq. 2.29). Furthermore, Eq. 2.30 states that for sufficiently short TE , $T_{2_{diff}}^*$ can be made as close to T_2 as one desires (see Figure 2-14). This effect comes from the fact that the shorter the echo-time the shorter the interval during which molecules may diffuse before application of a refocusing pulse.

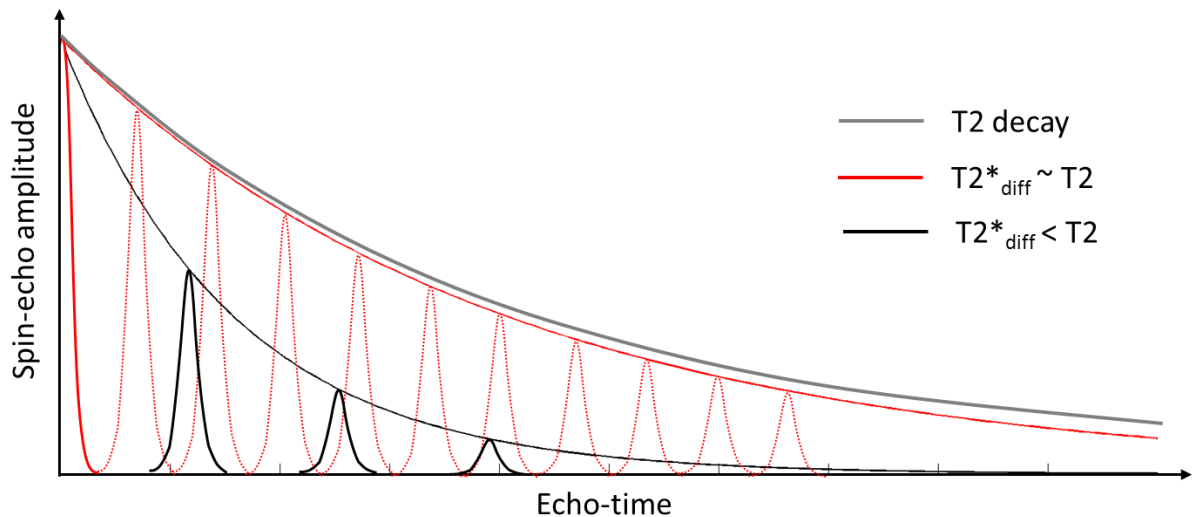


Figure 2-14 – The signal evolution in the Carr-Purcell method for different echo-times. The shorter the echo-time the shorter the diffusion interval and the closer is the observable $T_{2_{diff}}^*$ to the intrinsic T_2 .

In practice the 180° -pulses may be imperfect at some regions thus leading to incomplete refocusing and the signal will not be correctly described by Eq. 2.29 anymore. For the RF phase configuration of the Carr-Purcell (CP) method, FA errors of the

refocusing pulses will accumulate (Figure 2-15 a), resulting in faster amplitude decay from one echo to another. In order to solve this problem, an improvement of the Carr-Purcell method has been proposed (50) which allows correction of the 180°-pulse imperfection effects for the even echoes (Figure 2-15 b). To do so the refocusing pulses are applied 90° out of phase with respect to the excitation pulse.

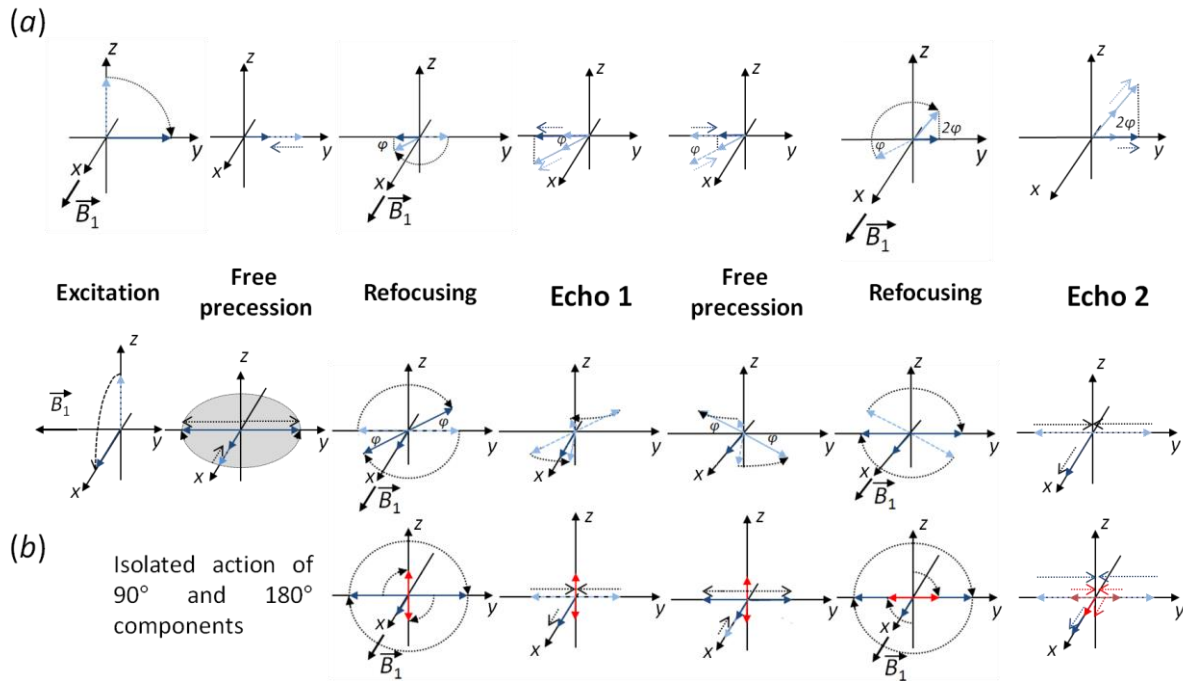


Figure 2-15 – Schematic illustration of the magnetization vector response to two consecutive imperfect refocusing pulses in the (a) Carr-Purcell method, and (b) Meiboom-Gill improved method. Observe the accumulation of the flip angle error in the Carr-Purcell method (a). Notice in (b) that the flip angle error, ϕ , is corrected after the second refocusing pulse. In (b), the 90° component of the first refocusing pulse will tip previously excited transverse magnetization to the longitudinal direction (red vectors). This longitudinally stored magnetization will be re-tipped to the transverse plane completing its 180° flip by the action of the 90° component of the second refocusing pulse. This magnetization will be refocused leading to the so called stimulated echo at a time $t = nTE$ with the same phase of the primary echo refocused by the action of the 180° component (blue vectors).

The time sequence diagram for the improved Carr-Purcell method is presented in Figure 2-16. It is referred to as the Carr-Purcell-Meiboom-Gill (CPMG) method and is still the method of choice for accurate T2 measurement.

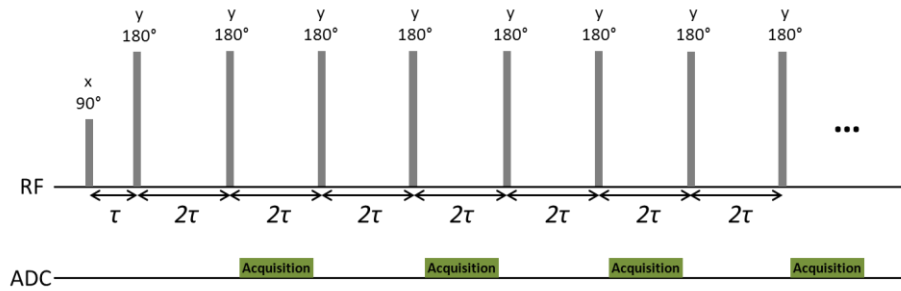


Figure 2-16 – Time sequence diagram of the CPMG technique. A series of equally spaced 180° -pulses is launched after an interval $TE/2$ from the 90° -pulse. The phase of the 180° -pulses is shifted of 90° from the 90° -pulses so that imperfect refocusing are corrected for the even echoes.

Deviation of the refocusing FA from 180° results in non-null 90° components which will tip previously excited transverse magnetization to the longitudinal direction (see Figure 2-15 b). This longitudinally stored magnetization will be re-tipped to the transverse plane completing its 180° flip by the action of the 90° component of the next refocusing pulse. This magnetization will be refocused leading to a spin-echo at a time $t = nTE$ with the same phase of the primary echo refocused by the action of the 180° component. This spin-echo which is refocused by the composed action of two 90° components is referred to as *stimulated-echo*. It is important to realize that during the TE interval in which magnetization is stored in the longitudinal direction it only experiences T1-relaxation. This will inevitably introduce some T1-weighting into the signal. However, when signal is acquired from sufficiently small volumes where FA accuracy and precision can be ensured, T1-weighting can be made negligible.

2.8. The issue of B1 in-homogeneity in practical NMRI applications at high field

In-homogeneities of the transmit RF field (B_1) constitutes one of the main problems concerning precision and accuracy in high field ($\geq 3T$) quantitative NMRI. When traveling across the body, the electromagnetic wave produced by the oscillatory magnetic field B_1 that is generated by the transmit coil will be partially reflected at each different interface media, e.g., from the air to the body and vice-versa. As the reflected waves will all have the same frequency, their mutual interference may produce the so called standing (or stationary) waves. To better visualize this phenomenon, let's consider two waves, $y_1(x, t)$ and $y_2(x, t)$, of same frequency, ω , and opposite directions, described by the Equations

$$y_1 = \sin(kx - \omega t) \text{ and } y_2 = \sin(kx + \omega t)$$

The wave, y , resulting from their interference will be given by

$$y = \sin(kx - \omega t) + \sin(kx + \omega t) = 2 \sin(kx) \cos(\omega t) \quad 2.31$$

Equation 2.31 describes a wave that is stationary in space. Note that the amplitude is only allowed to oscillate within a fixed sinusoidal modulation in space (Figure 2-17). Note that the amplitude of the stationary wave is zero at $x = \frac{\lambda}{2} + k \frac{\lambda}{2}$, $k = 1, 2, \dots$. At high fields the wave length, λ , becomes comparable or smaller than the dimensions of the human body, so that the existing standing waves will induce a modulation of the B_1 field amplitude through the imaged volume or slice (51, 52). At 2.89T the wavelength is about 243 cm in free space. Because of its dielectric properties of the human body, this wavelength is reduced to about 40 cm in practice. This phenomenon results in spatially non-uniform B_1 field distribution through the imaged volume even if the original field produced was perfectly homogeneous in free space. For this reason, it becomes very important to measure the spatial distribution of the B_1 field. This knowledge could allow to avoid biased data or to correct them with post-treatment.

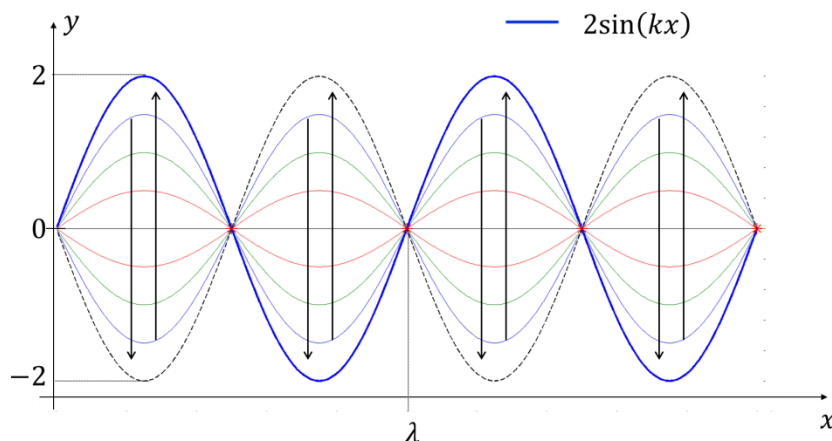


Figure 2-17 – Plots of a standing wave at different times. Note that its amplitude at each point in space is modulated by a constant value.

Available B_1 -mapping techniques are in general based on two scans acquired with two nominal FA-values (53, 54). To ensure that the observed difference between the obtained images do not depend on T_1 , the TR is usually chosen sufficiently long so that magnetization is completely relaxed between acquisitions. The idea is to use the images to extract quantitative information that depends only on the FA, which will be extracted from some identity equation. The drawback of such techniques is that they require 2D acquisitions. Slice profile imperfections related with the RF-pulse shape will bias the B_1 estimation. To avoid such problem, B_1 -mapping techniques that use 3D acquisitions have been developed (55, 56). Some methodologies that we have applied necessitate a B_1 -map for post-processing. The technique of choice was the so called accurate flip-angle imaging

(AFI) (55). This technique allows T_1 -independent B_1 -map extraction from a single scan procedure that consists on the application of two identical non-selective RF-pulses followed by two delays TR_1 and TR_2 , with $TR_1 < TR_2 < T_1$. Finally, the ratio between signals acquired after each RF-pulse may be expressed in terms of FA.

CHAPTER 3

A Spin-echo-based Method for T2-Mapping in Fat-infiltrated Muscles

3.1. Quantitative characterization of muscle inflammation

The T2-relaxation of ^1H -NMR signals from pure water is monoexponential with a T2-value close to the T1 (approximately 2.5 s at 3T). However, when observed in biological tissue, the T2-relaxation of water has been shown to be much faster than the T1-relaxation (31 vs. 1400 ms, at 3T) in normal skeletal muscle. This 80 fold reduction of the T2 is understood as resulting from the interactions of water with the macromolecules in the tissue, which makes its value dependent on the concentration of macromolecules. There is a variety of pathological conditions that cause an increase of average tissue water content such as necrosis, dystrophy, intracellular and interstitial oedema. An increase in water content might as well be seen as a decrease of macromolecules concentrations which leads imperatively to an increase of tissue water T2-value. Monitoring water T2 changes has been shown to reveal information on disease activity and progression, and has been proposed as an indicator of response to treatment (24, 57, 58).

The spin-echo method described in 2.7.1 may be applied to the imaging approach and images acquired at different echo-times will present different contrasts between different tissues and structures (see Figure 3-1). Analogously to the idea behind the CPMG method described in 2.7.4, if the excited magnetization is repeatedly refocused, images may be acquired at distinct echo-times during the transverse relaxation process. The gradient and RF-pulse time sequence of such NMRI method is usually called multi-spin-echo (MSE). In MSE sequences, images of the same slice are acquired at different echo-times. The idea is to acquire one line of the k-spaces corresponding to each image per repetition time. To do so, the excited magnetization is repeatedly refocused by application of 180° -pulses and all the echoes are encoded to the same k-space line. Details about MSE sequence may be found in (40).

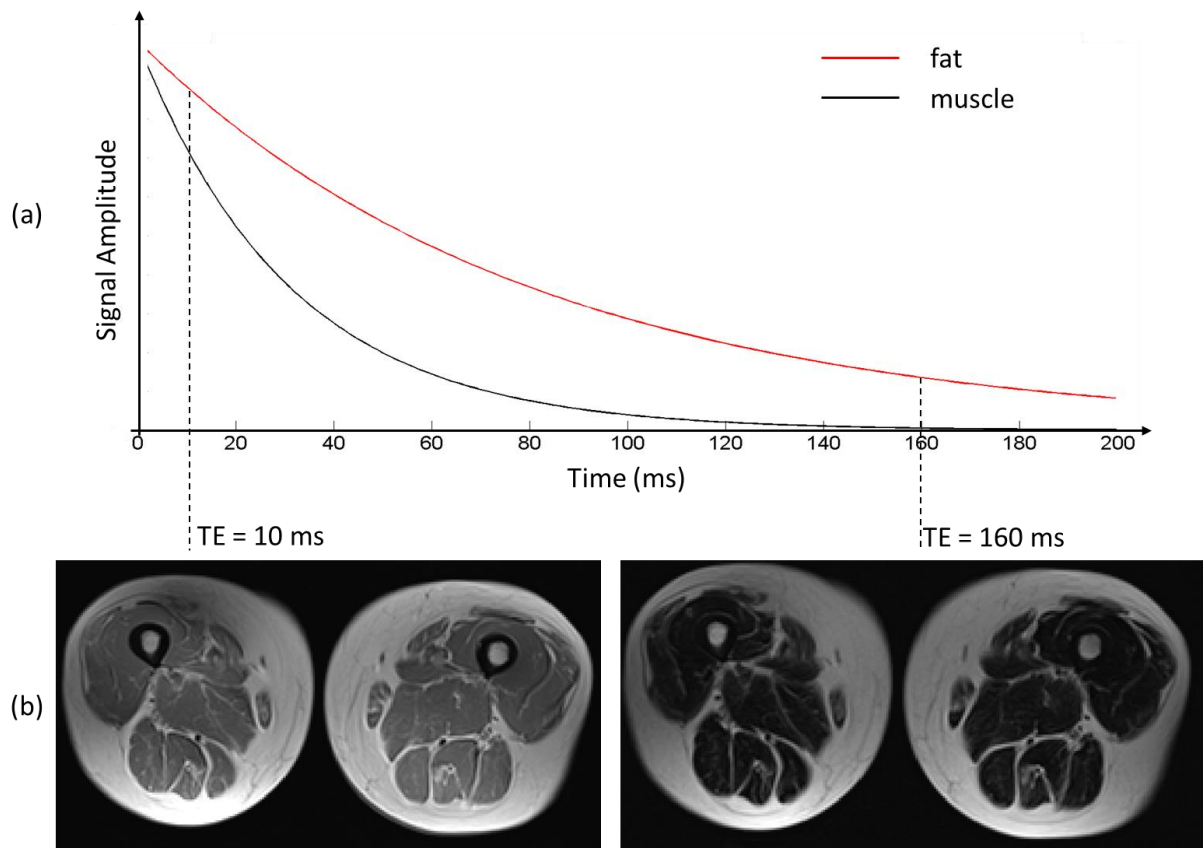


Figure 3-1 – (a) presents the theoretical T2-decay of muscle and fatty components. In (b) T2-weighted images of the thigh acquired at different echo-times, TE=10ms and 160ms (adjusted to the same contrast window level). The contrast between muscle and fatty components depends on the ration of their relative signal intensities which varies in time due to their different T2-values.

When images at different echo-times are acquired, T2-relaxation of ^1H -NMR signals from each voxel may be individually characterized by fitting the time evolution of the signal amplitude to a mono-exponential model (see Figure 3-2). This will result on an image of the actual T2-value distribution through the imaged slice, which is usually referred to as a T2-map.

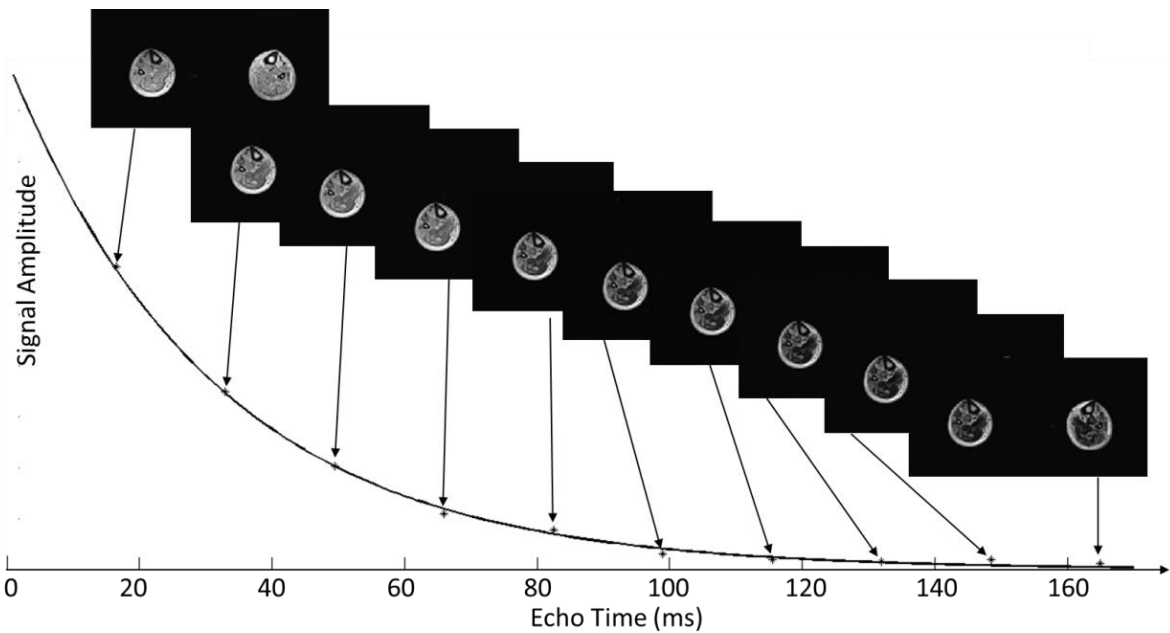


Figure 3-2 – *Signal amplitude vs. echo-time for a voxel within the muscle. Images of the lower legs acquired at different echo times with a multi-spin-echo sequence. Note the exponential T2-relaxation behaviour.*

Although MSE sequences are often referred to as CPMG, it is worthy to highlight here the important differences between the CPMG method and the MSE techniques that are applied in practice: (i) the application of imaging gradients limits the minimum inter-echo-spacing and increases diffusion effects; (ii) in NMRI applications, large volumes of magnetization are often excited, which result in important B_0 and B_1 field in-homogeneities through the imaged slice; (iii) selective RF-pulses are intrinsically imperfect due to truncation effects and B_0 -induced off resonance, which always result in imperfect slice profiles; (iv) combination of (ii) and (iii) leads to important deviations of the effective FA of the refocusing pulses from 180° , which results in important amplitudes of the stimulated echoes (see 2.7.4). If the Meiboom-Gill modifications of the Carr-Purcell sequence are satisfied, the stimulated echoes will sum coherently with the perfectly refocused spin echoes; in such NMRI techniques the gradient moment between each refocusing pulse must be the same so that CPMG conditions are re-established before each refocusing (Figure 3-3 a). If the amplitude of the stimulated echoes is sufficiently high, the signal is significantly T1-weighted and the resulting decay is usually slower. Instead, one may get rid of the stimulated echoes, by applying efficient crusher gradient schemes (59); in this method the phase relationship between net magnetization and the refocusing pulses required by the CPMG conditions are not satisfied (Figure 3-3 b), resulting in a faster relaxation and consequently shorter observed T2. Finally, even for the MSE sequences that respect the CPMG conditions, both odd and even echoes are acquired in practical qNMRI

in order to increase echo-time sampling, which is very important for ensuring reliable monoexponential fitting, and reducing acquisition time, which is crucial for reducing artefacts due to patient movement and to respect acceptable duration limits in clinical examination.

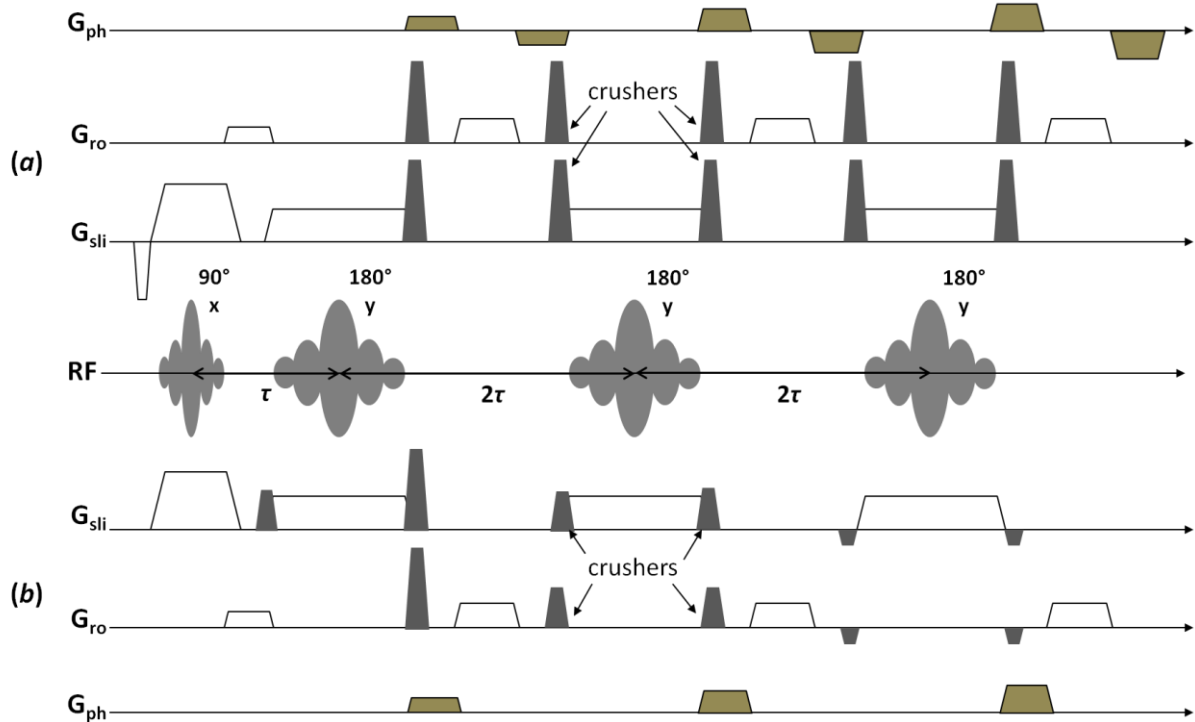


Figure 3-3 – Pulse sequence diagram of a (a) CPMG-like MSE sequence and (b) a MSE sequence with variable crusher gradients for nulling stimulated echo contributions. The RF-pulse time sequence is the same for both methods, except for the phase of the pulses that are only explicit for the CPMG-like MSE sequence (a). Note in (a) that the gradient moments are identical between refocusing pulses by application of the so called phase rewind gradients.

A new model in which stimulated echo amplitudes are taken into account for fitting relaxometry data acquired with CPMG-like MSE sequences (Figure 3-3 a) has been recently proposed (60). This method allows extraction of T2- and FA-maps given the T1-map and the slice profile of the excitation and all refocusing pulses. However, in chronically affected muscles, fatty degenerative changes complicate the situation. The T2-relaxation of $^1\text{H-NMR}$ signals from lipids is longer (approximately 80 ms at 3T) and, consequently, mono-exponential fit of non-fat-suppressed signal results in elevated “muscle” T2 mostly reflecting the degree of fat infiltration (61–65). As a result, possible underlying alterations in muscle water T2 are masked. Although a generalization of the Lebel’s method has been recently proposed (66), which allows extraction of multiple T2-components while compensating for stimulated echoes, it has only been validated for the

case in which different components have approximately the same T1-value and resonance frequency, which is not the case for water and lipids. In the following section the main techniques allowing to separate signal contributions from lipids and water are briefly presented.

3.2. Separation of ^1H -NMR signals from lipids and water

3.2.1. Spectral fat-water separation methods

Protons in lipid molecules experience a different magnetic environment than protons in water molecules, as a reflex of the intrinsic physical characteristics of each of these chemical compounds. In particular, the external magnetic field experienced by the protons within lipid molecules is slightly inferior, thus resulting in a chemically shifted local Larmor frequency. Although the difference in the precession frequency is very small (~ 3.5 ppm), signal contributions from water and fat may be separated in NMR spectra acquired at high enough fields (see Figure 3-4).

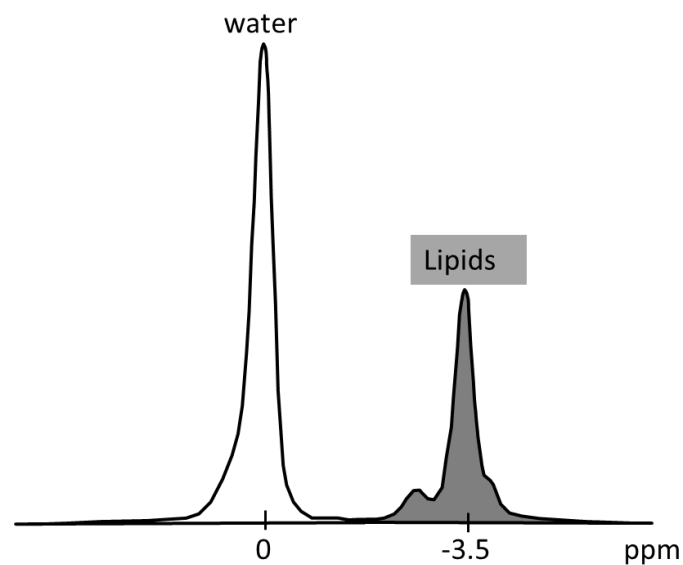


Figure 3-4 – Example of a ^1H -NMR spectrum acquired at 3T from a volume containing muscle and subcutaneous fat. Peaks containing contributions exclusively from lipids were painted grey.

By properly adjusting the frequency and bandwidth (BW) of RF-pulses to encompass the water or the fat peaks independently, one may excite water or fat separately. The spectral separation allows one to produce water images by either *water selective excitation* or *fat saturation*. On the later, fat is selectively excited with a 90° -pulse and its transverse magnetization has its phase coherence completely broken by the application of strong enough B0 field gradients. At this point the fat magnetization is null and the whole sample

is re-excited for imaging (see Figure 3-5). However, in practice the external static B₀ field is only homogeneous to within a precision of ppm, and the spectral selection techniques will only work over small enough volumes, where sufficient B₀ homogeneity can be achieved. This often represents an important limitation for whole body examinations and other separation methods based on the difference between other NMR parameters must be explored.

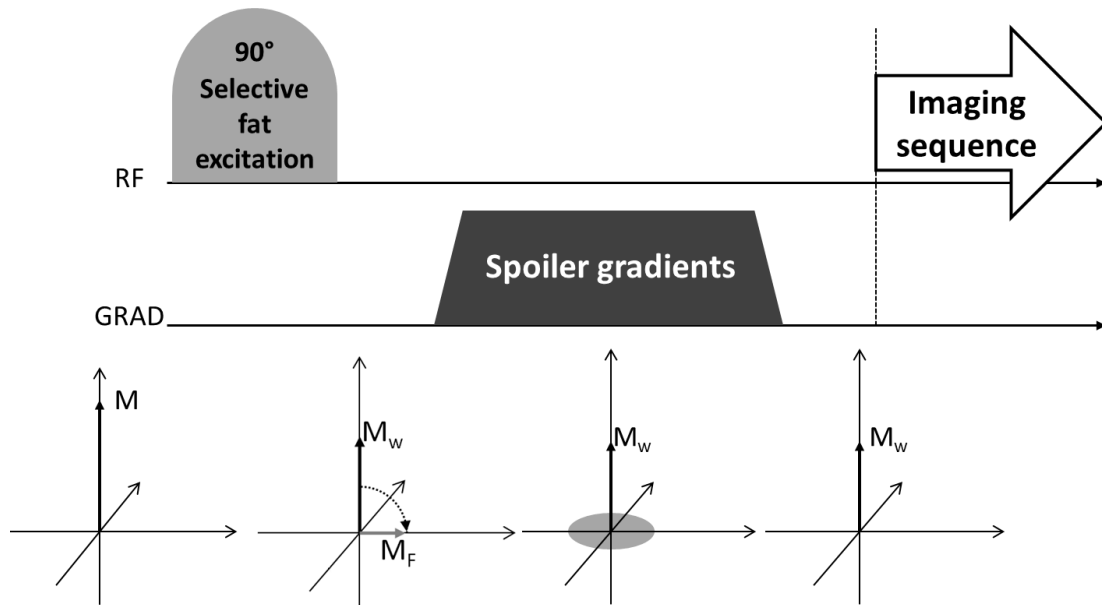


Figure 3-5 – Illustration of a selective fat saturation scheme. Fat magnetization is selectively excited with a 90°-pulse and spoiler gradients are applied immediately after, in order to null the transverse fat magnetization components. At the end only water longitudinal magnetization components will last, and a imaging sequence may be executed to produce water only images.

The Dixon method is an interesting approach in which both water and fat signals are simultaneously acquired, but in such a way to allow separation of fat and water signals with appropriate post-processing methods (67). The idea is to acquire images of the same slice at different times in which the dephasing between water and fat magnetization vectors are different. The a priori knowledge of the chemical shift of fat signals allows one to post-process the images in order to isolate its contributions.

On its first version two images are acquired; one at a time, t_{inl} , in which water and fat transverse spin isochromat components are in phase, and a second at a time, t_{opp} , in which the phase difference between them equals 180° (see Figure 3-6-(a)). Water and fat only images may then be extracted by simple summation and subtraction of the amplitude images, respectively. This method is referred to as the two point Dixon (2PD) and the principle behind it is illustrated in Figure 3-6-(a). However, when the relative fraction of

signal from lipids is greater than the relative fraction of signal from water in a given voxel, the calculated relative water and fat fractions will be switched.

In practice the magnetization will not have the same precession frequency through the entire imaged volume. As a consequence, although the water and fat spin isochromats will still be anti-parallel on the opposed-phase image, they might not be parallel and anti-parallel to the spin isochromats from the in-phase image (see Figure 3-6-(b)). A variation of the 2PD method has been proposed, in which an additional in-phase image is acquired at a time, t_{in2} , allowing to estimate a B_0 inhomogeneity map based on the phase difference between the two in-phase images. This method is referred to as three point Dixon (3PD) method and the idea underlying it is illustrated in Figure 3-6-(b). Estimation of the B_0 allows one to correct for the dephasing between the images and to estimate water and fat relative fractions without ambiguity.

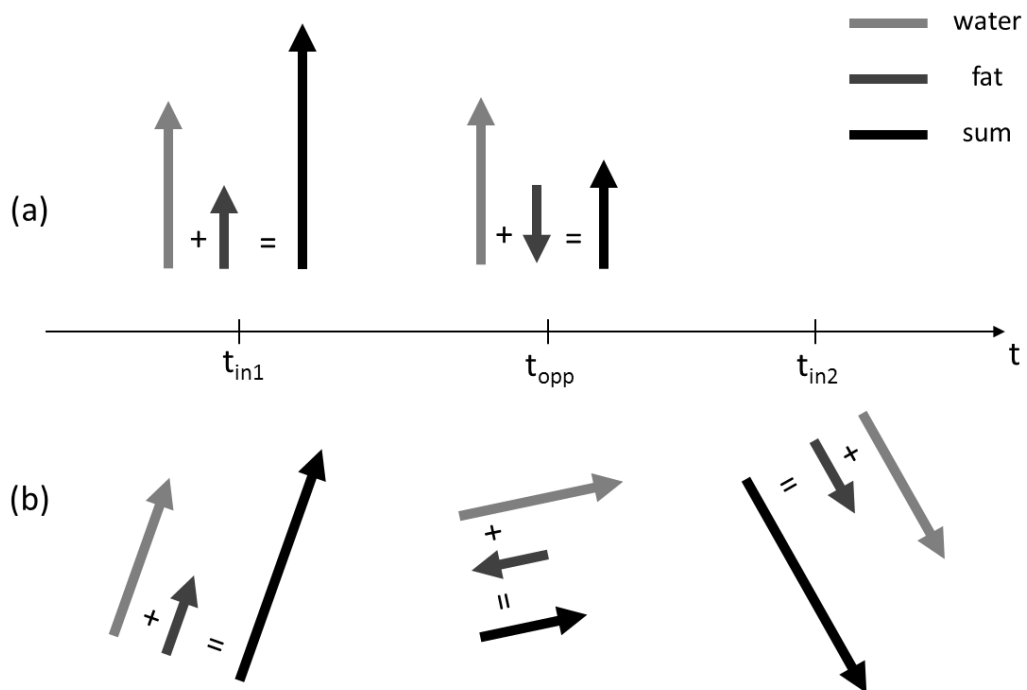


Figure 3-6 – (a) Illustration of the idea behind the 2PD method. The phase of fat spin isochromat is inverted at t_{opp} and might be trivially isolated from the water spin isochromat by simply summing or subtraction both magnitude images; note that when the fat fraction is the biggest, Water and fat fractions will be switched. (b) Illustration of the idea behind the 3PD method; the local B_0 -shift may be estimated from the phase difference between both in-phase images. Note that when in the presence of a B_0 -shift, although fat and water signal will be in-phase at t_{in1} and t_{in2} , and in opposed-phase at t_{opp} , they won't be parallel and antiparallel between images due to the shifted local precession frequency.

However, the periodic equivalence of phase values ($\theta = \theta + 2k\pi, k \in \mathbb{Z}$) results in an infinity of solutions for B0 inhomogeneity. This may lead to erroneous water and fat fraction estimations. Finally a generalization of the Dixon method has been proposed in which signal evolution from each image voxel is observed by acquiring n images at different times (68), with $n \geq 3$. The signal is then fitted with the following model

$$\mathbf{S}(TE) = \left(\rho_w + \rho_f \sum_k \alpha_k e^{-i\omega_k TE} \right) e^{\varphi(TE)} \quad 3.1$$

where ρ_w, ρ_f are the water and fat relative fractions, respectively, and the function φ accounts for the B0 in-homogeneities and relaxation effects. The expression $\sum_k \alpha_k e^{-i\omega_k TE}$ describes the complexity of the fat spectrum and may account for the contributions of the different hydrogen groups present in the different fatty acid chains of triglycerides.

3.2.2. Relaxation-based methods for fat-water separation

Besides the chemical shift, the relaxation of ^1H -NMR signals from water and fat are different. The difference of T1-value between fat (~ 350 ms at 3T) and tissue water (~ 1.4 s at 3T) is explored by the so called short TI inversion recovery (STIR) method. In this method, all the magnetization is inverted to the $-z$ direction by a 180° pulse and an imaging sequence is executed at the precise moment in which the longitudinal component of fat magnetization crosses zero during the recovery process, so that contributions from lipid on the acquired signal are negligible (see Figure 3-7). However, STIR images usually present small SNR and, imperfect refocusing pulses in the MSE will result in non-negligible 90° components that will end up exciting relaxed longitudinal components of lipid magnetization at later echo times.

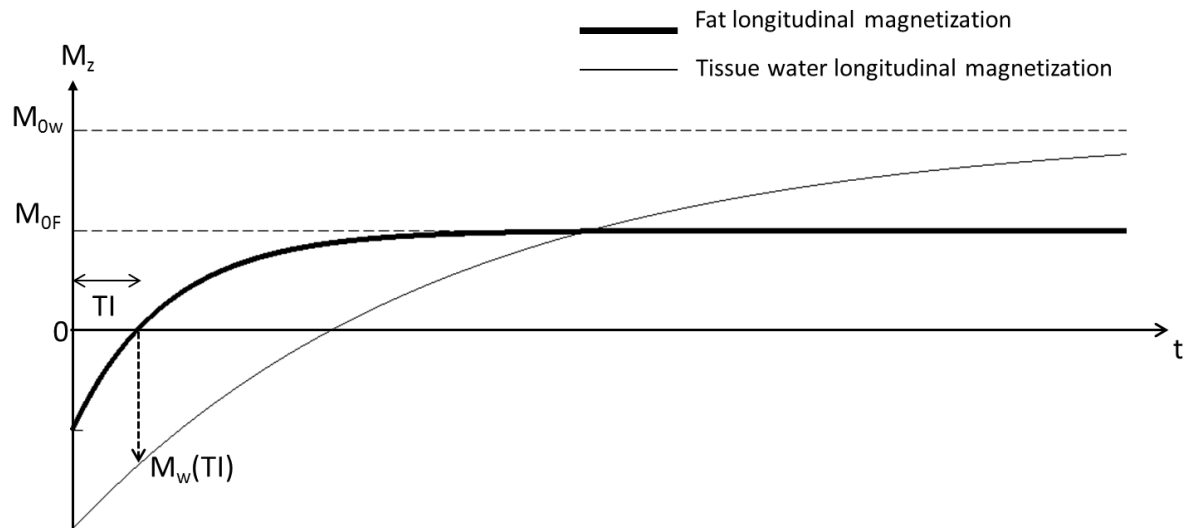


Figure 3-7 – Illustration of fat and tissue water longitudinal magnetization component recovery during T_1 -relaxation. In the STIR method, the imaging sequence is executed at the inversion time, TI , where only tissue water has non-zero longitudinal magnetization. M_{0w} and M_{0F} are the equilibrium fat and tissue water magnetizations.

On the following sections a methodology that explores the T_2 difference between lipids and tissue water for separating their corresponding contributions to the signal will be described.

3.3. Validation of an MSE-based method for quantification of muscle water T_2 in fat-infiltrated skeletal muscle

The NMR frequency spectrum of triglycerides is complex, composed of at least ten different peaks attributed to distinct hydrogen groups in the fatty acid chains (Figure 3-8). Besides the spectral complexity, the different peaks do not present equal relaxation rates (69, 70). This makes any fat saturation technique imperfect, and hampers the acquisition of completely fat free relaxation decay curves from fat saturated MSE images. Moreover, fat signal of only a few per cent will still increase mono-exponential T_2 and thus decrease measurement precision which is crucial for evaluating muscle lesion from qNMRI T_2 -maps.

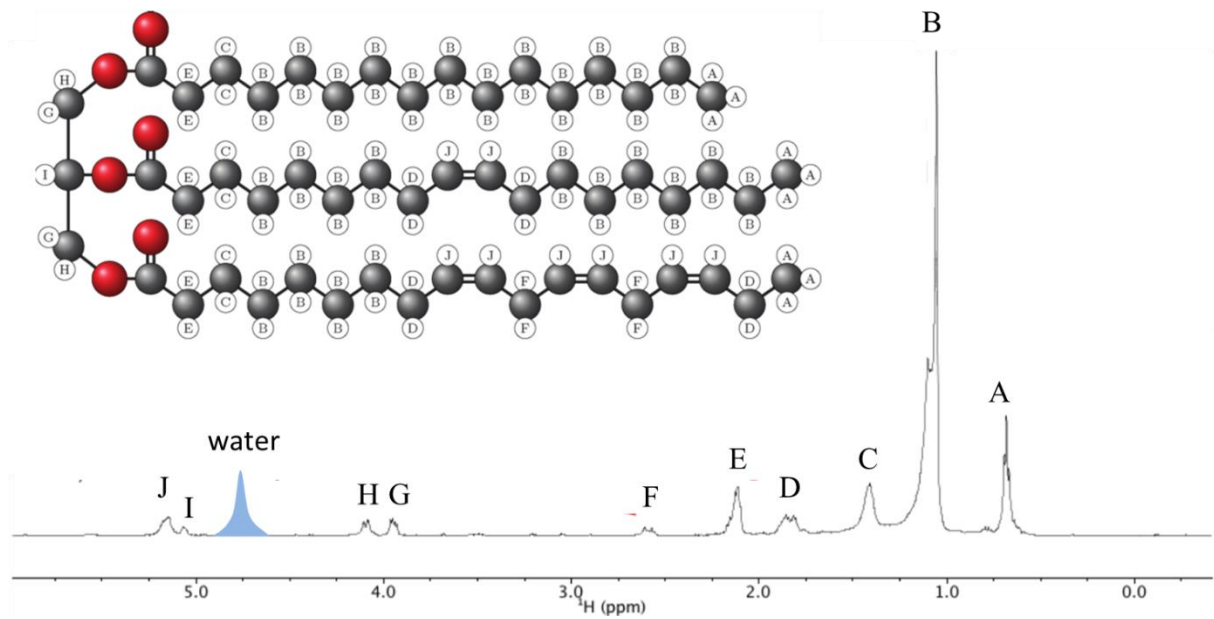


Figure 3-8 – Schematic illustration of a triglyceride molecule along with a proton (^1H) NMR spectrum of isolated triglyceride molecules extracted at 14 teslas. Triglycerides consist of one glycerol (to the left) and three fatty acids (to the right). In this example, the fatty acids are: palmitic acid (top), oleic acid (middle), and linolenic acid (bottom). Assignment of the different protons to the resonances A–J is indicated. A virtual water peak is superposed to the spectrum.

Instead of extracting T2-maps from fat saturated spin-echo images, muscle T2-relaxation might be modelled as a combination of the independent signal decays of lipids and muscle water. Such combination was introduced in (71) toward fat quantification using a bi-exponential model to describe the data, where T2-values of fat and water were assumed to be known. In a more recent work (19), the authors aimed to quantify water T2 using a bi-exponential approach. Basically, the T2-decay curves characterizing each voxel of the images are fitted to a biexponential model in which the T2-value of the fat is fixed as well as its relative fraction as obtained by supplementary fat quantification technique (Dixon). Although T2-values obtained with their method were not correlated to the degree of fat infiltration, it presents an important lack of precision, mainly for fat infiltrated muscles, thus limiting the detection of moderate inflammation.

In the following we introduce and validate *in vivo* a novel method for the determination of skeletal muscle water T2-value in fat-infiltrated tissues from CPMG-like MSE data. For validation of the method, 48 patients with various neuromuscular diseases were retrospectively selected and their thigh muscles analysed. Each patient was imaged using a multi-spin-echo (MSE) sequence with 17 echoes. Muscle water T2 and relative fat fraction were quantified using a tri-exponential signal decay model. Fat fraction maps

were also estimated with the 3PD method for comparison purposes.

The proposed method has been shown to offer muscle water T2-values that are independent of the relative fat fraction. Additionally, the estimated fat fraction by the proposed method has been shown to have a linear relationship with the Dixon-based fat fraction. The following sections describe the proposed methodology and the results that validate it.

3.3.1. Methodology

3.3.1.1. Data acquisition

For T2-determination, a standard multi-slice MSE sequence was applied with a TR = 3000 ms, a 90° excitation pulse and 180° refocusing pulses. The field of view was equal 224x448 mm², with a pixel size of 1.4x1.4 mm². We acquired 11 slices of 10 mm thickness with a 25 mm inter-space. Images were acquired at 17 echo-times ranging from 9.5 ms to 161 ms with 9.5 ms echo-spacing. The central slice was located at the mid-length of the femur. For assuring reproducibility of slice positioning between subjects, we have used the knee and the iliac spine as anatomical landmarks.

All examinations were performed on a 3 teslas (3T) whole-body Tim TRIO scanner (Siemens Healthcare, Erlangen, Germany) with the quadrature bird-cage body transmitter coil and two phased-array receiver coils covering the entire lower limb. From a list of patients referred to us, 28 women with average age 48 years ± 16 years and 20 men with average age 55 years ± 15 years with a variety of diagnosed neuromuscular diseases were selected to cover a range of muscle fat infiltration and inflammation : (a) myositis overlap syndrome (n=15), (b) Polymyositis (n=4), (c) congenital myopathy (n=7), (d) unlabelled myopathy (n=7), (e) type 2 glycogen storage disease (n=5), (f) limb girdle muscular dystrophy (n=2), (g) other diseases (n=8). Images from their thighs were retrospectively analysed. Diagnosis were made based on clinical (all), biological (a, b, e, f, g), immunological (a, b), histological (c, g) and imaging data (all). In order to have a control base, 20 healthy volunteers (10 women and 10 men aged of 23 ± 3 years) were scanned as a part of a methodology assessment protocol approved by the local ethics committee. Informed consent was obtained for all volunteers.

In five volunteers we acquired an additional mono-slice dataset with all other parameters otherwise identical, to quantify signal loss due to magnetization transfer effects in multi-slice imaging. The mono-slice and multi-slice MSME were identically centered at the femur mid-length.

In order to avoid bias introduced by FA errors, the spatial distribution of the transmit RF-field (B1+) was calculated using an optimized version of the actual flip angle imaging

(AFI) method (55). It was performed using two nominal excitation pulses of 60° ($300\mu\text{s}$ hard pulses) followed by delays of TR1 and TR2 respectively, with $\text{TR2} = 5\text{TR1}$ and $\text{TR1} + \text{TR2} = 100$ ms. $\text{TE} = 2.75$ ms, bandwidth = 550 Hz/voxel. Optimal spoiling of transverse magnetization was ensured by using an improved RF and gradient spoiling scheme as described in (72), assuming an isotropic scalar water diffusion coefficient $D = 0.75 \mu\text{m}^2/\text{ms}$. Relevant parameters for spoiling were: diffusion damping = 0.100, RF spoil phase increment = 129.3° . Field of view was equal to $224 \times 448 \times 320 \text{ mm}^3$, with pixel size of $4 \times 4 \times 10 \text{ mm}^3$.

Fat was independently quantified for validation purposes. This was performed using a standard three-point Dixon technique. To this end, we acquired 3D gradient echo volumes with the following parameters ($\text{TR} = 10\text{ms}$, $\text{TE1} = 2.75$ ms, $\text{TE2} = 3.95$ ms, $\text{TE3} = 5.15$ ms, flip angle = 3°). Field-of-view was equal to $224 \times 448 \times 320 \text{ mm}^3$ with a pixel resolution of $1 \times 1 \times 5 \text{ mm}^3$.

All the performed scans were part of a methodology assessment protocol approved by the local Ethics Committee and informed consent was obtained from the patients and volunteers.

3.3.1.2. Data treatment

Volume co-registration and definition of regions of interest

For each subject, the series of multiple TE volumes, the B1+ volume and the fat volume percentage were co-registered using an in-house MATLAB (The MathWorks, Natick, MA) program that extracts the position of each volume and automatically computes the translation and scale factors to be applied. Ten different muscles were identified and regions of interest (ROIs) manually drawn according to anatomical atlases on the left and the right thighs of the different patients. The ROIs delineated the interior of the muscle avoiding fascia and blood vessels. The analysed muscles are displayed in Figure 3-9. For all parameters, we computed the weighted mean value of the different ROIs belonging to the same muscle at different slices. Hence, a total of 960 muscles were analyzed.

Regarding healthy subjects, by thresholding the multi-slice MSME images to identify the muscle tissue region and differentiate it from the subcutaneous fat and bones. Then morphological erosion was applied to the binary images of muscle tissue, to smooth the region of muscle and discard the effect of noise and fascia.

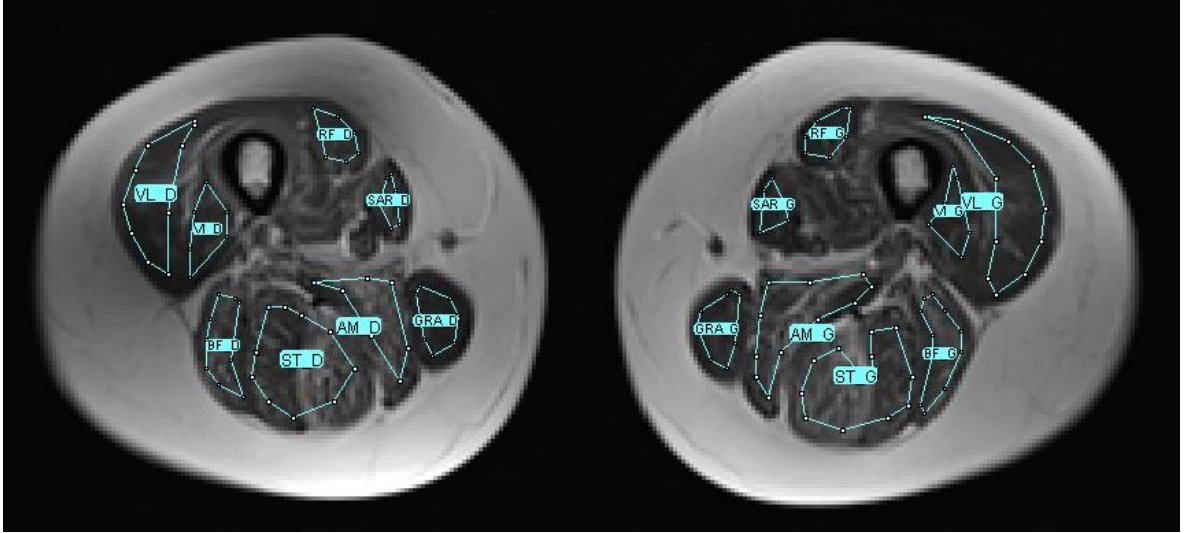


Figure 3-9 – Example of ROIs drawn manually to delineate muscles in the thigh.

Signal modelling and data fitting

The signal from almost any voxel in muscle will have contributions from water and lipid molecules, so that signal from non-fat saturated MSE sequences shall be described as a linear combination of signals from lipids and water. Various multiexponential models can be considered. In this work we proposed the following

$$S(TE) = A_f \left(c_l \cdot \exp\left(-\frac{TE}{T2_{fl}}\right) + c_s \cdot \exp\left(-\frac{TE}{T2_{fs}}\right) \right) + A_m \left(\exp\left(-\frac{TE}{T2_m}\right) \right) \quad 3.2$$

where $S(TE)$ is the signal for a given echo-time TE . $T2_{fl}$ and $T2_{fs}$ are the long and short relaxation times of the fat component respectively. $T2_m$ is the relaxation time of the muscle water component. A_f , A_m are the coefficients that reflect the relative fraction of signal contribution from fat and water, respectively. c_l and c_s are coefficients of the bi-exponential model of the fat signal.

Due to the limited number of measures (17 echoes), it is difficult to perform a tri-exponential fit (Eq.3.2) without constraints because the uniqueness of the solution is not ensured. For that reason, the subcutaneous fat signal was used to calibrate the fat related parameters in the first term of Eq.3.2. Doing so, it is assumed that the T2-relaxation of lipids in infiltrated fat is not significantly different from those in subcutaneous fat. Such an hypothesis is widely used in chemical shift based fat quantification approaches where frequency and amplitude of fat peaks are pre-defined (73). To verify this, we acquired spectroscopic data from voxels placed in infiltrated muscles and voxels placed in subcutaneous fat. For each voxel of $10 \times 10 \times 10 \text{ mm}^3$, we acquired 8 spectra at different echo times ranging from 30 ms to 150 ms, with $TR=3000$ ms and number of averages =12. Data were acquired with a stimulated echo sequence and analysed with the JMRUI software.

The T2-value of each spectral peak was obtained by monoexponential fitting the decay of each peak's area. Table 1 compare the results. Fat spectra were very similar and the main fat peak had similar T2-values in both cases. Therefore for our application, subcutaneous fat was taken to model intramuscular fat.

Table 3-1 - Spectral model of the fat resulting from spectroscopy data. For each peak were reported: the relative shifts to the water, the T2-relaxation time and the relative amplitude with respect to the fat component of the voxel.

Fat Peak	Subcutaneous fat			Intramuscular fat		
	Location (Hz)	T2 (ms)	Rel. Fraction	Location (Hz)	T2 (ms)	Rel. Fraction
-(CH ₂) _n -	404	76.9 ± 2.4	0.66	400	77.5 ± 3.5	0.68
-CH ₂ - CH ₂ -COO	307	35.6 ± 7.4	0.16	298	39.8 ± 7.5	0.13
-CH=CH-	-91	43.6 ± 4	0.09	-94	44.9 ± 10.4	0.09
-CH ₂ -CH ₃	452	-	0.07	449	-	0.08
CH=CH-CH ₂ -CH=CH	221	-	0.01	214	-	0.02

*Results are presented by means of *mean* ± *SD*.

Regarding the bi-exponential approximation of the fat signal decay in the subcutaneous fat region, it was selected after a comparison with the mono- and the tri-exponential models, using F statistics, which is defined as: $F(\text{model1}, \text{model2}) = \left(\frac{\text{RSS1} - \text{RSS2}}{p2 - p1} \right) / \left(\frac{\text{RSS2}}{n - p2} \right)$, where RSS1 (resp RSS2) is the residual sum of squares of the fit using model1 (resp model2), p1 (resp p2) is number of parameters in model1 (resp model2) and n the number of observations; in this formulation $p2 > p1$. The results showed that for a false-rejection probability of 5%, the bi-exponential model provides a significantly better fit than the mono- and the tri-exponential models.

In order to analyse signal decay from fat only species we segmented the subcutaneous fat, then using a non-negative least squares (NNLS) fitting approach, we obtained the parameters of the bi-exponential model corresponding to the fat ($T2_{fl}$, $T2_{fs}$, c_l and c_s). It is important to point out that multiexponential fitting of noisy data is an ill-posed mathematical problem. As a consequence parameter initialisation was crucial to find global minimum solutions. The initialization parameters for the bi-exponential fitting of subcutaneous fat signal were determined as follows: we tested all combinations of $T2_{fl}$ and $T2_{fs}$ values that ranged between 10ms and 900 ms with a step of 5 ms. For each combination of $T2_{fl}$ and $T2_{fs}$ we computed the corresponding c_l and c_s using simple linear fitting technique and evaluated the residual sum of square. Then we selected the

quadruplet ($T2_{fl}$, $T2_{fs}$, c_1 and c_s) with the minimum residual as initial point for the non-linear least squares fitting. Finally, once the parameters, $T2_{fl}$, $T2_{fs}$, c_1 and c_s , characterizing the subcutaneous fat were determined, the parameters $T2_m$, A_m and A_f characterizing the signal from muscle were estimated, by adjusting the model defined on Eq.3.2 to the time evolution of the signal amplitude from images at echo-1 to echo-17. Images from the first 2 echo-times were excluded to minimize the bias caused by the presence of stimulated echoes.

Voxel Sorting

In order to get rid of B1 problems, we have sorted the voxels for analysis based on the measured B1-map coming from the AFI acquisitions. At first we studied the B1+ field impact on the measured muscle T2-values. To do so we computed, for 20 healthy volunteers, muscle water T2-maps using the tri-exponential model and superimposed the 3D B1+ maps obtained from the AFI sequences. Figure 3-10 shows an example of the maps that were obtained. In order to identify the pixels that belong to muscles, we applied thresholds to MSME images. Thresholding allows differentiating muscle tissue region from subcutaneous fat and bones. Next, we applied morphological erosion to the binary images of muscle tissue, to exclude fascia and reduce noise related artifacts.

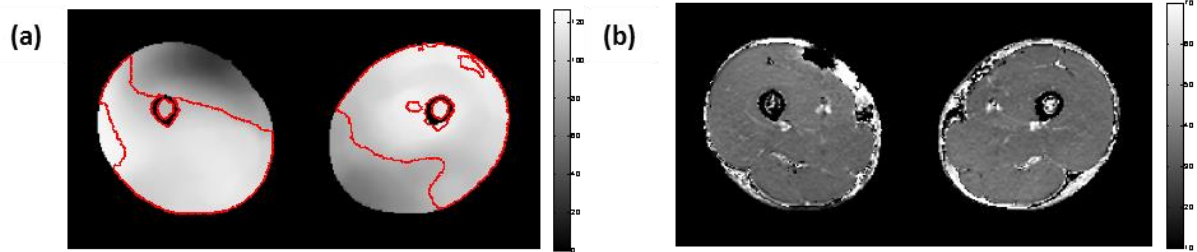


Figure 3-10 - (a) B1+ map (ratio between actual flip angle and the applied one) the area inside the red contours correspond to B1+ ranging between 85% and 130%. (b) The corresponding muscle water T2-map of a healthy volunteer's thigh.

Then we calculated a T2 mean value as well as a mean deviation with respect to a reference muscle water T2-value using the following expression:

$$\bar{T}_2(B1_{inf}^+, B1_{sup}^+) = \frac{1}{|\Omega|} \sum_{v \in \Omega} T2_m(v) \quad 3.3$$

and

$$\sigma_{T_2}(B1_{inf}^+, B1_{sup}^+) = \frac{1}{|\Omega|} \sqrt{\sum_{v \in \Omega} (T2_m(v) - T2_m^{ref})^2} \quad 3.4$$

with $\Omega = \{\text{muscle voxels } v \text{ such that } B1_{inf}^+ \leq B1^+(v) < B1_{sup}^+\}$ and $T2_m^{ref}$ is a reference water muscle T2-value computed in a region where B1+ values are comprised between 95% and 105% of the prescribed flip angle, and considered as homogeneous.

The deviation with respect to the T2 reference value was an indicator of the impact of B1+ on water T2-values and was used to select the optimal B1+ range that results in a low mean deviation. Doing so, we were assuming that the only source of variability between subjects and muscles are the B1+ in-homogeneities. Voxel sorting and ROIs drawing processes were completely independent and valid voxels were automatically selected within the ROIs.

Fat fraction estimation

Fat fraction (FF) was calculated as the ratio between the fat signal and the sum of the water and fat signals at TE = 0 ms. Based on the model introduced in Eq.3.2 it was defined as

$$FF = \frac{A_f(c_l + c_s)}{A_f(c_l + c_s) + A_m} \quad 3.5$$

It is important to point out that, due to the magnetization transfer process, the water signal was underestimated in the multi-slice acquisition as opposed to the mono-slice one (74). In the subjects for whom multi-spin echo sequences were acquired in both mono and multi-slice modes, the ratio between water signal in mono and multi-slice conditions was equal to 1.80 ± 0.15 , as determined from 55 ROIs. The expression for the fat fraction was therefore corrected to take magnetization transfer effects into account, and was given by:

$$FF_{corr} = \frac{A_f(c_l + c_s)}{A_f(c_l + c_s) + 1.8 \cdot A_m} \quad 3.6$$

3.3.2. Results

Definition of valid B1+ values and selection of valid voxels

When considering only voxels with flip angle deviation to no more than 5 % from the nominal flip angle, muscle water T2 of healthy volunteers was equal to 33.9 ± 2.5 ms, which was taken as reference value. Only 17% of the muscle volume matched this B1+ condition. Figure 3-11 describes the dependence of the measured T2-value to the B1+ field as established from the database of the 20 healthy volunteers. The obtained reference value for water T2 was $T2_m^{ref} = 33.9 \pm 2.5$ ms. The curve showed that muscle T2 was significantly over-estimated inside regions where the flip angle was lower than 100%. For

that reason, we decided to select in each ROI only voxels within a B1+ range that guarantees low variability with respect to the T2 reference value 33.9 ms.

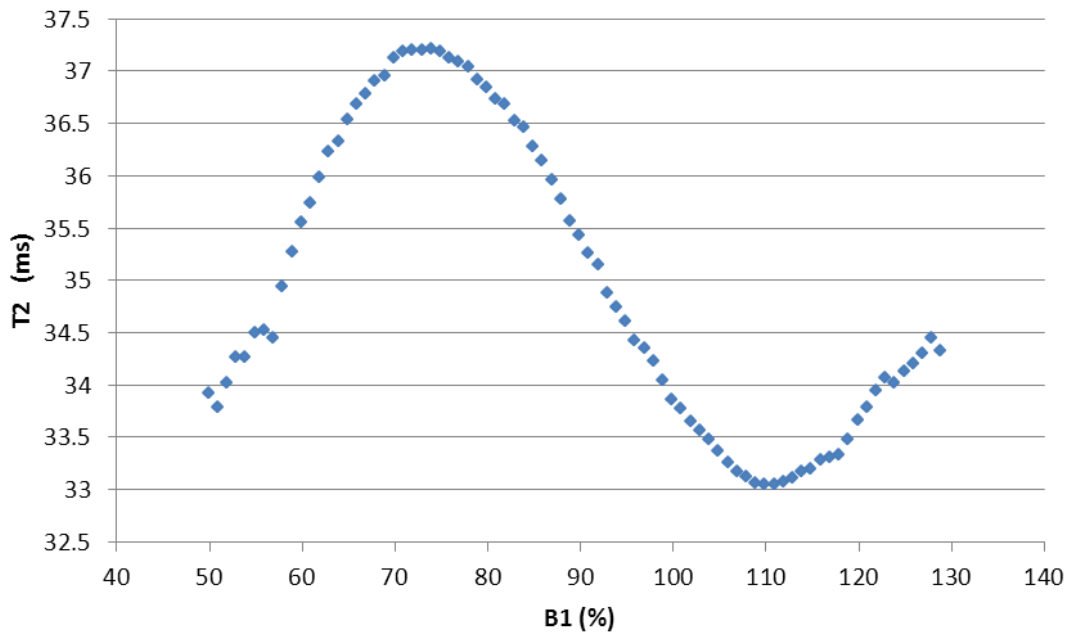


Figure 3-11 - Relationship between B1+ map (expressed as a percentage of the actual flip angle) and water T2-values determined on a group of 20 healthy volunteers.

At the same time, we had to keep as high as possible the number of voxels to be analysed. We fixed empirically a threshold of variability of 2.6 ms and based on results of Table 3-2 the best compromise was obtained when selecting voxels with flip angle between 85% and 130% of the nominal flip angle. Within this range the mean water T2-value was equal to 33.7 ± 2.5 ms. Taking 2 standard deviations as the upper normal limit, muscle T2 of 38.8 ms and above were classified as abnormal. In all results presented later in this paper, analyses were systematically made after selection of voxels falling within the 85% and 130% B1+ field range.

Table 3-2 - Mean (Eq. 3.3) and mean squared deviation with respect to a reference value (33.9 ms) of water T2 (Eq. 3.4), with respect to different B1+ range as well as the fraction of muscle voxels that are in the specified B1+ range with the respect to the total number of voxels.

B1+range (%)	Mean (ms)	Squared deviation (ms)	Fraction of voxels within B1+ range
95-130	33,49	2,48	0,51
90-130	33,61	2,51	0,58
85-130	33,75	2,56	0,63
80-130	33,90	2,62	0,67
75-130	34,05	2,70	0,71
95-120	33,42	2,50	0,44
90-120	33,57	2,52	0,51
85-120	33,72	2,57	0,56
80-120	33,89	2,65	0,60
75-120	34,06	2,73	0,64
95-110	33,61	2,51	0,28
90-110	33,83	2,55	0,34
85-110	34,05	2,63	0,39
80-110	34,28	2,74	0,44
75-110	34,51	2,85	0,47

Calibration of fat T2-relaxation model

Parameters of the subcutaneous fat were computed after exclusion of voxels that were not in the optimal B1+ range that is 85%-130%. For the 48 patients involved in the study, the parameters of the best fit on the subcutaneous fat signal were:

$$c_l = 0.35 \pm 0.01; T2_{fl} = 440 \pm 22 \text{ ms} \quad \text{and} \quad c_s = 0.65 \pm 0.01; T2_{fs} = 80 \pm 2 \text{ ms}$$

For healthy subjects the parameters were:

$$c_l = 0.35 \pm 0.01; T2_{fl} = 444 \pm 13 \text{ ms} \quad \text{and} \quad c_s = 0.65 \pm 0.01; T2_{fs} = 81 \pm 2 \text{ ms}$$

Validation of water T2-value extraction

To validate our method, we hypothesized that, for our patient group, muscle water T2-value, if properly extracted, should be independent of the relative fat fraction as extracted by the 3PD method. Hence, to verify this hypothesis, voxels within each ROI were sorted according to their fat signal fraction and two groups were established: voxels with fat fraction comprised between (a) 0 and 20% and (b) 20 and 50%. Global T2, obtained from simple monoexponential fit and water T2 extracted with the proposed method were compared for both voxel groups. Among the 960 ROIs that were analysed, 641 contained

voxels with fat ratio between 20% and 50%.

The proposed method based on the tri-exponential model yielded close $T2_m$ values for the two levels of fat infiltration. However, global T2-value estimated with a monoexponential fitting was abnormally high (>60 ms) and dependent on the fat infiltration degree. Normal and abnormal muscles, as determined by the observed water T2-value, also presented significantly distinct global T2-values. The mono-exponential approach yielded significantly higher T2-values for the abnormal muscles (71.7 ± 12.1 ms for [0-20] fat range and 93.3 ± 14 ms for [20-50]) when compared to the normal ones (60.6 ± 12.5 ms for [0-20] fat range and 79 ± 16.7 ms for [20-50]) ($p < 1e-4$). These results are resumed in Figure 3-12.

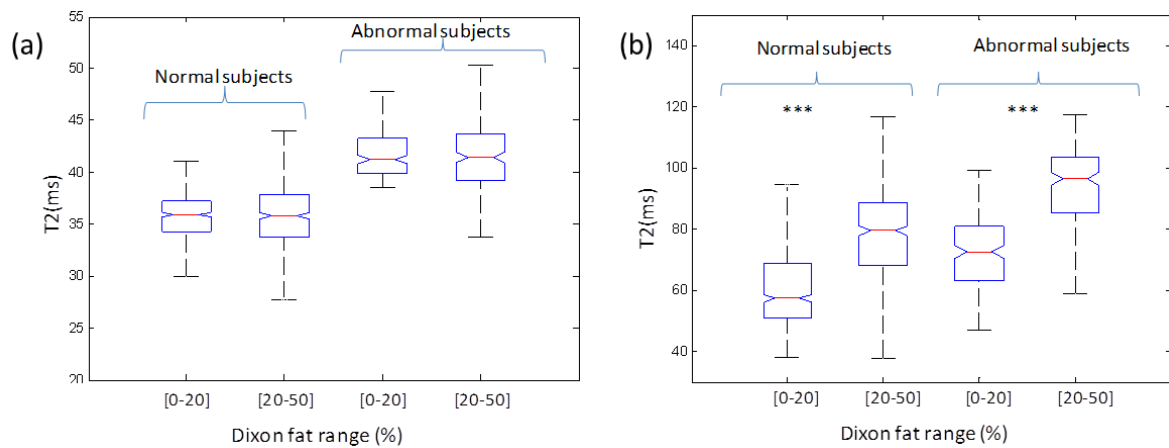


Figure 3-12 - Box plot of T2-values in voxels with different fat signal fractions calculated using (a) the tri-exponential model (b) the mono-exponential model. With the mono-exponential model, T2-values were systematically more elevated when fat content was higher. Significant differences in T2-values between normal and abnormal subjects were observed using both models ($p < 1e-4$).

The water T2-values were also computed for the entire ROIs (considering all voxels, regardless their fat ratio) and correlations with the respective ROI's mean fat fraction were investigated. Figure 3-13 presents the plots of the observed water T2-values and global T2-values against the fat fraction as determined with the 3PD method. Global T2 and fat fraction were highly correlated in normal muscles ($R^2 = 0.67$) as well as in abnormal ones ($R^2 = 0.83$), while water T2-value, as determined by the proposed method, was insensitive to the degree of fat infiltration, showing no correlation with the fraction either in normal ($R^2 = 0.002$) or abnormal muscles ($R^2 = 0.03$).

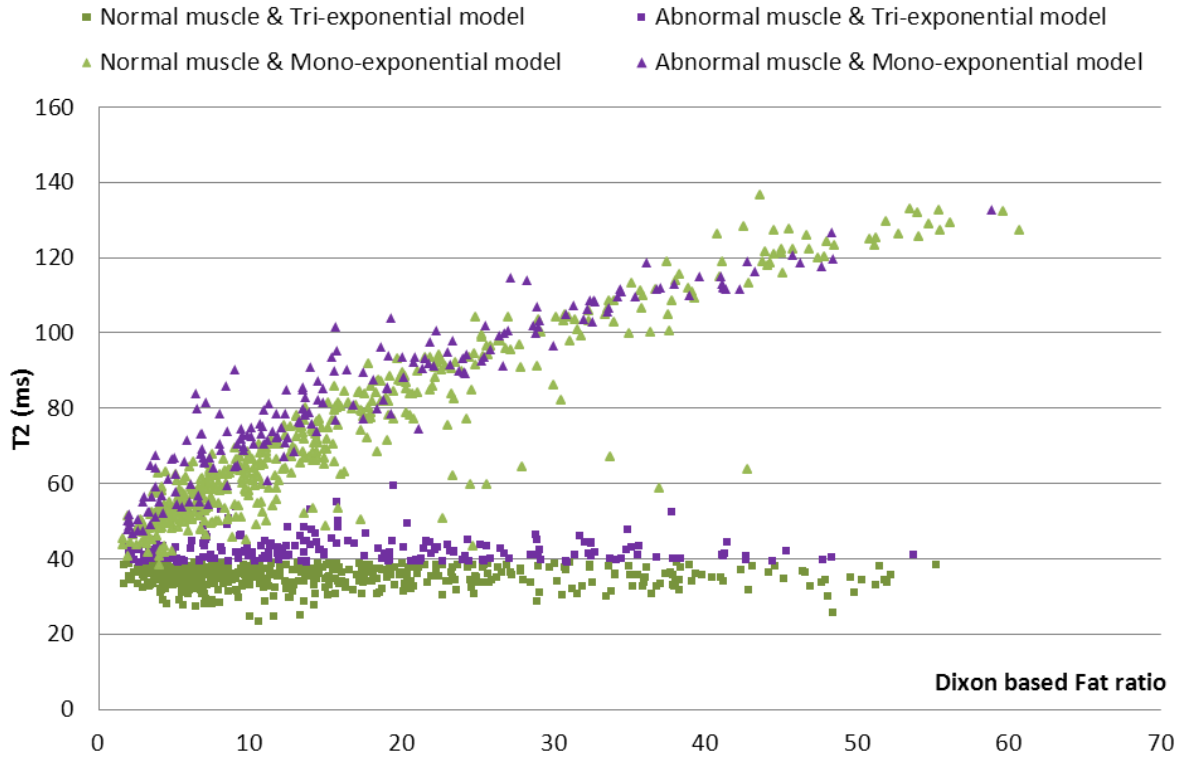


Figure 3-13 – Plots of the water T2-values, as determined with the proposed tri-exponential method, and the global T2-values obtained by simple monoexponential fitting against Dixon-based fat fraction. A strong correlation exists between global T2-value and fat content. In contrast, water T2-values derived from the tri-exponential model were independent from the Dixon fat fraction. Abnormal muscles are also identifiable by elevated global T2-values.

Confrontation of estimated fat fractions against the 3PD method

Finally, we verify that the proposed method allows independent and simultaneous estimation of water T2-value and fat fraction. The 3PD method is known to underestimate the signal from lipids because it accounts only for the methylene component in the triglyceride molecules (73, 75). In order to correct for this bias before comparing the estimated fat fractions with both methods, the underestimation of fat fraction with the 3PD method was quantified using numerical simulations. Synthetic signal from a spoiled gradient echo sequence was generated by the following model:

$$I(TE) = \left(W_0 + F_0 \sum_{k=1}^5 \alpha_k e^{i2\pi TE \Delta f_k} \right) \text{ with } \sum_{k=1}^5 \alpha_k = 1 = W_0 + F_0$$

W_0 and F_0 were randomly selected variable in order to simulate different water/fat ratio. α_k and Δf_k are respectively the relative fraction and the frequency of each fat peak,

obtained from the spectrum provided by the NMRS analysis of subcutaneous fat (Table1). $I(TE)$ represents the complex signal obtained at a given echo time TE . The signal was simulated at TE-values identical to those from our clinical protocol for the 3PD method (2.75, 3.95 and 5.15 ms). Fat and water amplitude signals were estimated with the same post processing of the 3PD method applied to our clinical images. By comparing them with the known simulated signals, F_0 and W_0 , we got the relations $F_{dx} = 0.55F_0$ and $W_{dx} = 0.99W_0$.

The fat ratio obtained using the 3PD method was then corrected according to the following relation:

$$FF_{dx_corrected} = \frac{F_0}{F_0 + W_0} = \frac{FF_{dx}}{(1 - p)FF_{dx} + p} \quad 3.7$$

where $FF_{dx} = \frac{F_{dx}}{F_{dx} + W_{dx}}$ and $p = \frac{0.55}{0.99} \cong 0.55$

For each ROI, we computed the fat fraction values based on the tri-exponential model according to Eq. 3.6 and compared them to the mean $FF_{dx_corrected}$ within the ROI. The results are presented in Figure 3-14.

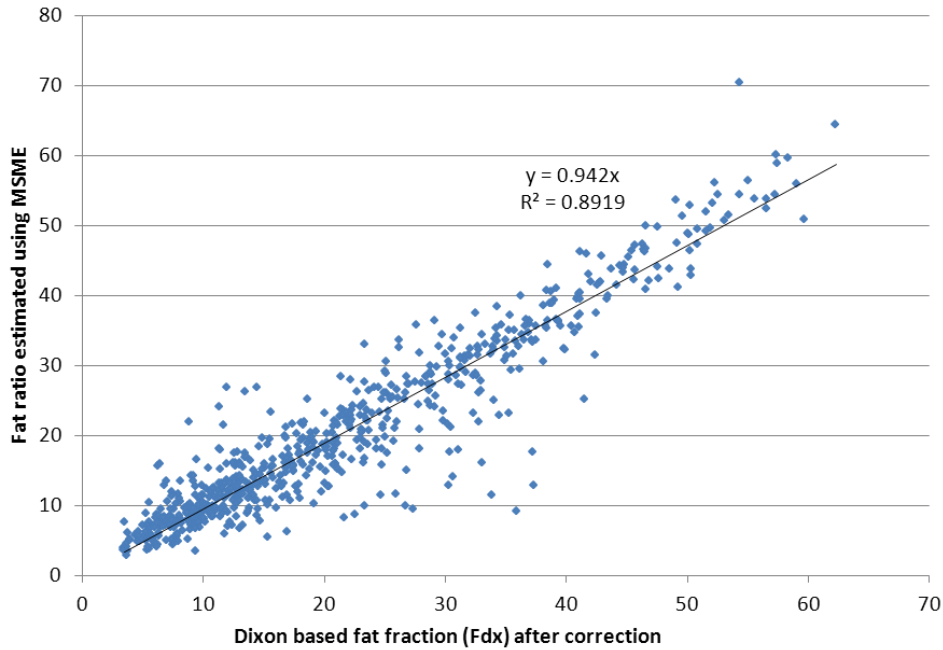


Figure 3-14 - Relationship between fat fractions extracted from Dixon-based fat fraction and MSME based fat fraction. Fat fraction values obtained with both techniques were highly correlated: $R^2=0.89$ with a slope close to unity (0.94).

3.3.3. Discussion and Conclusions

In this work, we introduced an improved post processing technique to quantify skeletal

muscle water T2, devoid of the bias generated by concurrent fat infiltration. Skeletal muscle T2 has been shown to be abnormally long in patients suffering from various neuromuscular disorders. When determined without accounting for fatty degenerative changes, the T2 changes essentially reflect the degree of fatty infiltration in the affected muscles. This then merely duplicates the information obtained with Dixon sequences and is essentially non-informative. It will not reveal the T2 abnormalities of the muscle water component, which have been shown to relate to disease activity, membrane leakiness, necrosis or inflammation, as demonstrated in animal models (76–79). Such alterations are simpler to be detected in animal models because fatty degenerative changes are absent or minimal, at least until advanced age.

Although the idea of exploring T2-relaxation differences between water and lipids had already been proposed (19), there are important differences between our method and theirs. First, fat signal decay was modelled for each subject, using subcutaneous fat as a reference, in order to take into account for variations of fatty acid composition between subjects. Second, tri-exponential fitting, with two components for fat decay yielded better agreement with experimental data than bi-exponential fitting, with only one fat component. Furthermore, the T2 value of the short fatty component as well as its proportion with respect to the total fat signal were very close to the parameters characterizing the methylene (CH_{2n}) peak, as determined by spectroscopy data presented in Table 3-1. Third, voxel sorting based on B1+ mapping by eliminating voxels which did not experience the prescribed flip angle, limited the scattering of reference water T2-values, which had the important benefit of improving discrimination of pathological muscles. While mean water T2-values were found to be almost identical in both studies, the standard deviation was four times smaller with our method (2.5 ms vs 7.2 ms). We also showed that muscle fat fraction can be determined directly from the decay analysis.

The most important contribution of this work was certainly the demonstration that muscle water T2, as determined by the tri-exponential fit, was not correlated muscle fat fraction. The robustness of the proposed method was further demonstrated by the observation that muscles that were identified as having abnormally high T2 with the tri-exponential method also had higher T2 values with the standard mono-exponential analysis, when compared to muscles with an identical level of fat content as determined by Dixon imaging. Hence, its insensitivity to fat infiltration makes the proposed technique a reliable tool that can monitor other structural changes inside the muscle, such as oedema and inflammation. However, it is important to point out that when the fat ratio is higher than 65% making the water signal small compared to the fat one, the fit quality is degraded and it becomes difficult to estimate a water T2 and fat fraction accurately. In practice, this

limitation doesn't have a major impact because for muscles highly infiltrated the water T2 information is not the most relevant one.

CHAPTER 4

A Steady-state-based Method for T2-Mapping in Fat-infiltrated Muscles

In this chapter we describe the application of a methodology for fast *in vivo* T2-mapping based on the recently proposed technique (80) of partially Spoiled Steady State Free Precession (pSSFP). In contrast to the T2-mapping technique described in the previous chapter, the method proposed in this chapter is based on a 3D gradient echo sequence. The absence of refocusing and slice-selective pulses renders this technique easily compatible with water-selective excitation for isolating only signal contributions from water protons. Although this method constitutes a simpler alternative for T2-mapping, which is more easily applicable in a clinical environment when compared to the MSE-based method presented in chapter 3, its application is restricted to tissues respecting some relaxation conditions which will be discussed in the following.

4.1. Introduction

4.1.1. Context

As discussed in chapter 3, B_0 and B_1 inhomogeneities constitute an important accuracy and precision constraint for T2 measurements based on a standard multi spin-echo (MSE) sequence. In the methodology described in chapter 3 these issues were avoided by limiting the T2-measurement to B1-sorted voxels (3.3.1.2). More sophisticated post-processing techniques that allow for correction of field in-homogeneity effects on observed T2-values have been presented (60). However they rely on the knowledge of excitation and refocusing slice profiles which render their application not straightforward in a clinical environment. Another important limitation of 2D MSE T2-mapping is the large inter-slice gap required in order to avoid cross-talking. Specific absorption rate (SAR) concerns can limit the number of echoes and/or the number of slices, particularly at 3T and/or if body coil is used as transmitter coil. This is an important drawback for studies requiring multiple

slices and large volume coverage.

Alternative methods based on SSFP sequences (see 2.7.3) have allowed 3D high-resolution ($1 \times 1 \text{ mm}^2$) T_1 - and T_2 -mapping of the brain in a clinically acceptable time (~ 15 min) (81–83).

The acquisition parameters, TR and TE , of spoiled GRE sequences might be adjusted in such way to result in T_1 -weighted signal (see Eq. 2.25), so that a T_1 -map may be extracted from spoiled GRE acquisitions applied with different sequence parameters, e.g. flip angle (FA) or repetition time (TR). With the knowledge of T_1 , a T_2 -map may be analogously extracted from at least two SSFP acquisitions, whose signal depends on both T_1 and T_2 . However, these methods suffer from high sensitivity to off-resonance effects, which render their accuracy and precision dependent on B_0 homogeneity, resulting in biased T_2 -measures for regions marked by high susceptibility-induced gradients. Techniques for minimizing this issue require acquisition of multiple phase-cycled data (84), which elongates the duration of the acquisitions. Moreover, as the signal from GRE sequences is strongly dependent on the applied FA, the accuracy and precision of such GRE-based T_1 - and T_2 -mapping demand accurate knowledge of actual B_1 field distribution. These constitute a major accuracy problem for the T_2 -map which relies on accurate knowledge of T_1 . Furthermore, these methods have also been recently shown to be prone to magnetization transfer (MT) effects, which require further post-processing corrections (85).

In conventional spoiled GRE sequences, the phase of the RF-pulse presents a quadratic dependence on the repetition index (see 2.7.3), and signal will only be efficiently spoiled for specific phase shift increments (e.g. $\Delta\phi = 50^\circ, 117^\circ, 123^\circ, \text{etc.}$). Absence of RF spoiling ($\Delta\phi = 0$) will produce SSFP signal. Intermediate $\Delta\phi$ values will produce the so called partially spoiled steady state condition, and the corresponding sequence will be referred to as partially spoiled steady state free precession pSSFP. An analytical solution for the pSSFP signal for small $\Delta\phi$ and TR/T_1 values have been first presented in a relatively recent work (86). In face of this analytical solution, a new fast T_2 -mapping method based on the pSSFP sequence was recently proposed which is insensitive to B_0 inhomogeneities, diffusion and magnetization transfer effects (87). This method allows extraction of high-resolution 3D T_2 -map in approximately 5 min, does not rely on accurate knowledge of T_1 and require no sophisticated post-processing. Such a technique is advantageous relative to the MSE-based method presented in chapter 3 to what concerns acquisition time and post-processing. Moreover, the knowledge of the FA errors allows direct correction of the extracted T_2 -value instead of eliminating voxels that do not present sufficient FA accuracy. Finally the method is also compatible with selective water

excitation, which allows robust isolation of water only contributions.

Some limitations of this method have been discussed in (88, 89). These authors pointed out that the T2-pSSFP method yields accurate results only for large RF flip angles ($\alpha \geq 70^\circ$) and for tissues exhibiting considerably high T_1/T_2 ratios (e.g. skeletal muscle), otherwise T_2 is underestimated. These conditions can be expressed by the relation $\frac{T_2}{T_1} \ll \tan^2 \frac{\alpha}{2}$ (87). Although a solution for such limitation has been presented (80) allowing a higher flexibility on the choice of FA, the method is iterative which hampers any analytical investigation of the dependency of the measures on the sequence and tissue parameters. This renders the adjustment of the method to specific applications rather complicated.

In this chapter we describe the application of the original T2-pSSFP method on skeletal muscle tissue and describe a simpler alternative to directly correct the extracted T2-values when the $\frac{T_2}{T_1} \ll \tan^2 \frac{\alpha}{2}$ condition is not respected. The new corrected method shall be referred to as the extended T2-pSSFP method. Moreover, we investigate the impact of B1-inhomogeneity on the measures and a simple method for correction of FA errors in T2-pSSFP measurements is experimentally demonstrated.

The feasibility of the method was demonstrated in vitro and in vivo, where it has been shown to be sensitive to variations on T2-value caused by inflammation responses following eccentric exercise, known to injury muscle cells. We also demonstrate the capability of the method in detecting inflammation sites also observed in fat-saturated T2-weighted images in the thighs of a myopathic patient. The method constitutes an alternative for water T2-mapping in normal and fatty infiltrated muscles.

4.1.2. Theory

4.1.2.1. The original T2-pSSFP method

The solution for the pSSFP signal, S_ϕ , for small parameters ϕ and $\delta \equiv \frac{TR}{T_1}$, cf. equation 35 of (86), states that S_ϕ is a function of the experimental parameters α , ϕ and TR and the tissue relaxation times T_1 and T_2 :

$$S_\phi / S_{eq} \approx \Gamma \delta \frac{\xi \phi + i \sigma \delta}{(\sigma^2 - \Gamma^2 \sigma) \delta^2 + \xi^2 \phi^2} \quad 4.1$$

Where S_{eq} is the longitudinal magnetization amplitude at thermal equilibrium, $\Gamma \equiv \left(\tan \frac{\alpha}{2}\right)^{-1}$, $\delta \equiv \frac{TR}{T_1}$, $\sigma \equiv -\frac{T_1}{T_2} \left(1 + \sqrt{1 + \Gamma^2 \frac{T_2}{T_1}}\right)$ and ξ depends only on the flip angle α . Typical values for $\xi(\alpha)$, which must be determined numerically via a continued fraction expansion, are given in table 1.

Table 4-1 - Typical values for $\xi(\alpha)$, which must be determined numerically, for different flip angles, α .

α	10°	20°	30°	40°	50°	60°	70°	80°	90°
$\xi(\alpha)$	0.47	0.16	0.090	0.061	0.047	0.038	0.032	0.028	0.025

* Data obtained from (86)

By defining $\lambda \equiv -\frac{\sigma\delta}{\xi}$ and Eq. 4.1 can be re-written as

$$S_{\phi} \approx S_{eq} \frac{\Gamma\delta}{\xi} \frac{\phi + i\lambda}{\kappa\lambda^2 + \phi^2} \Rightarrow |S_{\phi}| \approx S_{eq} \frac{\Gamma\delta\sqrt{\lambda^2 + \phi^2}}{\xi\kappa\lambda^2 + \phi^2} \quad 4.2$$

with $\kappa \equiv 1 - \frac{\Gamma^2}{\sigma} = \sqrt{1 + \Gamma^2 \frac{T_2}{T_1}}$ and $i \equiv \sqrt{-1}$.

If we impose that $\frac{T_2}{T_1} \ll \tan^2 \frac{\alpha}{2}$ then $x \equiv \Gamma^2 \frac{T_2}{T_1} \rightarrow 0$, $\kappa \rightarrow 1$ and $\lambda \rightarrow \frac{2TR}{\xi T_2}$, reducing Eq. 4.2 to

$$|S_{\phi}| \approx S_{eq} \frac{\Gamma\delta}{\xi} \frac{1}{\sqrt{\lambda^2 + \phi^2}} \quad 4.3$$

In this case, The T2-value can be estimated from two pSSFP acquisitions with different phase increments ϕ_1 and ϕ_2 (87) by the following relation derived from Eq. 4.3:

$$T_2^{est} = \frac{2TR}{\xi} \sqrt{\frac{S_{\phi_1}^2 - S_{\phi_2}^2}{S_{\phi_2}^2 \phi_2^2 - S_{\phi_1}^2 \phi_1^2}} \quad 4.4$$

4.1.2.2. The extended T2-pSSFP method

When the condition $\frac{T_2}{T_1} \ll \tan^2 \frac{\alpha}{2}$ is not respected, Eq. 4.4 will not be valid anymore and the T_2^{estim} will deviate from the theoretical value (89). In order to evaluate the impact on T_2^{estim} , let's re-write Eq. 4.2 in terms of the parameter $x \equiv \Gamma^2 \frac{T_2}{T_1}$. Assuming that x too big to be neglected but still small enough so that second or higher order terms on x are negligible, one gets that

$$\kappa = \sqrt{1+x} \cong 1 + \frac{x}{2}$$

$$\lambda \equiv \lambda_x = \frac{TR(1+\kappa)}{T_2 \xi} = \frac{2TR}{\xi T_2} \left(1 + \frac{x}{4}\right)$$

Substituting these expressions in Eq. 4.2, and defining $\lambda_0 = \frac{2TR}{\xi T_2}$, one obtains

$$|S_{\emptyset}| = \frac{\Gamma\delta}{\xi} \frac{\sqrt{\left(1 + \frac{x}{4}\right)^2 \lambda_0^2 + \emptyset^2}}{\left(1 + \frac{x}{2}\right) \left(1 + \frac{x}{4}\right)^2 \lambda_0^2 + \emptyset^2} \quad 4.5$$

From Eq. 4.5 one may directly derive the expression for the square norm, $|S_{\emptyset}|^2$. Conserving only the linear terms on x :

$$|S_{\emptyset}|^2 \cong \left(\frac{\Gamma\delta}{\xi}\right)^2 \frac{\left(1 + \frac{x}{2}\right) \lambda_0^2 + \emptyset^2}{\left(\left(1 + x\right) \lambda_0^2 + \emptyset^2\right)^2} \cong \left(\frac{\Gamma\delta}{\xi}\right)^2 \frac{1}{\left(1 + \frac{3}{2}x\right) \lambda_0^2 + \emptyset^2} \quad 4.6$$

From Eq.4.6 it is easy to derive the following expression for the estimated T2-value corrected for linear order terms on $\Gamma^2 \frac{T_2}{T_1}$:

$$T_2^2 = \left(\frac{2TR}{\xi}\right)^2 \frac{S_{\emptyset_1}^2 - S_{\emptyset_2}^2}{S_{\emptyset_2}^2 \emptyset_2^2 - S_{\emptyset_1}^2 \emptyset_1^2} \left(1 + \frac{3}{2} \Gamma^2 \frac{T_2}{T_1}\right) = (T_2^{est})^2 \left(1 + \frac{3}{2} \Gamma^2 \frac{T_2}{T_1}\right) \quad 4.7$$

where T_2^{est} is estimated T2-value obtained with the original T2-pSSFP method and is defined in Eq. 4.4. Further developing Eq. 4.7 and defining $\eta \equiv \frac{1}{2} \Gamma^2$ In order to keep the same notation from (86), we get

$$T_2 = T_2^{est} \left(1 + \frac{3}{2} \eta \frac{T_2}{T_1}\right) \quad 4.8$$

$$T_2 = \frac{T_2^{est}}{\left(1 - \frac{3}{2} \eta \frac{T_2}{T_1}\right)} \quad 4.9$$

Note that when $\eta \frac{T_2}{T_1} \rightarrow 0$, then $T_2 \rightarrow T_2^{est}$. The T2-value obtained from Eq. 4.9 extends the application of the T2-pSSFP method beyond the limits imposed by $\eta \frac{T_2}{T_1} \ll 1$.

The flip angle α will deviate from its nominal value due to miscalibration of RF pulse and/or B_1 inhomogeneity, which will lead to inaccurate determination of T_2 using the T2-pSSFP method. In vivo NMRI at high field ($\geq 3T$) suffers from intrinsic inhomogeneity of the active B_1 field (B_{1+}) as the RF wavelength approaches the typical dimensions of the human body (90, 91) (see 2.8). Large deviation from the nominal FA due to B_1 inhomogeneity has been reported in human lower limb imaging at 3T (92) and has been related to inaccurate estimation of NMR parameters in muscular qNMRI (93). To overcome this issue and avoid biased measures of T_2 using the extended T2-pSSFP method, the effective FA, obtained from a B1-map, must be applied into Eq. 4.9 in order to correct the value of η .

An alternative approach to dealing with the T_1 -contribution in T_2 -pSSFP measurements has been recently proposed in (80): Starting from Eq. 4.2 and writing the expression for the quotient of two acquisitions with different partial RF spoiling increments (ϕ_1, ϕ_2) as

$$S_{12} \equiv \left(\frac{S_{\phi_1}}{S_{\phi_2}} \right)^2 = \frac{\lambda^2 + \phi_1^2}{\lambda^2 + \phi_2^2} \left(\frac{\kappa\lambda^2 + \phi_2^2}{\kappa\lambda^2 + \phi_1^2} \right)^2 \quad 4.10$$

Eq. 4.10 can be re-written as a cubic equation of the form

$$\mathbf{a}_3 \mathbf{z} + \mathbf{a}_2 \mathbf{z}^2 + \mathbf{a}_0 \mathbf{a}_1 \mathbf{z}^1 + \mathbf{a}_0 = \mathbf{0} \quad 4.11$$

where $z \equiv \lambda^2$ and

$$\mathbf{a}_3 \equiv \kappa^2 (S_{12} - 1) \quad 4.12A$$

$$\mathbf{a}_2 \equiv S_{12} (2\kappa\phi_1^2 + \phi_2^2\kappa^2) - (2\kappa\phi_2^2 + \phi_1^2\kappa^2) \quad 4.12B$$

$$\mathbf{a}_2 \equiv S_{12} (\phi_1^4 + 2\kappa\phi_1^2\phi_2^2) - (\phi_2^4 + 2\kappa\phi_1^2\phi_2^2) \quad 4.12C$$

$$\mathbf{a}_2 \equiv S_{12} \phi_2^2 \phi_1^4 - \phi_1^2 \phi_2^4 \quad 4.12D$$

Assuming that the T_1/T_2 ratio (and therefore κ) is known, Bieri et al. argued that by finding the roots of this polynomial (using Cardano's method or numerical algorithms), T_2 can be derived as:

$$T_2 = (1 + \kappa) \frac{TR}{\xi} \frac{1}{\sqrt{z_1}} \quad 4.13$$

where z_1 is the real positive root. It should be mentioned that Bieri's approach yields an exact result for Eq. 4.10 provided that the T_1/T_2 ratio is known. For practical purposes, however, only T_1 is usually assessed. In this case, this method requires an approximate starting value for T_2 , which should be improved by iterative computation of the polynomial roots. In contrast to the Bieri's method, our approach avoids time-consuming iterations and potential convergence failure or inaccurate on the estimation T_2 arising from a bad starting value. Although it is only an approximation, the novel approach outlined here offers a simple way to evaluate the impact of each experimental and tissue parameter on estimation of T_2 , facilitating sequence optimization for a chosen application. And most importantly, for practical in vivo applications, such as quantitative muscle imaging, this approach yields accurate results, as will be demonstrated on the following.

4.2. Methodology

Volunteer and patient examinations were conducted in accordance with institutional

guidelines. Experimental data were acquired on a 3T whole-body scanner (Tim Trio, Siemens Healthcare, Erlangen, Germany). A commercial FLASH sequence was modified to allow flexible control of the linear phase increment ϕ by the user (resolution of 1°). Tunable dummy scans were added for pSSFP stabilization purposes.

Reference T_1 - and T_2 -values for the phantom were obtained using gold-standard sequences: T_1 was measured using an inversion recovery (IR) method which consisted of a non-selective adiabatic inversion pulse followed by acquisition of a single-slice, centric k -space ordering FLASH image, at the inversion time TI. Twenty one different TI-values were used, between 110 and 8000 ms. A delay of 20 s was inserted before each inversion pulse to allow for full longitudinal magnetization recovery. Average signal as a function of TI was measured in a region of interest (ROI) placed at the most central portion of the phantom. T_1 was calculated from monoexponential fitting of the experimental data by means of least-mean-squares. T_2 was measured using a non-localized CPMG sequence. 400 echoes were acquired with an inter-echo-space of 2.5 ms. Only even echoes were used and the 180° pulses were phase cycled in order to cancel out FID signals originated from imperfect refocusing. T_2 was calculated from monoexponential fitting by means of least mean squares.

Data analysis, visualization and numerical simulation were done in Matlab (The MathWorks, Inc., Natick, MA, USA).

Phantom NMRI: S_ϕ vs. α and ϕ

Equation 4.1 and the following were deduced assuming small $\xi\phi$ values (86). Therefore, the maximal ϕ value for which Eq. 4.1 is still applicable depends on α via ξ . In order to determine the regime of validity of this model for different α T2-pSSFP 3D experiments were acquired in a 0.1 mM 50 mL MnCl_2 phantom ($T_1/T_2 = 886/86$ ms), with a sagittal orientation on a $192 \times 66 \times 64$ matrix yielding 1.2 mm isotropic resolution. Relevant sequence parameters were $TR = 5$ ms, $TE = 3$ ms, bandwidth = 550 Hz/pixel, number of signal accumulations (NEX) = 4. A non-selective hard pulse of 300 μs length was used for excitation, with $\alpha = (20^\circ, 40^\circ \text{ and } 90^\circ)$, $\phi = (1^\circ, 5^\circ, 10^\circ, 15^\circ, 20^\circ \text{ and } 30^\circ)$. Experimental results were compared with those of numerical computation: S_ϕ was either calculated using Eq. 4.2 or numerically simulated using Bloch matrix formulation, as described in (94). Common parameters for both computations were $TR = 5$ ms, $TE = 3$ ms, $\alpha = (20^\circ, 40^\circ \text{ and } 90^\circ)$, $\phi = 1^\circ$ to 50° , in 0.5° steps, $T_1/T_2 = 886/86 \approx 10$.

Phantom NMRI: T_2^{estim} vs. α and ϕ

In the original T2-pSSFP approach (Eq. 4.4) it has been argued that this method yields

accurate estimation of T_2 only for $(T_1/T_2)/\eta \gg 1$. The primary purpose of this experiment was to investigate how T_2^{estim} , obtained from Eq. 4.4, depends on $(T_1/T_2)/\eta$. T2-pSSFP 3D experiments were acquired in a 50 mL MnCl₂ phantom, with a sagittal orientation on a 192 x 66 x 64 matrix yielding 1.2 mm isotropic resolution. Relevant sequence parameters were $TR = 5$ ms, $TE = 3$ ms, bandwidth = 550 Hz/pixel, NEX = 4. A non-selective hard pulse of 300 μ s length was used for excitation. $\alpha = (20^\circ, 40^\circ, 60^\circ, 80^\circ \text{ and } 90^\circ)$, $\phi_1 = 1^\circ$, $\phi_2 = 10^\circ$. T_2^{estim} was computed introducing experimental S_{ϕ_1} and S_{ϕ_2} values into Eq. 4.4 and then T_2^{estim}/T_2 was computed using the result of Eq. 4.4 divided by reference T_2 (=86 ms). Finally $(T_1/T_2)/\eta$ was computed using reference T1- and T2-values for each different nominal flip-angle α .

Since the derivation of Eq. 4.4 and following relies on the validity of Eq. 4.1, it is expected that in the low flip angle regime, for which Eq. 4.1 should not be valid (86), discrepancies between experimental and theoretical T_2^{estim} may occur. To investigate the regime of validity of Eq. 4.4 as a function of α , experimental results were compared with those from numerical simulation of the pSSFP signal: S_{ϕ_1} and S_{ϕ_2} were calculated for each different α using Eq. 4.2 and then T_2^{estim}/T_2 was computed using the result of Eq. 4.4 divided by reference T_2 . Computational parameters were $T_1 = 886$ ms, $T_2 = 86$ ms, $TR = 5$ ms, $\alpha = 5^\circ$ to 90° , in 5° steps, $\phi_1 = 1^\circ$ and $\phi_2 = 10^\circ$.

In order to validate Eq. 4.8, experimental and simulated data were superimposed on the analytical curve $T_2^{estim}/T_2 = x/(3/2 + x)$ where $x = (T_1/T_2)/\eta$. For this calculation only the x range was relevant: $0 < (T_1/T_2)/\eta \leq 40$.

Numerical simulation: Effect of T_1 error on T_2 measurements

It is expected from Eq. 4.9 that errors in the determination of T_1 may lead to a bias in the calculated T2-values. Simulations were performed to investigate this effect on of the measured T_2 for two different tissue models ($T_1/T_2 = 886/86 \sim 10$ and $T_1/T_2 = 1400/35 = 40$). Main computational parameters were: $TR = 5$ ms, $\alpha = 60^\circ$, $\phi_1 = 1^\circ$ and $\phi_2 = 10^\circ$. S_{ϕ_1} and S_{ϕ_2} were computed using Bloch simulation for both tissue models and then used to calculate T_2^{estim} (Eq. 4.4). Next, biased $T_1 (= \hat{T}_1)$ ranging between -50% to +50% of the true T_1 was introduced into Eq. 4.9 to calculate biased $T_2 (= \hat{T}_2)$. Results were compared with the analytical equation derived in the Appendix.

Numerical simulation: Effect of B_1 inhomogeneity on T_2 measurements

It has been argued in the Theory section that B_1 inhomogeneity may lead to inaccurate determination of T_2 using the pSSFP method. Numerical simulations were performed to

investigate the impact of B_1+ inhomogeneity on accuracy of T_2 for two different tissue models ($T_1/T_2 = 10$ and $T_1/T_2 = 40$). S_{ϕ_1} and S_{ϕ_2} were computed using Bloch simulation for FAs varying between 36° to 72° in 1° steps. This range corresponds to a deviation in the nominal FA of between -40% to $+20\%$ of 60° . Next, T_2 was calculated using Eqs. 4.4 and 4.9 assuming either nominal or actual FA. Other computational parameters were: $T_1 = 886$ ms, $T_2 = 86$ ms, $TR = 5$ ms, $\phi_1 = 1^\circ$ and $\phi_2 = 10^\circ$.

Phantom: Effect of B_1+ inhomogeneity on T_2 measurements

To study the influence of B_1+ inhomogeneity on T2-mapping, T2-pSSFP experiments were carried out on a cylindrical phantom (4 cm diameter x 20 cm length) filled with 1 L of 0.1 mM $MnCl_2$ solution. Images were acquired using the following experimental parameters: $TR = 5$ ms, $TE = 3$ ms, $\alpha = 60^\circ$, $\phi_1 = 1^\circ$ and $\phi_2 = 10^\circ$. B_1+ mapping procedure was carried out using the AFI technique (55) as described in (4.2.6). Maps of T_2^{estim} - and T_2 -values were generated using Eqs. 4.4 and 4.9 respectively, with or without FA correction. T_1 was set equal to 886 ms.

For comparison, T2-pSSFP maps were also obtained from the same dataset using the iterative method described in the Theory section (Eqs 4.11-4.13). The starting value for the T_1/T_2 ratio was 886/80. Computation stopped when the relative difference between two successive estimations of T_2 was ≤ 0.05 or after 100 iterations.

B_1+ mapping (phantom and in vivo)

The spatial distribution of the B_1 transmit field (B_1 -map) was evaluated using an optimized version of the actual flip angle imaging (AFI) method (55, 95). This method determines a calibration factor, calculated as the ratio of the true FA to the prescribed FA. This calibration factor was subsequently used to correct the parameter α in pSSFP experiment calculations.

AFI was performed using two nominal excitation pulses of 60° (300 μ s length hard pulses) followed by delays TR_1 and TR_2 respectively, with $TR_2 = 5TR_1$ and $TR_1 + TR_2 = 100$ ms. $TE = 2.75$ ms, bandwidth = 550 Hz/pixel. Optimal spoiling of transverse relaxation was ensured by using an improved RF and gradient spoiling scheme as described in (95), assuming an isotropic scalar water diffusion coefficient $D = 0.75$ $\mu\text{m}^2/\text{ms}$. Relevant parameters for spoiling were: diffusion damping = 0.100, RF spoil phase increment = 129.3° .

Numerical simulation: influence of SNR and ϕ

Measurement of T_2 using the pSSFP approach requires two consecutive acquisitions

(S_{ϕ_1} and S_{ϕ_2}) carried out with two different phase increments $\phi_1 < \phi_2$. Optimal setting of ϕ_1 and ϕ_2 to achieve the best precision for T_2 is a complex task, which depends on FA and T_1/T_2 ratio. Roughly speaking, for a given tissue and FA, sensitivity to T_2 is increased by increasing the gap between the two ϕ values. Setting $\phi_1 = 0$ corresponds to performing an SSFP-FID (FISP) acquisition, which is highly flow-sensitive, resulting in undesirable flow artifacts. So the best choice would be setting $\phi_1 = 1^\circ$ and setting ϕ_2 to the highest value theoretically possible (*i.e.*, the largest ϕ_2 (ϕ_{max}) for which Eq. 4.1 is still valid). In this study, the dependence of T_2 measurements upon the signal-to-noise ratio (SNR) and ϕ_2 was also investigated. Bloch simulation was used to calculate S_{ϕ_1} and S_{ϕ_2} with $T_1 = 1400$ ms, $T_2 = 35$ ms, $TR = 6.3$ ms, $TE = 2.8$ ms, $\alpha = 60^\circ$, $\phi_1 = 1^\circ$ and $\phi_2 = (5^\circ, 10^\circ \text{ and } 15^\circ)$. T_1 - and T_2 -values were chosen to approximately match skeletal muscle relaxation times at 3T (Gold et al., 2004; Pai, Li, & Majumdar, 2008), allowing further comparison between simulated and in vivo experimental results. A dataset was generated consisting of 10^6 repetitions of S_{ϕ_1} and S_{ϕ_2} . Complex Gaussian noise with normal distribution was then added to S_{ϕ_1} and S_{ϕ_2} . By changing the noise level, σ , the signal-to-noise ratio of S_{ϕ_1} , $SNR_1 \equiv \langle S_{\phi_1} \rangle / \sigma$ was set to 25, 50 and 100, which correspond to realistic values obtained for in vivo pSSFP. T_2 -values were calculated using Eq. 4.9 and assuming ideal FA.

Eccentric exercise protocol

To demonstrate the potential of the T_2 -pSSFP method for applications in muscle studies, an exercise protocol was chosen to produce a long-term and selective pattern of changes in muscle T_2 -value. These changes were induced by eccentric exercise of the right vastus medialis muscle using an isokinetic dynamometer (Biodex Multi-Joint System 3, Biodex Medical Systems, New York, NY, USA). Basically, eccentric exercise involves developing active tension in a muscle as it opposes a stronger force, which causes the muscle to lengthen while contracted (98). Throughout exercise, the volunteer stayed seated, with the backrest reclined 5° from vertical and straps fixing the trunk, waist and distal thigh. The dynamometer pad was fastened around the leg 5 cm proximally to the medial malleolus. Just before the exercise, the volunteer performed a series of three submaximal contractions for familiarization. Next, the subject performed 6 series of 12 consecutive maximal eccentric isokinetic contractions; the knee was moved by the dynamometer through the range of motion from 165° to 90° of knee flexion at an angular velocity of $30^\circ/\text{s}$. Each series was preceded by two minutes of resting, and there were no pauses between the 12 contractions.

The quadriceps femoral muscles were evaluated by quantitative NMRI before exercise and during the 10-day recovery period. The subject was positioned in the scanner feet-first and supine, and thigh was centered inside of a circularly polarized transmit/receive knee coil (inner diameter = 154 mm, length = 265 mm). 3D pSSFP images were acquired with a sagittal orientation on a 256 x 152 x 160 matrix yielding 1.1 mm isotropic resolution. Sequence parameters were $TR = 6.6$ ms, $TE = 2.8$ ms, $\alpha = 60^\circ$, $\phi_1 = 1^\circ$ and $\phi_2 = 15^\circ$, bandwidth = 550 Hz/pixel. A non-selective water-excitation pulse (1-2-1 binomial 300 μ s length hard pulses) was used for avoiding fat signal contributions. An average of two acquisitions (NEX = 2) was used to improve SNR. The overall T2-pSSFP acquisition time was ~10 min.

T2-maps were calculated using Eq. 4.9 assuming muscle $T_1 = 1400$ ms (96). FA correction was applied in Eqs. 4.4 and 4.9, using the correction factor determined from the B1 mapping experiment. Regions of interest (ROIs) were drawn on 3D FLASH T1-weighted anatomic images, excluding all the visible vessels, and then transposed to the T2-pSSFP images and T2-maps.

For comparison, T2-maps were also obtained in the same subject/days using standard fat-suppressed MSME acquisitions, with the following parameters: TR = 3 s, 17 echo times (TE) range = 8.1 to 137.7 ms, in-plane resolution = 1.4 x 1.4 mm², 11 slices, slice thickness = 8 mm, slice gap = 20 mm, acquisition time ~ 5 min.

Bland-Altman analysis was used to quantify the limit of agreement between T_2 assessed by pSSFP and MSME sequences (99). Bias is the mean difference between the two methods of measurement and represents systematic error. A 95% confidence interval range expected to include 95% of the differences between measurements is set at approximately 2 SD of the mean.

T2-mapping in a myopathic patient

To demonstrate the potential of the T2-pSSFP method for the quantitative assessment of muscular disease, T2-maps were acquired in a myositis patient, as a complement to an ongoing clinical study, which included whole-body T1- and fat-suppressed T2-weighted imaging, 3pt-Dixon imaging and dynamic Gd-DOTA contrast enhanced imaging. Because of the long duration of the clinical NMRI protocol it was not possible to include reference T2 measurements using the MSME method. For comparison, T2-pSSFP experiments were also carried out in a healthy volunteer using the same experimental setup.

Subjects were positioned in the scanner feet-first and supine, and a set of phased-array “body-flex” and “spine” surface receiver coils covered the volume of interest. T2-pSSFP images were acquired with an axial orientation on a 320 x 160 x 64 matrix yielding 1.4 x

1.4 x 5.0 mm³ resolution. Sequence parameters were TR = 6.6 ms, TE = 2.8 ms, $\alpha = 60^\circ$, $\phi_1 = 1^\circ$ and $\phi_2 = 15^\circ$, bandwidth = 550 Hz/pixel. A non-selective water-excitation pulse was used. Overall T2-pSSFP acquisition time was ~3 min.

Fat-suppressed T2-weighted (T2w) images were carried out using standard Turbo Spin-Echo (TSE) acquisition with an optimized inversion-recovery fat suppression technique, SPAIR (for Spectral Adiabatic Inversion Recovery). Relevant experimental parameters were: TR = 3 s, TE = 45 ms, turbo-factor = 6, in-plane resolution = 1 x 1 mm², 39 slices, slice thickness = 6 mm, acquisition time ~ 5 min.

4.3. Results

Reference phantom relaxation times

Phantom relaxation times obtained from independent IR and CPMG experiments were (best-fit value \pm 95% confidence interval) $T_1 = 886 \pm 5$ ms and $T_2 = 85.5 \pm 0.1$ ms, respectively.

In vitro validation: S_ϕ vs. α and ϕ

The experimental pSSFP signals (S_ϕ) of the MnCl₂ phantom, which were measured at three different α values (90°, 40° and 20°), are given as a function of ϕ in Fig. 1a. Numerical estimations for S_ϕ using either Eq. 4.2 or Bloch simulation were superimposed on the experimental data. In Fig. 1b the relative differences between S_ϕ derived from Eq. 4.2 and from numerical Bloch simulation are plotted against $\xi\phi$ for the same previous α and ϕ values.

The Bloch simulation and experimental results demonstrate that Eq. 4.2 correctly describes the transition from unspoiled ($\phi = 0$) to completely spoiled transverse magnetization (represented by the dotted line) for all α values considered. Fig. 1a also shows that the largest ϕ ($=\phi_{max}$) for which Eq. 4.2 is still applicable depends on α . It can be seen from Fig. 1b that Eq. 4.2 is only valid (S_ϕ deviation $\leq 5\%$) for $\xi\phi \leq 1$. Similar numerical results were obtained for different T_1/T_2 ratios (data not shown) and allowed the limits of validity of Eq. 4.2 to be determined as a function of ϕ and α for in vivo experiments. As example, for quantitative mapping of muscle T_2 at 3T ($T_1/T_2 \sim 40$), if $\alpha = 40^\circ$ then Eq. 4.2 is only valid for $\phi \leq 16^\circ$ ($1/\xi = 16.4^\circ$).

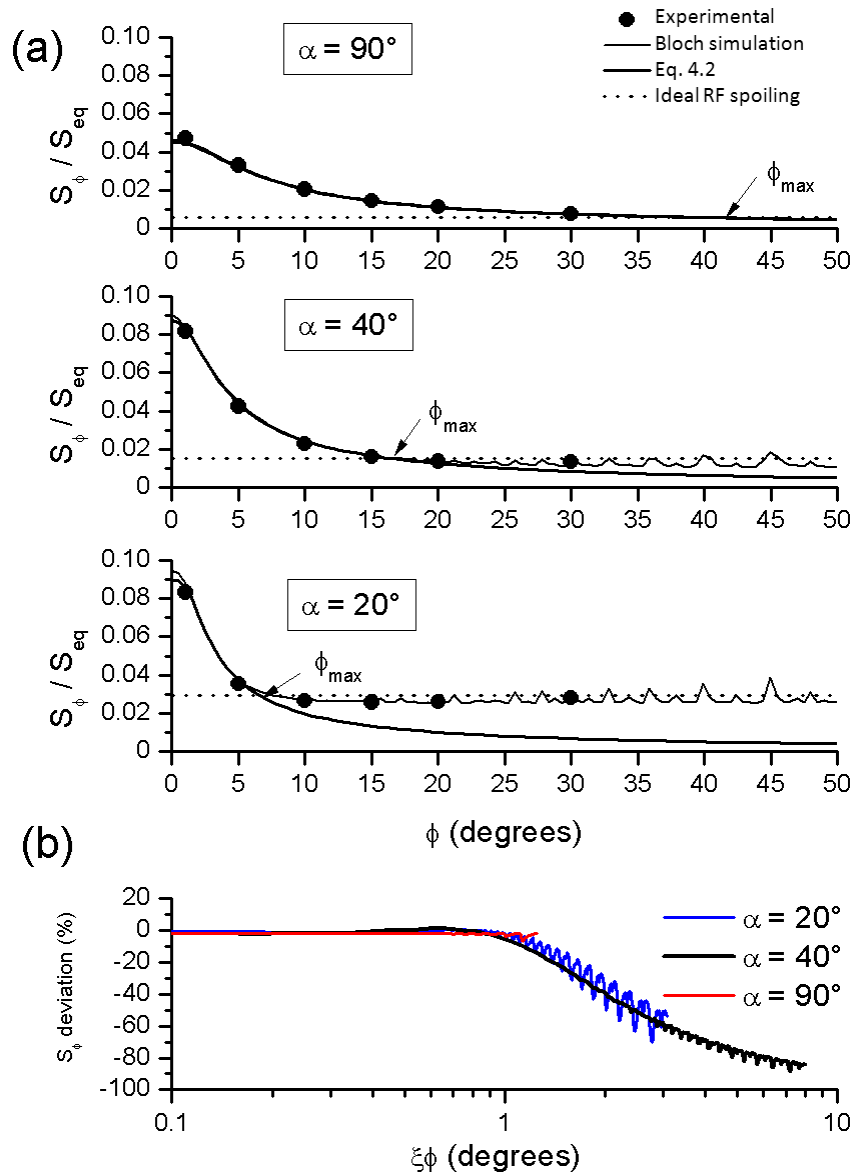


Figure 4-1 - (a) SFP signal as a function of α and ϕ calculated with Bloch simulation (thin line) or using an approximate analytical model (Eq. 4.2) (thick line). Experimental data (closed circles) acquired in a 0.1 mM $MnCl_2$ phantom were superimposed on simulated curves. The constant value (dotted line) represents the ideal RF spoiled signal: $S_{spoil} = S_{eq} \left(1 - e^{-\frac{TR}{T_1}}\right) \sin \alpha / \left(1 - \cos \alpha e^{-\frac{TR}{T_1}}\right)$. Arrows indicate the largest ϕ ($\alpha\phi_{\mu\alpha\xi} = 1/\xi$) for which Eq. 4.2 is still applicable. In (b) the calculated S_ϕ deviation (i.e., the relative difference between S_ϕ derived from Eq. 4.2 and from Bloch simulation) is plotted against $\xi\phi$ for the same α and ϕ values, as in (a). Relevant experimental parameters were $TR = 5$ ms, $TE = 3$ ms, $\alpha = (20^\circ, 40^\circ \text{ and } 90^\circ)$, $\phi = (1^\circ, 5^\circ, 10^\circ, 15^\circ, 20^\circ \text{ and } 30^\circ)$. Common parameters for both computations in Fig. 1 (Bloch simulation and Eq. 4.2) were $TR = 5$ ms, $\alpha = (20^\circ, 40^\circ \text{ and } 90^\circ)$, $\phi = 1^\circ$ to 50° , in 0.25° steps, $T_1/T_2 = 886/86 \approx 10$.

In vitro validation: T_2^{estim} vs. $(T_1/T_2)/\eta$

Experimental results (Fig. 2a, closed circles) confirm that accuracy in T_2 determination using Eq. 4.4 increases with increasing $(T_1/T_2)/\eta$. For $(T_1/T_2)/\eta \sim 21$, which corresponds to $\alpha = 90^\circ$ for this phantom, the T_2^{estim}/T_2 ratio was ~ 0.94 . Fig. 2a also shows that the approximated first-order model (solid line) described by Eq. 4.8 agrees very well with the numerical simulation of Eq. 4.4 (*open squares*) and experimental data (*closed circles*) for $(T_1/T_2)/\eta \geq 4$.

A significant discrepancy is observed between experimental and simulated results for $\alpha = 20^\circ$. For this α value $\phi_{max} = 1/\xi(20^\circ) = 6.25^\circ$. Since experimental data were obtained using $\phi_2 = 10^\circ$, it is clear from Fig. 1b that Eq. 4.2 and following are only valid for $\frac{1}{\xi} \geq 10^\circ$ which corresponds to $\alpha \geq 28^\circ$. For lower α values T_2 measurements derived from Eqs. 4.4 and 4.9 will therefore be inaccurate.

Note that while numerical simulation of Eq. 4.4 assumes $T_1/T_2 = 886/86$, the solid line (Eq. 4.9) was calculated for an arbitrary T_1/T_2 ratio. These findings validate the use of Eqs. 4.8 and 4.9 for the accurate determination of T_2 based on pSSFP experiments, provided that $\phi \leq \phi_{max}$.

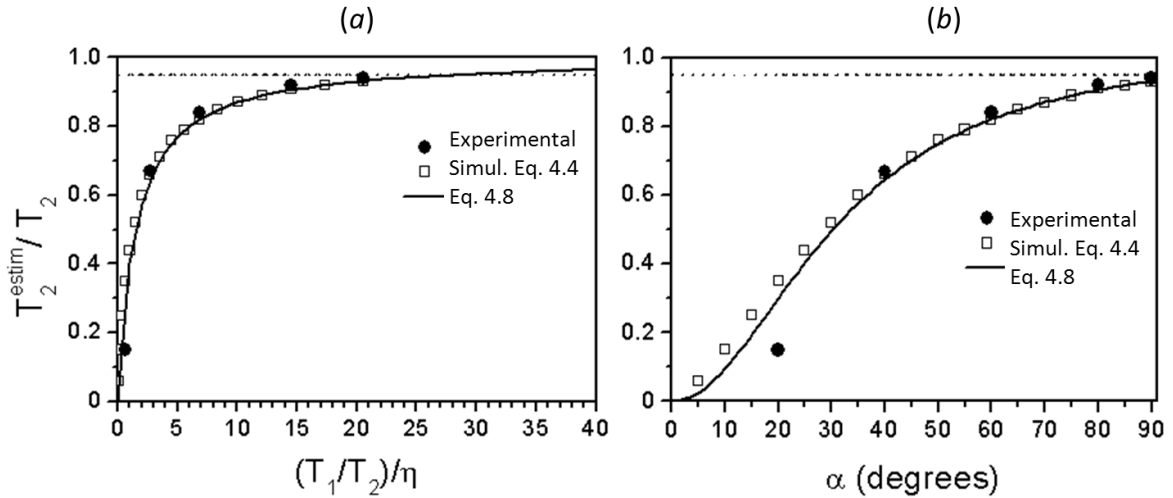


Figure 4-2 – (a) T_2^{estim}/T_2 ratio as a function of $(T_1/T_2)/\eta$ calculated using either numerical simulation of Eq. 4.4 (*open squares*) or the analytical function derived from Eq. 4.8 (*solid line*). To gain insight on the flip angle dependence of T_2 estimation, T_2^{estim}/T_2 ratio was also plotted as function of α in (b). Experimental data (*closed circles*) acquired in a 0.1 mM $MnCl_2$ phantom were superimposed on the simulated curves. The constant value (*dotted line*) represents $T_2^{estim}/T_2 = 0.95$. Relevant experimental parameters were $TR = 5$ ms, $\alpha = (20^\circ, 40^\circ, 60^\circ, 80^\circ$ and $90^\circ)$, $\phi_1 = 1^\circ$, $\phi_2 = 10^\circ$. Computational parameters were $T_1 = 886$ ms, $T_2 = 86$ ms, $TR = 5$ ms, $\alpha = 5^\circ$ to 90° , in 5° steps, $\phi_1 = 1^\circ$ and $\phi_2 = 10^\circ$.

Effect of T_1 error on T_2 measurements

The impact of T_1 inaccuracy ($= \Delta T_1$) on T_2 computation using Eq. 4.9 is shown in Fig. 3 for two different tissue models ($T_1/T_2 = 10$ and $T_1/T_2 = 40$) and two different FA (80° and 60°). Numerical simulations corroborated with the analytical solution obtained in the Appendix: the sensitivity of T_2 to T_1 errors becomes more important with decreasing FA or T_1/T_2 ratio. As seen in Fig. 3, for tissues with $T_1/T_2 = 40$ (e.g. skeletal muscle at 3T), T_2 quantification using the pSSFP method (Eq. 4.9) is practically insensitive to T_1 errors for $FA \geq 60^\circ$.

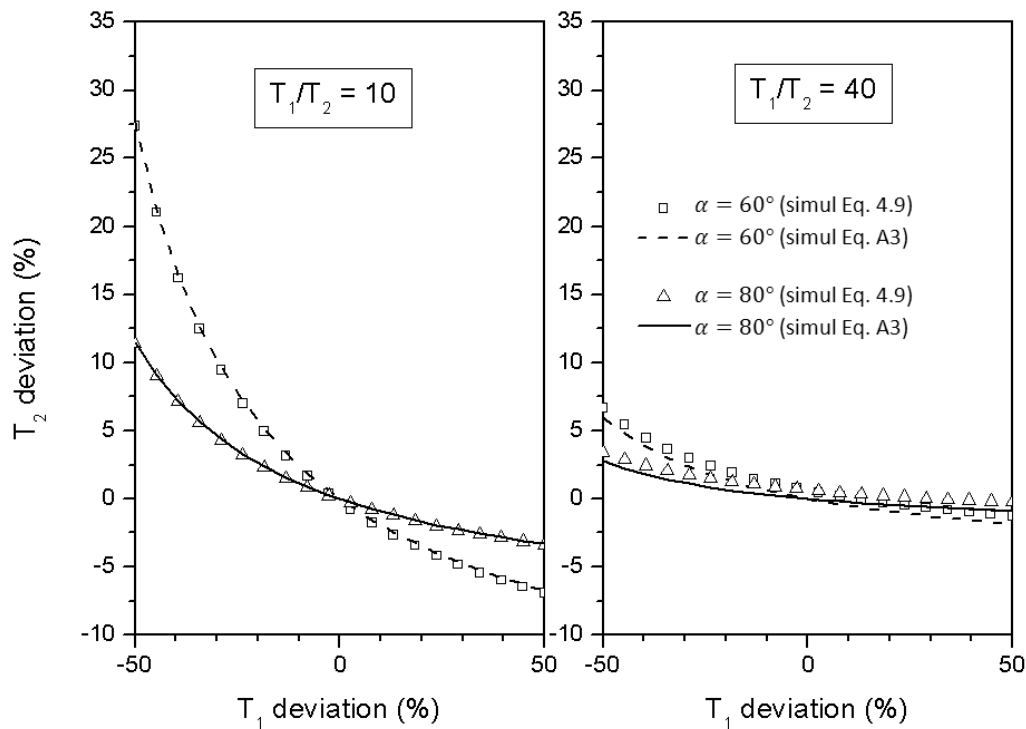


Figure 4-3 - Impact of inaccuracy of T_1 on T_2 computation using Eq. 4.9: Numerical simulations (symbols) and analytical solution (lines) show that the sensitivity of T_2 to T_1 errors becomes more important with decreasing FA or T_1/T_2 ratio. Relevant computational parameters were: $TR = 5$ ms, $\alpha = 60^\circ$ or 80° , $\phi_1 = 1^\circ$, $\phi_2 = 15^\circ$.

Effect of B_1+ inhomogeneity on T_2 measurements

The results of numerical simulation (Figure 4-4) show that inaccuracy in FA is an important source of error in T_2 estimation based on the pSSFP method (Eq. 4.9). Interestingly, the sensitivity of T_2 estimation to FA errors increases with (T_1/T_2) ratio. For $T_1/T_2 = 10$ the relative T_2 error is practically equal to the relative FA error. It is also shown in Figure 4-4 that correction for FA errors allows accurate T_2 quantification using pSSFP for a large range of FA.

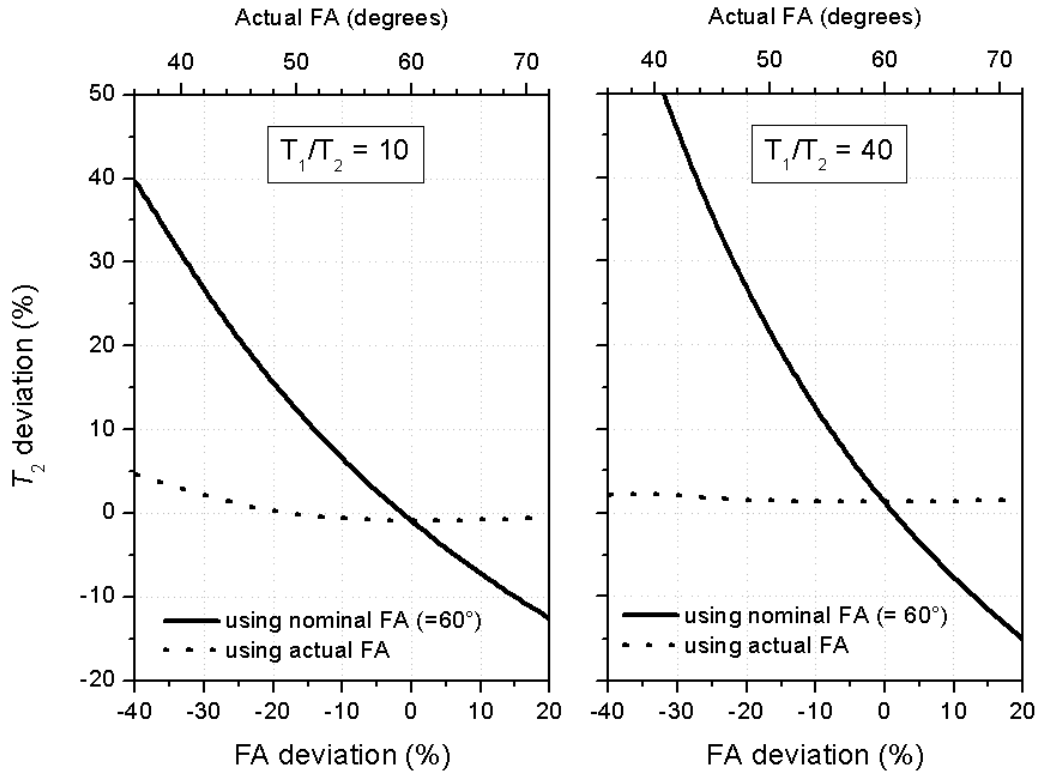


Figure 4-4 - Flip angle sensitivity in T_2 -pSSFP mapping: Percent change in T_2 derived values as determined by Bloch simulation for two tissue models ($T_1/T_2 = 10$ and $T_1/T_2 = 40$) as a function of FA deviation. In the presence of inaccurate FA, T_2 measurement presents a significant bias which becomes more important with increasing T_1/T_2 ratio (solid lines). Accurate T_2 quantification is achieved if actual FA is used in Eqs. 4.4 and 4.9 (dotted lines). Relevant computational parameters were: $T_1 = 886$ ms, $T_2 = 86$ ms, $TR = 5$ ms, $\phi_1 = 1^\circ$, $\phi_2 = 10^\circ$.

Figure 4-5 illustrates the effectiveness of the pSSFP method for quantitative T_2 -imaging in the presence of inhomogeneous B_1+ . Figure 4-5(a-d) show a coronal slice of the 3D T_2^{estim} and T_2 -maps and respective histograms obtained using Eq. 4.4 and 4.9, with and without FA correction. Close to coil extremities, T_2 was overestimated due to reduction in the FA, confirming the predictions of numerical simulation (Figure 4-4). Respective T_2^{estim} and T_2 measurements for Figure 4-5(a-d), expressed as median (range P25-P75), were: (a) 75 (71-84) ms, (b) 66 (61-69) ms, 93 (86-106) ms and (d) 85 (83-87) ms. Note that T_1 and FA corrections were indispensable for accurate and homogeneous T_2 -mapping.

For comparison, T_2 pSSFP maps were also calculated using the iterative approach outlined in the Theory section. T_2 measurements for Figure 4-5(e-f) were: (e) 92 (85-104) ms and (f) 84 (81-86) ms.

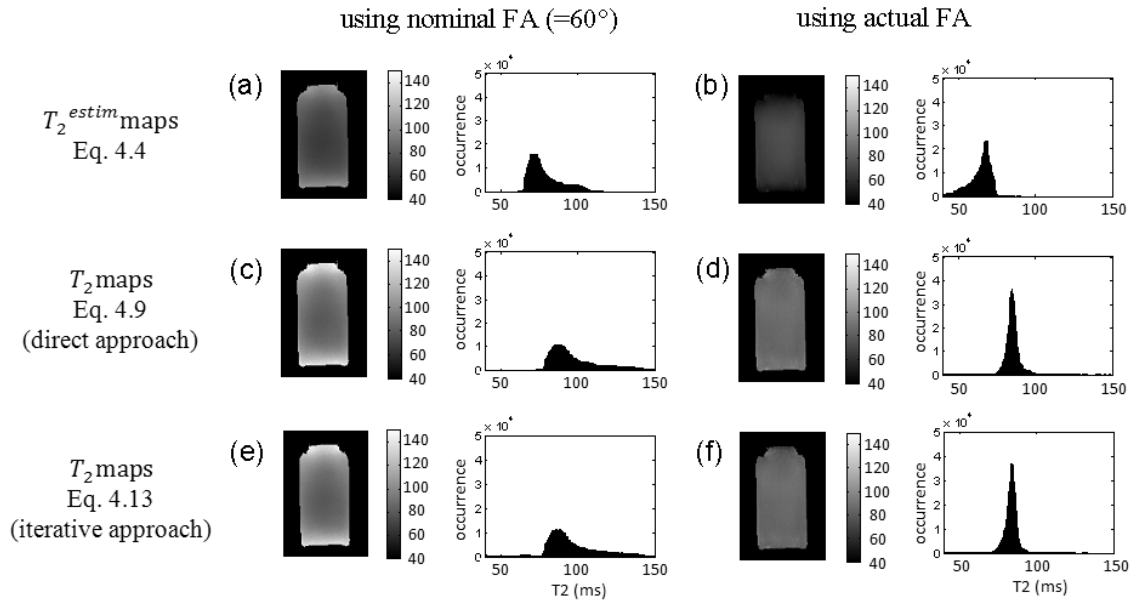


Figure 4-5 - T_2 -mapping of a liquid phantom at 3T (reference $T_2 = 86$ ms): T_2 -maps and respective histograms derived from Eq. 4.4 (a, b), Eqs. 4.4 and 4.9 (direct approach) (c, d) assuming $T_1 = 886$ ms and from Eq. 4.13 (iterative approach) (e, f) assuming $T_1 = 886$ ms and starting $T_2 = 80$ ms. Accurate and precise T_2 -mapping was only possible after concomitant T_1 and FA corrections for both approaches (d, f). Relevant experimental parameters were: $TR = 5$ ms, $TE = 3$ ms, $\alpha = 60^\circ$, $\phi_1 = 1^\circ$, $\phi_2 = 10^\circ$.

Numerical simulation: influence of SNR and ϕ

Impact of SNR on T_2 precision was evaluated through numerical simulation for a set of three SNR1 levels. For realistic SNR1 (≥ 50), precise and accurate T_2 measurements were obtained from muscle-like tissues at 3T ($T_1/T_2 = 40$) by setting $\phi_1 = 1^\circ$ and $\phi_2 = 15^\circ$. For simulated SNR1 = 25, 50 and 100, T_2 was (mean \pm standard deviation) 36 ± 1 ms, 36 ± 2 ms and 36 ± 5 ms, respectively. Keeping SNR1 = 50 and decreasing ϕ_2 to 10° or 5° changed T_2 estimations to 36 ± 3 ms and 39 ± 6 ms, respectively.

In vivo validation: human thigh T_2 -mapping following an eccentric exercise session

Figure 6 displays T_2 -maps (axial and sagittal views) acquired in the quadriceps muscles of a healthy volunteer, immediately before and on the 1st, 2nd, 3rd and 10th day following an eccentric exercise session. Axial views correspond to representative medial and distal sections of the quadriceps muscles and their relative positions are indicated in the anatomical T_1 weighted images (solid lines). SNR1 measured on pSSFP images was higher than 50 for all analyzed muscles. Representative FA deviation maps derived from

B1+ measurements in the volunteer are also show in Fig. 6.

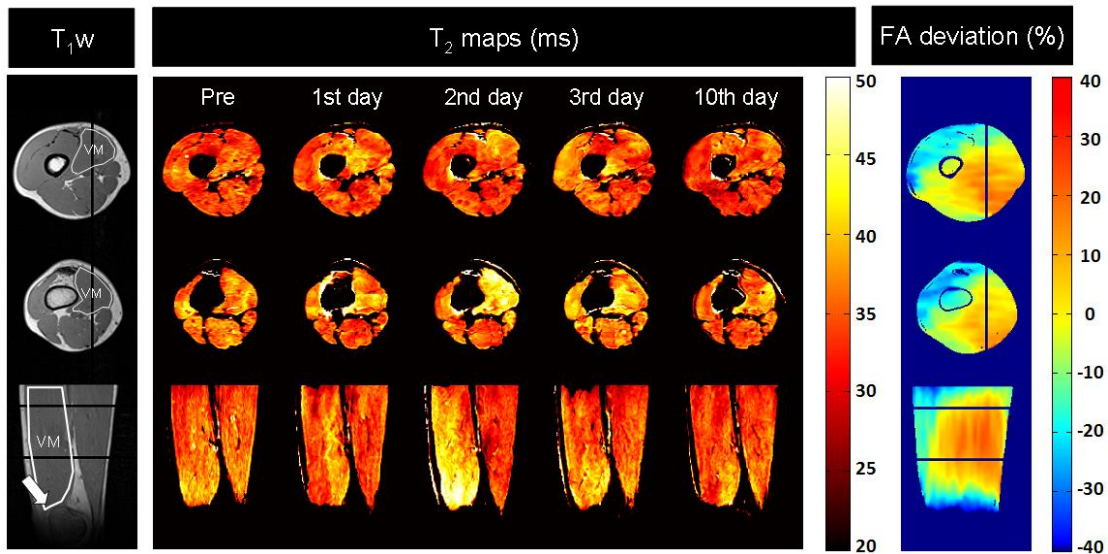


Figure 4-6 - *In vivo* skeletal muscle T_2 -mapping at 3T: T_2 -maps (axial and sagittal views) derived from 3D pSSFP scans. Images were acquired in quadriceps muscles of a volunteer, immediately before and on the 1st, 2nd, 3rd and 10th day following an eccentric exercise session. FA deviation maps are also shown to illustrate the B_1+ inhomogeneity in the knee coil. Axial views correspond to representative medial and distal sections of the quadriceps muscles and its relative positions are indicated in the anatomical T_1 weighted images (black lines). Parametric maps present large areas of T_2 increases at two days post-exercise, corresponding probably to muscle injury. T_2 changes were predominantly located in the distal portion of the vastus medialis (VM) muscle and close to the muscle–tendon junction (arrow). Experimental parameters for T_2 -pSSFP imaging were $\alpha = 60^\circ$, $\phi_1 = 1^\circ$ and 15° , $TR/TE = 6.3/2.8$ ms, $NEX = 2$. All T_2 -maps were corrected for B_1+ inhomogeneity and T_1 . Overall T_2 -pSSFP acquisition time was ~ 10 min.

Before exercise, average quadriceps muscle T_2 was 34 (32-37) ms, which is in good agreement with the literature (Gold et al., 2004; Pai et al., 2008). Parametric maps detected large areas of T_2 increases at two days post-exercise, revealing excessive muscle exposure to strain. T_2 changes were predominantly located in the distal portion of the vastus medialis (VM) muscle and close to the muscle–tendon junction, suggesting selective topography of strain distribution. In the distal portion of VM, T_2 reached its maximal value = 45 (42-47) ms at 2 days post-exercise and progressively returned to baseline, reaching 37 (33-40) ms on the tenth day post-exercise. No significant T_2 modifications were observed in VM on the contralateral side during the same time period.

A comparison between MSME and pSSFP T_2 estimations is displayed in Fig. 7. In Fig. 7a, T_2 measurements for both methods carried out in all quadriceps muscles and on all days were plotted against FA deviation. Error bars were omitted for the sake of clarity. On average, the standard deviation for both methods was ~ 3 ms. Fig. 7a shows that agreement

between both methods decreases for large FA deviation. This can be explained by the fact that FA errors were compensated in the T2-pSSFP method but not in MSME. Therefore, to limit the impact of B1+ inhomogeneity in Bland-Altman analysis, only five slices localized at the center of the transmitter coil were considered. The good agreement between T2 assessed by both methods is illustrated in Fig. 7b. The Bland-Altman analysis showed that ~95% of values (118 of 125) are within the limits of agreement (-8.2 to -0.7 ms), suggesting a normal distribution of differences. A systematic difference between the both methods was found (bias = -4.4 ms).

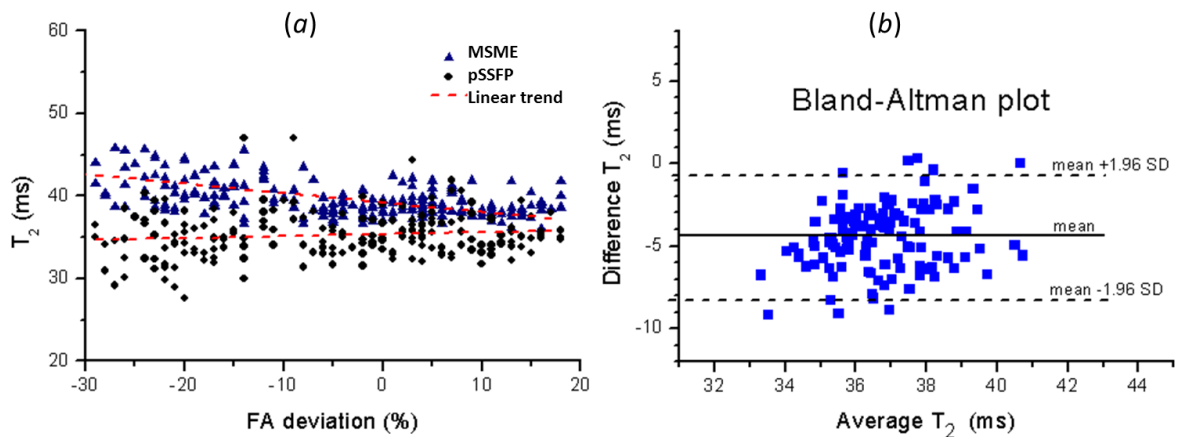


Figure 4-7 - Comparison of T_2 in quadriceps muscles of a volunteer as measured by MSME and T2-pSSFP methods: (a) Overall T_2 measurements (all days, all slices, all ROIs) as a function of FA deviation (symbols). Error bars were omitted for the sake of clarity. On average, standard deviation for both methods was ~ 3 ms. Dashed lines are just guidelines. (b) Bland-Altman plots showing the limits of agreement between T_2 as determined by pSSFP (Eq. 4.9) and standard MSME method. The center line represents the mean differences between the two methods, and the other two lines represent ± 1.96 SD from the mean. To limit the impact of B₁+ inhomogeneity in Bland-Altman analysis only five slices localized at the center of the transmitter coil were considered. Relevant experimental parameters for MSME scans were: TR = 3 s, 17 echo times (TE) range = 8.1 to 137.7 ms, in-plane resolution = 1.4×1.4 mm², 11 slices, slice thickness = 8 mm, slice gap = 20 mm, acquisition time ~ 5 min.

In vivo: mapping in a myopathic patient

The potential of T2-pSSFP for quantitative assessment of muscular disease is illustrated in Fig. 8. The T2-map obtained in a healthy volunteer with this sequence showed a homogeneous distribution of T2-values (Fig. 8a), centered on 37 ms (Fig. 8e). The FA deviation map is also shown to illustrate the effectiveness of the pSSFP method for quantitative lower limb T2-imaging in the presence of inhomogeneous B1+. Using the same pSSFP sequence and parameters, T2-distribution was widely spread in the myopathic

patient (Fig. 8c) and its median value was shifted to 44 ms (Fig. 8e). Regions of highly elevated T2 (up to 180 ms) were visible in the patient T2-map, reflecting a massive tissue edema. These same regions were observed as hyper-signal in a fat suppressed T2w image (Fig. 8d), confirming the T2-pSSFP findings. In addition, all apparently normal heads of patient quadriceps (i.e., excluding edematous tissues) were abnormal with a median T2-values > 40 ms (P50/P25/P75 = 43/39/47 ms), a fact that was totally overlooked by visual inspection of T2w images.

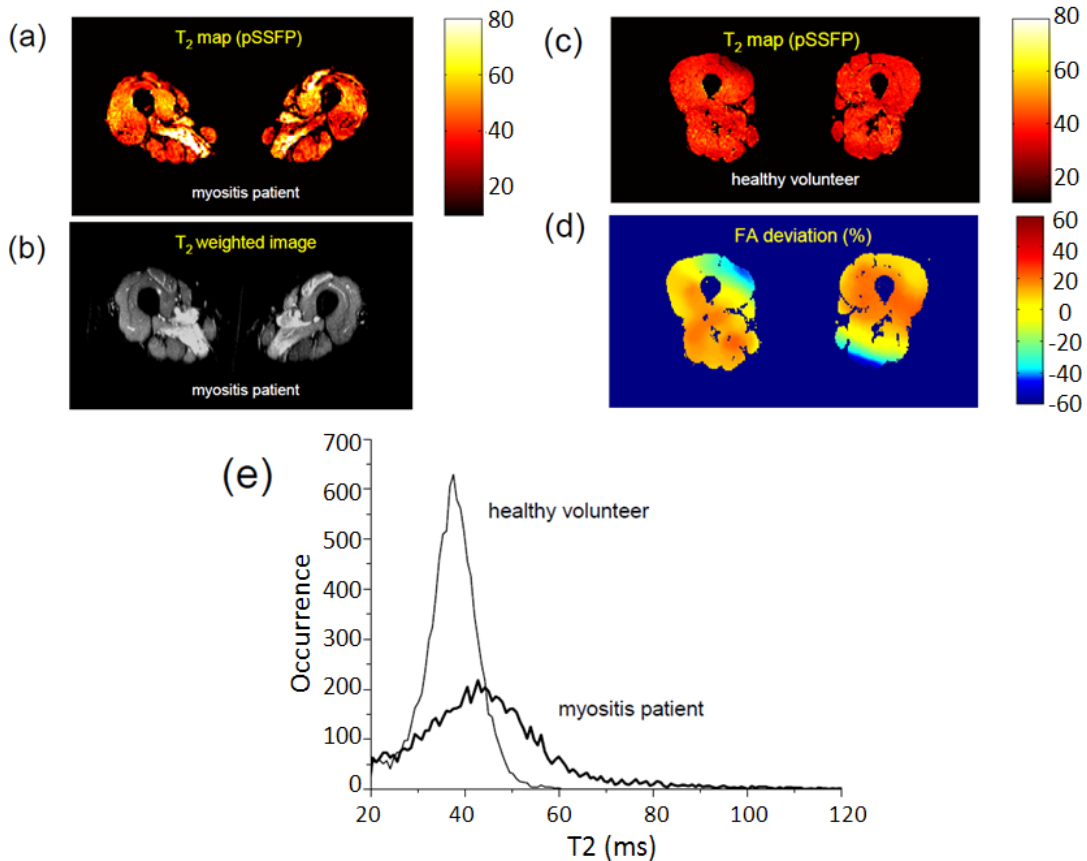


Figure 4-8 - Axial T2-maps obtained from T2-pSSFP experiments carried out in a myopathic patient (a) and in a healthy volunteer (c). For comparison, a fat-suppressed T2-weighted image from the same patient is displayed in (b). An FA deviation map measured in the volunteer is also shown to illustrate the asymmetric B_1+ inhomogeneity in the thighs (d). Histograms extracted from T2-maps are shown in (e). A homogeneous distribution of T2-values, centered on 37 ms, is observed for the healthy volunteer (thin line), whereas for the patient (thick line), median T2 is shifted to 44 ms. Note regions of increased T2 (up to 180 ms) in the patient, reflecting muscle edema. Experimental pSSFP parameters were: in-plane resolution = $1.4 \times 1.4 \text{ mm}^2$, slice thickness = 5 mm, 64 slices, $\alpha = 60^\circ$, $\phi_1 = 1^\circ$ and 15° , TR/TE = 6.3/2.8 ms, NEX = 1. Total T2-pSSFP acquisition time was ~ 3 min. T2-maps were corrected for B_1+ inhomogeneities and T_1 . SNR_1 was higher than 50 for all analysed muscles. Relevant experimental parameters for T2w imaging were: TR = 3 s, TE = 45 ms, Turbo-factor = 2 ms, in-plane resolution = $1 \times 1 \text{ mm}^2$, 27 slices, slice thickness = 5 mm, slice gap = 5 mm, acquisition time ~ 5 min.

4.4. Discussion

The aim of this study was to investigate all experimental (α , ϕ , SNR) and tissue (T_1 , T_2) parameters affecting the accuracy and precision of T2-mapping with the T2-pSSFP technique. Analysis of the pSSFP equation allowed us to introduce a novel approach that takes into account the $(T_1/T_2)/\eta$ dependence of the T2-pSSFP measurements. In contrast to the original approach (87), which imposes T_2/T_1 ratio and the use of large FA as a prerequisite to eliminate T_1 dependence in Eq. 4.4 the herein presented method extends the application of the T2-pSSFP technique to lower FA and higher T2/T1 ratios. This is of importance because SAR concerns may put some constraints on the choice of large FA on clinical scanners, particularly at high field strengths, and the condition $(T_1/T_2)/\eta \gg 1$ might not be respected for tissues with small T_1/T_2 ratios. Moreover, SNR is reduced when large FAs are used, affecting accuracy on T_2 .

Compared to the iterative algorithm recently introduced in (80) our method is computationally advantageous because estimation of T_2 is directly performed using Eq. 4.9, without needed of a starting value for T_2 and without time-consuming iterations.

Bloch simulations made possible an accurate prediction of pSSFP signal and derived measurements of T_2 . They also helped to establish the limits in the approximate pSSFP model, particularly dependencies on α and ϕ .

Simulations and experiments both show that for tissues with $T_1/T_2 \geq 10$, Eq. 4.9 yields an accurate result for T_2 provided that T_1 is known. These results were obtained assuming perfect FA. For in vivo experiments at 3T, FA deviations up to 40% were observed in phantom and in human thigh. Experimental and numerical simulations indicated that without FA correction, relative T_2 error can reach 40% or more in the regions where B1 field is very inhomogeneous. In this study, taking into account the measured FA distribution across the volume of interest resulted in an important improvement in T_2 accuracy and precision.

A potential objection to or limitation of the novel T2-pSSFP approach is the requirement for T_1 to be known. For homogeneous tissues, if a single T_1 is expected, an average T_1 value can be applied in Eq. 4.9. For heterogeneous tissues, rapid 3D mapping of T_1 can be carried out using the variable flip angle method (VFA) (81). It has been demonstrated that B1+ inhomogeneity, inefficient RF spoiling and low SNR may reduce the accuracy and precision of T_1 measurements derived from VFA experiments (Preibisch & Deichmann, 2009; Cheng & Wright, 2006; Schabel & Morrell, 2009). In order to take into account any potential discrepancy between true and apparent T_1 , the impact of T_1 error on T_2 measurements was analyzed. Fig. 3 shows that sensitivity to T_1/T_2 is a function of

(T_1/T_2) and α . For tissues with $T_1/T_2 \sim 10$ (e.g., white and gray matter at 1.5T), sensitivity to T_1 is low for large FA. As example, setting $\alpha = 60^\circ$, a precision of 5% in T_2 can be obtained for these tissues if uncertainty (or systematic error) in T_1 is lower than 20%. For tissues with $T_1/T_2 \gg 1$ (e.g., muscle at 3T) measurement of T_2 is practically insensitive to errors in T_1 for $\alpha \geq 60^\circ$.

A practical demonstration of our technique was given in human skeletal muscle imaging at 3T. In healthy muscles, T_2 -measurements obtained from pSSFP experiments agreed well with literature values. FA correction and relatively high SNR resulted in low scatter on T_2 -values.

In vivo experiments demonstrated that T_2 -pSSFP was sensitive enough to detect the long-term and selective pattern of changes in muscle T_2 following eccentric exercise. Although we can only speculate about the mechanism behind these changes in T_2 , since no blood analysis or muscle biopsies were carried out, other studies have identified it as an indicator of systemic inflammatory response (102, 103). It is well documented that eccentric contractions are related to muscle damage and delayed muscle soreness (104). In our study, muscle soreness peaked between 2 and 4 days post-exercise and gradually disappeared afterwards, suggesting a reduction in inflammatory activity.

T_2 -pSSFP was also used to assess muscle damage in a severe form of necrotizing myopathy. Severely inflamed and/or oedematous muscle regions, which were well detected by fat-suppressed T_2w imaging, were confirmed by T_2 -pSSFP mapping. However, other areas, in which T_2 -pSSFP pointed to a significant increase in T_2 , just appeared normal on T_2w images. This indicates that simple visual analyses cannot properly assess the subtle changes in contrast between normal and moderately inflamed and/or oedematous muscle. This is a typical example of the many situations where quantitative evaluation of T_2 will provide greater sensitivity in the detection of muscle damage than the subjective evaluation of T_2w images. The same will hold true for segments with uniform inflammation, which would go unnoticed on T_2w images but which would be detected with T_2 -pSSFP.

4.5. Conclusion

In summary, we have performed a comprehensive analysis of the T_2 -pSSFP method. The impact of each experimental and tissue parameter on the estimation of T_2 was identified, allowing for practical sequence optimization for in vivo applications. T_2 -pSSFP demonstrated robustness to B_0 inhomogeneities and efficient correction to FA errors, two essential characteristics for quantitative imaging at high field strength.

In contrast to the MSE-based T2-mapping method presented in chapter 3, the extended T2-pSSFP method presents a simpler post-processing, the possibility for correction of FA-related errors on T2 measurements and much better volume coverage without the need of inter-slice gaps. Although no information about fat fraction is offered, T2-pSSFP is compatible with spectral water selective excitation, which is a simple and robust method for isolating only signal contributions from water protons.

High resolution 3D T2-maps of human skeletal muscle were obtained in a clinically acceptable examination time (< 10 min for 1.2 mm isotropic acquisition). Because T2-pSSFP is compatible with larger geometry, parallel NMRI acceleration and fat-suppression techniques, including the 3pt-Dixon approach (see 3.2.1), it is expected that this method can improve the use of quantitative imaging in the studies of muscular dystrophies and inflammatory myopathies.

APPENDIX

Starting from Eq. 4.9 we can write the error in estimation of T_2 ($\Delta T_2 = \hat{T}_2 - T_2$) corresponding to the error in T_1 (ΔT_1) as

$$\Delta T_2 = \frac{a \cdot \hat{T}_1}{\hat{T}_1 - a \cdot b} - \frac{a \cdot T_1}{T_1 - a \cdot b} \quad (\text{A1})$$

where \hat{T}_i corresponds to the biased estimation of the relaxation time T_i , $a = T_2^{\text{estim}}$ and $b = (3/2)\eta$. Then

$$\begin{aligned} \frac{\Delta T_2}{T_2} &= \left(\frac{a \cdot \hat{T}_1}{\hat{T}_1 - a \cdot b} - \frac{a \cdot T_1}{T_1 - a \cdot b} \right) \bigg/ \frac{a \cdot T_1}{T_1 - a \cdot b} \\ &= \frac{a \cdot b \cdot T_1 - a \cdot b \cdot \hat{T}_1}{(\hat{T}_1 - a \cdot b) \cdot T_1} \\ &= -b \cdot \left(\frac{\hat{T}_1 - T_1}{\hat{T}_1} \right) \cdot \frac{\hat{T}_2}{T_1} \\ &= -b \cdot \left(\frac{\hat{T}_2}{\hat{T}_1} \right) \cdot \frac{\Delta T_1}{T_1} \end{aligned} \quad (\text{A2})$$

The fractional uncertainty in T_2 can therefore be written as

$$\frac{\Delta T_2}{T_2} = -(3/2)\eta \left(\frac{\hat{T}_2}{\hat{T}_1} \right) \cdot \frac{\Delta T_1}{T_1} \quad (\text{A3})$$

CHAPTER 5

Significance of T2 Relaxation of ^1H -NMR Signals in Human Skeletal Muscle

5.1. Relaxation in biological tissues

In the chapter 1 we highlighted the importance of detecting inflammation which, in contrast to fatty infiltration, may be indicative of early stages of disease activity, and relies on the possibility of detecting alterations in the T2-relaxation of the tissue. In chapters 3 and 4 we presented and validated two methodologies for extraction of T2-maps and detection of inflammation sites in skeletal muscle. However, muscle water T2-value as measured by NMRI techniques has been shown to be elevated in different pathological scenarios such as necrosis, intracellular and/or interstitial oedema (Jong et al. 2011; de Sousa et al. 2012; Arpan et al. 2013), thus leading to a lack of specificity of T2 measurements with NMRI methods to the underlying mechanisms responsible for the observed abnormal tissue relaxation. It follows that the development of techniques that might offer more specific characterization of SKM tissue alterations relies on the understanding of the mechanisms controlling proton relaxation in SKM.

In chapter 2 we introduce the idea of relaxation and how it reflects the interactions of the studied nuclei with its neighbouring atoms and molecules. Biological tissues are chemically and structurally heterogeneous so that diffusing water molecules experience a wide variety of environments and chemical species with which interact. This complex interactive dynamics affects the local dipolar fields experienced by water protons in many different ways. This is evidenced at first by the increased relaxation rates of tissue water relative to pure water. Studies in macromolecule solutions show that the T2-relaxation rate increases, in general linearly, with solute concentration (105–107). However, it has been verified that the relaxation rate per concentration of solid content in tissue is significantly greater than for isolated protein solutions (Gore et al. 1986; Zhong et al. 1990). This

indicates that although part of the alterations on tissue water relaxation behaviour may be reproduced with macromolecule solutions, these models are incomplete. Nonetheless, T₂-relaxation behaviour closer to that of tissue has been observed in gel-like solutions, in which proteins and biopolymers become more organized and structured (109). This further indicates that observed tissue water relaxation shall be influenced by the tissue ultrastructural organization. Besides that, biological tissues are histologically organized into chemically and structurally different compartments that may present restricted water diffusion and exchange.

In tissue, water molecules are expected to be found in two distinct environments: (i) in absorbing sites on relatively immobile macromolecular constituents such as hydroxyl and amine groups, that present strong electrostatic dipole-dipole interactions with hydrogen atoms in water molecules, usually referred to as “bound water” or “hydration water” and; (ii) in a so called bulk aqueous phase, which is distant enough from this constituents (more than one water molecule radius) and shall present hydrogen bonding characteristics similar to pure water. The magnetic dipolar interactions experienced within each of these environments are different. Bound water may experience intermolecular magnetic dipolar interactions with protons and nitrogen nuclei at the surface of macromolecules or even exchange protons with labile groups at the surface (110). In addition, the correlation times for the hydrogen atoms in bound water may be largely increased because of the much more restricted movement of large molecules. This will result in significant increase of relaxation rates of bound water. This increase in relaxation rate may propagate through the sample by proton exchanges between bound and bulk water pools, affecting the entire tissue relaxation.

5.2. Multiexponential muscle water T₂-relaxation and compartmentation hypotheses

Proton spin-spin relaxation in skeletal muscle tissue has been shown to be multi-exponential. Three exponential components are systematically observed in ex-vivo and in-vivo studies (106, 109, 111–116); a “short” one ($T_2 < 10$ ms) accounting for less than 15% of the signal, an “intermediate” component ($20 < T_2 < 50$ ms accounting for 75 to 95%, and a “long” one ($T_2 > 100$ ms) accounting for less than 15% of the observed signal. There is general agreement that the “short” component correspond to signal from protons in the hydration water pool, although some authors have attributed part of it to non-rigid protons in organic molecules. The “intermediate” and “long” T₂-components are both attributed to the bulk water pool. Interpretation of this biexponential behaviour of bulk water is not yet consensual (112, 113). One hypothesis states that it reflects distribution of myowater in

different anatomical compartments having intrinsically different transverse relaxation rates (111, 112) determined by compartment-characteristic magnetization transfer processes. These anatomical compartments are supposed to be in slow enough water exchange regimes such that separate T2-components become observable. The other hypothesis states that it must be a consequence of the complex magnetization transfer processes taking place at various intermediate rates within the same microscopic compartments, thus discarding any direct attribution of the observed “intermediate” and “long” T2-components to specific anatomical compartments (113).

Although further experimental support for the anatomical compartmentation theory has been provided in previous studies (106, 114, 117, 118), distinct interpretations of these results still emerge, in which the “intermediate” and “long” components have been attributed respectively to: (I) intra and extra-cellular water (111, 112), assuming that T2-relaxation from both interstitial and vascular spaces are described by the “long” component; and (II) extra and intravascular water (114, 118, 119); assuming that relaxation from both intracellular and interstitial spaces are described by the “intermediate” component. The first hypothesis (I) was based on the observation of the similarities between the relative fractions of the T2-components with previous relative volume estimations of intra- and extracellular spaces (2, 3). Furthermore, it relies on the suppositions that: transcytolemmal water exchange is sufficiently slow to allow observing separated T2-components for each of these spaces and; the interstitial T2-value is much longer than intracellular T2 due to the lower macromolecular content of the interstitium. The second hypothesis (II) was based in later studies showing that changes in microvascular volume correlate with changes in the relative fraction of the “long” component (114), and that its T2-value correlates with the level of blood O₂ saturation (118, 119), which is known to correlate with blood T2. Furthermore, both “intermediate” and “long” T2-values were reduced after intravenous administration of gadolinium diethylenetriaminepentaacetate (GdDTPA) (117). GdDTPA is a paramagnetic contrast agent that increases local relaxation rates and distributes exclusively within the interstitial and vascular spaces, so that the reduction of the “intermediate” component shall be explained by inclusion of the interstitium.

The potential applications of a non-invasive tool that offers information about histological compartmentation of myowater urge the quest for a definitive answer to this question. The purpose of the work described in this chapter was to obtain new information that might help elucidating the matter concerning the interpretation of T2-relaxation measurements in SKM tissue and to verify the potential applications of the proposed method in the clinical field of NMD.

5.3. New insights on human skeletal muscle tissue compartments revealed by in vivo T2-relaxometry

Extraction of T2-spectra from relaxation data, usually referred to as T2-deconvolution, constitutes an inverse Laplace transform problem. T2-deconvolution of noisy data is a mathematical ill-posed problem, which makes the precision and confidence of T2-spectra measurements highly dependent on the quality of the data, as reflected by *SNR* and echo-time sampling. These conditions are not attained with currently available NMRI techniques and in vivo multi-T2-relaxation studies are done with methods that combine the basic spectroscopic CPMG sequence with volume selection techniques. In vivo applications of a localized CPMG technique confirmed the multiexponential behaviour of T2-relaxation in skeletal muscle (115, 120–122). In the following sections of this chapter we will describe the implementation of a technique that allows acquisition of localized T2-relaxation data, and the methodology for the extraction of corresponding T2 spectra. The results are analysed on the bases of compartmental exchange theory in order to investigate the impacts of exchange processes on skeletal muscle T2-relaxation behaviour and to further elucidate the corresponding histological interpretation.

5.3.1. Methodology

5.3.1.1. Data acquisition

A CPMG (49, 50) sequence was implemented on a 3 teslas whole-body scanner (Tim Trio, SIEMENS Healthcare, Erlangen, Germany). Magnetization excitation and refocusing were performed with a 250 and a 500 μ s hard pulses, respectively. Spatial localization was accomplished with the Image-Selected In vivo Spectroscopy (ISIS) localization technique (123). ISIS was selected because it is the localization technique that allows acquisition with the shortest possible echo-time. In ISIS, complete selection of a rectangular volume of interest (VOI) is accomplished after 8 acquisitions. The VOI is defined by the intersection of 3 orthogonal slices which are selectively inverted following an eight step combination (Figure 5-1). The signal from the VOI is isolated by specially combining the eight acquisitions.

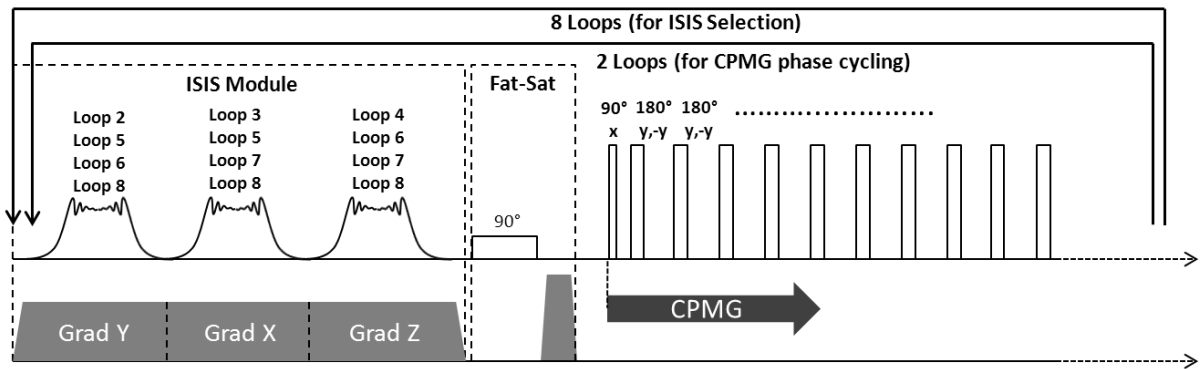


Figure 5-1- RF-pulse and B_0 gradient time sequence diagram representing the implemented ISIS-CPMG method. In the ISIS module adiabatic inversion pulses are selectively turned on following an 8 steps combination as indicated. Fat saturation is accomplished with a 90° hard pulse with 1.5 ms long 90° hard pulse centred at -432 Hz from water proton frequency, and is launched just after each of the ISIS steps. CPMG pulse train is launched 2 ms after the Fat-Sat module.

ISIS was implemented using an adiabatic quadratic phase inversion pulse of 8 ms with 10 kHz of selection bandwidth (BW), which was designed using the Shinnar-Le Roux algorithm (124, 125). Figure 5-2 presents the plot the x and y components of the designed RF- B_1 field wave form and the simulated 20 mm slice profiles for a short and a long T_2 -species characterized by T_1 - and T_2 - values observed in previous in-vivo studies (Araujo et al. 2011; Gold et al. 2004).

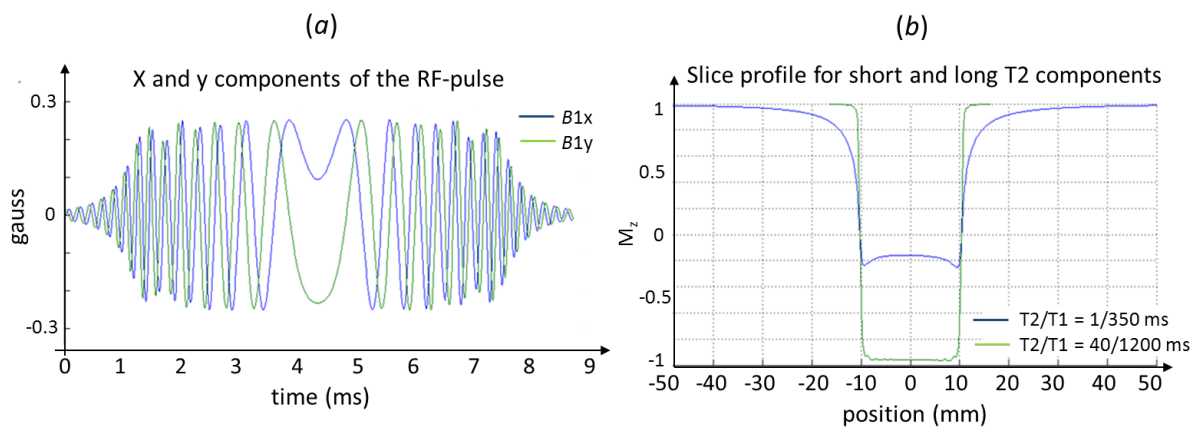


Figure 5-2 – (a) plot the x and y components of the designed RF- B_1 field wave form and (b) the simulated 20 mm slice profiles for short and long T_2 -species. Short T_2 -species are characterized by $T_2/T_1 = 1/350$ ms, and long T_2 -species were characterized by $T_2/T_1 = 40/1200$ ms.

As previously discussed in chapter 3, lipids present a different T_2 -decay than water and, as a consequence, signal contributions from lipids must be suppressed. In order to avoid contamination by signal from intramuscular lipids, a fat saturation module was applied after each of the ISIS steps. Fat saturation was performed with a 1.5 ms long 90°

hard pulse centred at -432 Hz from water proton frequency followed by a spoiler gradient. CPMG pulse train was applied 2 ms after the Fat-Sat module (Figure 5-1).

At each loop, 1000 echoes were acquired with an inter-echo spacing (echo-time) of 1 ms. The repetition time between each loop was 18.75 s, long enough to allow for complete longitudinal magnetization recovery. Full BW was 320 kHz and each echo was composed of 64 pts. In order to avoid contamination from unwanted FID signal coming from imperfect refocusing, each CPMG acquisition was repeated once with application of 180° phase shift on the refocusing pulses, so that FID signals cancelled out after summation of the two acquisitions (Figure 5-3). Such a method is largely used in NMR techniques and is usually referred to as phase cycling.

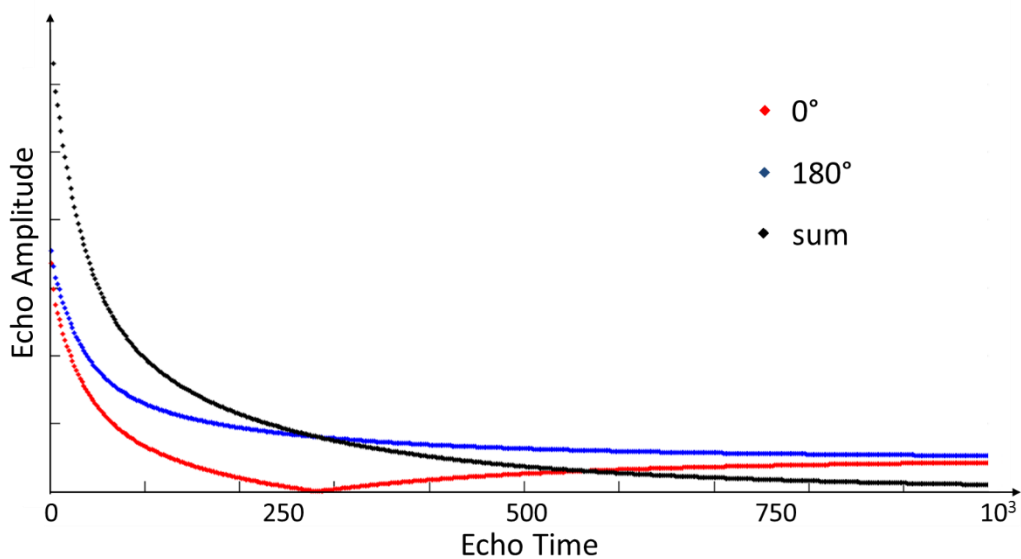


Figure 5-3 – *Experimental demonstration of CPMG phase cycling. Plots of echo amplitude vs. echo-time resulting from two CPMG acquisitions with opposed refocusing pulse phases (red and blue). Note that after summation (black), FID signal contributions cancel out and signal amplitude approaches zero asymptotically.*

Total acquisition of a localized T₂-decay curve took 5 min. Only even echoes were used as data, resulting in a T₂-decay observation window of 1s sampled at 500 Hz. The amplitude of each echo was given by the average amplitude of its 20 central points. RF-pulse transmission and detection was performed with a cylindrical mono-channel birdcage transceiver coil (QED CP-extremity, Siemens Healthcare, Erlangen, Germany).

T₂-spectra were extracted from a rectangular volume of interest (VOI) localized within the right soleus of 8 healthy volunteers (age 36.5±11.6 years) under 3 different vascular preparation conditions:

Vascular draining:

- In step1: Manual compression of the calf from foot to thigh by means of a medical compression band (Figure 5-4).
- In step2: Inflation of a cuff wrapped around the thigh at 250 mmHg to completely block both arterial inflow and venous outflow.
- In step3: release of the medical compression band while keeping the cuff inflated.

Vascular filling:

- Cuff pressure is decreased from 250 to 60 mmHg in order to block the venous outflow only and to fill the capacitance vessels;

Normal condition:

- Release the cuff.



Figure 5-4 – Picture of a subject’s leg, placed on the inferior half of the transceiver coil, after step 1 of the vascular draining procedure. Note the cuff wrapped around the thigh.

Appropriate signed informed consent was obtained from all subjects. The protocol was conceived in such a way as to allow the application of different vascular conditioning without any need of moving the subject inside the coil or the magnet from one condition to another. The cuff pressure was controlled and monitored from outside the examination room. The protocol timeline is presented in Figure 5-5. With the patient in “supine foot first” position and its calf centred in the transceiver coil, the vascular draining procedure was started. A T1-weighted FLASH sequence gave anatomical reference images. The VOI was carefully positioned within the soleus excluding any visible blood vessels and fascia. The average size of VOI was 52 cm³. The first ISIS-CPMG acquisition was then launched. Once the acquisition was finished, the cuff pressure was reduced from 250 to 60 mmHg and a 5 min period was allowed to attain equilibrium for the vascular filling condition. At this point the second ISIS-CPMG was acquired. Once it was completed, the cuff pressure was fully released to resume normal conditions and the last ISIS-CPMG was launched

after another 5 min break.

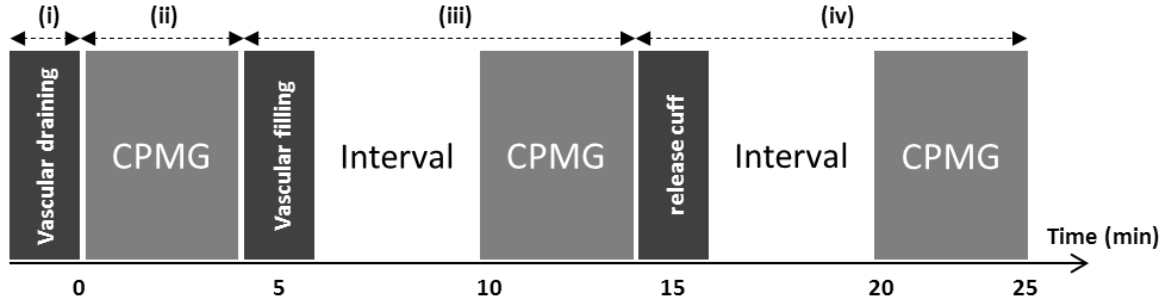


Figure 5-5 - Protocol timeline for the T2-spectra acquisitions at different vascular filling conditions: (i) With the patient in « supine, foot first » orientation, and its calf positioned in the transceiver coil, the vascular draining procedure was first applied; (ii) Localized CPMG signal was acquired with the VOI located within the soleus during 5 min; (iii) Vascular filling step is performed and another CPMG acquisition of 5 min is launched over the same VOI after a 5 min interval; (iv) Pressure is released from the cuff and another CPMG acquisition of 5 min is performed over the same VOI after a 5 min interval.

5.3.1.2. Data treatment

T2 deconvolution

Acquired T2-relaxation decay curves might be analytically described by

$$y(t) = \int_0^{\infty} p(T) e^{-\frac{t}{T}} dT + \varepsilon(t) \quad 5.1$$

where $y(t)$ is the echo amplitude at time t , $p(T)$ is the fraction density of the magnetization characterized by a decay constant $T_2 = T$, and $\varepsilon(t)$ is the experimental error usually reflecting the noise on the acquired data. A discrete approach to Eq. 5.1 is given by

$$y(t_n) = \sum_{m=1}^M p_m e^{-\frac{TE_n}{T_{2,m}}} + \varepsilon(TE_n) \quad 5.2$$

where p_m is the relative fraction of protons with a decay constant $T_2 = T_{2,m}$, and $n = 1, 2, \dots, N$ in which N is the number of observations (number of echoes). Eq. 5.2 may be written in the matrix form

$$Y = A \times P + E \quad 5.3$$

where Y is a $(N \times 1)$ vector containing the echo amplitudes $y(TE_n)$, P is a $(M \times 1)$ vector containing the values p_m , A is a $(N \times M)$ matrix with elements $A_{n,m} = e^{-\frac{TE_n}{T_{2,m}}}$, and E is a $(N \times 1)$ vector containing the values $\varepsilon(TE_n)$.

Conversion of the noisy relaxation data, Y , into a continuous distribution of relaxation times, P , is an ill-posed inverse Laplace transform (ILT) problem, even for $N > M$, and robust noise-free solutions are usually obtained by regularized inversion methods (126). One possible solution for the system described by Eq. 5.3 may be obtained by solving the following minimization problem:

$$\min_{P \geq 0} \{ \|Y - A \times P\|_2 + \alpha \|P\|_2 \} \quad 5.4$$

where α is the L_2 -norm regularization parameter, which controls the smoothness of the solution, eliminating non-representative values on the solution vector P . We have solved the problem 5.4 for each set of data by using a non-negative least squares (NNLS) method. Observable T2-domain was defined as a vector of 499 logarithmically spaced values between 1 and 500ms. All data was treated using MATLAB (The MathWorks, Natick, MA, USA). Appropriate choice for the regularization parameter, crucial for obtaining accurate and stable solutions, was done using the L-curve criterion (127). The resulting fitted decay curve is then obtained by

$$Y_{fit} = A \times P \quad 5.5$$

Separated T2 peaks could be observed in each obtained T2 spectra, P , allowing to identify distinct T2-components. Separated T2-peaks were identified as the largest intervals $[P_{m_0}, P_{m_1}]$ in the solution vector, P , containing values higher than 10^{-4} . The corresponding T2-components were characterized by a relative fraction, \hat{P} , and a T2-value, \hat{T}_2 , given by

$$\hat{P} = \frac{\sum_{k=m_0}^{m_1} P_k}{\sum_{k=1}^M P_k} \quad 5.6$$

$$\hat{T}_2 = \frac{\sum_{k=m_0}^{m_1} P_k T_{2,k}}{\sum_{k=m_0}^{m_1} P_k} \quad 5.7$$

The T2-components with $\hat{P} < 2\%$, were considered spurious and were not taken into account.

On a second approach, data were fitted by means of least mean squares to a biexponential model, expected to identify and characterize the “intermediate” and “long” components observed in previous works.

Data fitting was initialized with the T2-values, \hat{T}_2 , and relative fractions, \hat{P} , characterizing the “intermediate” and “long” peaks from the corresponding previously obtained T2 spectra. Finally, all data were also fitted to a simple monoexponential decay model, in order to investigate the possible effects of the vascular filling preparations on the

monoexponential approach for T2 quantification in muscle.

Compartmental Exchange Analysis

Let's consider an isolated system of N exchanging pools characterized by intrinsic spin-spin relaxation times $T_{2,n}$ and equilibrium magnetizations $M_{0,n}$. Let τ_{ij} is the average time spent by a nuclear spin within the pool i before it transfers to the pool j. If P_n is the relative water fraction of the nth pool at equilibrium, then

$$\frac{P_i}{\tau_{ij}} = \frac{P_j}{\tau_{ji}} \quad 5.8$$

If the magnetization is excited, as by a CPMG RF pulse sequence, the time evolution of the transverse magnetization will be governed by a set of coupled ordinary differential equations, commonly referred to as the Bloch-McConnell equations (128), expressed as

$$\frac{dM_{\perp}(t)}{dt} = A \times M_{\perp}(t) \quad 5.9$$

where M_{\perp} is a $(N \times 1)$ vector, containing the transverse magnetization amplitudes from each pool, and A is a $(N \times N)$ matrix given by

$$A = \begin{pmatrix} -\frac{1}{T_{21}} - \sum_{i \neq 1} \frac{1}{\tau_{1i}} & \dots & \frac{1}{\tau_{N1}} \\ \vdots & \ddots & \vdots \\ \frac{1}{\tau_{1N}} & \dots & -\frac{1}{T_{2N}} - \sum_{i \neq N} \frac{1}{\tau_{Ni}} \end{pmatrix} \quad 5.10$$

Equation 5.9 admits a general solution given by

$$M_{\perp}(t) = T \times \begin{pmatrix} e^{\gamma_1 t} & \dots & 0 \\ \vdots & \ddots & \vdots \\ 0 & \dots & e^{\gamma_N t} \end{pmatrix} \times T^{-1} \times M_{\perp}(0) \quad 5.11$$

where γ_i are the eigenvalues of the matrix A and T is a $(N \times N)$ matrix whose columns are the corresponding eigenvectors. Equation 5.11 states that the magnetization from each pool evolves as a sum of N exponentials characterized by relaxation times $\hat{T}_i = -\frac{1}{\gamma_i}$ and relative fractions \hat{P}_i , which are themselves functions of the intrinsic properties of the system, $M_{0,i}$, $T_{2,i}$ and τ_{ij} . We shall refer to \hat{T}_i and \hat{P}_i as the apparent relaxation time and relative fraction of the observed pseudo compartment i . These pseudo compartments correspond to the T2-components that are characterized by T2 deconvolution of relaxation data, and may be interpreted as the constituents of a virtual non-exchanging system which presents T2-relaxation behaviour identical to that of the real exchanging system (Figure 5-6).

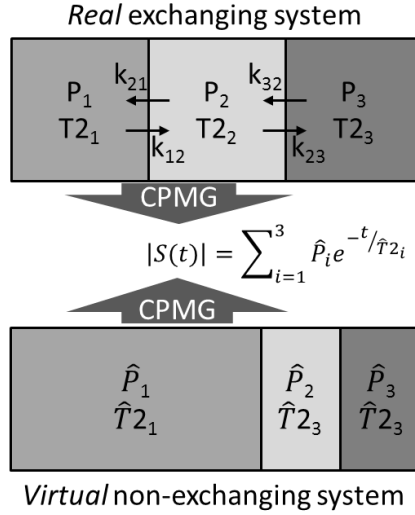


Figure 5-6 - Illustration of a virtual non-exchanging system that presents T2-relaxation behaviour identical to that of a real exchanging system. The apparent T2-values and relative fractions characterizing the pseudo compartments of the virtual system are functions of the intrinsic relative fractions, T2-values and exchange rates of the real system. In this case, a tri-compartmental two-exchange system with no direct exchange between compartments 1 and 3.

Finally, unknown intrinsic parameters characterizing the compartmental exchange system may be extracted by directly fitting the relaxation data by Eq. 5.11 (107). We have investigated two analytical compartmental exchange models as possible candidates for explaining the observed T2-relaxation behaviour: a two-site exchange (2SX) model, representing either an intra-/extracellular or an extra-/intravascular compartmental system; and a three-site two exchange (3S2X) model representing the histological compartmentation into intracellular, interstitial and vascular spaces, in which no direct exchange occurs between the vascular and intracellular spaces and the interstitial space works as a junction compartment, exchanging with both intracellular and vascular compartments. The matrices characterizing the 2SX and 3S2X models are given respectively by

$$A_{2SX} = \begin{pmatrix} -\frac{1}{T2_a} - \frac{1}{\tau_a} & \frac{1}{\tau_b} \\ \frac{1}{\tau_a} & -\frac{1}{T2_b} - \frac{1}{\tau_b} \end{pmatrix}$$

$$A_{3S2X} = \begin{pmatrix} -\frac{1}{T2_i} - \frac{1}{\tau_i} & \frac{1}{\tau_{ei}} & 0 \\ \frac{1}{\tau_i} & -\frac{1}{T2_e} - \frac{1}{\tau_{ei}} - \frac{1}{\tau_{ec}} & \frac{1}{\tau_c} \\ 0 & \frac{1}{\tau_{ec}} & -\frac{1}{T2_c} - \frac{1}{\tau_c} \end{pmatrix}$$

For the 2SX model, τ_a and τ_b represent the average time spent by a nuclear spin within the compartments a and b , respectively, before it exchanges, and are usually referred to as residence times. In the 3S2X model, τ_{ei} and τ_{ec} represent the average time spent by a nuclear spin within the interstitial space before it transfers to intracellular and vascular spaces, respectively, while τ_i and τ_c correspond to the intracellular and intravascular residence times, respectively. In order to check if the observed relaxation behaviours for the different vascular filling condition could be explained by the proposed models we have proceeded as follows: at first, characteristic relaxation curves for each vascular filling condition were defined as

$$y(t) = \hat{P}_i e^{-\frac{t}{\hat{T}_i}} + \hat{P}_l e^{-\frac{t}{\hat{T}_l}} \quad 5.12$$

where, \hat{T}_i , \hat{T}_l and \hat{P}_i , \hat{P}_l are the mean observed “intermediate” and “long” T2-values and corresponding relative fractions obtained from the biexponential fitting between volunteers for each vascular filling condition; finally, the characteristic curves were fitted by means of least means squares to the right side of Eq. 5.11.

The 2SX and 3S2X models were constrained based on the results of previous works that studied relative fractions and residence times of tissue compartments. For the 2SX model, the intrinsic T2-values and relative fractions were estimated for exchange regimes characterized by residence times τ_a , set to 1 and 10 s respectively, and with $T2_b < 500$ ms. For the 3S2X model, the intracellular residence time was set to 1 s and the vascular T2 was set to the T2-value of the blood, $T2_b = 186$ ms, as determined from CPMG data acquired with the same echo time (129). Interstitial and vascular relative fractions, interstitial T2, intravascular residence time and intracellular T2 were estimated within the predefined intervals $7 < P_e < 12\%$, $1 < P_c < 15\%$, $10 < T_e < 186$ ms and $150 < \tau_c < 10^4$ ms and $10 < T_i < 100$, respectively. The intracellular T2 was only estimated for the vascular draining condition and then set at the same value for the others. Each set of data was fitted with different sets of initial values chosen at the limits of each predefined interval in order to identify possible convergence to local minima.

5.3.2. Results

Examples of obtained T₂-decay curves for each of the vascular filling conditions, and the corresponding obtained T₂-spectra from the regularized inversions are presented in Figure 5-7. The continuous lines through the decay points (Figure 5-7 a) correspond to the fitted curves. Two separated T₂-peaks are clearly identified for each spectrum in Figure 5-7 b.

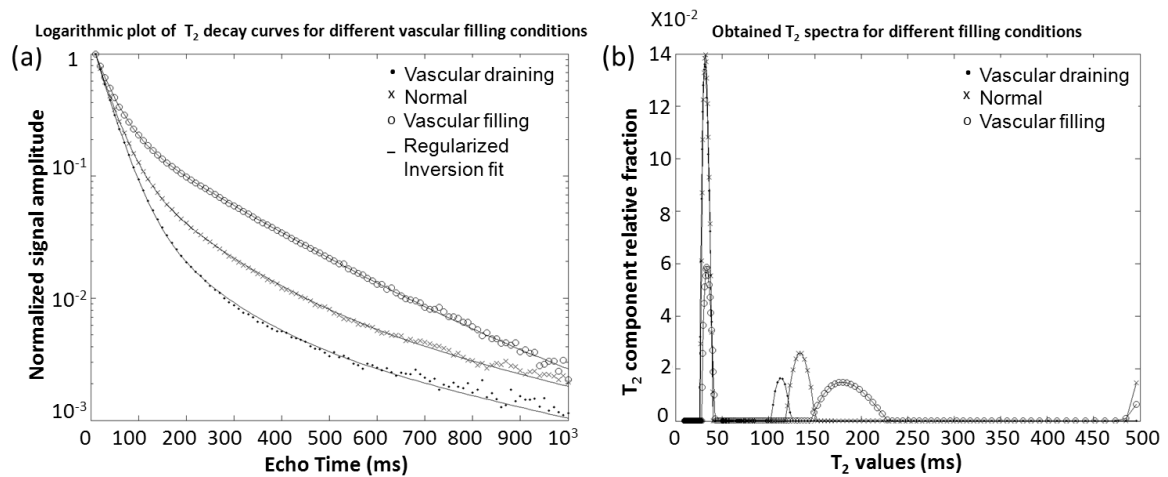


Figure 5-7 - (a) Plot of T₂-decay curves obtained for a subject under different vascular filling conditions. The lines passing through the points correspond to the fitted curves resulting from the regularized inversion solution, and (b) presents the corresponding obtained T₂-spectra.

All mono- and biexponential fits converged and the results are presented in Table 5-1, along with the results from Eqs. 5.6 and 5.7 characterizing the T₂-spectra resulting from the regularized inversions. Results are expressed by means of average and standard deviation of the relative fractions and corresponding T₂-values between subjects for each vascular filling condition.

Table 5-1 - Results obtained from the mono- and biexponential fits and regularized Laplace inversions for the relative fractions and corresponding T2-values, by means of mean(SD), between subjects for each vascular filling condition.

Vascular condition		Monoexp. model	R^2 ($\times 10^{-3}$)	Biexponential model		R^2 ($\times 10^{-4}$)	Regularized Inversion		R^2
				intermediate	long		intermediate	long	
Vascular draining	Rel. Frac. [%]	-	998(1)	94.6(1.5)	5.4(1.5)	9999(1)	96.0(2.1)	4.0(2.1)	1(0)
	T2 [ms]	35.3(1.8)		31.7(0.5)	139(23)		32.6(0.6)	119(24)	
Free perfusion	Rel. Frac. [%]	-	997(2)	92.0(2.4)	8.0(2.4)	9999(1)	92.8(2.7)	7.2(2.7)	1(0)
	T2 [ms]	38.1(2.4)		32.1(0.4)	159(25)		32.8(0.4)	132(24)	
Vascular filling	Rel. Frac. [%]	-	993(7)	85.8(4.7)	14.2(4.7)	9999(2)	86.7(4.9)	13.3(4.9)	1(0)
	T2 [ms]	45.8(6)		32.6(0.7)	181(20)		33.4(0.9)	176(28)	

The results for the estimated intrinsic parameters of the 2SX system for the three vascular filling conditions at transcytolemmal and transendothelial exchange regimes are presented in Table 5-2. All the different initializations converged to the same minimum.

Table 5-2 - Extracted intrinsic parameters of the 2SX model for the three vascular filling conditions at transcytolemmal and transendothelial exchange regimes; SE is presented within brackets.

τ_i [s]	Vascular condition	P_a [%]	$T2_a$ [ms]	$T2_b$ [ms]	R^2 ($\times 10^{-3}$)
1	Vascular draining	92.7(2.5)	30.0(0.5)	500(1216)	999.8
	Free perfusion	90.2(1.0)	30.1(0.3)	500(312)	999.6
	Vascular filling	85.2(0.5)	30.5(0.2)	500(81)	999.4
10	Vascular draining	95.4(0)	31.8(0)	195.2(0)	1000
	Free perfusion	92.8(0)	32.2(0)	199.5(0)	1000
	Vascular filling	86.5(0)	32.7(0)	204.6(0)	1000

The characteristic relaxation curves for the three vascular filling conditions, defined with Eq. 5.12, and the corresponding fitted curves characterized by the extracted intrinsic parameters of the 2SX model for both transcytolemmal and transendothelial exchange regimes are presented in Figure 5-8.

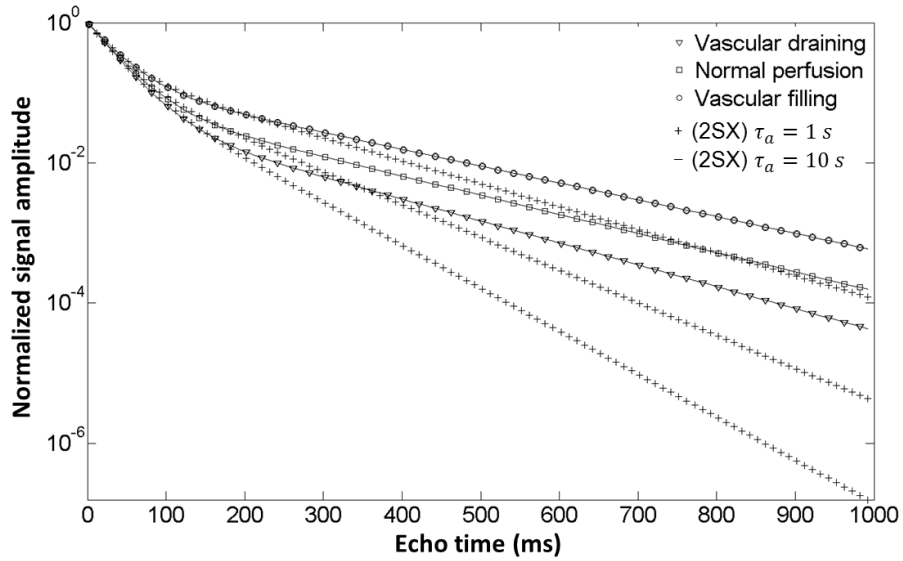


Figure 5-8 - Characteristic relaxation curves of the vascular draining (triangles), normal (squares) and vascular filling (circles) conditions, and the corresponding fitted curves characterized by the extracted intrinsic parameters of the 2SX model for both transcytolemmal (crosses) and transendothelial (lines) exchange regimes.

The results for the estimated intrinsic parameters of the 3S2X system, characterizing the intracellular, interstitial and vascular spaces are presented in Table 5-3. All the different initializations converged to the same minimum.

Table 5-3 - Extracted intrinsic parameters of the 3S2X system characterizing the intracellular, interstitial and vascular spaces for the three vascular filling conditions; SE is presented within brackets.

Vascular condition	P_c [%]	P_i/P_e	$T2_i$ [ms]	$T2_e$ [ms]	τ_c [ms]	R^2
Vascular draining	4.6(0)	12.7(0.3)	31.5(0)	35.8(1.0)	535(5)	1
Free perfusion	7.3(0)	6.73(0.04)	31.5	37.4(0.3)	1122(3)	1
Vascular filling	13.8(0)	6.18(0.04)	31.5	41.1(0.5)	9813(333)	1

The fitted characteristic relaxation curves with the 3S2X model are presented in Figure 5-9 a. Figure 5-9 b presents the corresponding obtained T2-spectra from regularized inversion of the fitted curves.

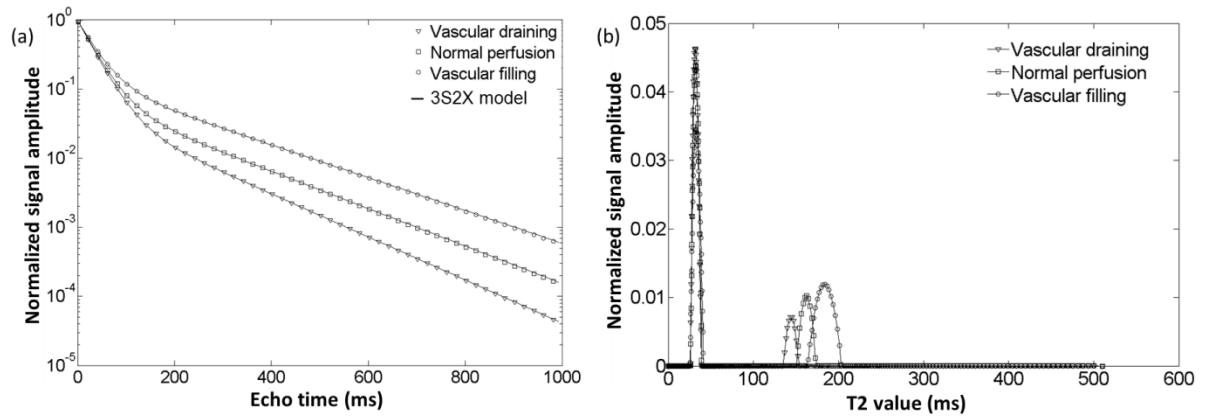


Figure 5-9 - (a) Characteristic relaxation curves of the vascular draining (triangles), normal (squares) and vascular filling (circles) conditions, and the corresponding fitted curves (lines) characterized by the extracted intrinsic parameters of the 3S2X model; (b) Obtained T2-spectra from regularized inversion of the fitted curves resulting from the 3S2X model.

5.3.3. Discussion

In contrast to previous relaxation studies in muscle, no “short” component was observed in the present study. This may be explained by differences related to the RF-pulse sequence and the methodology applied for data treatment. The RF-pulses of the ISIS module were too long to be efficient over the short-T2-components (130). This resulted in decreased contributions of the already small fraction of these “short” components, which have probably been completely filtered out of the T2-spectra by the regularization. No special attention was dedicated to this fact in this work that focused on the origin of the longer T2 fractions.

Results from the monoexponential fittings showed a systematic increase of the observed T2-values following progressive vascular filling (Table 5-1). This result confirmed the importance of extracellular water content on T2-relaxation of muscle tissue as measured by monoexponential approaches.

The T2-spectra obtained with the regularized inversion method systematically presented 2 relevant ($\hat{P} > 2\%$) T2-components characterized by T2-values and relative fractions that correspond to the “intermediate” and “long” components also observed in previous studies (Figure 5-7). This demonstrated the reproducibility of the methodology and supported the approach of a bi-exponential fit to analyse our data. Additionally, the results obtained from both methods were quite similar (Table 5-1). The vascular filling preparations impacted exclusively the “long” T2-component, whose relative fraction and value systematically increased following progressive augmentation of the extracellular space. These were strong evidences in favour of the anatomical compartmentation

hypotheses. Deeper analysis of the compartmental exchanges is needed in order to elucidate the histological interpretation of this compartmentation. Our analyses showed that a 2SX model is only capable of explaining the observed relaxation data for slow exchange regimes (Figure 5-8). In previous studies investigating transcytolemmal water exchange, the intracellular residence time in muscle has been estimated between 550 and 1100 ms (24, 25) and, for such values, the observed T2-relaxation data cannot be explained with a 2SX model representing an intra-/extracellular compartmental model. However, intravascular residence times have been estimated between 0.3 and 3 s (131, 133, 134), and vascular water fraction shall be about 4% (1). For these values the extravascular residence time at homeostasis must be between 7 and 72 s (Eq. 5.8), which characterizes slow exchange regime. These evidences supported preferably an extra-/intravascular compartmental interpretation, suggesting that relaxation of transverse magnetization from both intracellular and interstitial spaces are described by the “intermediate” component. This implies that the apparent intracellular and interstitial T2-values, T_{ic} and T_{int} , shall be close enough to the observed “intermediate” T2. In order to investigate the intrinsic system parameters that might satisfy this condition, we have studied a system composed by the intracellular and interstitial spaces according to a 2SX model. The analytical solution of Eq. 5.9, for the apparent T2-values, $\hat{T}2_a$ and $\hat{T}2_b$, in the 2SX model has been previously presented by Hazlewood et al. (112) and is given by

$$\hat{T}2_a = \frac{1}{(C_1 + C_2)} \quad 5.13$$

$$\hat{T}2_b = \frac{1}{(C_1 - C_2)} \quad 5.14$$

with

$$C_1 = \frac{1}{2} \left(\frac{1}{T2_a} + \frac{1}{T2_b} + \frac{1}{\tau_a} + \frac{1}{\tau_b} \right) \quad 5.15$$

$$C_2 = \frac{1}{2} \left(\left(\frac{1}{T_a} - \frac{1}{T_b} + \frac{1}{\tau_a} - \frac{1}{\tau_b} \right)^2 + \frac{4}{\tau_a \tau_b} \right)^{1/2} \quad 5.16$$

The average observed interstitial to intracellular water volume ratio is around 0.13 (1, 2). Consequently, an intracellular residence time of 1 s would imply an interstitial residence time of 130 ms, at homeostasis. By applying these values into Eqs. 5.13-5.16, one may verify that for $T_{int} > 80$ ms, the apparent T2-values, $\hat{T}2_a$ and $\hat{T}2_b$, would differ by more than 20 ms, which should be easily resolved in the obtained T2-spectra, considering the precision of our results for the observed “intermediate” T2-peaks (Figure 5-7 b and Table 5-1). Usually, T_{int} is assumed to be considerably lengthened relative to the intracellular T2 due to the lower protein concentration in the interstitium. However, the

macromolecules constituting the extracellular matrix have been shown to have non-negligible relaxivities (105), and values as short as $T_{int} = 25$ ms have been observed for synthetic interstitial models (106). This was further confirmed by the observed short T2-value in muscle sites with abnormally high endomysial accumulation such as fibrosis (33), and the long T2-values characteristic of interstitial oedema (135).

The 3S2X model has been previously shown to allow more accurate estimates of extracellular and vascular spaces, and blood-to-tissue contrast agent transfer in pharmacokinetic studies (136). In the present work this model was shown to be capable of accurately predicting the characteristic relaxation curves for realistic physiological residence times (131–134) (Figure 5-9 and Table 5-3). The estimated interstitial T2-value lied within the range, $T_{int} < 80$ ms, predicted by our 2SX analysis, and increased following progressive augmentation of its water content, as observed by the variations of the estimated intracellular to interstitial volume fraction ratio P_i/P_e (Table 5-3). The estimated compartmental relative fractions in normal conditions were in good agreement with results of previous studies (1, 2).

Estimated relative fraction of the vascular space increased following augmentation of extracellular volume. The augmentation of the intravascular residence, τ_c , must reflect attainment of quasi-normal equilibrium transendothelial exchange after fluid redistribution within vascular and interstitial spaces at each vascular condition. The observed non-linear increase of τ_c with the vascular volume must reflect contributions of small veins and arteries within the VOI which could not be seen in the localization images, as they present a much higher compliance than capillaries and experience negligible exchange with the parenchyma. Vascular and interstitial water fractions varied differently between the imposed vascular filling conditions. While the vascular space varied progressively from one condition to another, the interstitial water fraction doubled when passing from the vascular draining to the vascular filling condition and presented a very small reduction (8%) when passing from the vascular filling to the normal condition. The rapid variation must be a result of the manual compression which led to interstitial space draining while the slower variation shall reflect interstitial volume inertia as a consequence of the interstitial oedema-preventing mechanisms, as reviewed by Aukland and Nicolaysen (137). Furthermore, it has been previously shown that interstitial space volume varies at a much slower rate than the vascular space following imposed variations on vascular hydrostatic pressure (138).

Finally, extracted T2-spectra from the fitted characteristic relaxation curves demonstrated that indeed only two T2-compartments may be obtained from the proposed 3S2X model characterized by the extracted intrinsic parameters (Figure 5-9 b).

In a previous *in vivo* study (118), the “long” T₂-value resulting from biexponential fitting of relaxation data obtained within the soleus of healthy volunteers increased with hyperoxia exposure. This result was explained as reflecting the well-known blood oxygenation level-dependent effect (139) and the “long” T₂-component was attributed to vascular water. In the present work, the observed increase of the “long” T₂-value following vascular filling was explained by an increase of the intravascular residence time. It is possible that blood O₂ saturation was lower at vascular draining condition due to the imposed muscular ischemia of the procedure. However, the 3S2X model has too many parameters and vascular T₂ had to be set constant in order to constrain the 3S2X model and obtain stable parameter estimations. Two-dimensional correlation NMR experiments have been previously proposed as a means for studying exchange dynamics (140); these methods allow simultaneous and independent estimation of compartment-intrinsic T₂-value and exchange rates (107). The results from the present work encourage the application of such methods for more precise parameter estimation of compartmental exchange models of myowater distribution.

5.3.4. Conclusions

I - The biexponential T₂-relaxation behavior of ¹H-NMR signals observed in skeletal muscle reflects an anatomical compartmentation of myowater.

II - Water in the vascular space has non-negligible contributions to observed muscle T₂-values as obtained from monoexponential fitting of T₂-relaxation data.

III - The biexponential T₂-relaxation behaviour observed in skeletal muscle cannot be explained with a 2SX model representing an intra-/extracellular anatomical compartmentation of myowater for realistic transcytolemmal exchange rates. However for the slower transendothelial exchange rates a 2SX model representing an extra-/intravascular compartmentation allows precise prediction of the observations.

IV - A 3S2X model representing water exchange dynamics between intracellular, interstitial and vascular spaces is capable of explaining T₂-relaxation behaviour observed in skeletal muscle tissue for realistic transmembrane exchange rates and allowed estimating interstitial T₂-value which has been shown to be close to the intracellular T₂ for healthy tissue in normal conditions.

V - For healthy skeletal muscle tissue in normal conditions, the observed “intermediate” T₂-component reflects the relaxation behaviour of water within the intracellular and interstitial spaces while the “long” T₂-component reflects the relaxation of water within the vascular space.

5.4. Insights on the T2-relaxometry of diseased skeletal muscle tissue

The objective of this preliminary study was to check for the potential applications of the developed methodology in the study of muscle pathology. To do so, we further explored the 3S2X system in order to represent tissue alterations, such as interstitial oedema, inflammation and necrosis. Simulated data from such altered models were analysed with the aim of getting some insight about the potential sensitivity of the developed methodology for to the alterations which we tried to model. Finally, the simulated data were compared with in-vivo data acquired in three patients with NMDs.

5.4.1. Methodology

5.4.1.1. Simulations

The 3S2X system was used to simulate T2-relaxation data for normal and abnormal SKM tissue. This was done by changing the intrinsic parameters characterizing the 3S2X systems. The intravascular T2-value, T_c , was set to 170 ms for all simulations. Interstitial oedema was characterized by increased relative fraction of interstitial water, P_e , and interstitial T2-value, T_e ; inflammation was simulated by moderate interstitial oedema with increased perfusion (simulated by decreasing the intravascular residence time, τ_c). Necrosis was characterized by inflammation and cellular swelling (simulated by decreasing the intravascular relative fraction, P_c , and increasing the intracellular T2-value, T_i) with increased membrane permeability (simulated by decreasing the intracellular residence time, τ_i). The applied intrinsic parameters characterizing the simulated systems are organized in Table 5-4 and are classified by the tissue alteration they are expected to represent.

Table 5-4 – *Intrinsic parameters characterizing the simulated systems modelled in order to represent oedematous, inflamed and necrotizing tissue.*

Intrinsic parameters	Normal tissue	Interstitial Oedema			Inflammation	Necrosis
		moderate	intermediate	important		
P_i (%)	85	75	70	60	75	85
P_e (%)	10	20	25	35	20	13
T_i (ms)	30	30	30	30	30	35
T_e (ms)	35	60	70	80	60	70
τ_i (ms)	1000	1000	1000	1000	1000	700
τ_c (ms)	500	500	500	500	200	200

With the intrinsic parameters we could determine the system-characteristic matrix A

from Eq. 5.10. The T2-decay curve for the system defined by A was then directly calculated using Eq. 5.11. Ten decay curves were simulated for each set of system parameters by superposing the calculated decay curve to ten simulated vectors of Gaussian noise. The amplitude of the added noise was determined by $\sigma = Y_1/SNR$, where Y_1 is the first decay point at $TE = 2$ ms and σ is the standard deviation of the noise. The SNR was determined as the mean ratio Y_1/σ , obtained from the in-vivo data. σ was calculated from one CPMG data set acquired with all the RF pulses turned off. A T2-spectrum was extracted for each of the ten decay curves with the T2 deconvolution method described in 5.3.1.2. A final T2-spectrum characterizing the simulated system was determined by superposition of the ten extracted spectra.

5.4.1.2. In-vivo data acquisition

The localized CPMG sequence described in 5.3.1.1 was applied to study the T2-relaxation in SKM tissue of three patients with NMDs as a complement to an ongoing clinical study, which included whole-body T1. Patient examinations were conducted in accordance with institutional guidelines. In the first patient (man aged 24 years) diagnosed with Charcot-Marie-Tooth disease, a T2-decay curve was acquired from VOI located within the soleus (Figure 5-10 *a*); in the second patient (woman aged 40 years) diagnosed with eosinophilic fasciitis (or Shulman's syndrome), decay curves were acquired from two VOIs located within the soleus (Figure 5-10 *b*) and the tibialis anterior (Figure 5-10 *c*), respectively; in the third patient (man aged 78 years) diagnosed with a necrotizing myopathy, a decay curve was acquired from a VOI located within the tibialis anterior (Figure 5-10 *d*). A T1-weighted FLASH sequence gave anatomical reference images and the VOIs were carefully positioned excluding any visible blood vessels. Muscle selection criterion was minor fat replacement as observed in T1-weighted images acquired as a part of the whole examination protocol.

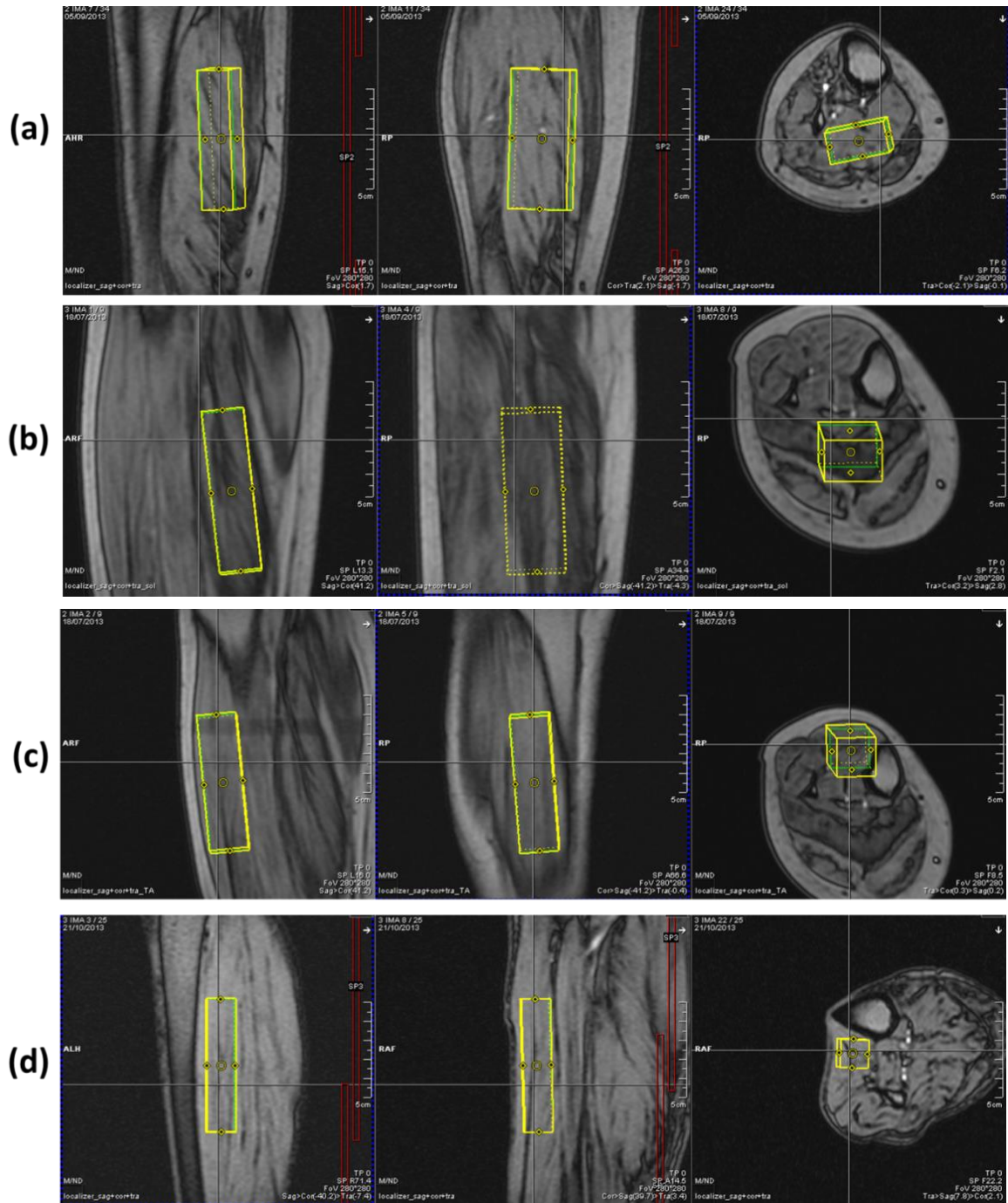


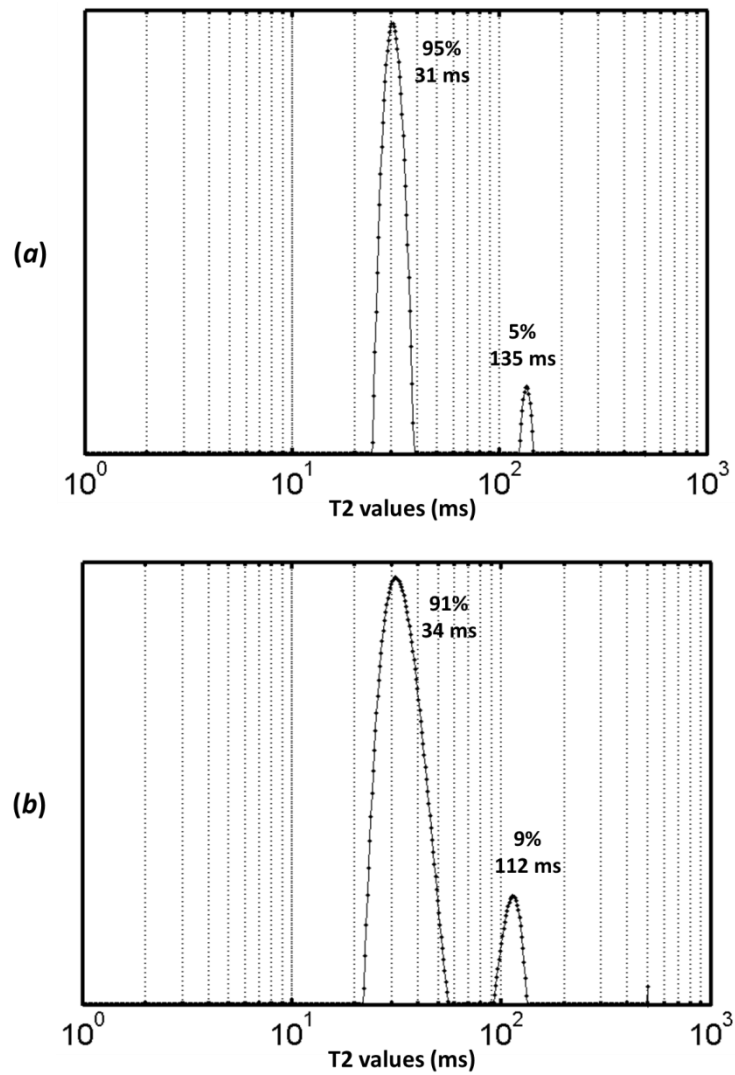
Figure 5-10 - Projection of the VOIs on the sagittal, coronal and axial T1-weighted FLASH images of the calf of the patients (from left to right). (a) VOI located within the soleus of a patient diagnosed with Charcot-Marie-Tooth disease; (b) and (c) show the VOIs located within the soleus and tibialis anterior of a patient diagnosed with eosinophilic fasciitis, respectively; (d) VOI located within the tibialis anterior of a patient diagnosed with a necrotizing myopathy.

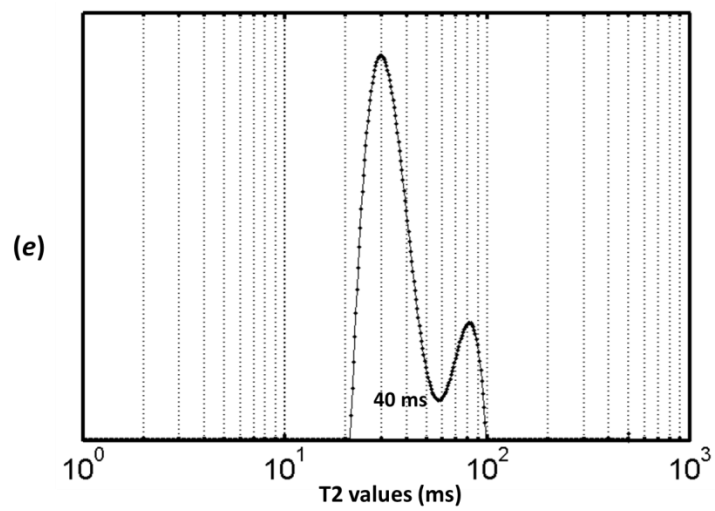
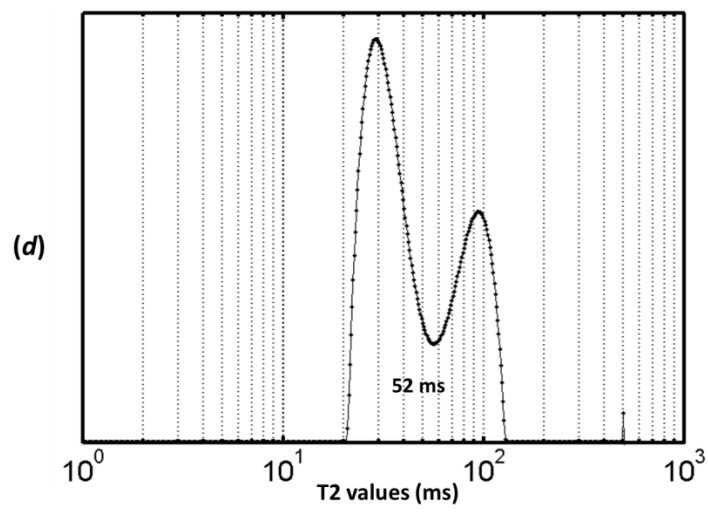
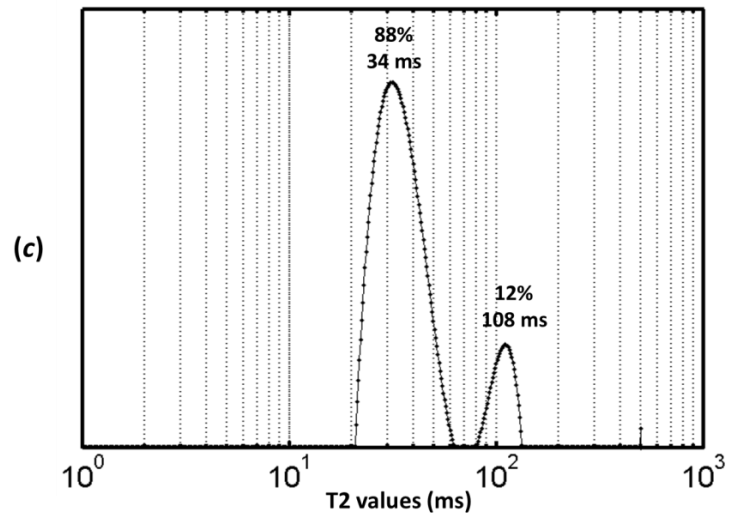
T2 deconvolution of data was done with the regularized inversion method described in 5.3.1.2. The intrinsic relative fractions, residence times and relaxation rates of the intracellular and interstitial compartments may be significantly different from those

observed in healthy tissue. This prevents any prior knowledge about the studied system, which hampers the application of the compartmental exchange analysis described in 5.3.1.2, because there would not be enough constraints and inversion of Eq. 5.11 would lead to numerous minima.

5.4.2. Results

Figure 5-11 presents the extracted T2-spectra characterizing the simulated systems defined in Table 5-4.





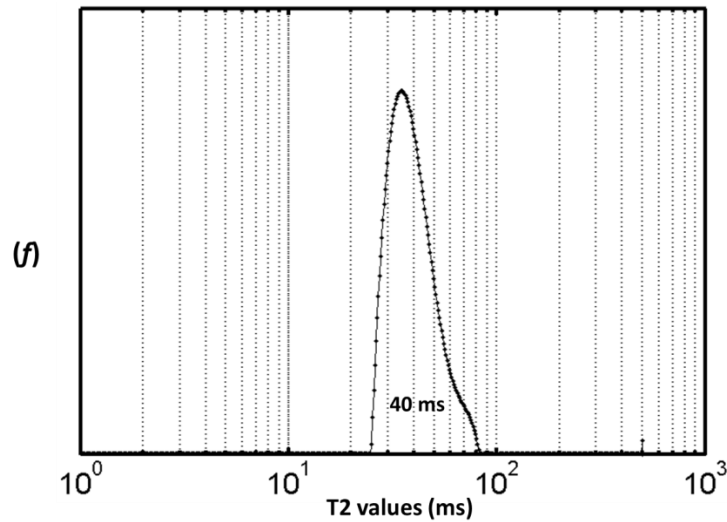
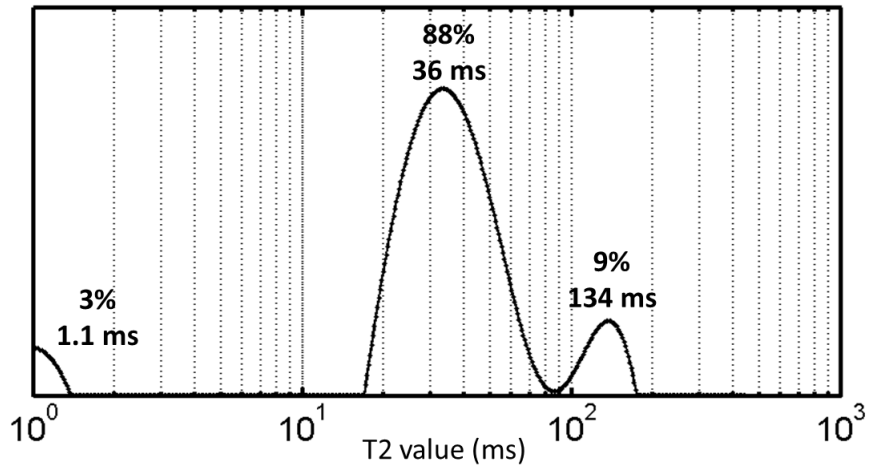
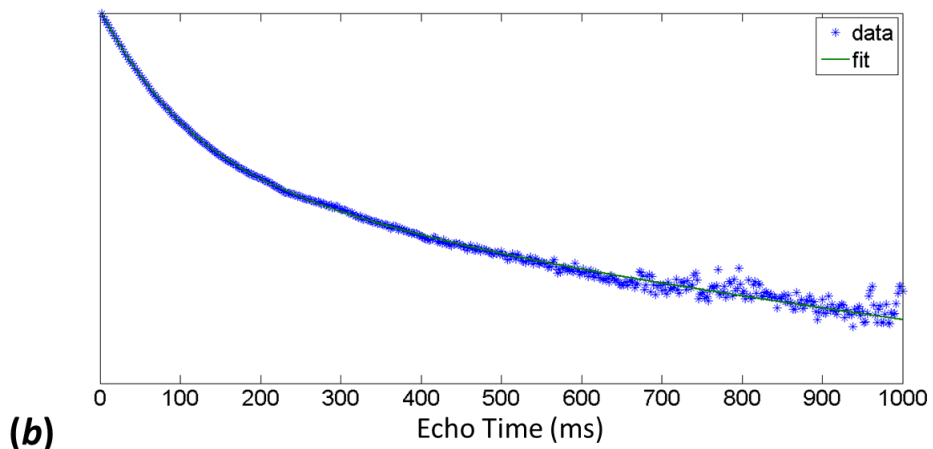
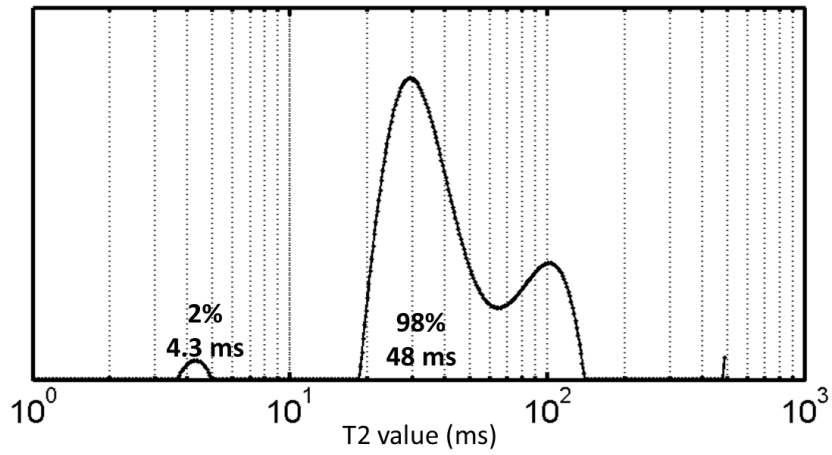
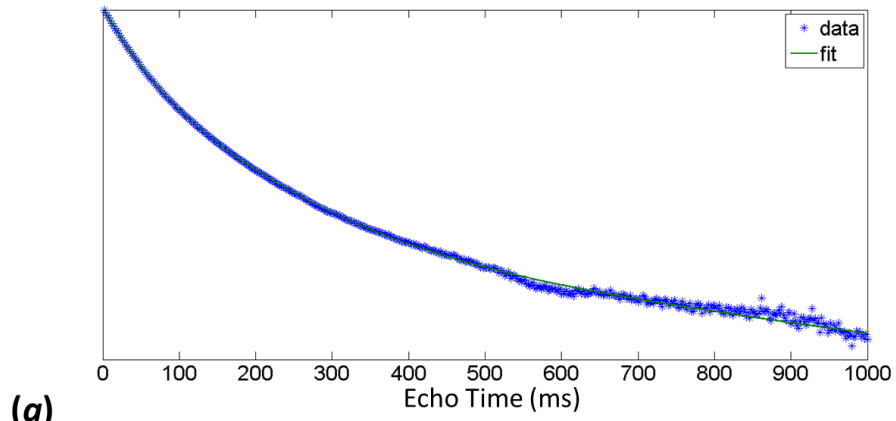
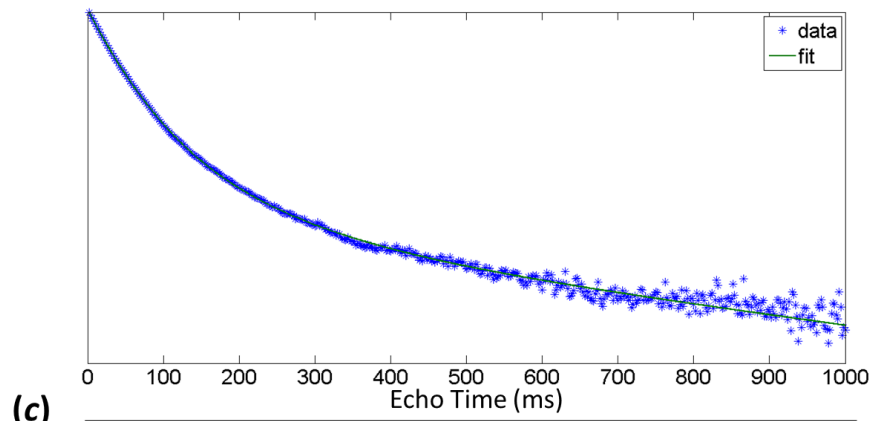


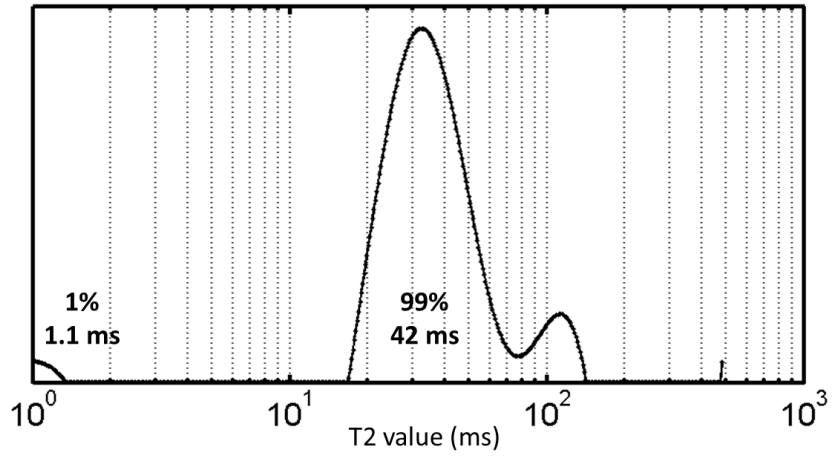
Figure 5-11 – Extracted T2-spectra characterizing each system defined by the intrinsic parameters presented in Table 5-4, representing respectively: (a) Normal tissue; From (b) to (d) there is progressive increase in interstitial oedema; (e) inflammation, characterized by interstitial oedema and higher perfusion; and (f) is supposed to represent necrotizing tissue, characterized by inflammation with high membrane permeability. T2-spectra are plotted with logarithmically scaled abscise for correct visualization of peak area. The T2-value and relative fraction (Eqs. 5.6, 5.7) characterizing the T2-peaks are indicated in the plots.

The decay curves and the T2-spectra obtained for each in vivo data set is presented in Figure 5-12: (a) soleus of the patient diagnosed with Charcot-Marie-Tooth disease; (b) soleus and (c) tibialis anterior of the patient diagnosed with Shulman’s syndrome; and (d) tibialis anterior of the patient diagnosed with a necrotizing myopathy. , The T2-spectra obtained in the soleus of a healthy subject (age 53 years) is presented in Figure 5-12 for comparison.

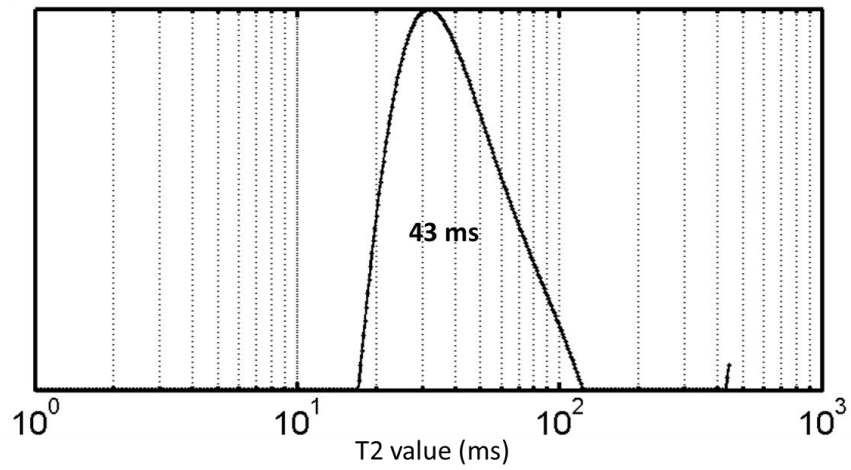
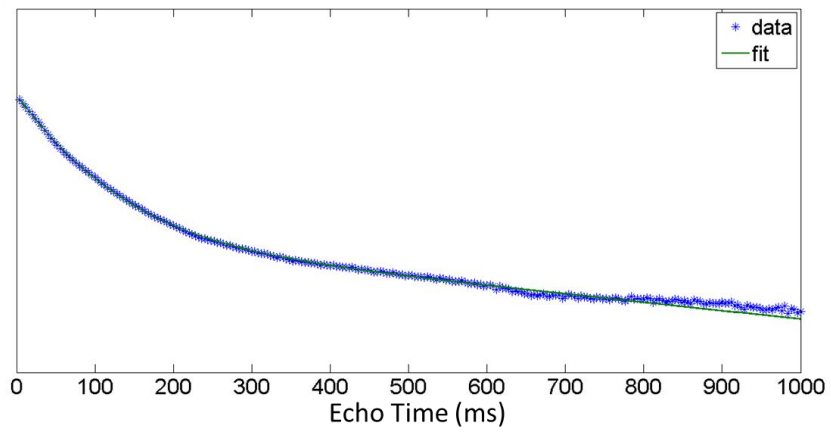




(c)



(d)



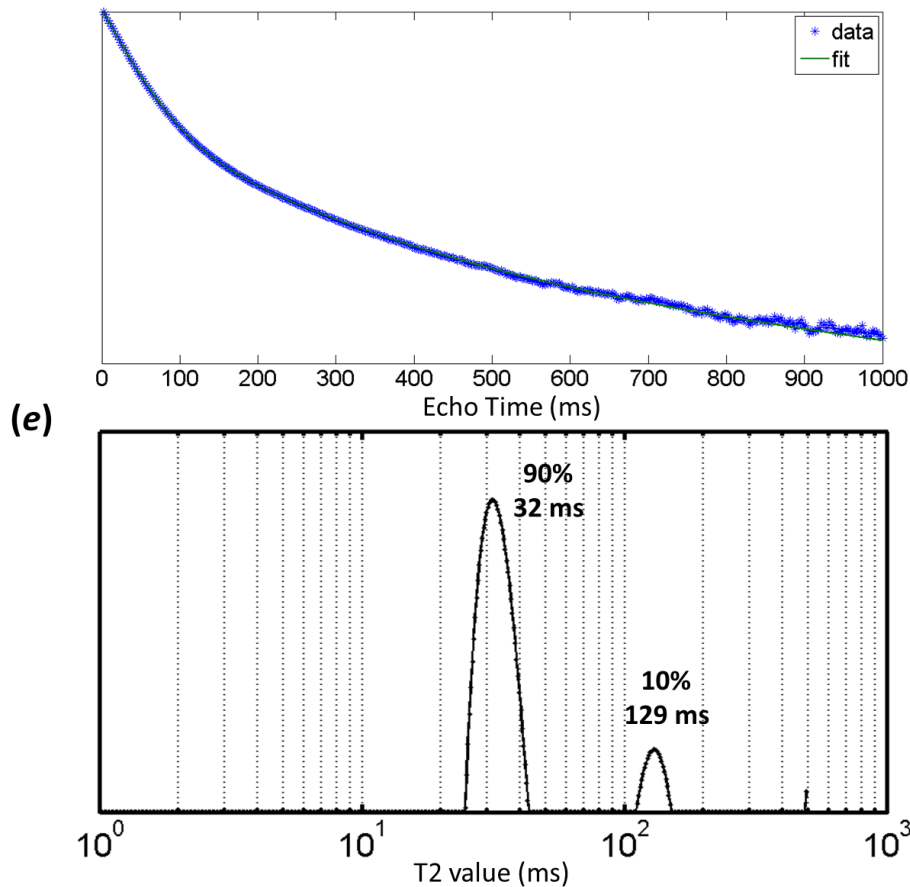


Figure 5-12 – *T2-decay curves and the T2-spectra obtained for each in vivo data set: (a) soleus of the patient diagnosed with Charcot-Marie-Tooth disease; (b) soleus and (c) tibialis anterior of the patient diagnosed with Shulman’s syndrome; (d) tibialis anterior of the patient diagnosed with a necrotizing myopathy; and (e) soleus of a healthy subject. T2-spectra are plotted with the abscise in logarithmic scale for correct visualization of peak area.*

5.4.3. Discussion and conclusions

The T2-spectra has been shown to be quite sensitive to the simulated tissue alterations. In the normal case (Figure 5-11 *a*) the short and long T2-peaks are well separated and the relative fraction of the long T2-peak coincides with the vascular fraction as was observed in in healthy volunteers. In the spectra characterizing the models that simulate interstitial oedema, the relative fraction and T2-value characterizing the long T2-peak are not representative of the vascular space anymore. Furthermore, we may observe that the “intermediate” and “long” T2-peaks move closer to each other (Figure 5-11 *b*). Further increase in interstitial volume fraction and T2-value results in the coalescence of the two peaks (see Figure 5-11 *c-d*). Figure 5-11-*e* shows the spectrum obtained for a system trying to simulate inflammation by adding alteration of vascular permeability, which did not fundamentally modify the pattern obtained for interstitial oedema. Finally, we intended to

reproduce the scenario of necrotizing tissue, in which cellular swelling and inflammation coexist and the sarcolemma permeability is increased; the obtained spectrum is characterized by a single peak with a high T2-value (see Figure 5-11 *f*).

The T2-spectra observed in the patients (see Figure 5-12 *a-d*) showed significant differences from the T2-spectra observed in controls (see example in Figure 5-12 *e*). These results indicated that the methodology proposed for extracting T2-spectra was sensitive to some pathology-induced tissue alterations and might have revealed interstitial space expansion in a CMT patient, inflammatory and myocyte lesional changes.

In the study presented in 5.3, we have demonstrated that the T2-relaxation observed in normal SKM tissue may be explained with a 3S2X model. Moreover, we could determine the mean intrinsic parameters characterizing such model. The results from the study presented in 5.4 show that, by varying these intrinsic parameters, we can simulate “abnormal” compartmentalized systems that are characterized by T2-spectra that share qualitative similarities with the in-vivo T2-spectra observed in diseased muscles. This encourages further development of this preliminary study to include more patients, and to confront the results with biopsy analysis, with the aim to investigate possible correlations between patterns of T2-spectra and histological scenarios.

The consolidation of a non-invasive tool that is sensitive to specific mechanisms associated with pathological alterations of skeletal muscle tissue would offer new possibilities for longitudinal studies and the monitoring of pathological mechanisms of disease. Such information will improve our understanding of disease onset and progression, and would be of great importance for the follow up of therapeutic trials.

CHAPTER 6

Application of Ultra-short Time to Echo Methods to Study Short-T2-components in Skeletal Muscle Tissue

The intramuscular connective tissue (IMCT) plays a fundamental role on the functioning of muscles, ensuring necessary mechanic properties in order to withstand stretching, and efficient transmission of the force produced by each myofiber to the bones. The basal lamina attaches the cytoskeleton and the cell membrane to the endomysial layers surrounding each muscle cell. From the endomysium the force is progressively transmitted until the external epimysium layers that surround the whole muscle and end up as fibrous collagenous cords that attach the muscle to the bones (see 1.1.1). Alterations on the collagen content of the extracellular matrix will alter mechanical properties which will inevitably impact the muscle functions.

In some neuromuscular disorders we may observe an excessive accumulation of fibrous connective tissue in the extracellular matrix, revealed by enlarged endomysial layers observed in histological analysis (Figure 6-1 *c*) (141). Although the etiology and pathophysiology of this mechanism is still investigated and debated, it is becoming widely accepted that the chronic nature of the inflammatory response to the continuous tissue degeneration taking place in diseased muscles is a key driver of the fibrotic response (9–11), by inhibiting myofiber regeneration and promoting the formation of fibrotic tissue, eventually leading to complete myofiber replacement by fibrous connective tissue, usually referred to as fibrosis.

It follows that quantitative information about connective tissue distribution in muscle could constitute a very important biomarker for the characterization of muscle involvement, disease progression, and the follow-up of treatments (10, 142, 143).

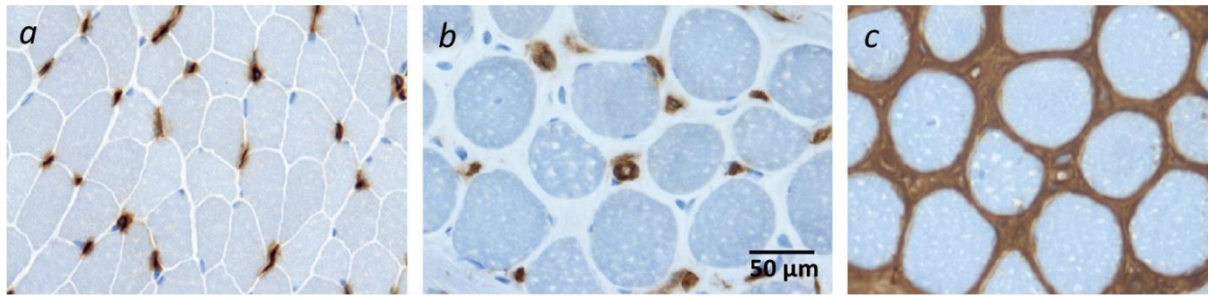


Figure 6-1 – *Comparative morphologic features of histology between control (a) and Duchenne muscular dystrophy (DMD) cases (b, c). Note that in control (a) the transverse section of the myofibers (clear blue texture) present a rather polygonal shape and occupy almost the totality of the tissue volume; the capillaries are stained (brown) and may be identified in the corners of the myofibers. In DMD (b, c) the transverse section of the myofibers is rather round in shape; In contrast to (a), bigger capillary-to-muscle fiber distances may be seen in (b). In (c) collagen I immunostaining highlights the endomysial layers which are abnormally thick in the dystrophic tissue. Taken from (141).*

6.1. The NMR signal from connective tissues

Connective tissue structures present high protein content and concentration, majorly constituted of collagen and glycosaminoglycans (GAG), and might be identified in NMR images as hypo-intensity zones, e.g. tendon, fascia (Figure 6-2 a) and muscle fibrosis (Figure 6-2 b). Their hypo-signal is caused by their characteristic short T2-value (< 10 ms). This is understood as a consequence of the important macromolecular concentration of these tissues, which results in a high proportion of hydration water, characterized by T2-values on the order of 1 ms; magnetization transfer processes between the hydration and bulk water pools synergistically decrease the apparent T2-value of these tissues.

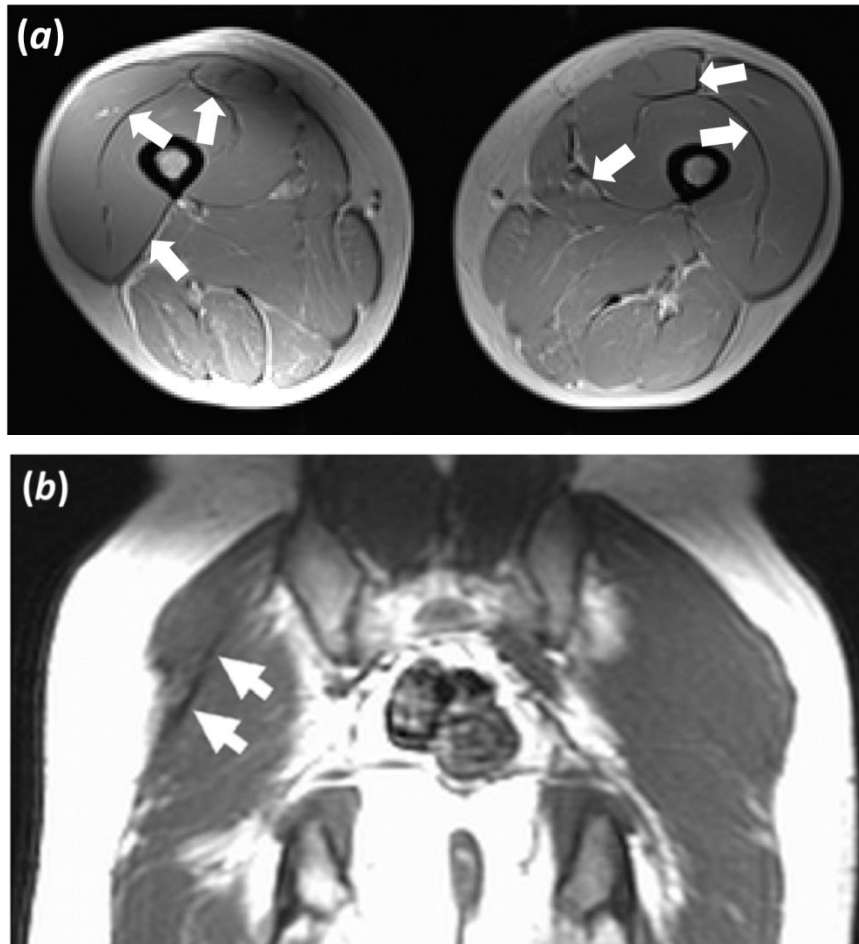


Figure 6-2 – The hypo-signal of compact collagenous tissue structures observed in NMR images. (a) Spin-echo PD image ($TE = 9.5\text{ ms}$) of the thighs. The arrows point to the dark visible fascia with its characteristic hypo-signal. (b) Spin-echo T1-weighted image ($TE = 16\text{ ms}$) of both buttocks. The Arrows point to a dark visible thin fibrotic cord in atrophic right gluteus maximus muscle. Normal left side may be used for comparison. Image in (b) was taken from (144).

Although these large collagenous structures can be visually identified in standard NMR images, the limited spatial resolution ($\sim 1 \times 1 \times 1\text{ mm}^3$) attainable with standard NMRI methods hampers the direct visualisation of enlarged endomysium, characteristic of initial stages of disease (see Figure 6-1 c). Attempts to indirectly detect it by studying heterogeneous distribution of T2-values or water content are also hampered by the presence of inflammation and fatty-infiltration.

Specially designed NMRI methods that offer the possibility of very short echo-times (~ 10 to $100\ \mu\text{s}$), usually referred to as Ultra-short Time to Echo (UTE) methods, have been successfully applied to image and characterize collagenous structures of the musculoskeletal tissue such as tendon, cartilage (38, 145, 146) and even fibrosis in infarcted myocardium (33). In the present work we have applied the UTE method to study

the short-T2-components of the SKM tissue, with the aim of assessing information about IMCT content.

6.2. The UTE method

In conventional NMRI the phase of the magnetization must be properly encoded before the readout in order to correctly sample the k-space. This is done by the application of the so called *phase encoding gradients* (see 2.6) during the interval between excitation and readout, resulting in a *dead time* in which no data can be acquired (Figure 6-3). As a consequence the shortest attainable echo-times in clinical NMRI systems are not inferior to 2 or 3 ms (147). As a result these techniques do not offer the possibility for imaging species with T2*-values on the order 10 to 10² μs.

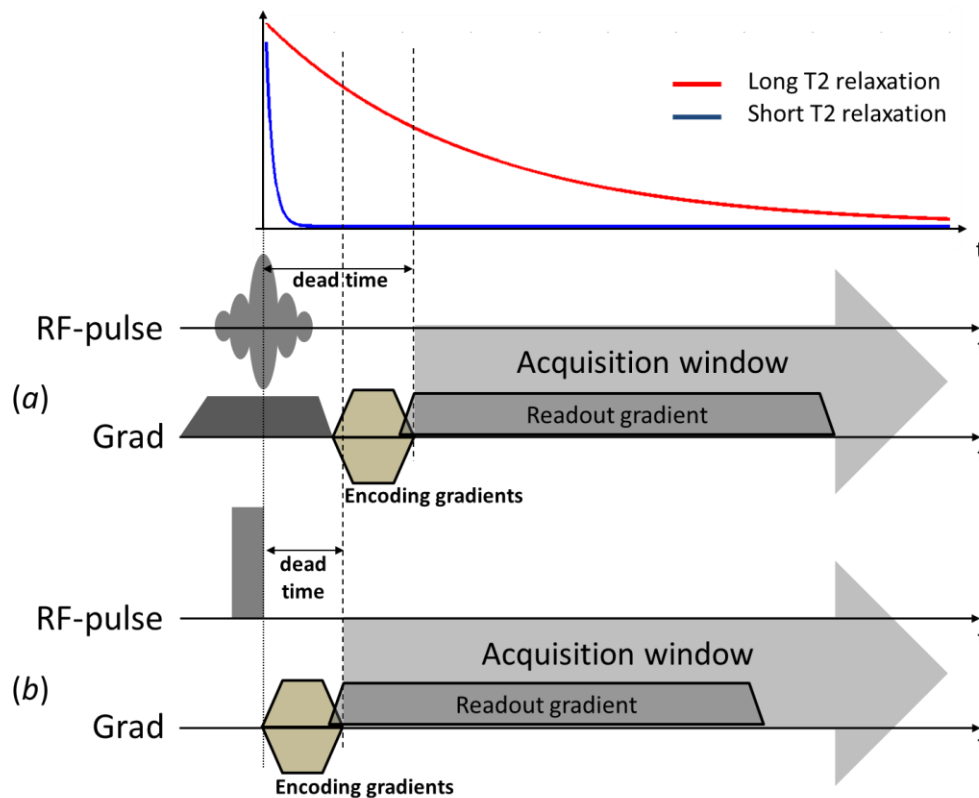


Figure 6-3 – Simplified RF-pulse and gradient time sequence for (a) 2D-GRE and (b) 3D-GRE NMRI techniques. For both methods, the phase encoding gradients imposes a minimum dead time in which no signal is acquired. For the 2D case, a slice selection mode is applied which elongates the dead time due to relaxation effects during excitation process.

Radial acquisition techniques avoid the application of phase encoding gradients (see 2.6), resulting in important reduction of the dead time, especially for 3D-NMRI in which it decreases theoretically to the ramp-time of the readout gradient, i.e., the time needed for

the readout gradient to attain a predefined readout value (see Figure 6-6 *b*). The negative point of radial sampling methods is the undersampling of k-space borders, which contain high frequency information responsible for the definition of borders and contours of the imaged object. In 3D radial acquisition, the readout gradient direction is varied in order to sample an entire sphere (Figure 6-4 *a*), so that when high spatial resolution and sharpness is required, as for imaging small structures, the number of radial lines to be acquired may become extremely high in order to obtain necessary high frequency k-space sampling. This may result in too long examination times.

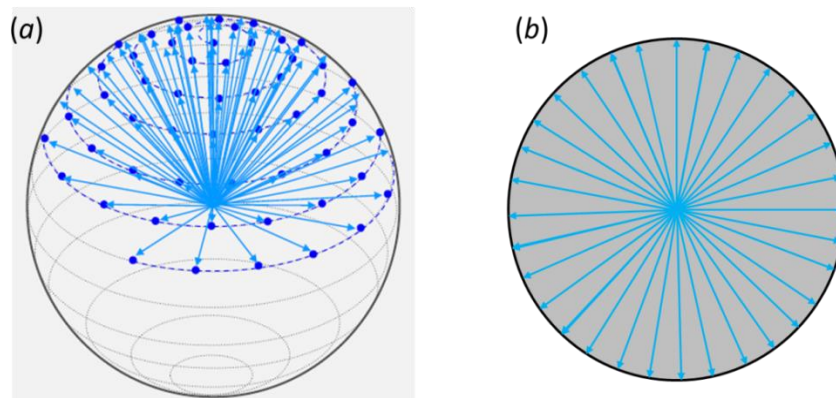


Figure 6-4 – Schematic illustration of k-space sampling for (a) 3D and (b) 2D radial acquisition methods.

In 2D-NMRI this issue is less important, once the gradient directions must be varied in order to sample a disc (Figure 6-4 *b*). However, in two dimensional (2D) NMRI, magnetization is selectively excited from the slice of interest, which is done by application of an RF-pulse in combination with a so called slice selective gradient. Even after excluding phase encoding gradients, conventional slice selection techniques limit the minimum dead time to more than half of the RF-pulse duration (Figure 6-3 *a*). In order to get rid of this problem an interleaved half-pulse excitation may be applied (148, 149), in which signal is acquired right after excitation. In this method, complete slice selection is accomplished in two acquisitions; in each of them half of the RF-pulse is applied and the selection gradient polarity is inverted in the second acquisition, so that resulting gradient moment is null after summation of signals (Figure 6-5).

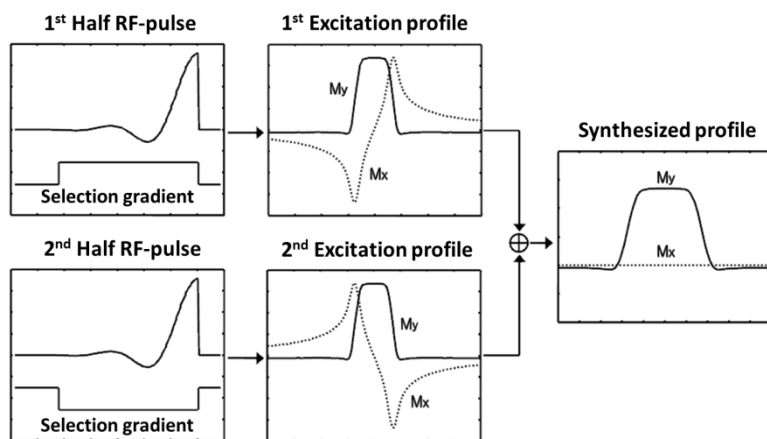


Figure 6-5 – Principle of half RF-pulse selection for acquisition of short relaxing NMR signal. Slice profile is completely selected after summation of acquisitions with inverted polarity of selection gradient.

This allows excitation to be concluded at the moment in which bulk transverse magnetization has been effectively created and signal can be acquired right after excitation (Figure 6-6). Such technique was previously applied for imaging collagen-containing structures such as knee menisci and Achilles tendon with a 2D-NMRI technique with a dead time of 0.2 ms (38).

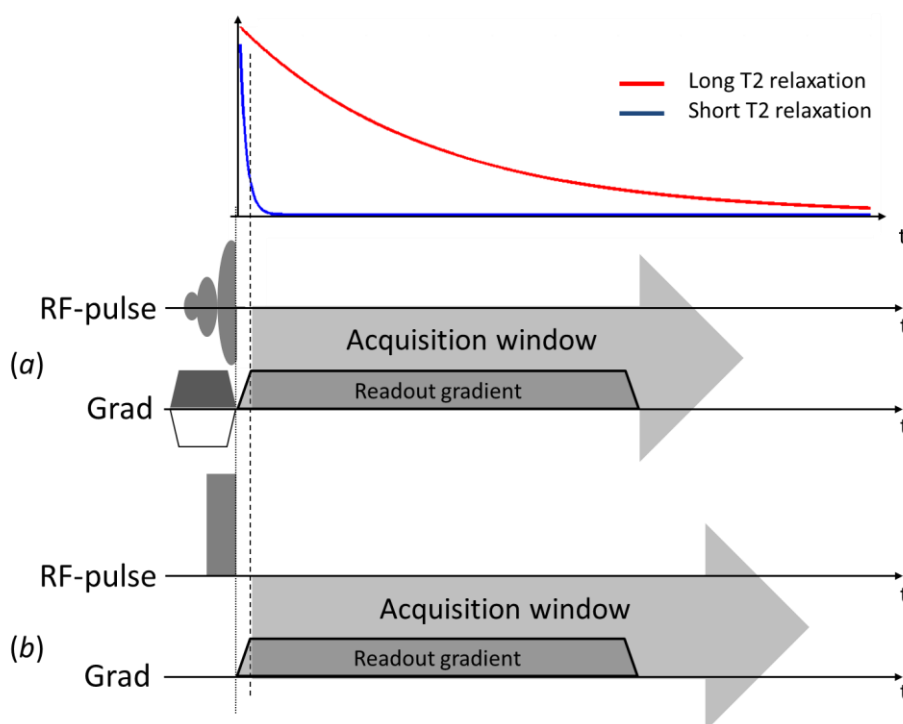


Figure 6-6 - Simplified FR-pulse and gradient time sequence for (a) a 2D-GRE sequence with half excitation pulse and (b) a 3D-GRE sequence. Radial acquisition allows acquiring data right after the excitation. The dead time is determined by the time it takes for the RF system to change from transmission to acquisition mode, usually on the order of 10 to 100 μ s.

Finally, the dead time can be further reduced (theoretically to zero) by acquiring signal during the gradient ramp. This leads to a non-linear sampling of the centre of the k -space which demands special post-processing treatment for image reconstruction. Dead times on the order of ten microseconds have been attained with such NMRI techniques (146, 150, 151), which are referred to as UTE sequences.

6.3. Application of a 3D-UTE sequence for the detection and characterization of a short-T2-component in skeletal muscle tissue

The goal of this study was to determine whether a short-T2-component was detectable in normal skeletal muscle, to characterize this component and to collect indices as to whether it might or not reflect connective tissue content.

6.3.1. Methodology

A 3D-UTE sequence was applied to image the calf of a healthy volunteer (age 28 years). The NMRI system was a 3 teslas whole-body scanner (Tim Trio, SIEMENS Healthcare, Erlangen, Germany). Signal acquisition and RF transmission were done with a cylindrical mono-channel birdcage transceiver coil (CP-extremity, Siemens Healthcare, Erlangen, Germany). The same volume was imaged for eight different echo-times, $TE = 0.2, 0.4, 0.6, 1, 2.46, 5, 10, 15$ ms. Relevant sequence parameters were: $TR = 30$ ms, FOV = 240 mm, resolution = 256, BW = 1 kHz/px, $FA = 30^\circ$ transverse slice thickness was 1 mm and k -space was radially sampled with 10^4 lines. Water magnetization was selectively excited by application of a binomial (1-1) pulse composed of two hard-pulses of 100 μ s each, spaced by 610 μ s.

Regions of interest (ROIs) were drawn within the gastrocnemius (medial head), gastrocnemius (lateral head), soleus, peroneus longus and tibialis anterior (Figure 6-7 *a*). ROIs were also traced in order to delimit the hypointense streaks between the soleus and gastrocnemius muscles, representing fascia and aponeuroses; a second enlarged ROI was also traced in order to include adjacent muscle structures (Figure 6-7 *b*). In order to cover enough muscle volume, ROIs were traced over 11 slices, the central one and the closest five from both sides of the FOV.

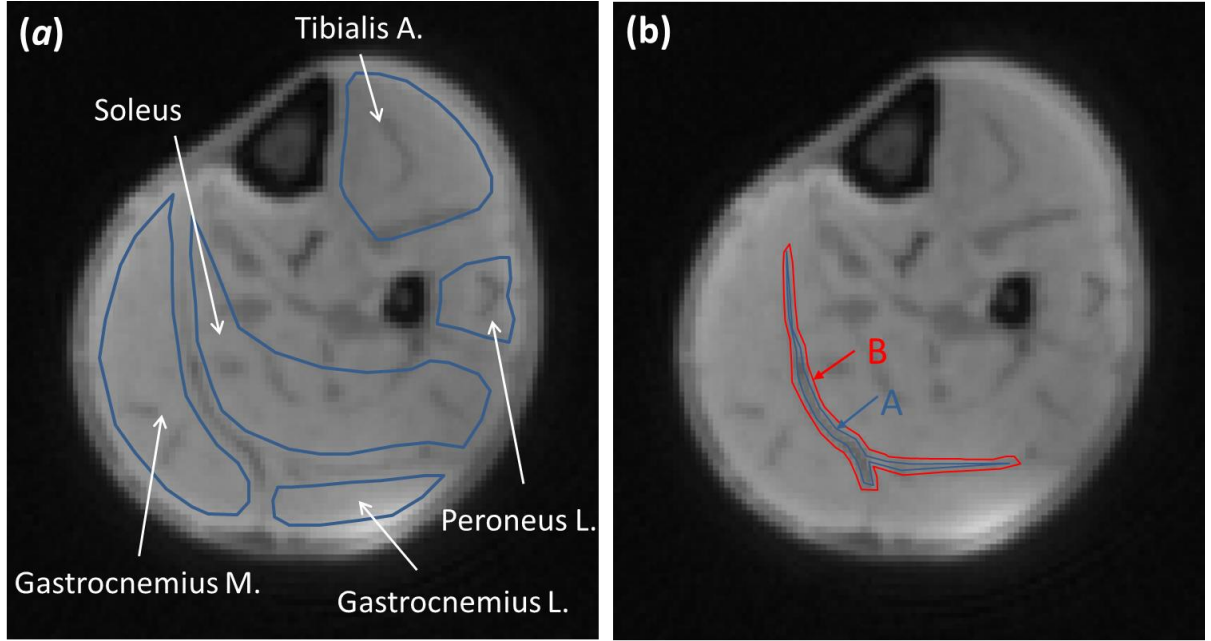


Figure 6-7 – (a) The ROIs drawn inside the gastrocnemius (medial head), gastrocnemius (lateral head), soleus, peroneus longus and tibialis anterior over the central slice. (b) ROIs A and B delimiting fascia and aponeuroses between the gastrocnemius and the soleus; ROI-B was traced in order to include adjacent muscle structures.

The time evolution of the superposed signal amplitude of all the pixels within all ROIs in each muscle was fitted to a bi-exponential decay model given by

$$S(t) = \rho_s e^{-\frac{t}{T_2^s}} + \rho_l e^{-\frac{t}{T_2^l}} \quad 6.1$$

where ρ_s and T_2^s are the signal amplitude at $t = 0$ and the T_2^* of the explored short- T_2 -component, respectively, and ρ_l and T_2^l are the amplitude at $t = 0$ and the T_2^* of the usually observed muscle signal. The parameters ρ_s , ρ_l , T_2^s and T_2^l were extracted by solving the minimization problem defined by

$$\min_{\rho_s, \rho_l, T_2^s, T_2^l} \sum_k (S(TE_k) - Y_k)^2 \quad 6.2$$

where Y_k is the superposed signal amplitude of all the pixels within all ROIs traced within a given muscle. The relative fraction of the short- T_2 -component was calculated as $\rho_s / (\rho_s + \rho_l)$. All data was processed using Matlab (The MathWorks, Inc., Natick, MA, USA).

6.3.2. Results

The time evolution of the signal amplitude obtained from the ROIs traced in each muscle are plotted in Figure 6-8 with the corresponding fitted curves.

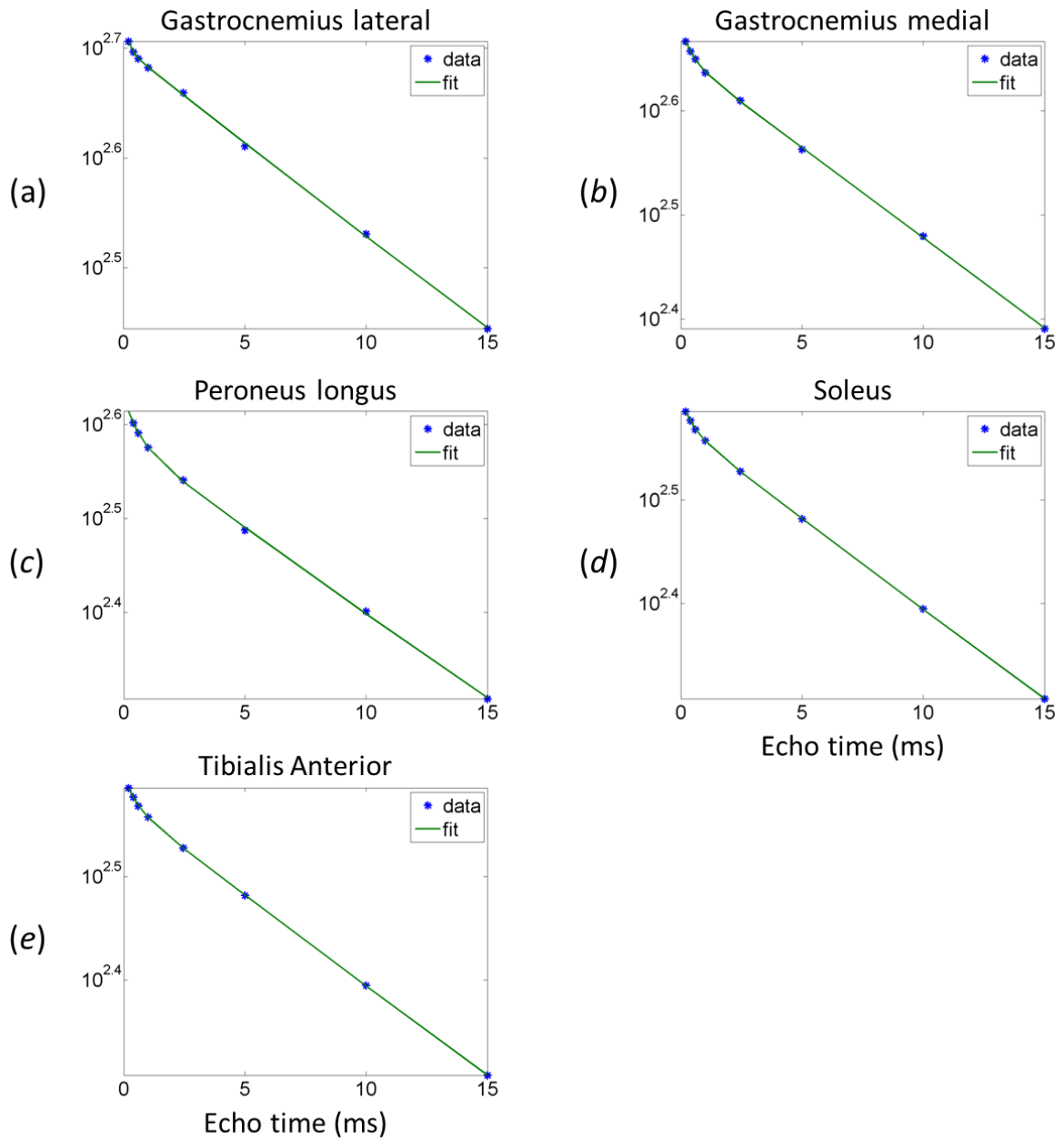


Figure 6-8 – *Logarithmic plot of the time evolution of the signal amplitude obtained from the ROIs traced in the gastrocnemius lateral (a), gastrocnemius medial (b), peroneus longus (c), soleus (d) and tibialis anterior (e), along with the corresponding fitted curves.*

The time evolution of the signal amplitude obtained from the ROIs A and B traced around the fascia between the gastrocnemius and soleus muscles (see Figure 6-7 b) are plotted in Figure 6-9 with the corresponding fitted curves.

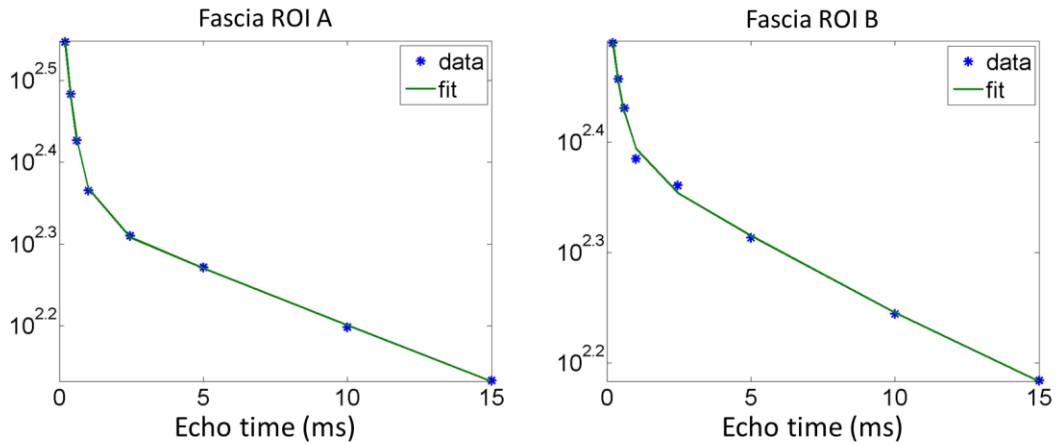


Figure 6-9 - Logarithmic plot of the time evolution of the signal amplitude obtained from the ROI-A delimiting the fascia between the soleus and the gastrocnemius and the enlarged ROI-B including adjacent muscle tissue, along with the corresponding fitted curves.

Table 6-1 presents the results for the mean extracted relative fraction and T2*-value of the short component along with the T2*-value of the long component obtained from the ROIs traced in the muscles (see Figure 6-7 a) and from the ROIs A and B traced around the fascia (see Figure 6-7 b).

Table 6-1 - Results for the extracted mean relative fraction and T2*-value of the short component, and the T2*-value of the long component for the ROIs traced in the muscles (see Figure 6-7 a) and for the ROIs A and B traced around the fascia (see Figure 6-7 b). Results are presented as mean(SD) for the muscles and as mean(SE) for each ROI around the fascia.

Structure	Relative fraction of the short-T2-component (%)	Short T2* value (ms)	Long T2* value (ms)
Muscles	7.3(1.8)	0.40(0.18)	23.5(1.8)
Fascia (ROI A)	52.2(2.4)	0.43(0.04)	27(29)
Fascia (ROI B)	37.8(7.1)	0.43(0.18)	19(25)

6.3.3. Discussion

In this study a short-T2-component with a T2*-value around 400 μ s, was reproducibly identified in SKM tissue of a healthy volunteer. In the fascia, which is predominantly composed of connective tissue, we could identify an important fraction of a short-T2-component with a similar T2*-value. Although this result suggested that the short-T2-component observed in muscles might represent connective tissue, we did not have final proof of its origin.

The signal from water protons characterized by short T2-value observed in SKM tissue is generally attributed to hydration shells of macromolecules. However there is no study

describing the subcellular distribution of such hydration water pools, and the observed signal might come from water hydrating the macromolecules of the contractile apparatus, as well as the macromolecules constituting the extracellular matrix.

Further investigations of this short-T2-component in muscles presenting specific alterations of the collagen content and confrontation with histological analysis might offer more insight to help elucidating this problem.

6.4. UTE applications for imaging of short-T2-components in SKM tissue

Although UTE sequences allow the acquisition of signal from fast relaxing structures, the signal from within each voxel will have contributions from both slow and fast relaxing structures. As a consequence, short-T2-components are not directly identified in UTE images because of lack of contrast. Furthermore, different tissue structures may present different relative fractions of short-T2-components, which may themselves be characterized by different short T2-values. As a result even images acquired at echo-times as short as 0.2 ms will be T2-weighted (Figure 6-10). Table 6-2 presents a list of tissue structures along with the short T2-values characterizing their short-T2-components.

Table 6-2 – *Observed T2* values of some tissue structures at 3 T.*

Tissues	Deep radial and calcified cartilage	Menisci	Ligaments	Tendons	Entheses	Cortical Bone
T2* (ms)	~1	~4	~3	~2	~4	~0.3

Data borrowed from (150, 152)

Different methods have been proposed in order to highlight signals from short-T2 structures, such as application of T2-selective RF pulses for suppressing contributions from long T2-species (38, 145, 153, 154), or post-processing techniques for isolation of contributions from short-T2 species (33, 155).

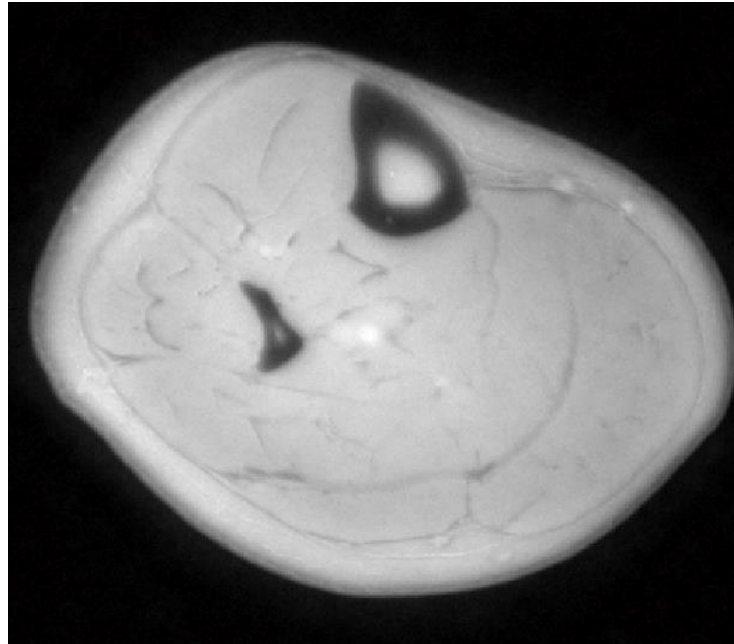


Figure 6-10 – NMRI of an axial slice of the calf of a healthy volunteer using a 2D-UTE sequence with an echo-time of 0.2 ms, TR = 30 ms and FA = 5°. Note that structures with elevated relative fraction of short-T2-components such as fascia and cortical bone still present smaller signal intensity. However, cortical bone presents higher contrast with other tissue structures due to the high relative fraction of its short-T2-components and to the very short T2-value that characterizes them.

When the T_2 -values are comparable to the RF-pulse duration, the simultaneous magnetization tipping and relaxation processes will compete. If the rate of magnetization tipping $\omega_1 \equiv \gamma B_1$, is smaller than the transverse relaxation rate, $1/T_2$, then the RF-pulse is inefficient because magnetization relaxes faster than it is excited. This efficiency dependence on T_2 has been explored in order to selectively excite long T2-species (153, 154, 156). The idea behind long-T2 selective excitation is to apply long RF-pulses with small amplitude. Analogously to fat saturation techniques such as spectral excitation (see 3.2.1) or SITR (see 3.2.2), the magnetization from long T2-species may be selectively saturated before excitation of short-T2 species. Such techniques have been shown to provide high image contrast for short-T2-species such as the deep radial and calcified layers of cartilage, cortical bone, and the Achilles tendon (145, 146, 150). However, the presence of lipids in muscles, prevent isolation of water short-T2 species with such techniques. Long RF pulses have small frequency selective bandwidths which renders them very spectrally selective. Because of the chemical shift between lipids and water, especially in high fields ($B_0 \geq 3 T$), these compounds must be individually saturated (145). Nonetheless, any spectral fat suppression technique is imperfect (see 3.3), resulting in residual signal contributions from lipids. Observed short-T2-components in SKM have a

small relative fraction (~ 10%), so that even small signal contaminations may preclude any attempts for extracting quantitative information.

Alternative post-processing techniques have been proposed, which are based in the direct algebra of two amplitude images acquired at different echo times, and shall be referred to as *dual-echo* methods. The idea is to subtract an image acquired at a longer echo time, which contains negligible contributions from short-T2-components, from an image acquired at the shortest possible echo time, in which signal from fast relaxing species are still significant. Many variants of this basic technique have been explored, offering the possibility of visualising short-T2 structures in musculoskeletal tissue (33, 155, 157). However, fat signal contamination must be carefully considered in order to access non-biased information when studying SKM tissue. The frequency spectrum of triglycerides (see Table 6-3) is rather complicated (see 3.3), leading to frequency and amplitude modulation of the fat signal (see Figure 6-11), which result in fat signal contributions in the subtracted image.

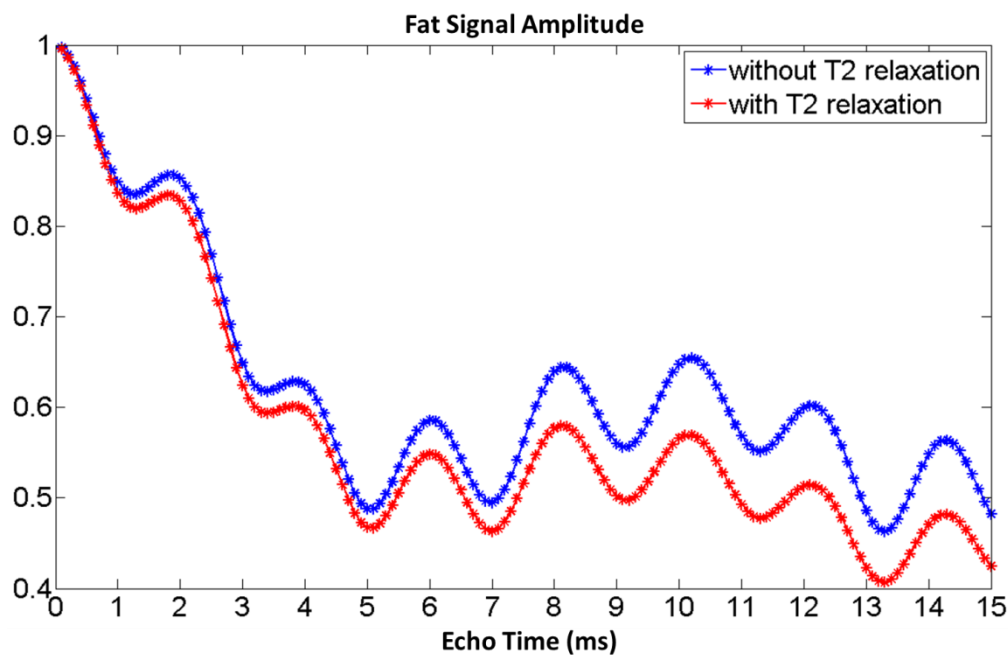


Figure 6-11 – Plot of amplitude modulation of the theoretical fat signal as a function of time for the fat model given in Table 6-3. Two fat signals were simulated; one in which no T2-relaxation was considered (blue) and a second inserting the T2 of each individual hydrogen group of the lipid molecule. Note that the impact of the phase shift accumulation between the different hydrogen groups in the amplitude modulation is much more important than the T2-relaxation effects.

Assuming that the T2-relaxation has minor effects on the modulation of the fat signal amplitude compared to its natural dephasing, the UTE signal from muscle might be approximated by the following model defined as

$$S(t) = W_s e^{i\omega_0 t - \frac{t}{T_2^s}} + (W_l + F(t)) e^{i\omega_0 t - \frac{t}{T_2^l}} \quad 6.3$$

Where T_2^s and T_2^l are the T2* of the short and long T2-components, respectively, ω_0 is the B0 related off-resonance frequency, W_s and W_l are the amplitude of short and long T2 water signal components right after excitation ($t = 0$), respectively. $F(t)$ is the complex fat signal described by

$$F(t) = F_0 \sum_k \rho_k e^{i\omega_k t} \quad 6.4$$

$$\sum_k \rho_k = 1$$

where F_0 is the amplitude of fat signal right after excitation ($t = 0$), ρ_k and ω_k are the relative fraction and intrinsic Larmor precession frequency of each peak of the fat spectrum. Average values of ρ_k and ω_k obtained from NMRS are presented in Table 6-3.

Table 6-3 – Relative fraction and Larmor precession frequency of the different peaks in the fat spectrum at 3T.

Type	Average relative fraction (%)	Chemical shift relative to water (ppm)	Frequency shift relative to water (Hz)	T2 (ms)
Olefinic Methine	5	0.6	75	47(1)
Glycerol Methine		0.5	75	
Glycerol Methylene α	1	-0.4	-60	31(3)
Glycerol Methylene β		-0.6	-60	
Diallylic Methylene	1	-1.9	-237	48(5)
Methylene α	6	-2.5	-301	47(5)
Allylic Methylene	9	-2.7	-329	36(2)
Methylene β	7	-3.1	-383	38(3)
Bulk Methylene	63	-3.4	-418	83(5)
Terminal Methyl	8	-3.8	-468	79(2)

Data borrowed from (70)

For echo-times in which water magnetization is in-phase with the fat magnetization, here defined as the vector sum of the magnetization vectors of each fat component, the signal amplitude may be easily derived from Eq. 6.3, and will be given by

$$|S(t)| = W_s e^{-\frac{t}{T_2^s}} + (W_l + |F(t)|) e^{-\frac{t}{T_2^l}} \quad 6.5$$

From eq. 6.5 we may derive the expression for the subtraction of the amplitude images acquired at two in-phase times:

$$|S(t_0)| - |S(t_1)| = W_s(E_0^s - E_1^s) + W_l(E_0^l - E_1^l) + |F(t_0)|E_0^l - |F(t_1)|E_1^l \quad 6.6$$

where $E_i^s \equiv e^{-\frac{t_i}{T_2^s}}$ and $E_i^l \equiv e^{-\frac{t_i}{T_2^l}}$.

If the ratio $(t_1 - t_0)/T_2^l$ is sufficiently small so that $E_0^l - E_1^l \approx 0$ and the fat signal contributions are negligible then

$$|S(t_0)| - |S(t_1)| = W_s \left(e^{-\frac{t_0}{T_2^s}} - e^{-\frac{t_1}{T_2^s}} \right) \quad 6.7$$

Equation 6.7 contains only signal contributions from short-T2-components of water.

However, in practice, these conditions are not respected and it follows that the amplitude of the subtracted image, described by Eq. 6.6, contains signal contributions from long T2-components of water and lipid protons. Figure 6-12 presents the image resulting from the subtraction of an UTE image acquired at $TE = 2.5$ ms, first in-phase point after $TE = 0$, from an UTE image acquired at $TE = 0.2$ ms (Figure 6-10). Notice the high intensity from short-T2 structures such as cortical bone and fascia. Although non null intensity is observed in SKM tissue, pixels within subcutaneous fat and spongy bone present a significantly higher intensity, which puts in evidence that there must be confounding signal contributions from lipids in the pixels within muscle.

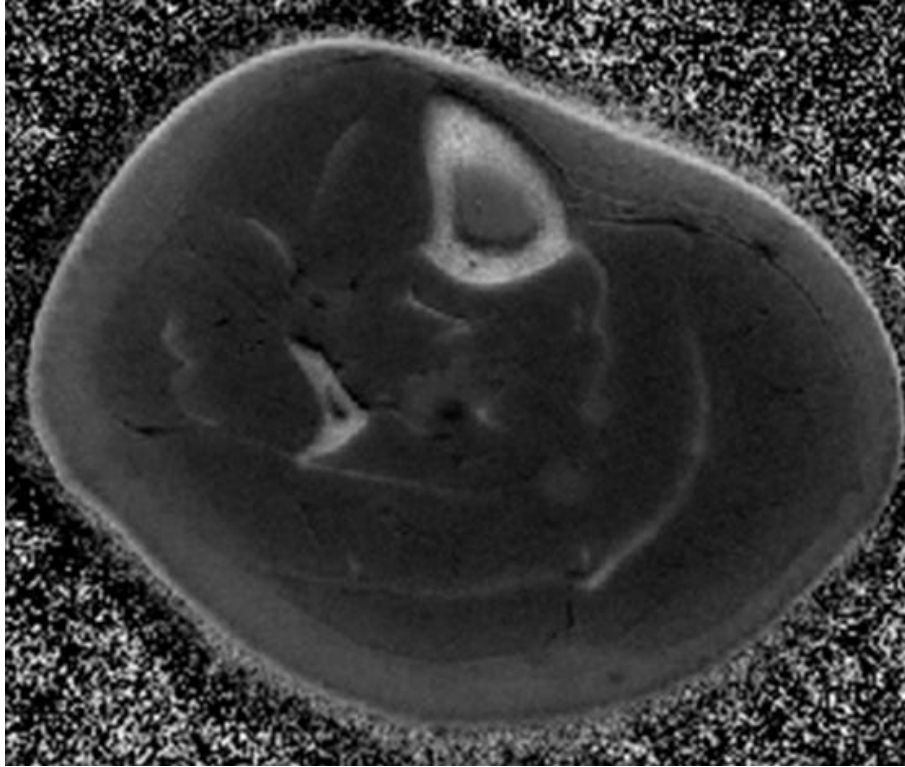


Figure 6-12 - image resulting from the subtraction of an UTE image acquired at 2.5 ms from another UTE image acquired at 0.2 ms (see Figure 6-10). Note the high residual signal from short-T2 structures such as cortical bone and fascia. Notice also the important residual signal on the subcutaneous fat.

In the following we describe a methodological approach that allows isolating the signal from short-T2-components. It is an extension of the basic dual-echo method, in which the T2* relaxation and fat contributions are taken into account.

Echo Subtraction with T2* and fat amplitude modulation corrections

The signal from long T2 structures experience T2* decay and their signal amplitude will be smaller in the second image ($E_0^l - E_1^l \neq 0$). If not corrected, this results in non-null contributions from long T2-components in the subtracted image. If the T2*-map is available one can overcome this problem by demodulating the signal from each pixel in the image before subtraction. The resulting subtracted signal will be given by

$$|S(t_0)|e^{\frac{t_0}{T_2^l}} - |S(t_1)|e^{\frac{t_1}{T_2^l}} = W_s \left(e^{-\frac{t_0+t_0}{T_2^s+T_2^l}} - e^{-\frac{t_1+t_1}{T_2^s+T_2^l}} \right) + |F(t_0)| - |F(t_1)| \quad 6.8$$

which contains no signal contributions of long T2-components of water.

In order to eliminate the fat signal contributions, we must subtract the quantity $|F(t_0)| - |F(t_1)|$, pixel by pixel. From Eq. 6.4, we have that

$$|F(t_0)| - |F(t_1)| = F_0 \left(\sum_k \rho_k (e^{i\omega_k t_0} - e^{i\omega_k t_1}) \right) \quad 6.9$$

If F_0 is known for each pixel, then based on the fat signal model described in Eq. 6.4, we can calculate the fat contributions, which are given by

$$F_0(f_0 - f_1) \quad 6.10$$

where $f_i \equiv \sum_k \rho_k e^{i\omega_k t_i}$, which can be calculated for the values given in Table 6-3. If the relative fraction of fat signal, \bar{F} , is known, F_0 can be calculated by

$$F_0 = \bar{F} M_0 \quad 6.11$$

where, $M_0 = W_s + W_l + F_0$, is the total magnetization amplitude just after excitation ($t = 0$).

If an image is acquired at a short enough TE , so that relaxation effects can be neglected, then $|S(TE \sim 0)| \cong W_s + W_l + F_0$, and the contributions from fat may be eliminated from the subtracted image:

$$\begin{aligned} |S(t_0)| e^{\frac{t_0}{T_2^l}} - |S(t_1)| e^{\frac{t_1}{T_2^l}} - \bar{F} |S(t_0)| (f_0 - f_1) &\cong W_s \left(e^{-\frac{t_0}{T_2^s} + \frac{t_0}{T_2^l}} - e^{-\frac{t_1}{T_2^s} + \frac{t_1}{T_2^l}} \right) \\ &\cong W_s \left(1 - e^{-\frac{t_1}{T_2^s} + \frac{t_1}{T_2^l}} \right) \end{aligned} \quad 6.12$$

Equation 6.12 contains only contributions from short-T2-components of water. Although the above proposed method allows imaging of short-T2-components of water, the T2* and the fat-fraction maps are usually not available.

Fat-fraction maps are usually extracted with the Dixon method (3.2.1), while T2*-maps are usually obtained by monoexponential fitting of the signal amplitude evolution obtained from GRE images (see 2.7.2) acquired at different echo-times. Alternatively, both T2* and fat-fraction maps may be simultaneously extracted with more sophisticated techniques in which the complex signal evolution is fitted to a predefined signal model (158). Such model is usually identical to the one defined in Eq. 6.3, without the contributions from short-T2, and may be defined as follows

$$S(t) = (W + Ff(t))e^{i\psi t} \quad 6.13$$

where W and F are complex variables representing water and fat magnetization right after excitation ($t = 0$), $f(t) \equiv \sum_k \rho_k e^{i\omega_k t}$ is defined by the fat spectrum, and $\psi \equiv \omega_0 + \frac{i}{T_2^*}$ is the generalized complex field-map. Solution of the problem defined in Eq. 6.13 is usually done in two steps. At first an initial value for the complex field ψ is searched by direct

inversion of Eq. 6.13, which is linear for a given value of ψ ; this step is usually regularized by some field homogeneity constrain because of the existence of multiple minima. Once the initial field map ψ_0 is obtained, it can be demodulated from the signal. In the second step, small errors of ψ_0 , $\Delta\psi$, are considered and Eq. 6.13, which is still valid for the demodulated signal is linearized for small values of $\Delta\psi$, and the complex variables W , F and ψ are iteratively optimized (68, 159). Notice that no short-T2-component is considered in Eq. 6.13, except for signals dominated by water short-T2-components, for which Eq. 6.13 is still valid considering short T_2^* -values.

6.5. In-vivo NMRI of short-T2-components in SKM tissue

6.5.1. Methodology

2D-UTE data was acquired from 8 healthy volunteers, three women (37 ± 11 years) and 5 men (37 ± 7 years). The NMRI system was a 3 teslas whole-body scanner (Tim Trio, SIEMENS Healthcare, Erlangen, Germany). Signal acquisition and RF transmission were done with a cylindrical mono-channel birdcage transceiver coil (QED CP-extremity, Siemens Healthcare, Erlangen, Germany). Eleven UTE images of the same axial slice were acquired in the calf at the echo-times $TE = 0.2, 2.5, 3, 4, 5, 6, 10, 12.5, 15, 20, 26.5$ ms. Relevant sequence parameters were: $TR = 30$ ms, $FA = 5^\circ$, $BW = 357$ kHz and a slice thickness of 6 mm; k -space was radially sampled with 1024 lines, and line resolution was 512, resulting in dwell time of 2.8 μ s. Readout gradient ramp-time and slew-rate were 400 μ s and 70 mT/m/ms, respectively. The reconstructed image matrices were 400x400 with isotropic in-slice resolution of 0.34 mm. Slice selection was done with a half-sinc RF-pulse (160) with a duration of 600 μ s. One hundred dummy scans were applied for establishing steady state before actual k -space sampling.

Acquired data was treated with a robust chemical-shift based method (158) for simultaneous extraction of fat-fraction and T2* maps. As Eq. 6.13 thus not take short-T2-components into account, the image acquired at $TE = 0.2$ ms was not used for extraction of the maps. With the T2* and fat-fraction maps available, the dual-echo method described in Eq. 6.12 was applied with $t_0 = 0.2$ ms and $t_1 = 2.5$ ms. Short T2 fraction maps were calculated by

$$S_f = \frac{|S(t_0)|e^{\frac{t_0}{T_2^*}} - |S(t_1)|e^{\frac{t_1}{T_2^*}} - \bar{F}|S(t_0)|(f_0 - f_1)}{S(t_0)e^{\frac{t_0}{T_2^*}}} \quad 6.14$$

All post-processing was done using Matlab (The MathWorks, Inc., Natick, MA, USA).

6.5.2. Results

Figure 6-13 presents the extracted short-T2 fraction map, calculated using Eq. 6.14, of the same slice (volunteer) presented in Figure 6-10 and Figure 6-12, by using the echo-subtraction method described by Eq. 6.12.

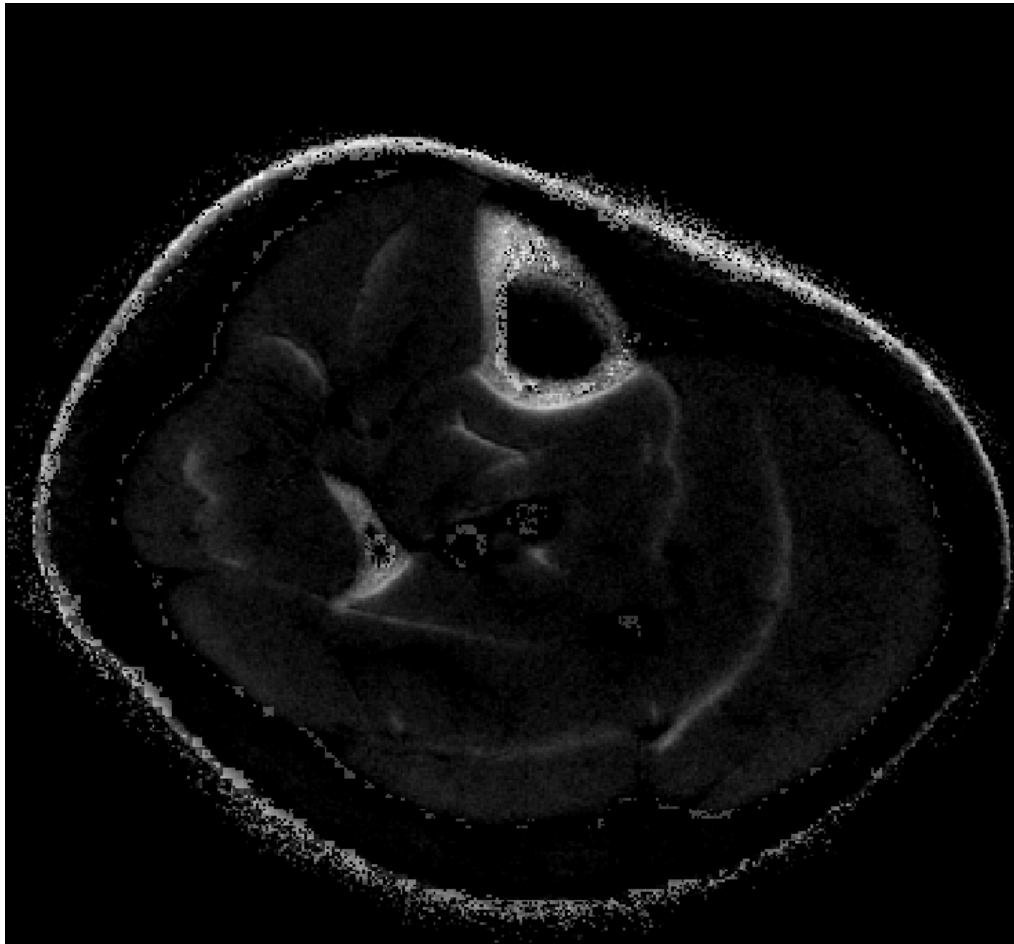


Figure 6-13 – *Extracted Short T2-map fraction, using the dual-echo method with correction for T_2^* of long T2-components and fat signal contributions.*

Note that short-T2 structures such as cortical bone and fascia, which have hypo-signal in conventional NMRI, present relatively high fractions of short-T2-components. We may also observe high relative fraction of signal from short-T2-components in the connective tissue layer of the skin. Note that no signal from short-T2 is observed in the subcutaneous fat and spongy bone, which indicates that fat contributions have been suppressed. Pixels within muscles, however, present significant short-T2 fractions. Figure 6-14 presents the histogram of the relative fraction, S_f , of signal from short-T2-components for pixels with $S_f \geq 0.2\%$.

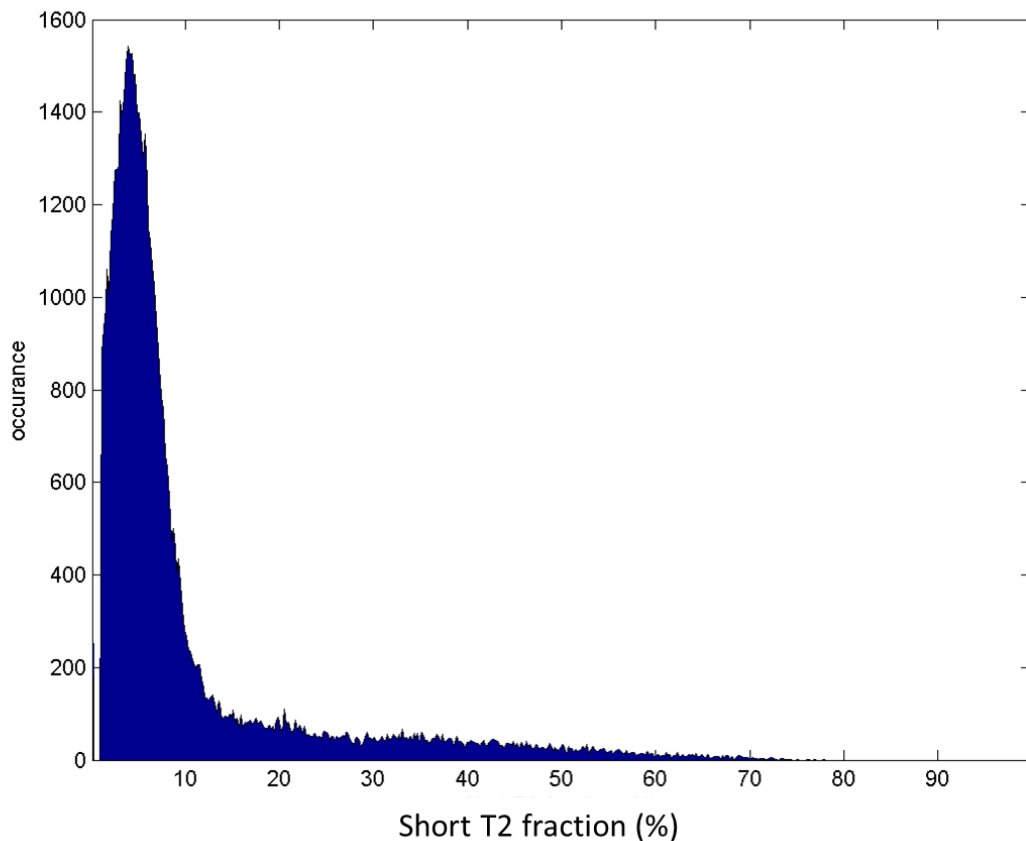


Figure 6-14 – Histogram of the relative fraction, S_f , of signal from short-T2 for pixels with $S_f \geq 0.2\%$.

The higher observed relative fractions are found within the cortical bone, skin and fascia. The average relative fraction of signal from short-T2-components observed in pixels located within muscles was calculated for each subject for pixels with $S_f \leq 10\%$, the obtained mean and SD of the calculated average between subjects was 4.2 and 0.7 % respectively.

6.5.3. Discussion and conclusions

We introduced a methodology that allowed imaging, for the first time, fast relaxing structures in SKM tissue of a healthy volunteer. The analysis of the sensitivity of the post-processing method described in 6.4 (see Eq. 6.12) to tissues with different T2-values identifies the range of T2-values detected in these images. Figure 6-15 presents the plots of sensitivity profiles (calculated from Eq. 6.12) for different values of the echo-time of the first image. For the 2D-UTE sequence applied in 6.5, the minimum TE was limited to 200 μs ; in this case the imaged signal will have significant contributions of any components with T2-values between 0.1 and 7 ms (see the *blue curve* in Figure 6-15). The curves also show that the sensitivity profile strongly depends on the echo-time of the first image. This

means that if shorter echo-times became feasible, this methodology could be applied to produce images corresponding to different sensitivity profiles, offering the possibility to extract information about the T2-distribution characterizing the imaged components.

If we hypothesise that besides the difference in protein concentration between intra- and extra-cellular spaces, the average relaxivity of the proteins forming the contractile apparatus might differ from that of the proteins constituting the extracellular matrix then we could suppose the distinct hydration water pools to be characterized by different relaxation times. In such a scenario, the application of the proposed method could help characterizing these different hydration water pools, which would offer crucial information for the implementation of quantitative tools for studying IMCT.

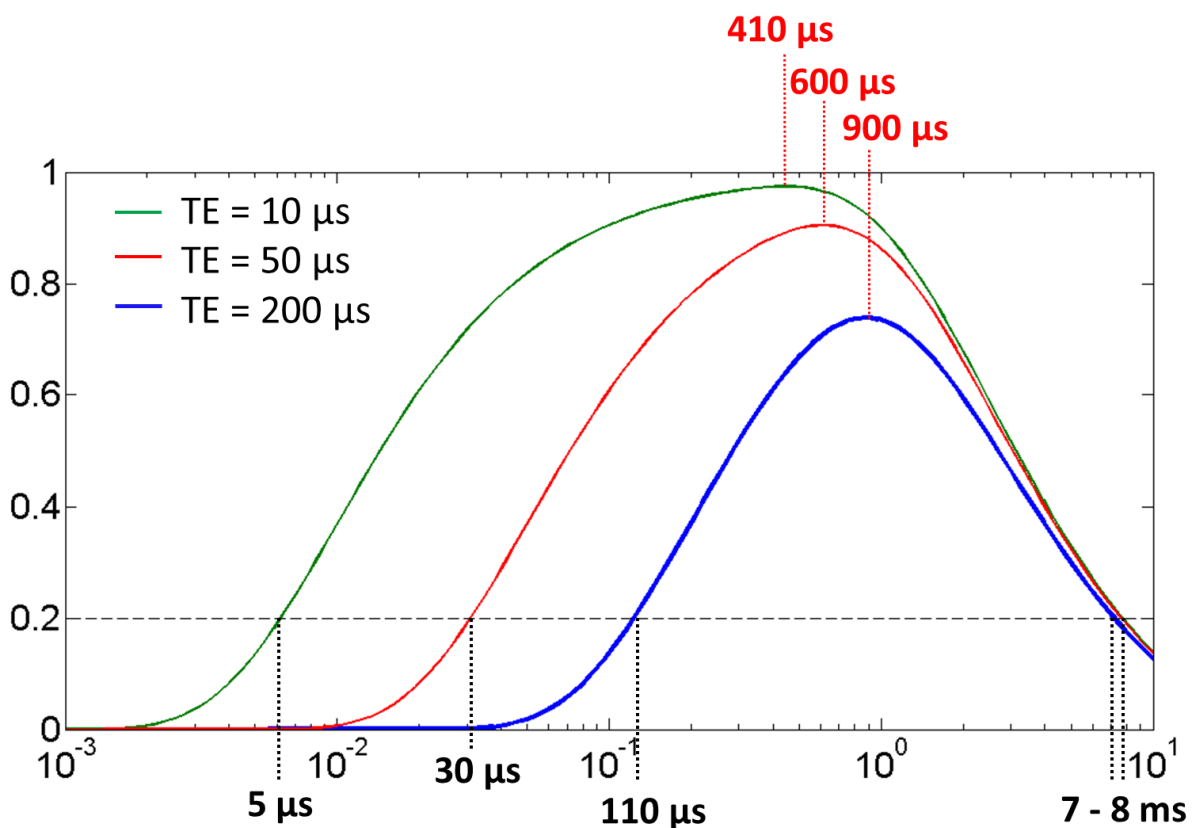


Figure 6-15 - Sensitivity profiles of the short-T2-imaging technique describe in Eq. 6.12 to tissues with different short T2-values (1 μs to 10ms) for different minimum echo-times (10, 50 and 200 μs). The horizontal dashed line represents the limit of 20% contribution from a short-T2-component. Note that the T2 of maximum sensitivity decreases with the minimum echo time, along with the minimum T2 whose contributions to the image will be greater than 20% of its own total signal.

Although the issue related with IMCT imaging has not been solved yet, the results presented in this chapter highlighted the potential of ultra-short time to echo methods such as UTE for studying IMCT and strongly encourage further methodological development.

CHAPTER 7

Conclusions and Perspectives

The objective of this thesis was to adapt and develop NMR techniques and post-processing methods to the level of clinically applicable tools for the quantification of variables that are sensitive/specific to pathological alterations of the SKM tissue in NMD, such as inflammation, oedema, necrosis and fibrosis. The quantification of the fibro-fatty replacement observed in advanced stages of disease is currently well accomplished by spectral fat-water separation techniques (20, 21) and, as such, was not primarily addressed in this thesis.

Inflammation, oedema and necrosis are signs of active stages of diseases, and have been shown to be characterized by elevated T2-values, being visually assessed in fat-saturated T2-weighted (FS-T2w) images (12, 15). However, such a qualitative visual approach relies on subjective detection of contrast between presumed healthy and oedematous and inflamed tissue, which is strongly sensitive to system imperfections such as transmit and receive field inhomogeneities. This results in a lack of precision and sensitivity that hampers the application of FS-T2w methods for studying disease progression and the efficacy of treatments. Actual measurement of the T2-value offers more sensitivity to such pathology-induced tissue alterations and can be made much less sensitive to system imperfections, which is a crucial feature for the feasibility of multicentre studies. This explains the current interest in developing more precise, fast and accurate methods for T2-mapping, which are currently proposed as a solution to the issues related with detection and characterization of inflammation in SKM by NMRI (161).

In chapter 3 we demonstrated experimentally in a patient group with different NMDs, in muscles presenting different degrees of fat-infiltration, that the alterations observed in T2-value as measured by monoexponential fitting of the signal from protons in water and lipid molecules reflect the degree of fatty infiltration in the affected muscles. This demonstrates the necessity of measuring the T2 that characterizes exclusively the signal from protons in water in order to be able of characterizing tissue alterations other than fat degeneration in patients with NMD. Although global T2 measure has been demonstrated to

be a biomarker of disease progression in some NMDs (162), it is known to be completely non-specific to what concerns disease activity and fat replacement.

In chapters 3 and 4 we have presented and experimentally validated two methodologies allowing the extraction of muscle T2-maps with the main concern for not being sensitive to the degree of fat infiltration. The post-treatment developed in chapter 3 allows simultaneous quantification of the T2-value and the fat-fraction for muscles with degrees of fatty infiltration up to 65% by using an MSE sequence that is available in most clinical NMRI systems. Although the idea of exploring T2-relaxation differences between water and lipids had already been proposed (19), our method provides improved precision of reference T2-values, which is vital for increasing discrimination of pathological muscles. The method described in chapter 4 does not offer information about fat fraction, however it presents a simpler post-processing and overcome some important difficulties of the MSE-based method, such as: the possibility for correcting the T2-measurement errors resulting from B1 inhomogeneity; dense 3D space coverage, avoiding inter-slice gaps necessary to avoid cross-talking in multi-slice acquisitions. B1 inhomogeneity constitutes a major issue in high-field NMRI, and the T2-pSSFP method provides a potential solution for T2-mapping in the current and next generation of clinical systems. Both methods have been shown to be able to characterize tissue alterations caused either by direct strain injury or disease activity such as inflammation, oedema and necrosis in SKM tissue.

A different method for simultaneous quantification of fat and water T2 has been recently proposed (163), in which a spoiled gradient echo (SPGR) sequence is coupled with a CPMG like MSE sequence, in which three SPGR images are acquired during the interval between each pair of refocusing pulses of the CPMG train. This allows for application of the IDEAL method (68) for extraction of separated fat and water amplitude images at each echo-time of the CPMG echo train from the three corresponding SPGR images. Fitting of the separated signal amplitude decays from water and fat allows simultaneous quantification of water and fat T2-values and relative fat fraction. In contrast to the method proposed in chapter 3, the IDEAL-CPMG method presents no limitation of fat fraction for ensuring accuracy and precision. However, this method requires a more RF-pulse sequence that is not available in most clinical scanners and also makes use of a post-treatment that is considerably more complex.

The observed T2 alterations reflecting disease activity are understood to be caused by an increase of tissue water content. However, SKM tissue is structurally compartmentalized and the water content may vary differently within individual compartments depending on the mechanisms underlying the pathology-induced tissue alterations. Muscle T2-relaxation has been long known to be multiexponential (111, 112),

and this behaviour has been hypothesised to be a consequence of such compartmentalization. It follows that the monoexponential T2, as measured by NMRI techniques, is an apparent T2 characterizing an approximate monoexponential tissue relaxation and, consequently, offers no means of determining the specific mechanism underlying the observed T2 alteration.

Extraction of T2-distributions from relaxation data is an ill-posed mathematical problem, and the extracted results are strongly dependent on the SNR. Optimization of inversion methods for T2-deconvolution is still a matter of research (164–166), and current methods still impose restrictions to the data set, such as high SNR (> 1000) and time sampling of the decay curves ($\sim 10^2$ to 10^3 Hz) in order to decrease the sensitivity to noise and allow extraction of reproducible T2-distributions. Such constraints are not respected by conventional NMRI-MSE sequences, and multiexponential T2-relaxometry studies are currently done with the spectroscopic CPMG sequence. Spatial localization is necessary for assuring meaningful in vivo measurements. Implementation of a technique allowing localized CPMG acquisitions is not straightforward, which explains why such a small number of localized CPMG methods have been reported to date. These make use of either: outer-volume-suppression (OVS) for saturation of magnetization from outside the VOI (167); 2D selective RF pulses for direct selection of a generic shape volume (168); or ISIS-based methods(169). In the methodology presented in chapter 5, the author implemented a localized CPMG method in a clinical scanner, which allowed performing multiexponential T2 studies in vivo.

Although it has been more than 40 years since the first observations of the non-exponential T2 relaxation behaviour of proton NMR signals in muscle (111, 112), the interpretation of such behaviour is still an open problem. Although most of the works reported to date support the anatomical compartmentation hypothesis (106, 114, 116, 118, 167), they have led to no consensual theories concerning the attribution of the observed T2-components to specific anatomical compartments. In chapter 5 we have addressed the issue related with the interpretation of the multiexponential T2-relaxation observed in SKM tissue, and this study constitutes the most important contribution of this thesis. First, we offered strong in-vivo experimental evidence that the multiexponential behaviour observed in human SKM tissue is a consequence of the anatomical compartmentation of myowater. Then we demonstrated that the simplest compartmentalized model capable of explaining the experimental data for the currently known physiological compartmental exchange rates is a two-site-exchange (2SX) model describing an extra-/intra-vascular compartmentation. It has been also shown that a three-site-two-exchange (3S2X) model, describing the intracellular, interstitial and vascular compartments explains the data with

high precision and accuracy, taking transcytolemmal and transendothelial exchanges into account. Analysis of the extracted T2-spectra by the 3S2X model allowed extracting intrinsic T2-value and relative fraction characterizing each of the three histological compartments. Furthermore, our results strongly suggest that the “intermediate” and “long” T2-components observed in T2-relaxometry studies in normal SKM tissue shall be attributed to the extra- and intra-vascular spaces respectively, and invalidate the commonly assumed intra-/extra-cellular compartmentation model (106, 111, 112, 115, 170). Although such interpretation had been previously proposed (114, 118), no compartmental exchange analysis taking realistic transmembrane exchange rates into account had ever been provided to support it. In summary the results of this study demonstrate that multiexponential relaxation analysis offer new physiological information about the state of the tissue.

Finally, we verified experimentally the sensitivity of the method to pathology-induced tissue alterations. The T2-spectra observed in patients was drastically altered which highlights the sensitivity of the measurement to tissue alterations induced by disease. The results of this pilot study suggest that the abnormal T2-spectra observed in patients with NMD, may be explained with a 3S2X model characterized by corresponding abnormal intrinsic parameters. Such information would allow for a more precise and specific characterization of pathological insults to tissue. However, the high number of parameters characterizing a 3S2X model imposes the necessity of establishing constraints in order to reduce the number of possible solutions to the inversion problem of the compartmental exchange analysis. The lack of prior knowledge about the specific physiological alterations taking place in a diseased muscle makes difficult the determination of restrictions to transmembrane exchange rates, which precludes the analysis and interpretation of the T2-spectra.

The relationship between tissue water relaxation and its structural compartmentation may be further explored by multidimensional NMR methods, which may be classified into correlation or exchange methods (107, 171, 172). In correlation methods, independent NMR parameters characterizing the tissue may be correlated in order to mutually characterize each other, offering complementary information that helps to validate and optimize the compartmental exchange model. In exchange methods, measurements of the same parameter are repeated and spaced by different mixing times; the water molecules that do not exchange during the mixing time will exhibit the same parameter-value between the different measurements and will appear as diagonal peaks in the bi-dimensional distribution, while protons that exchange during the mixing time will exhibit different parameter-values for each measurement and will appear as off-diagonal peaks.

Such exchange measurements allow assessing information about compartmental exchange rates, and might offer the necessary boundary conditions for analysing T2-distributions observed in unknown systems such as diseased tissue. The results of the study presented in Ch. 5 strongly encourage further investigation of myowater compartmentation models with the application of such multidimensional NMR methods.

This thesis work is to be continued, and the next steps include a T2-T2-relaxation exchange spectroscopy (REXSY) and a D-T2 diffusion relaxation correlation spectroscopy (DRCOSY) study. The choice of these methods was based on the conclusions concerning the interpretation of muscle T2-relaxation, which establish the conceptual bases for analysing T2-T2 and D-T2 data. The objectives of this future work are to further develop the compartmental exchange model for characterizing myowater distribution in healthy and diseased SKM tissue and to extend the compartmentation exchange analysis to other NMR parameters, offering a more complete knowledge about the variables characterizing the different anatomical tissue compartments, with the aim of contributing to the establishment of NMR tools that might offer more precise and specific characterization of the SKM tissue.

Relaxation data allowing the multiexponential study presented in chapter 5 respond to certain SNR and temporal sampling conditions that are not currently attainable with CPMG-like MSE imaging sequences. However one might wonder that the technological progress in the NMR field might eventually offer the necessary conditions for realising multiexponential analysis of NMRI data. Moreover, further understanding of the relaxation behaviour in SKM tissue shall offer more prior knowledge that will facilitate such analysis. Anatomical distribution of the information provided by multiexponential analysis would constitute an amazing non-invasive tool for clinical studies.

In Ch. 6 we addressed the problem related to the detection and characterization of IMCT by NMR methods. In previous studies, an NMRI technique, referred to as UTE, which allows acquisition of signal from fast relaxing protons ($T_2 \geq 10 \mu\text{s}$) has been shown to be able to image and characterize short-T2 structures such as tendon, cartilage, cortical bone, etc. (146, 150, 152). We have applied this technique to study the SKM tissue. Our results revealed a short-T2-component with a T_2^* -value around $400 \mu\text{s}$, and we could collect indices to what this component might represent connective tissue. Furthermore we proposed a method that allowed imaging, for the first time, diffuse short-T2-component in SKM tissue. Our results did not allow us to answer the question of what this short-T2-component might represent. The signal from water protons that are characterized by short T2-values observed in SKM tissue is generally agreed to come from hydration shells of macromolecules (112). As a consequence, the observed signal might come from water

hydrating the macromolecules of the contractile apparatus, as well as the macromolecules constituting the extracellular matrix.

An interesting *ex vivo* study that combines magnetization transfer (MT) and T2 relaxation measurements (170) revealed important differences in signal loss due to MT between the “intermediate” and “long” T2 components. In this technique, named MTCPMG, application of off-resonance pulses at different amplitudes with different frequency shifts are followed by a CPMG acquisition. Characterization of intrinsic anatomical compartments by compartmental exchange analysis might offer intrinsic information about compartmental MT properties. Such information shall give more insight to what concerns the anatomical distribution of short T2 components in SKM tissue. Finally, application of the presented studies in muscles presenting specific alterations of the collagen content, confirmed by histological analysis, and confrontation with other methods that offer indirect detection of fibrotic tissue distribution such as delayed gadolinium enhancement (173) shall offer valuable information in order to elucidate this issue.

Bibliography

1. Robertson, J.D. 1961. Studies on the Chemical Composition of Muscle Tissue. *J. Exp. Biol.* 38: 707–728.
2. Ling, G.N., and M.H. Kromash. 1967. The extracellular space of voluntary muscle tissues. *J. Gen. Physiol.* 50: 677–694.
3. Neville, B.Y.M.C., and S. White. 1979. From the Department of Physiology , University of Colorado Medical Center , . : 71–83.
4. Cullen, M.J., and D. Weightman. 1975. The ultrastructure of normal human muscle in relation to fiber type. *J. Neurol. Sci.* 25: 43–56.
5. Staron, R.S., E.S. Malicky, M.J. Leonardi, J.E. Falkel, F.C. Hagerman, et al. 1989. Muscle hypertrophy and fast fiber type conversions in heavy resistance-trained women. *Eur. J. Appl. Physiol.* 60: 71–79.
6. Kovanen, V., H. Suominen, and L. Peltonen. 1987. Effects of aging and life-long physical training on collagen in slow and fast skeletal muscle in rats. A morphometric and immuno-histochemical study. *Cell Tissue Res.* 248: 247–55.
7. Purslow, P.P., and J.A. Trotter. 1994. The morphology and mechanical properties of endomysium in series-fibred muscles; variations with muscle length. *J. Muscle Res. Cell Motil.* 15: 299–304.
8. DeGirolami, U., and T.W. Smith. 1982. Pathology of skeletal muscle diseases. *Am. J. Pathol.* : 235–276.
9. Huard, J., Y. Li, and F.H. Fu. 2002. Muscle injuries and repair: current trends in research. *J. Bone Joint Surg. Am.* 84-A: 822–32.
10. Burks, T.N., and R.D. Cohn. 2011. Role of TGF- β signaling in inherited and acquired myopathies. *Skelet. Muscle.* 1: 19.
11. Serrano, A.L., C.J. Mann, B. Vidal, E. Ardite, E. Perdiguero, et al. 2011. Cellular and molecular mechanisms regulating fibrosis in skeletal muscle repair and disease. .
12. Wattjes, M.P., R. a Kley, and D. Fischer. 2010. Neuromuscular imaging in inherited muscle diseases. *Eur. Radiol.* 20: 2447–60.
13. Tasca, G., E. Iannaccone, M. Monforte, M. Masciullo, F. Bianco, et al. 2012. Muscle MRI in Becker muscular dystrophy. *Neuromuscul. Disord.* 22 Suppl 2: S100–6.
14. Schulze, M., I. Kötter, U. Ernemann, M. Fenchel, N. Tzaribatchev, et al. 2009. MRI findings in inflammatory muscle diseases and their noninflammatory mimics. *AJR. Am. J. Roentgenol.* 192: 1708–16.

15. Schramm, N., C. Born, S. Weckbach, P. Reilich, M.C. Walter, et al. 2008. Involvement patterns in myotilinopathy and desminopathy detected by a novel neuromuscular whole-body MRI protocol. *Eur. Radiol.* 18: 2922–36.
16. Quijano-Roy, S., D. Avila-Smirnow, and R.Y. Carlier. 2012. Whole body muscle MRI protocol: pattern recognition in early onset NM disorders. *Neuromuscul. Disord.* 22 Suppl 2: S68–84.
17. Lampa, J., I. Nennesmo, H. Einarsdottir, and I. Lundberg. 2001. MRI guided muscle biopsy confirmed polymyositis diagnosis in a patient with interstitial lung disease. *Ann. Rheum. Dis.* 60: 423–6.
18. Udd, B. 2012. Distal myopathies--new genetic entities expand diagnostic challenge. *Neuromuscul. Disord.* 22: 5–12.
19. Yao, L., and N. Gai. 2012. Fat-corrected T2 measurement as a marker of active muscle disease in inflammatory myopathy. *Am. J. Roentgenol.* 198: W475–W481.
20. Willis, T. a, K.G. Hollingsworth, A. Coombs, M.-L. Sveen, S. Andersen, et al. 2013. Quantitative muscle MRI as an assessment tool for monitoring disease progression in LGMD2I: a multicentre longitudinal study. *PLoS One.* 8: e70993.
21. Wren, T. a L., S. Bluml, L. Tseng-Ong, and V. Gilsanz. 2008. Three-point technique of fat quantification of muscle tissue as a marker of disease progression in Duchenne muscular dystrophy: preliminary study. *AJR. Am. J. Roentgenol.* 190: W8–12.
22. Walter, G., L. Cordier, D. Bloy, and H.L. Sweeney. 2005. Noninvasive monitoring of gene correction in dystrophic muscle. *Magn. Reson. Med.* 54: 1369–1376.
23. Friedman, S.D., S.L. Poliachik, G.T. Carter, C.B. Budech, T.D. Bird, et al. 2012. The magnetic resonance imaging spectrum of facioscapulohumeral muscular dystrophy. *Muscle Nerve.* 45: 500–506.
24. Arpan, I., S.C. Forbes, D.J. Lott, C.R. Senesac, M.J. Daniels, et al. 2013. T2 mapping provides multiple approaches for the characterization of muscle involvement in neuromuscular diseases: a cross-sectional study of lower leg muscles in 5-15-year-old boys with Duchenne muscular dystrophy. *NMR Biomed.* 26: 320–328.
25. Mattei, J.P., D. Bendahan, and P. Cozzzone. 2004. P-31 Magnetic Resonance Spectroscopy . and pathophysiological insights in muscle diseases. 56: 9–14.
26. Park, J.H., J.P. Vansant, N.G. Kumar, S.J. Gibbs, M.S. Curvin, et al. 1990. Dermatomyositis: correlative MR imaging and P-31 MR spectroscopy for quantitative characterization of inflammatory disease. *Radiology.* 177: 473–479.
27. Pacak, C. a, G. a Walter, G. Gaidosh, N. Bryant, M. a Lewis, et al. 2007. Long-term skeletal muscle protection after gene transfer in a mouse model of LGMD-2D. *Mol. Ther.* 15: 1775–81.

28. Azzabou, N., P.L. de Sousa, E.C.A. Araujo, and P.G. Carlier. 2014. Validation of a generic approach to muscle water T2 determination in fat-infiltrated skeletal muscle. *J. Magn. Reson. Imaging*. .
29. De Sousa, P.L., A. Vignaud, E. Caldas de Almeida Araújo, and P.G. Carlier. 2012. Factors controlling T2 mapping from partially spoiled SSFP sequence: optimization for skeletal muscle characterization. *Magn. Reson. Med.* 67: 1379–1390.
30. Araujo, E.C.A., A. Vignaud, and P.G. Carlier. 2013. In Vivo muscle T2 spectra measurement with an ISIS CPMG sequence: Preliminary Findings in the Calf of Volunteers. In: *Proc. 30th ESMRMB, Toulouse/FR.* .
31. Araujo, E.C.A., Y. Fromes, and P.G. Carlier. 2014. Experimental confirmation of anatomical compartmentation theory for interpretation of T2-relaxation data. In: *Proc. 22nd ISMRM, Milan/Italy.* .
32. Araujo, E.C.A., Y. Fromes, and P.G. Carlier. 2014. New Insights on Human Skeletal Muscle Tissue Compartments Revealed by In Vivo T2 NMR Relaxometry. *Biophys. J.* 106: 2267–2274.
33. Jong, S. de, J.J. Zwanenburg, F. Visser, R. Van der Nagel, H. V van Rijen, et al. 2011. Direct detection of myocardial fibrosis by MRI. *J. Mol. Cell. Cardiol.* 51: 974–979.
34. Araujo, E.C.A., A. V. Vignaud, V. Jellus, and P.G. Carlier. 2012. Skeletal muscle short T2* component evaluated in the presence of fat by UTE imaging: preliminary findings in calf of human volunteers. In: *Proc. 17th WMS, Perth/Australia.* .
35. Araujo, E.C.A., A. Vignaud, V. Jellus, and P. Carlier. 2011. Skeletal Muscle Short T2* Component Evaluated by UTE Imaging : Preliminary Findings in the Calf of Volunteers. In: *Proc. 28th ESMRMB, Leipzig/DE.* .
36. Haacke, E.M., R.W. Brown, M.R. Thompson, and R. Venkatesan. 1999. *Magnetic Resonance Imaging - Physical Principles and Sequence Design.* New York: John Wiley & sons, Inc.
37. Lauterbur, P.C. 1973. Image Formation by Induced Local Interactions: Examples Employing Nuclear Magnetic Resonance. *Nature.* : 190–191.
38. Gold, G.E., J.M. Pauly, A. Macovski, and R.J. Herfkens. 1995. MR spectroscopic imaging of collagen: tendons and knee menisci. *Magn. Reson. Med.* 34: 647–654.
39. Hahn, E.L. 1950. Spin Echoes. *Phys. Rev.* 80: 580–601.
40. Bernstein, M.A., K.F. King, and X.J. Zhou. 2004. *Handbook of MRI pulse sequences.* Oxford, UK: Elsevier Academic Press.
41. Crawley, a P., M.L. Wood, and R.M. Henkelman. 1988. Elimination of transverse coherences in FLASH MRI. *Magn. Reson. Med.* 8: 248–60.

42. Zur, Y., M.L. Wood, and L.J. Neuringer. 1991. Spoiling of transverse magnetization in steady-state sequences. *Magn. Reson. Med.* 21: 251–63.
43. Duyn, J.H. 1997. Steady state effects in fast gradient echo magnetic resonance imaging. *Magn. Reson. Med.* 37: 559–68.
44. Carr, H.Y. 1958. Steady State Free Precession in Nuclear Magnetic Resonance. *Phys. Rev.* 112: 1693–1701.
45. Perkins, T.G., and F.W. Wehrli. 1986. CSF signal enhancement in short TR gradient echo images. *Magn. Reson. Imaging.* 4: 465–467.
46. Hendrick, R.E., J.B. Kneeland, and D.D. Stark. 1987. Maximizing signal-to-noise and contrast-to-noise ratios in flash imaging. *Magn. Reson. Imaging.* 5: 117–127.
47. Hawkes, R.C., and S. Patz. 1987. Rapid Fourier Imaging Using Steady-State Free Precession. 4: 9–23.
48. Buxton, R.B., C.R. Fisel, D. Chien, and T.J. Brady. 1989. Signal intensity in fast NMR imaging with short repetition times. *J. Magn. Reson.* 83: 576–585.
49. Carr, H., and E. Purcell. 1954. Effects of diffusion on free precession in nuclear magnetic resonance experiments. *Phys. Rev.* 94: 630–638.
50. Meiboom, S., and D. Gill. 1958. Modified spin-echo method for measuring nuclear relaxation times. *Rev. Sci. Instrum.* 29: 688–691.
51. Tofts, P.S. 1994. Standing waves in uniform water phantoms. *J. Magn. Reson.* 104: 143–147.
52. Yang, Q.X., J. Wang, X. Zhang, C.M. Collins, M.B. Smith, et al. 2002. Analysis of wave behavior in lossy dielectric samples at high field. *Magn. Reson. Med.* 47: 982–9.
53. Stollberger, R., and P. Wach. 1996. Imaging of the Active B₁ Field in Vivo. *J. Magn. Reson. Med.* 35: 246–251.
54. Cunningham, C.H., J.M. Pauly, and K.S. Nayak. 2006. Saturated double-angle method for rapid B₁₊ mapping. *Magn. Reson. Med.* 55: 1326–33.
55. Yarnykh, V.L. 2007. Actual flip-angle imaging in the pulsed steady state: a method for rapid three-dimensional mapping of the transmitted radiofrequency field. *Magn. Reson. Med.* 57: 192–200.
56. Dowell, N.G., and P.S. Tofts. 2007. Fast, accurate, and precise mapping of the RF field in vivo using the 180 degrees signal null. *Magn. Reson. Med.* 58: 622–30.
57. Maillard, S.M., R. Jones, C. Owens, C. Pilkington, P. Woo, et al. 2004. Quantitative assessment of MRI T₂ relaxation time of thigh muscles in juvenile dermatomyositis. *Rheumatology (Oxford).* 43: 603–8.

58. Friedman, S.D., S.L. Poliachik, G.T. Carter, C.B. Budech, T.D. Bird, et al. 2012. The magnetic resonance imaging spectrum of facioscapulohumeral muscular dystrophy. *Muscle Nerve*. 45: 500–6.
59. Poon, C.S., and R.M. Henkelman. 1992. Practical T2 quantitation for clinical applications. *J. Magn. Reson. Imaging*. 2: 541–53.
60. Lebel, R.M., and A.H. Wilman. 2010. Transverse relaxometry with stimulated echo compensation. *Magn. Reson. Med*. 64: 1005–1014.
61. Horn, P.S., J.M. Racadio, B. Wong, and B.J. Dardzinski. 2010. T2 Mapping in Duchenne Muscular Dystrophy : Distribution of Disease Activity and Correlation with Clinical Assessments 1 Purpose : Methods : Results : 255: 899–908.
62. Huang, Y., S. Majumdar, H.K. Genant, W.P. Chan, K.R. Sharma, et al. 1994. Quantitative MR relaxometry study of muscle composition and function in Duchenne muscular dystrophy. *Magn. Reson. Imaging*. 4: 59–64.
63. Phoenix, J., D. Betal, N. Roberts, T.R. Helliwell, and R.H. Edwards. 1996. Objective quantification of muscle and fat in human dystrophic muscle by magnetic resonance image analysis. *Muscle Nerve*. 19: 302–310.
64. Garrod, P., K.G. Hollingsworth, M. Eagle, B.S. Aribisala, D. Birchall, et al. 2009. MR imaging in Duchenne muscular dystrophy: quantification of T1-weighted signal, contrast uptake, and the effects of exercise. *Magn. Reson. Imaging*. 30: 1130–1138.
65. Gloor, M., S. Fasler, A. Fischmann, T. Haas, O. Bieri, et al. 2011. Quantification of fat infiltration in oculopharyngeal muscular dystrophy: comparison of three MR imaging methods. *Magn. Reson. Imaging*. 33: 203–210.
66. Prasloski, T., B. Mädler, Q.-S. Xiang, A. MacKay, and C. Jones. 2012. Applications of stimulated echo correction to multicomponent T2 analysis. *Magn. Reson. Med*. 67: 1803–14.
67. Dixon, W.T. 1984. Simple proton spectroscopic imaging. *Radiology*. 153: 189–94.
68. Reeder, S.B., A.R. Pineda, Z. Wen, A. Shimakawa, H. Yu, et al. 2005. Iterative decomposition of water and fat with echo asymmetry and least-squares estimation (IDEAL): application with fast spin-echo imaging. *Magn. Reson. Med*. 54: 636–44.
69. Schick, F., B. Eismann, W.I. Jung, H. Bongers, M. Bunse, et al. 1993. Comparison of localized proton NMR signals of skeletal muscle and fat tissue in vivo: two lipid compartments in muscle tissue. *Magn. Reson. Med*. 29: 158–67.
70. Peterson, P., and S. Månsson. 2012. Simultaneous quantification of fat content and fatty acid composition using MR imaging. *Magn. Reson. Med*. 000.
71. Kan, H.E., T.W.J. Scheenen, M. Wohlgemuth, D.W.J. Klomp, I. van Loosbroek-Wagenmans, et al. 2009. Quantitative MR imaging of individual muscle

- involvement in facioscapulohumeral muscular dystrophy. *Neuromuscul. Disord.* 19: 357–362.
72. Nehrke, K. 2009. On the steady-state properties of actual flip angle imaging (AFI). *Magn. Reson. Med.* 61: 84–92.
 73. Reeder, S.B., P.M. Robson, H. Yu, A. Shimakawa, C.D.G. Hines, et al. 2009. Quantification of hepatic steatosis with MRI: the effects of accurate fat spectral modeling. *Magn. Reson. Imaging.* 29: 1332–1339.
 74. Dixon, W.T., H. Engels, M. Castillo, and M. Sardashti. 1990. Incidental magnetization transfer contrast in standard multislice imaging. *Magn. Reson. Imaging.* 8: 417–422.
 75. Hines, C.D.G., H. Yu, A. Shimakawa, C. a McKenzie, J.H. Brittain, et al. 2009. T1 independent, T2* corrected MRI with accurate spectral modeling for quantification of fat: validation in a fat-water-SPIO phantom. *J. Magn. Reson. Imaging.* 30: 1215–22.
 76. Yokota, T., Q.-L. Lu, T. Partridge, M. Kobayashi, A. Nakamura, et al. 2009. Efficacy of systemic morpholino exon-skipping in Duchenne dystrophy dogs. *Ann. Neurol.* 65: 667–676.
 77. Tardif-de Géry, S., J. Vilquin, P. Carlier, J.S. Raynaud, C. Wary, et al. 2000. Muscular transverse relaxation time measurement by magnetic resonance imaging at 4 Tesla in normal and dystrophic dy/dy and dy(2j)/dy(2j) mice. *Neuromuscul. Disord.* 10: 507–513.
 78. Liu, M., P. Bose, G. a Walter, D.K. Anderson, F.J. Thompson, et al. 2006. Changes in muscle T2 relaxation properties following spinal cord injury and locomotor training. *Eur. J. Appl. Physiol.* 97: 355–361.
 79. Thibaud, J.-L., A. Monnet, D. Bertoldi, I. Barthélémy, S. Blot, et al. 2007. Characterization of dystrophic muscle in golden retriever muscular dystrophy dogs by nuclear magnetic resonance imaging. *Neuromuscul. Disord.* 17: 575–584.
 80. Bieri, O., K. Scheffler, G.H. Welsch, S. Trattnig, T.C. Mamsch, et al. 2011. Quantitative mapping of T2 using partial spoiling. *Magn. Reson. Med.* 66: 410–418.
 81. Deoni, S.C.L., B.K. Rutt, and T.M. Peters. 2003. Rapid combined T1 and T2 mapping using gradient recalled acquisition in the steady state. *Magn. Reson. Med.* 49: 515–526.
 82. Schmitt, P., M. a Griswold, P.M. Jakob, M. Kotas, V. Gulani, et al. 2004. Inversion recovery TrueFISP: quantification of T(1), T(2), and spin density. *Magn. Reson. Med.* 51: 661–6677.
 83. Newbould, R.D., S.T. Skare, M.T. Alley, G.E. Gold, and R. Bammer. 2010. Three-dimensional T(1), T(2) and proton density mapping with inversion recovery balanced SSFP. *Magn. Reson. Imaging.* 28: 1374–1382.

84. Deoni, S.C.L. 2009. Transverse relaxation time (T2) mapping in the brain with off-resonance correction using phase-cycled steady-state free precession imaging. *J. Magn. Reson. Imaging.* 30: 411–7.
85. Crooijmans, H.J. a, M. Gloor, O. Bieri, and K. Scheffler. 2011. Influence of MT effects on T(2) quantification with 3D balanced steady-state free precession imaging. *Magn. Reson. Med.* 65: 195–201.
86. Ganter, C. 2006. Steady state of gradient echo sequences with radiofrequency phase cycling: analytical solution, contrast enhancement with partial spoiling. *Magn. Reson. Med.* 55: 98–107.
87. Bieri, O., K. Scheffler, and C. Ganter. 2009. Fast T2 Mapping Using Partially Spoiled Steady State Free Precession (T2-pSSFP). In: *Proc. 17th ISMRM, Honolulu, Hawaii, USA.* . p. 2634.
88. Bieri, O., K. Scheffler, and C. Ganter. 2010. T1 corrected Fast T2 Mapping Using Partially Spoiled SSFP. In: *Proc. 18th ISMRM, Stockholm, Sweden.* . p. 3715.
89. De Sousa, P.L., A. Vignaud, L. Cabrol, and P.G. Carlier. 2010. Simultaneous T1 and T2 mappings using partially Spoiled Steady State Free Precession (pSSFP). In: *Proc. 18th ISMRM, Stockholm, Sweden.* . p. 2968.
90. Schick, F. 2005. Whole-body MRI at high field: technical limits and clinical potential. *Eur. Radiol.* 15: 946–59.
91. Dietrich, O., M.F. Reiser, and S.O. Schoenberg. 2008. Artifacts in 3-T MRI: physical background and reduction strategies. *Eur. J. Radiol.* 65: 29–35.
92. Storey, P., V. Lee, D. Sodickson, D. Santoro, B. Zhang, et al. 2009. B1 inhomogeneity in the thigh at 3T and implications for peripheral vascular imaging. In: *Proc. 17th ISMRM, Honolulu, Hawaii, USA.* .
93. Sinclair, C.D.J., R.S. Samson, D.L. Thomas, N. Weiskopf, A. Lutti, et al. 2010. Quantitative magnetization transfer in in vivo healthy human skeletal muscle at 3 T. *Magn. Reson. Med.* 64: 1739–48.
94. Preibisch, C., and R. Deichmann. 2009. Influence of RF spoiling on the stability and accuracy of T1 mapping based on spoiled FLASH with varying flip angles. *Magn. Reson. Med.* 61: 125–35.
95. Nehrke, K. 2009. On the steady-state properties of actual flip angle imaging (AFI). *Magn. Reson. Med.* 61: 84–92.
96. Gold, G., E. Han, J. Stainsby, G. Wright, J. Brittain, et al. 2004. Musculoskeletal MRI at 3.0 T: relaxation times and image contrast. *Am. J. Roentgenol.* : 343–351.
97. Pai, A., X. Li, and S. Majumdar. 2008. A comparative study at 3 T of sequence dependence of T 2 quantitation in the knee. *Magn. Reson. Imaging.* 26: 1215–1220.

98. Kellis, E., and V. Baltzopoulos. 1995. Isokinetic eccentric exercise. *Sport. Med.* 19: 202–222.
99. Bland, J.M., and D.G. Altman. 1986. Statistical methods for assessing agreement between two methods of clinical measurement. *Lancet.* 1: 307–10.
100. Cheng, H.-L.M., and G. a Wright. 2006. Rapid high-resolution T(1) mapping by variable flip angles: accurate and precise measurements in the presence of radiofrequency field inhomogeneity. *Magn. Reson. Med.* 55: 566–74.
101. Schabel, M.C., and G.R. Morrell. 2009. Uncertainty in T(1) mapping using the variable flip angle method with two flip angles. *Phys. Med. Biol.* 54: N1–8.
102. Foley, J.M., R.C. Jayaraman, B.M. Prior, J.M. Pivarnik, and R. a Meyer. 1999. MR measurements of muscle damage and adaptation after eccentric exercise. *J. Appl. Physiol.* 87: 2311–2318.
103. Marqueste, T., B. Giannesini, Y. Le Fur, P.J. Cozzone, and D. Bendahan. 2008. Comparative MRI analysis of T2 changes associated with single and repeated bouts of downhill running leading to eccentric-induced muscle damage. *J. Appl. Physiol.* 105: 299–307.
104. Proske, U., and D.L. Morgan. 2001. Muscle damage from eccentric exercise: mechanism, mechanical signs, adaptation and clinical applications. *J. Physiol.* 537: 333–45.
105. Laurens, E., E. Schneider, C. Winalski, and A. Calabro. 2012. A synthetic cartilage extracellular matrix model: hyaluronan and collagen hydrogel relaxivity, impact of macromolecular concentration on dGEMRIC. *Skeletal Radiol.* 41: 209–217.
106. Cole, W.C., a D. LeBlanc, and S.G. Jhingran. 1993. The origin of biexponential T2 relaxation in muscle water. *Magn. Reson. Med.* 29: 19–24.
107. Dortch, R.D., R.A. Horch, and M.D. Does. 2009. Development, simulation, and validation of NMR relaxation-based exchange measurements. *J. Chem. Phys.* 131: 164502.
108. Gore, J.C., M.S. Brown, C.T. Mizumoto, and I.M. Armitage. 1986. Influence of glycogen on water proton relaxation times. *Magn. Reson. Med.* 3: 463–466.
109. Bertram, H.C., A.H. Karlsson, M. Rasmussen, O.D. Pedersen, S. Dønstrup, et al. 2001. Origin of multiexponential T2 relaxation in muscle myowater. *J. Agric. Food Chem.* 49: 3092–3100.
110. Edzes, H.T., and E.T. Samulski. 1977. Cross relaxation and spin diffusion in the proton NMR of hydrated collagen. *Nature.* 265: 521–523.
111. Belton, P.S., R.R. Jackson, and J. Packer. 1972. Pulsed NMR studies of water in striated muscle. I. Transverse nuclear spin relaxation times and freezing effects. *Biochim. Biophys. Acta.* 286: 16–25.

112. Hazlewood, C.F., D.C. Chang, B.L. Nichols, and D.E. Woessner. 1974. Nuclear magnetic resonance transverse relaxation times of water protons in skeletal muscle. *Biophys. J.* 14: 583–606.
113. Fung, B.M., and P.S. Puon. 1981. Nuclear magnetic resonance transverse relaxation in muscle water. *Biophys. J.* 33: 27–37.
114. Le Rumeur, E., J. De Certaines, P. Toulouse, and P. Rochcongar. 1987. Water phases in rat striated muscles as determined by T₂ proton NMR relaxation times. *Magn. Reson. Imaging.* 5: 267–272.
115. Saab, G., R.T. Thompson, and G.D. Marsh. 1999. Multicomponent T₂ relaxation of in vivo skeletal muscle. *Magn. Reson. Med.* 42: 150–7.
116. Kimura, M., S. Takemori, M. Yamaguchi, and Y. Umazume. 2005. Differential osmotic behavior of water components in living skeletal muscle resolved by ¹H-NMR. *Biophys. J.* 89: 1143–1149.
117. Adzamli, I.K., F. Jolesz, A.R. Bleier, R. V Mulkern, and T. Sandor. 1989. The effect of gadolinium DTPA on tissue water compartments in slow- and fast-twitch rabbit muscles. *Magn. Reson.* 11: 172–181.
118. Noseworthy, M.D., J.K. Kim, J. a Stainsby, G.J. Stanisz, and G. a Wright. 1999. Tracking oxygen effects on MR signal in blood and skeletal muscle during hyperoxia exposure. *J. Magn. Reson. Imaging.* 9: 814–820.
119. Stainsby, J. a, and G. a Wright. 2001. Monitoring blood oxygen state in muscle microcirculation with transverse relaxation. *Magn. Reson. Med.* 45: 662–72.
120. Saab, G., R.T. Thompson, and G.D. Marsh. 2000. Effects of exercise on muscle transverse relaxation determined by MR imaging and in vivo relaxometry. *J. Appl. Physiol.* 88: 226–33.
121. Saab, G., R.T. Thompson, G.D. Marsh, P.A. Picot, and G.R. Moran. 2001. Two-Dimensional Time Correlation Relaxometry of Skeletal Muscle In Vivo at 3 Tesla. *J. Magn. Reson. Med.* 46: 1093–1098.
122. Saab, G., G.D. Marsh, M. a Casselman, and R.T. Thompson. 2002. Changes in human muscle transverse relaxation following short-term creatine supplementation. *Exp. Physiol.* 87: 383–389.
123. Ordidge, R., A. Connelly, and J. Lohman. 1986. Image-selected in Vivo spectroscopy (ISIS). A new technique for spatially selective NMR spectroscopy. *J. Magn. Reson.* 66: 283–294.
124. Le Roux, P., R.J. Gilles, G.C. McKinnon, and P.G. Carlier. 1998. Optimized outer volume suppression for single-shot fast spin-echo cardiac imaging. *J. Magn. Reson. Imaging.* 8: 1022–1032.
125. Balchandani, P., J. Pauly, and D. Spielman. 2010. Designing adiabatic radio

- frequency pulses using the Shinnar-Le Roux algorithm. *Magn. Reson. Med.* 64: 843–851.
126. Whittall, K.P., and A.L. MacKay. 1989. Quantitative interpretation of NMR relaxation data. *J. Magn. Reson.* 84: 134–152.
 127. Lawson, C.L., and R.J. Hanson. 1974. *Solving Least Squares Problems*. Society for Industrial and Applied Mathematics, Philadelphia.
 128. McConnell, M.H. 1958. Reaction rates by nuclear magnetic resonance. *J. Chem. Phys.* 28: 430–431.
 129. Chen, J., and G. Pike. 2009. Human whole blood T2 relaxometry at 3 tesla. *Magn. Reson. Med.* 61: 249–254.
 130. Norris, D., H. Lüdemann, and D. Leibfritz. 1991. An analysis of the effects of short T2 values on the hyperbolic-secant pulse. *J. Magn. Reson.* 92: 94–101.
 131. Quirk, J.D., G.L. Bretthorst, T.Q. Duong, A.Z. Snyder, C.S. Springer, et al. 2003. Equilibrium water exchange between the intra- and extracellular spaces of mammalian brain. *Magn. Reson. Med.* 50: 493–499.
 132. Landis, C.S., X. Li, F.W. Telang, P.E. Molina, I. Palyka, et al. 1999. Equilibrium transcytolemmal water-exchange kinetics in skeletal muscle in vivo. *Magn. Reson. Med.* 42: 467–478.
 133. Rose, C.P., C.A. Goresky, and G.G. Bach. 1977. The capillary and sarcolemmal barriers in the heart. An exploration of labeled water permeability. *Circ. Res.* 41: 515–533.
 134. Donahue, K.M., D. Burstein, W.J. Manning, and M.L. Gray. 1994. Studies of Gd-DTPA relaxivity and proton exchange rates in tissue. *Magn. Reson. Med.* 32: 66–76.
 135. Ploutz-Snyder, L.L., S. Nyren, T.G. Cooper, E.J. Potchen, and R. a Meyer. 1997. Different effects of exercise and edema on T2 relaxation in skeletal muscle. *Magn. Reson. Med.* 37: 676–682.
 136. Paudyal, R., H. Poptani, K. Cai, R. Zhou, and J.D. Glickson. 2013. Impact of transvascular and cellular-interstitial water exchange on dynamic contrast-enhanced magnetic resonance imaging estimates of blood to tissue transfer constant and blood plasma volume. *J. Magn. Reson. Imaging.* 37: 435–444.
 137. Aukland, K., and G. Nicolaysen. 1981. Interstitial fluid Volume: local regulatory mechanisms. *Physiol. Rev.* 61: 556–643.
 138. Schütze, H., W. Hildebrandt, and J. Stegemann. 1991. The interstitial fluid content in working muscle modifies the cardiovascular response to exercise. *Eur. J. Appl. Physiol.* 62: 332–336.

139. Wright, G.A., B.S. Hu, and A. Macovski. 1991. Estimating oxygen saturation of blood in vivo with MR imaging at 1.5 T. *J. Magn. Reson. Imaging.* 1: 275–283.
140. Lee, J., C. Labadie, C.S. Springer, and G.S. Harbison. 1993. Two-dimensional inverse Laplace transform NMR: altered relaxation times allow detection of exchange correlation. *J. Am. Chem. Soc.* 115: 7761–7764.
141. Desguerre, I., M. Mayer, F. Leturcq, J.-P. Barbet, R.K. Gherardi, et al. 2009. Endomysial Fibrosis in Duchenne Muscular Dystrophy: A Marker of Poor Outcome Associated With Macrophage Alternative Activation. *J. Neuropathol. Exp. Neurol.* 68: 762–773.
142. Zhou, L., and H. Lu. 2010. Targeting fibrosis in Duchenne muscular dystrophy. *J. Neuropathol. Exp.* 69: 771–776.
143. Klingler, W., K. Jurkat-Rott, F. Lehmann-Horn, and R. Schleip. 2012. The role of fibrosis in Duchenne muscular dystrophy. *Acta Myol.* 31: 184–95.
144. Chen, C.K.H., L. Yeh, W.-N. Chang, H.-B. Pan, and C.-F. Yang. 2006. MRI diagnosis of contracture of the gluteus maximus muscle. *AJR. Am. J. Roentgenol.* 187: W169–74.
145. Du, J., A.M. Takahashi, W.C. Bae, C.B. Chung, and G.M. Bydder. 2010. Dual inversion recovery, ultrashort echo time (DIR UTE) imaging: Creating high contrast for short- T 2 species. *Magn. Reson. Med.* 63: 447–455.
146. Filho, G.H., J. Du, B.C. Pak, S. Statum, R. Znamorowski, et al. 2009. Quantitative characterization of the Achilles tendon in cadaveric specimens: T1 and T2* measurements using ultrashort-TE MRI at 3 T. *AJR. Am. J. Roentgenol.* 192: W117–24.
147. Park, J.-Y., S. Moeller, U. Goerke, E. Auerbach, R. Chamberlain, et al. 2012. Short echo-time 3D radial gradient-echo MRI using concurrent dephasing and excitation. *Magn. Reson. Med.* 67: 428–36.
148. Conolly, S., D. Nishimura, and A. Macovski. 1988. Variable-rate selective excitation. *J. Magn. Reson.* 78: 440–458.
149. Pauly, J.M., S.C. M., D.G. Nishimura, and A. Macovski. 1989. Slice selective excitation for very short T2 species. In: *Proc. 8th SMRM, Amsterdam, Netherlands.* . p. 28.
150. Du, J., A.M. Takahashi, and C.B. Chung. 2009. Ultrashort TE spectroscopic imaging (UTESI): Application to the imaging of short T2 relaxation tissues in the musculoskeletal system. *J. Magn. Reson. Imaging.* 29: 412–421.
151. Carl, M., M. Bydder, J. Du, A. Takahashi, and E. Han. 2010. Optimization of RF excitation to maximize signal and T2 contrast of tissues with rapid transverse relaxation. *Magn. Reson. Med.* 64: 481–90.

152. Bae, W.C., P.C. Chen, C.B. Chung, K. Masuda, D. D’Lima, et al. 2012. Quantitative ultrashort echo time (UTE) MRI of human cortical bone: correlation with porosity and biomechanical properties. *J. Bone Miner. Res.* 27: 848–857.
153. Larson, P.E.Z., S.M. Conolly, J.M. Pauly, and D.G. Nishimura. 2007. Using adiabatic inversion pulses for long-T2 suppression in ultrashort echo time (UTE) imaging. *Magn. Reson. Med.* 58: 952–961.
154. Larson, P.E.Z., P.T. Gurney, K. Nayak, G.E. Gold, J.M. Pauly, et al. 2006. Designing long-T2 suppression pulses for ultrashort echo time imaging. *Magn. Reson. Med.* 56: 94–103.
155. Du, J., M. Bydder, A.M. Takahashi, M. Carl, C.B. Chung, et al. 2011. Short T2 contrast with three-dimensional ultrashort echo time imaging. *Magn. Reson. Imaging.* 29: 470–82.
156. Sussman, M.S., J.M. Pauly, and G.A. Wright. 1998. Design of practical T2-selective RF excitation (TELEX) pulses. *Magn. Reson. Med.* 40: 890–899.
157. Li, C., J.F. Magland, H.S. Rad, H.K. Song, and F.W. Wehrli. 2012. Comparison of optimized soft-tissue suppression schemes for ultrashort echo time MRI. *Magn. Reson. Med.* 68: 680–689.
158. Hernando, D., P. Kellman, J.P. Haldar, and Z.-P. Liang. 2010. Robust water/fat separation in the presence of large field inhomogeneities using a graph cut algorithm. *Magn. Reson. Med.* 63: 79–90.
159. Hernando, D., J.P. Haldar, B.P. Sutton, J. Ma, P. Kellman, et al. 2008. Joint estimation of water/fat images and field inhomogeneity map. *Magn. Reson. Med.* 59: 571–80.
160. Pauly, J.M., S.M. Conolly, D.G. Nishimura, and A. Macovski. 1989. Slice-selective excitation for very short T2 species. In: *Proc. 8th SMRM, Amsterdam, Netherlands.* . p. 28.
161. Hollingsworth, K.G., P.L. de Sousa, V. Straub, and P.G. Carlier. 2012. Towards harmonization of protocols for MRI outcome measures in skeletal muscle studies: consensus recommendations from two TREAT-NMD NMR workshops, 2 May 2010, Stockholm, Sweden, 1-2 October 2009, Paris, France. *Neuromuscul. Disord.* 22 Suppl 2: S54–67.
162. Willcocks, R.J., I. a Arpan, S.C. Forbes, D.J. Lott, C.R. Senesac, et al. 2014. Longitudinal measurements of MRI-T2 in boys with Duchenne muscular dystrophy: Effects of age and disease progression. *Neuromuscul. Disord.* .
163. Janiczek, R.L., G. Gambarota, C.D.J. Sinclair, T.A. Yousry, J.S. Thornton, et al. 2011. Simultaneous T2 and lipid quantitation using IDEAL-CPMG. *Magn. Reson. Med.* 66: 1293–302.
164. Airapetyan, R.G., and A.G. Ramm. 2000. Numerical Inversion of the Laplace

- Transform from the Real Axis. *J. Math. Anal. Appl.* 248: 572–587.
165. Jibia, A.U., and M.-J.E. Salami. 2012. An Appraisal of Gardner Transform-Based Methods of Transient Multiexponential Signal Analysis. *Int. J. Comput. Theory Eng.* 4: 16–25.
 166. Clayden, N. 1992. Pade–Laplace analysis in the fitting of multi-exponential nuclear magnetic resonance relaxation decay curves. *J. Chem. Soc., Faraday Trans.* 88: 2481–2486.
 167. Radiology, D., and L. Imaging. 1990. Projection Presaturation : A Fast and Accurate Technique for Multidimensional Spatial Localization. *Isis.* 583: 567–583.
 168. Qin, Q., J.C. Gore, R. a de Graaf, and M.D. Does. 2007. Quantitative T2 measurement of a single voxel with arbitrary shape using pinwheel excitation and CPMG acquisition. *MAGMA.* 20: 233–40.
 169. Connelly, A., C. Counsell, and J.A.B. Lohman. 1988. Outer volume suppressed image related in vivo spectroscopy (OSIRIS), a high-sensitivity localization technique. *J. Magn. Reson.* 78: 519–525.
 170. Harrison, R., M.J. Bronskill, and R.M. Henkelman. 1995. Magnetization Transfer and T2 Relaxation Components in Tissue. *Magn. Reson. Med.* 33: 490–496.
 171. Peled, S., D.G. Cory, S. a Raymond, D. a Kirschner, and F. a Jolesz. 1999. Water diffusion, T(2), and compartmentation in frog sciatic nerve. *Magn. Reson. Med.* 42: 911–918.
 172. Qiao, Y., P. Galvosas, and P.T. Callaghan. 2005. Diffusion correlation NMR spectroscopic study of anisotropic diffusion of water in plant tissues. *Biophys. J.* 89: 2899–905.
 173. Schelbert, E.B., L. Hsu, S.A. Anderson, and B.D. Mohanty. 2012. NIH Public Access. 3: 743–752.